

UC Irvine

UC Irvine Electronic Theses and Dissertations

Title

Large-Scale Testing of Reinforced Concrete Moment Resisting Frame Beams with Rectangular Web Openings

Permalink

<https://escholarship.org/uc/item/27v267tp>

Author

Herrera, Luis

Publication Date

2017

Peer reviewed|Thesis/dissertation

UNIVERSITY OF CALIFORNIA,
IRVINE

Large-Scale Testing of Reinforced Concrete Moment Resisting Frame Beams with Rectangular
Web Openings

DISSERTATION

submitted in partial satisfaction of the requirements
for the degree of

DOCTOR OF PHILOSOPHY

in Civil Engineering

by

Luis Herrera

Dissertation Committee:
Assistant Professor Anne Lemnitzer, Chair
Associate Professor Farzin Zareian
Professor Lizhi Sun
Associate Professor Leonardo Massone

2017

DEDICATION

To

my parents: Jose Luis and Olga Herrera

TABLE OF CONTENTS

	Page
LIST OF FIGURES	vi
LIST OF TABLES	xvi
ACKNOWLEDGMENTS	xviii
CURRICULUM VITAE	xix
ABSTRACT OF THE DISSERTATION	xx
Chapter 1 Introduction	1
1.1 Background.	1
1.2 Objectives	4
1.3 Organization	5
Chapter 2 Literature Review	6
2.1 Research Performed on RC Beams with Openings	6
2.1.1 Beams with Small Openings	7
2.1.2 Beams with Large Openings	12
2.1.3 Deep Beams with Openings	15
2.1.4 Externally Strengthened Beams with Openings	18
2.2 Cyclically Loaded RC Beams	20
2.2.1 SMRF Beam Design	20
2.2.2 Experimental Investigations on Cyclically Loaded RC Beams	26
2.3 Strut and Tie Modeling	33
2.3.1 STM Development and Research	33

2.3.2 ACI STM Design	36
2.3.3 Nonlinear Strut and Tie Modeling	42
2.4 Conclusions on Literature Review	51
Chapter 3 Specimen Details	53
3.1 Specimen Design and Test Matrix	53
3.2 Test Specimen Details	55
Chapter 4 Experimental Program	64
4.1 Construction	64
4.2 Test Setup	71
4.2.1 Reaction System	72
4.2.2 Load Application System	75
4.3 Loading Protocol	77
4.4 Instrumentation	80
4.5 Material Properties	92
4.5.1 Concrete	92
4.5.2 Steel	94
Chapter 5 Experimental Results	97
5.1 Experimentally Observed Damage and Behavior	97
5.1.1 Specimen 1	103
5.1.2 Specimen 2	106
5.1.3 Specimen 3	110
5.1.4 Specimen 4	115
5.2 Summary of Test Results	119

5.3 Boundary Condition: Rotation of Reaction Blocks	121
5.4 Load versus Tip Displacement	123
5.5 Moment Rotation Relationships	129
5.6 Beam Deflection Profiles	136
5.7 Dissipated Energy	139
5.8 Deflection Components	140
5.9 Beam Axial Elongation	151
Chapter 6 Nonlinear Strut and Tie Modelling	154
6.1 Strut and Tie Model Formulation	154
6.1.1 Monotonic Model Formulation	155
6.1.2 Cyclic Model Formulation	163
6.2 Monotonic STM Results	166
6.3 Cyclic STM Results	182
6.3.1 Cyclic STM 1	182
6.3.2 Cyclic STM 2	194
6.3.3 Hysteretic Steel Material for Cyclic STM	201
Chapter 7 Summary and Conclusions	211
References	214
Appendix A- Material Properties	219

LIST OF FIGURES

	Page
Figure 1.1: Typical layout of a moment resisting frame structure with expected plastic hinging	2
Figure 2.1: Two modes of shear failure of small openings. Left: beam type failure, Right: Frame type failure [Mansur (2005)]	9
Figure 2.2: Shear resistance provided by shear reinforcement at opening [Mansur (2005)]	10
Figure 2.3: Free body diagram at opening [Mansur (2005)]	12
Figure 2.4: Beam with large opening under bending and shear [Mansur (2006)]	13
Figure 2.5: Left: Truss action, Right: Arrangement of reinforcement [AIJ 1994]	14
Figure 2.6: Structural idealization of deep beams with openings [Kong and Sharp (1972)]	18
Figure 2.7: Left: story mechanism, Middle: intermediate mechanism, Right: beam mechanism [Moehle 2008]	21
Figure 2.8: Beam flexural reinforcement requirements [Moehle 2008]	23
Figure 2.9: Design beam shear based on probable moment strengths combined with factored gravity loads [Moehle 2008]	24
Figure 2.10: Hoop and stirrup location and spacing requirement [Moehle 2008]	25
Figure 2.11: Hoop configurations (a) single closed hoop, (b) overlapping hoops, (c) stirrups with crossties [Visnijić 2014]	26
Figure 2.12: B- and D-regions [ACI 318-14]	37
Figure 2.13: Modeling of concrete and reinforcing steel elements [Park and Eom (2007)]	43
Figure 2.14: Cyclic stress-strain relationship for concrete (left) and steel (right) used in Park and Eom (2007)	44

Figure 2.15: Analytical results of a cantilever beam from Park and Eom (2007)	45
Figure 2.16: Composition of arch and truss action that leads to compatibility strut-and-tie model Scott et al. (2012)	45
Figure 2.17: Concrete stress-strain behavior for C-STM [Scott et. al. (2012)]	47
Figure 2.18: Analytical results of C-STM [Karthick et. al. (2016)]	48
Figure 2.19: Formulation of beam-truss model for a T-shape section wall [Lu and Panagiotou 2013)]	49
Figure 2.20: Stress-strain relationship for concrete [Lu and Panagiotou (2013)]	50
Figure 2.21: Analytical results from beam-truss model [Lu et.al. (2014)]	51
Figure 3.1: Elevation view of generic test specimen with geometry and reinforcement	54
Figure 3.2: General reinforcement description in cross-section of sections A (left), B (center), and C (right). Dimensions in inches and SI units shown in brackets [mm]	58
Figure 3.3: Beam elevation geometry and reinforcement details for S1	59
Figure 3.4: Beam elevation geometry and reinforcement details for S2	60
Figure 3.5: Beam elevation geometry and reinforcement details for S3	61
Figure 3.6: Beam elevation geometry and reinforcement details for S4	62
Figure 3.7: Top view of reaction block and beam specimen	63
Figure 4.1: Rebar delivery to the UCI structural laboratory	64
Figure 4.2: Stirrup assembly at the UCI structural lab using a prefabricated mold	65
Figure 4.3: Left: Assembly of stirrups for the reaction block stacked in front of the strong wall; Right Construction of the reaction block for S1	66
Figure 4.4: Left: Completed rebar cages for S4(left) and S1(right); Right: Formwork panels for the reaction block.	67

Figure 4.5: Left: Top view of reaction block for S1 reinforcement with PVC pipes into strong wall and strong floor; Right: Completed reaction block formwork and construction of beam formwork	67
Figure 4.6: Almost completed formwork for S4	67
Figure 4.7: Left: Completed formwork for S1 and view of top slab reinforcement; Middle: Lateral formwork bracing; Right: Formwork around opening of S1	68
Figure 4.8: Schematic showing typical concrete pouring schedule with construction joint	69
Figure 4.9: Left: Completion of concrete placement stage 1 (beam and bottom block) of S1; Right: Top slab for S1 is completely poured; Pumper fills up the top of the reaction block	69
Figure 4.10: Left: Concrete placement of S3 and simultaneous slab finishing; Right: Completed concrete pour of S4	70
Figure 4.11: Left: Inspector prepares concrete cylinders for strength tests; Middle & Right: Slump tests for concrete in S1 (slump~6.5 in.)	70
Figure 4.12: Schematic of test setup	71
Figure 4.13: Photograph of typical completed test setup	72
Figure 4.14: Left: Elevation view of reinforcement of the reaction block; Right: Section view of the reaction block demonstrating the reinforcement details	73
Figure 4.15: Photograph of completed reinforcement for reaction block	74
Figure 4.16: Left: Method of post-tensioning of steel anchors; Right: Completed test setup with arrows pointing to anchorage points	75
Figure 4.17: Left: Loading frame with actuator, anchors into the strong floor and chains around the top of the beam and into the strong floor; Right: U-plate system at load application point with post-tensioned rods	76

Figure 4.18: Loading sequence for specimens S1 to S4	78
Figure 4.19: Left: Strain gauges installed along the longitudinal rebar before cage construction; Right: Strain gauge attached to a #8 bar during installation process	81
Figure 4.20: Left: String potentiometer sensor before installation; Right: Calibration of LVDT	82
Figure 4.21: Horizontal LVDTs	84
Figure 4.22: Diagonal LVDTs	84
Figure 4.23: Location of external sensors	85
Figure 4.24: Layout of strain gauges on S1	86
Figure 4.25: Layout of string potentiometers on S1	86
Figure 4.26: Layout of horizontal and diagonal LVDTs on S1	87
Figure 4.27: Layout of strain gauges on S2	87
Figure 4.28: Layout of string potentiometers on S2	88
Figure 4.29: Layout of horizontal and diagonal LVDTs on S2	88
Figure 4.30: Layout of strain gauges on S3	89
Figure 4.31: Layout of string potentiometers on S3	89
Figure 4.32: Layout of horizontal and diagonal LVDTs on S3	90
Figure 4.33: Layout of strain gauges on S4	90
Figure 4.34: Layout of string potentiometers on S4	91
Figure 4.35: Layout of horizontal and diagonal LVDTs on S4	91
Figure 4.36: Concrete compressive strength development over curing time for S1-S4	93
Figure 4.37: Concrete stress strain curves at 22 days of concrete curing for S1 and S4	94
Figure 4.38: Stress strain curves from rebar testing of #3 samples	95
Figure 5.1: Cracking patterns at failure for S1-S4	98

Figure 5.2: Crack pattern at 2.0% drift for S1	103
Figure 5.3: Crack pattern at 3.0% drift for S1	103
Figure 5.4: Crack pattern at 4.5% drift for S1	104
Figure 5.5: Crack pattern at 6.0% drift for S1	104
Figure 5.6: Left: Widening of flexural cracks at 3.0% drift; Right: Crack were approximately 5/8-1.0-inch wide	105
Figure 5.7: View of opening region on both sides of beam during 6.0% drift	105
Figure 5.8: Cracking pattern on top of slab of S1	106
Figure 5.9: Crack pattern at 2.0% drift for S2	106
Figure 5.10: Crack pattern at 3.0% drift for S2	107
Figure 5.11: Crack pattern at 4.5% drift for S2	107
Figure 5.12: Crack pattern at 5.0% drift for S2	108
Figure 5.13: Cracking pattern at the fixed end at 2.0% drift on both sides of beam	108
Figure 5.14: Plastic hinge region at both sides of beam for S2	109
Figure 5.15: Buckling of bottom bars for S2	109
Figure 5.16: Opening region of S2 at end of test	110
Figure 5.17: Crack pattern at 1.5% for S3	110
Figure 5.18: Crack pattern at 2.0% drift for S3	111
Figure 5.19: Crack pattern at 3.0% drift for S3	111
Figure 5.20: Crack pattern at 4.0% drift for S3	112
Figure 5.21: Cracking pattern at the fixed end at 3.0% drift on both sides of beam	112
Figure 5.22: Plastic hinge region at both sides of beam for S3	113
Figure 5.23: Exposed bottom longitudinal reinforcement at end of test for S3	113

Figure 5.24: Opening region of S3 at end of test	114
Figure 5.25: Crack pattern at 1.5% drift for S4	115
Figure 5.26: Crack pattern at 2.0% drift for S4	115
Figure 5.27: Crack pattern at 3.0% for S4	116
Figure 5.28: Crack pattern at 4.0% drift for S4	116
Figure 5.29: Cracking pattern at the fixed end at 3.0% drift on both sides of beam	117
Figure 5.30: Plastic hinge region at both sides of beam for S4	117
Figure 5.31: Buckling of bottom bars for S4	118
Figure 5.32: Time histories of string potentiometers used to measure the rotation of the reaction block for S1	121
Figure 5.33: Time histories of string potentiometers used to measure the rotation of the reaction block for S2	122
Figure 5.34: Time histories of string potentiometers used to measure the rotation of the reaction block for S3	122
Figure 5.35: Time histories of string potentiometers used to measure the rotation of the reaction block for S4	122
Figure 5.36: Load (shear)-displacement relationship specimens S1	127
Figure 5.37: Load (shear)-displacement relationship specimens S2	127
Figure 5.38: Load (shear)-displacement relationship specimens S3	128
Figure 5.39: Load (shear)-displacement relationship specimens S4	128
Figure 5.40: Load-displacement backbone curve for all beams	129
Figure 5.41: Monotonic moment-curvature (ϕ) relationships: (a) at section A (fixed end), and (b) at section B (opening)	131

Figure 5.42: Moment-rotation relationships specimens S1	134
Figure 5.43: Moment-rotation relationships specimens S2	134
Figure 5.44: Moment-rotation relationships specimens S3	135
Figure 5.45: Moment-rotation relationships specimens S4	135
Figure 5.46: Beam deflection profile for S1	137
Figure 5.47: Beam deflection profile for S2	137
Figure 5.48: Beam deflection profile for S3	138
Figure 5.49: Beam deflection profile for S4	138
Figure 5.50: Cumulative normalized hysteretic energy (NHE) dissipation	140
Figure 5.51: Schematic of beam segments used to analyze shear and flexural deformations	144
Figure 5.52: Load vs. shear displacement for specimen S1	146
Figure 5.53: Load vs. flexural displacement for specimen S1	146
Figure 5.54: Load vs. shear displacement for specimen S2	147
Figure 5.55: Load vs. flexural displacement for specimen S2	147
Figure 5.56: Load vs. shear displacement for specimen S3	148
Figure 5.57: Load vs. flexural displacement for specimen S3	148
Figure 5.58: Load vs. shear displacement for specimen S4	149
Figure 5.59: Load vs. flexural displacement for specimen S4	149
Figure 5.60: Axial deformation for S1	152
Figure 5.61: Axial deformation for S2	152
Figure 5.62: Axial deformation for S3	153
Figure 5.63: Axial deformation for S4	153
Figure 6.1: Discretization of B- and D-regions along with element types in monotonic STM	155

Figure 6.2: Width and depth of concrete core	157
Figure 6.3: Stress-Strain relationship for concrete (left) and steel (right) [To (2005)]	158
Figure 6.4: Stress-strain curve for a concrete tie [To (2005)]	165
Figure 6.5: Resultant forces in openings [Muttoni et al. (1996)]	167
Figure 6.6: STM for a T-beam with an opening [Cook and Mitchell (1988)]	168
Figure 6.7: STM formulation for a simply supported beam with an opening and point loads [Mansur and Tan (1999)]	168
Figure 6.8: STM of a simply supported beam with two openings	170
Figure 6.9: Stress-strain relationship for Steel01 (left) and Concrete02 (right)	170
Figure 6.10: Monotonic STM for S1 trial 1	173
Figure 6.11: Monotonic STM for S1 trail 2	173
Figure 6.12: Monotonic STM for S1 trail 3	174
Figure 6.13: Monotonic analytical results for S1 trials 1-3	174
Figure 6.14: Monotonic STM for S1	178
Figure 6.15: Monotonic STM for S2	178
Figure 6.16: Monotonic STM for S3	179
Figure 6.17: Monotonic STM for S4	179
Figure 6.18: Monotonic analytical results for S1	180
Figure 6.19: Monotonic analytical results for S2	180
Figure 6.20: Monotonic analytical results for S3	181
Figure 6.21: Monotonic analytical results for S4	181
Figure 6.22: Discretization of B- and D-regions along with element types in cyclic STM	183
Figure 6.23: Stress-strain relationship for ElasticPP material in OpenSees	184

Figure 6.24: Cyclic STM 1 for S1 trial 1.	185
Figure 6.25: Cyclic analytical results for trial 1 of S1	185
Figure 6.26: Cyclic STM 1 for S1	190
Figure 6.27: Cyclic STM 1 for S2	190
Figure 6.28: Cyclic STM 1 for S3	191
Figure 6.29: Cyclic STM 1 for S4	191
Figure 6.30: Cyclic analytical results for STM 1 of S1	192
Figure 6.31: Cyclic analytical results for STM 1 of S2	192
Figure 6.32: Cyclic analytical results for STM 1 of S3	193
Figure 6.33: Cyclic analytical results for STM 1 of S4	193
Figure 6.34: Cyclic STM 2 for S1 trial 1	195
Figure 6.35: Cyclic analytical results for trial 1 of S1	195
Figure 6.36: Cyclic STM 2 for S1	196
Figure 6.37: Cyclic STM 2 for S2	196
Figure 6.38: Cyclic STM 2 for S3	197
Figure 6.39: Cyclic analytical results for STM 2 of S1	198
Figure 6.40: Cyclic analytical results for STM 2 of S2	198
Figure 6.41: Cyclic analytical results for STM 2 of S3	199
Figure 6.42: Comparison of cyclic analytical results for STM 1 & 2 of S1	199
Figure 6.43: Comparison of cyclic analytical results for STM 1 & 2 of S2	200
Figure 6.44: Comparison of cyclic analytical results for STM 1 & 2 of S3	200
Figure 6.45: Stress-strain relationship for Hysteretic material in OpenSees	203
Figure 6.46: Cyclic analytical results for STM 1 of S1 with Hysteretic steel material model	204

Figure 6.47: Cyclic analytical results for STM 1 of S2 with Hysteretic steel material model	204
Figure 6.48: Cyclic analytical results for STM 1 of S3 with Hysteretic steel material model	205
Figure 6.49: Cyclic analytical results for STM 1 of S4 with Hysteretic steel material model	205
Figure 6.50: Cyclic analytical results for STM 2 of S1 with Hysteretic steel material model	206
Figure 6.51: Cyclic analytical results for STM 2 of S2 with Hysteretic steel material model	206
Figure 6.52: Cyclic analytical results for STM 2 of S3 with Hysteretic steel material model	207
Figure 6.53: Comparison of cyclic analytical results for STMs 1 & 2 of S1 with Hysteretic steel material model	207
Figure 6.54: Comparison of cyclic analytical results for STMs 1 & 2 of S2 with Hysteretic steel material model	208
Figure 6.55: Comparison of cyclic analytical results for STMs 1 & 2 of S3 with Hysteretic steel material model	208
Figure 6.56: Cumulative NHE dissipation comparison between cyclic STMs and experimental results for S1	209
Figure 6.57: Cumulative NHE dissipation comparison between cyclic STMs and experimental results for S2	209
Figure 6.58: Cumulative NHE dissipation comparison between cyclic STMs and experimental results for S3	210
Figure 6.59: Cumulative NHE dissipation comparison between cyclic STMs and experimental results for S4.	210

LIST OF TABLES

	Page
Table 2.1: Previous experimental tests cited by Visnjic (2014) where BF = bond failure; EDC = excessive diagonal cracking; HY = hoop yielding; LRB = longitudinal reinforcement buckling; LRF = longitudinal reinforcement fracture; NF: no failure	32
Table 2.2: Strut coefficient factors	39
Table 2.3: Nodal zone coefficient factors	41
Table 2.4: Elastic truss member axial rigidities for C-STM [Scot et. Al (2012)]	46
Table 3.1: Comparison of full-scale and 4/5 th scale beam parameters	54
Table 3.2: Test matrix of main beam specimen variables	55
Table 3.3: Reinforcement details	57
Table 4.1: Applied load-displacement sequences	79
Table 4.2: Concrete compressive strengths at the day of testing	94
Table 4.3: Summary table of rebar test results	96
Table 5.1: Analytical results summary: (a) Section A (Fixed End); (b) Section B (Opening)	102
Table 5.2: Experimental hysteresis results	120
Table 5.3: Flexural, shear and bond slip displacement components	150
Table 6.1: Monotonic STM properties for S1	175
Table 6.2: Monotonic STM properties for S2	176
Table 6.3: Monotonic STM properties for S3	177
Table 6.4: Monotonic STM properties for S1	177
Table 6.5: Cyclic STM properties for S1	186
Table 6.6: Cyclic STM properties for S2	187

Table 6.7: Cyclic STM properties for S3	188
Table 6.8: Cyclic STM properties for S4	189

ACKNOWLEDGMENTS

I would like to express the deepest appreciation to my committee chair, Professor Anne Lemnitzer. The invaluable guidance and support in all matters have truly been fundamental to my success in my graduate studies at the University of California, Irvine. I would also like to express my gratitude to the committee members Professor Lizhi Sun and Professor Farzin Zareian for imparting their knowledge and assistance during the past several years. Additionally, I would like to thank Professor Leonardo Massone for his insight into analyzing the experimental results.

The work presented was supported by funding from Grant No. 130726. Dr. W. Chai and Mr. T. Erickson were paramount to the completion of this project. I would also like to express my deepest appreciation to Senior Development Engineer Steve Keowen; UCI Structural Engineering Testing Hall laboratory managers Dr. Rashid Miraj and Dr. Sergio Carnalla; Dr. Alberto Salamanca; and Dr. Volker Slowik. Their contributions to the test setup and data acquisition were essential to the completion of this project. Special thanks are given to Daniel Fabrega who has been a friend and adviser since my UC LEADS experience. I could complete my doctorate through the financial assistance of UCI's Graduate Division with the Eugene Cota-Robles and President's Dissertation Year Fellowships.

I would also like to express my gratitude to my colleagues and friends who have offered me their support in the past five years, including Camilla Favaretti, Hesam Sajed, Susana Anacleto, Loharsb Keykhosropour, Chris Motter, Brian Botello, Riccardo Cappa, and Chris Segura. I would additionally like to thank Mohammed Badawi, Eric Shibley, Andy Nguyen, John Sanchez, Raul Lozada, Adrea Xiao, Gavin Grimes, Alexander Six, Andrew Kim, Jesse Plasmyer, Carter Cox, George Yap, Teresa Pham, Wes Agee and Miguel Garibay for their help with specimen construction, test preparation, and test completion.

Finally, I would like to acknowledge my family, particularly my parents Jose Luis and Olga Herrera for their love and support. To my sister Nancy who is currently completing her doctorate program- there is light at the end of the tunnel. To my close friends and brothers Misael Ovalle and Anthony Ramos who have always encouraged me with their humor. Sarah, your love has brightened my days and I cannot express in words how you have positively impacted my life. I love you.

CURRICULUM VITAE

Luis Herrera

- 2012 B.S. in Civil Engineering,
University of California, Irvine
- 2012-16 Research Assistant, Department of Civil and Environmental Engineering
University of California, Irvine
- 2014 M.S. in Civil Engineering,
University of California, Irvine
- 2014-15 Teaching Assistant, Department of Civil and Environmental Engineering,
University of California, Irvine
- 2017 Ph.D. in Civil Engineering,
University of California, Irvine

PUBLICATIONS AND PRESENTATIONS

Herrera, L., Anacleto, S., Lemnitzer A. (2017) “Seismic Performance of RC SMRF Beams with Web Openings” American Society of Civil Engineers-Structures Congress, *Denver, Colorado*

Herrera, L., Anacleto, S., Lemnitzer A. (2016), “Seismic Performance of RC SMRF Beams with Web Openings” Society for the Advancement of Chicanos/Hispanics and Native Americans in Science, *Long Beach, California*

Anacleto, S., Herrera, L., Lemnitzer A. (2016), “Large-Scale Testing of FRP Retrofitted RC-SMRF Beams with Rectangular Web Openings” 16th World Conference on Earthquake Engineering, *Santiago, Chile*

Herrera, L., Lemnitzer A. (2014), “Cyclic Performance of RC Beams with Web Openings” Second European Conference on Earthquake Engineering and Seismology, *Istanbul, Turkey*

Herrera, L., Anacleto, S., Lemnitzer A. (submitted 2017) “Experimental Performance of RC Moment Frame Beams with Rectangular Openings” *Engineering Structures*

ABSTRACT OF THE DISSERTATION

Large-Scale Testing of Reinforced Concrete Moment Frame Beams with Rectangular Web Openings

By

Luis Herrera

Doctor of Philosophy in Civil Engineering

University of California, Irvine, 2017

Assistant Professor Anne Lemnitzer, Chair

Large scale cyclic testing was carried out to study the nonlinear behavior of T-shaped, moment resisting frame beams (MRF) with openings. The beams are located in an existing structure in the western U.S., and were designed according to ACI 31-95 and UBC97. Four test specimens were constructed as half-length replicas and scaled by 80% in all cross-sectional dimensions compared to their in-situ counterparts. Cross sections had geometries of 38.4 in. x 24.0 in., and beam lengths varied from 12.4 ft. to 17.5 ft. Three experimental specimens had openings with dimensions of 38.4 in. x 14.4 in.; the control specimen did not have openings. Each beam replica was instrumented with internal and external instrumentation consisting of strain gauges, linear voltage differential transducers (LVDTs), and string potentiometers, and tested to complete structural failure under quasi-static, cyclic load reversals. The cyclic performance of all beams was evaluated in terms of failure progression and plastic hinge development, strength and stiffness degradation, and energy dissipation capacity. In addition, the contribution of shear and flexural deformations to the overall displacement profile was studied.

A nonlinear strut and tie model procedure was applied to predict the cyclic envelope and the load versus displacement relationship of the beam specimens. One monotonic and two cyclic strut and tie model arrangements were developed. Additionally, the cyclic truss models were compared using two different steel material models.

Chapter 1 Introduction

1.1 Background

Reinforced concrete (RC) moment-resisting frames (MRF) are utilized in building design as a means of resisting the lateral loads imposed by severe ground shaking caused by earthquakes. Their popularity in construction stems from their ability to provide architectural flexibility as MRFs do not obstruct the vertical space in the system plane (Visnjic, 2014). All components in an MRF are detailed to resist the flexural, axial, and shearing demands resulting from earthquake loading with the objective to provide sufficient ductility to the overall structural system. When undergoing inelastic behavior, the system is expected to behave per strong column-weak beam design concept, in which the beam ends at every floor and columns at the base of the structure behave as a fuse and plastic hinging is developed near the beam column interface (See Figure 1.1). Moment-resisting frames are often termed “special” when stringent requirements imposed to maximize their seismic resistance in contrast to less detailed intermediate or ordinary moment frames are satisfied (Moehle et al.2008). The structural element is then termed “special moment resisting frame” (SMRF).

In the United States, design requirements for SMRFs are provided in the American Concrete Institute (ACI) Committee 318 Building Code Requirements for structural concrete. These requirements pertain to materials, design, framing members, construction procedures and inspection and are intended to ensure the life safety of occupants by minimizing sudden and brittle failure such as: shear failure of beams, columns or joints, axial load failures in columns or joints due to concrete crushing, buckling of longitudinal reinforcement bars in beams or columns, and rupture of transverse reinforcement.

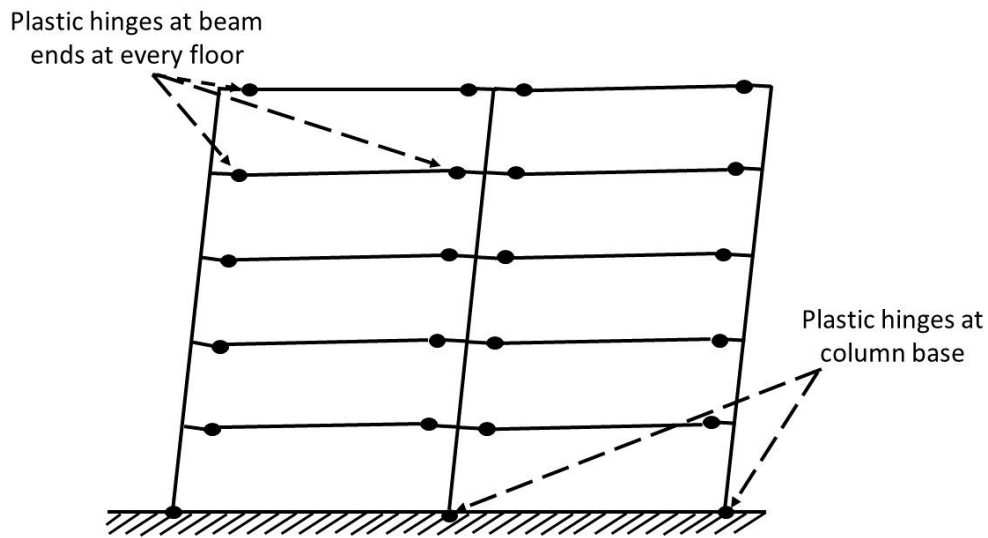


Figure 1.1: Typical layout of a moment resisting frame structure with expected plastic hinging

The use of openings in reinforced concrete beams is common practice in non-seismic regions and allows for passage of service lines such as water supply, electricity, air conditioning, sewage, and other mechanical services. Additionally, it reduces ceiling dead space and enables larger story heights, provides compact designs, and economical efficiency. Simultaneously, the introduction of openings modifies the structural response of a beam and creates a source of weakness in the form of discontinuities in the normal flow of stresses (Mansur and Tan 1999). Current code recommendations do not provide straight forward design procedures for beams with openings. Section 11.1.1.1 notes that the shear strength in opening regions is significantly reduced. The commentary to this section (ACI Committee 426, Section 4.7) discusses work conducted by Lorentsen (1962) and Nasser *et al* (1967). Both researchers concluded that (1) openings in beams should be avoided near inflection points and (2) additional stirrups are necessary around both sides of the opening.

Previous work on RC beams with openings has focused almost exclusively on RC gravity beams and deep beams with openings. Several experimental studies have been conducted on simply supported beams in which the specimen was subjected to monotonic loading until failure [Mansur (2006), Mansur (1998), Salam (1977), Somes and Corely (1974)]. The majority of the tests conducted were small-scale and lacked detailed instrumentation. To date, no studies or experimental work discuss the introduction of openings to moment resisting frame beams and/or propose similar design procedures as currently available for moment frames without openings.

In order to obtain some assessment of the available capacity, the ACI code recommends the use of Strut-and-Tie Models (STM) when the regular beam theory does no longer apply. Strut and tie modeling forces the designer to embody the flow of stresses in a discontinuous region into a truss system and ensures that each of the truss elements can resist the external forces applied. Advances STM models were utilized to predict the nonlinear monotonic and cyclic response of structural systems with various reinforcing schemes [Kim and Mander (1999), To et al. (2005), Park and Eom (2007), Panagiotou et al. (2013)]. These nonlinear models assign effective material properties to the steel and concrete components. The effective area for each component is also delineated based on each element. From model to model the computation of these properties changes as well as the different element types. Once these properties are calculated they are inputted to a nonlinear program (i.e SAP 2000, Drain 2DX, OpenSEES, etc.) where their response is measured. The results of the models capture the response of the structural system reasonably accurate and will be used in this work to validate the experimental results.

1.2 Objectives

This dissertation describes the experimental and analytical results of a comprehensive study regarding the performance of large-scale RC MRF T-beams with rectangular web openings. Current literature has never addressed the issue of an opening occurring in a MRF beam due to their stringent code requirements. The experimental program will give insight into the behavior of such beams when subjected to displacements and loads expected during a seismic event. Furthermore, the study will investigate and validate strut and tie modeling procedures and assess their accuracy when dealing with MRF beams with openings. The objectives are as follows:

- Design a test set-up to test existing SMRF beams with openings of largest scale feasible to assess their cyclic behavior at a realistic scale.
- Provide insight into the nonlinear cyclic response of MRF beams with rectangular openings and how the opening impacts the global behavior, including damage states, failure modes, and load versus deformation relations.
- Determine the distribution and magnitude of deformations due to flexure and shear.
- Validate and compare test results with current nonlinear Strut-and-Tie Modeling procedure in literature.
- Use load-displacement relations obtained through testing and results from nonlinear STM to provide design and modeling recommendations that may be used by practicing engineers.

1.3 Organization

This dissertation is divided into 7 chapters and 1 appendix. After providing a general introduction to MRF beams and the current state of design, Chapter 2 will provide a detailed review of previous experimental work conducted on beams with web openings, cyclically loaded RC beams, and strut and tie modeling. Next, Chapter 3 will focus on the specimen details and the test variables considered for each test specimen and Chapter 4 will offer details about the experimental test setup and testing protocol. Chapter 5 presents the processing, evaluation, and analyzes of the experimental results for all beam specimens. Chapter 6 discusses the analytical modeling of the test specimens using nonlinear strut and tie procedure. Lastly, Chapter 7 delineates the specific conclusions drawn from the test results and the analytical modeling. Appendix A provides additional material data.

Chapter 2 Literature Review

A limited amount of studies has been performed on reinforced concrete beams with openings. Most research work focused on investigating the change in structural behavior due to the introduction of beam discontinuities and involved parametric studies on the opening size, location, shape, and manner in which the beam is loaded. The following discussion will summarize experimental studies on non-perforated and perforated moment resisting frame beams and will then focus on analytical research work, such as strut and tie modeling. The chapter will end with conclusions drawn from the literature review and identify gaps in our knowledge of MRF beams with openings.

2.1 Research Performed on RC Beams with Openings

There is a general consensus that most openings are either rectangular or circular. This geometry is dictated by the shape of the utility service lines (pipes and air conditioning ducts) that pass through the beam. Mansur and Tan (1999), have performed extensive work on beams with rectangular openings, and suggested that a classification of an opening should be entirely defined by the structural response of the beam. Web openings can be considered small if beam-type behavior can be maintained even when cracks initiate around the opening at early stages due to the reduced moment of inertia; conversely, large openings prevent beam-type behavior. Mansur and Tan (1999) furthermore proposed that the criteria of small or large opening should be based on whether the length of the opening, l_0 , is less or equal than the height of the thickest chord member of the opening, h_{max} . In other words, the opening is "small" when $l_0 \leq h_{max}$ and is regarded

"large" when $l_0 > h_{max}$. An earlier study by Some and Corley (1974) investigated 19 simply supported beam specimens with varying opening size, location, and quantities. According to this study, a circular opening may be considered large when its diameter is larger than 0.25 times the depth of the beam.

2.1.1 Beams with Small Openings

Typical failures of beam specimens with openings are characterized by failure planes that pass directly through the opening, unless the opening is located in very close proximity to the support. In such cases, the potential inclined failure plane bypasses the opening area. Within the abovementioned 19 test studies performed by Some and Corely (1974), beam specimens with openings near the support did not experience any significant reduction in strength, and experienced typical failure for experienced for the control beams without an opening. As the opening moved away from the support towards the point load, a gradual reduction in strength was observed until a plateau of about 40% of the strength of the control beams. Furthermore, test results also indicated that the vertical position of the opening has no particular effect, but the increase in the size of the opening leads to an almost linear decrease in strength. The study also suggested that the strength of a longitudinally reinforced beam may be fully restored by using stirrups on either side of the opening.

Salam (1977), conducted work on perforated beams with the objective to find a reinforcement scheme capable of providing the equivalent strength of a beam without an opening. His study suggested that in addition to the longitudinal reinforcement above and below the opening and full

depth stirrups, the use of short stirrups in the chord members above and below the opening is necessary to help reduce the loss in strength. Finite Element Method (FEM) studies conducted by Amiri et al. (2011) investigated the behavior of concrete beams without additional reinforcement in the opening region and concluded that the introduction of a circular opening with a diameter less than 48% of the depth of the beam has no effect on the ultimate load capacity of the RC rectangular beam. On the other hand, for openings larger than 48% of the depth, a reduction in ultimate load capacity by at least 26% was observed and the beam is expected to fail by reaching its shear capacity in the opening region.

Within a series of experimental studies, Mansur and Tan (1999) verified that for beams designed for pure bending the placement of a small opening within the tension zone is highly recommended. The ultimate moment capacity of a beam is not affected by the presence of the opening if the minimum depth of the compression chord, h_c , is greater than or equal to the depth of ultimate compressive stress block:

$$h_c \leq \frac{A_s f_y}{0.85 f'_c b} \quad (2.1)$$

where A_s is the area of flexural reinforcement, f_y is the yield strength of the flexural reinforcement, f'_c is the cylinder compressive strength of the concrete, and b is the beam width. Although the ultimate moment capacity is retained, due to the decreased moment of inertia at the opening, cracks will appear during an earlier stage of loading. Despite this early appearance of cracks, it has been proven that the effects on maximum crack width and deflection under service load are marginal and may safely be disregarded in design.

For adequately reinforced beams, subjected to bending and shear, with openings located in a region with high shear demands, Some and Corely (1974), Salam (1977), and Mansur (1998) identified two main failure modes. The first failure mode is beam-type failure (Figure 2.1 Left) characterized by the failure plane passing through the center of the opening. The second type is frame-type failure (Figure 2.1 Right) which occurs by the formation of two diagonal cracks, in the opening chords. The design procedure, proposed by Mansur (1998), is capable of accounting for both failure types separately but focuses on the traditional shear design approach in which the nominal shear resistance, V_n , is provided by both the concrete, V_c , and the by the reinforcement crossing the failure plane, V_s . Therefore,

$$V_n = V_c + V_s \quad (2.2)$$

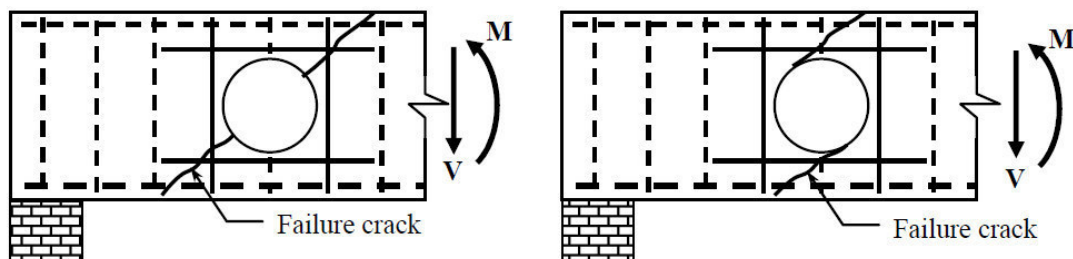


Figure 2.1: Two modes of shear failure of small openings. Left: beam type failure, Right: Frame type failure [Mansur (2005)]

For the beam-type failure the assumed failure plane is 45 degrees just as in a solid beam. The total shear resistance is simply the resistance of the net area of the concrete and using the simplified ACI Code approach.

$$V_c = \frac{1}{6} \sqrt{f'_c} b_w (d - d_o) \quad (2.3)$$

Where b_w is the web width, d is the effective depth, and d_o is the diameter of the opening. The shear resistance provided by the steel consist of the two stirrups at the side of the opening as seen in Figure 2.2. As a result,

$$V_s = \frac{A_v f_{yv}}{s} (d_v - d_o) \quad (2.4)$$

Where A_v is the area of vertical legs of stirrups per spacing s , f_{yv} is the yield strength of the stirrups, and d_v is the distance between the top and bottom longitudinal bars. Obtaining the two values allows for the calculation of the nominal shear capacity as well as the amount of web reinforcement which is calculated in the usual manner. Mansur (1998) recommends that this amount should be contained a distance $(d_v - d_o)/2$ or should be lumped together on either side of the opening.

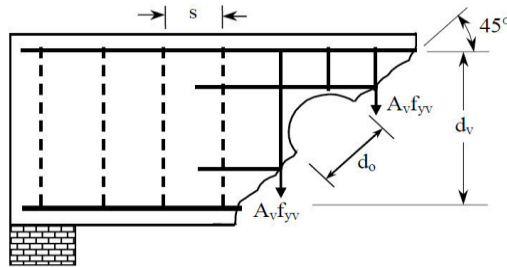


Figure 2.2: Shear resistance provided by shear reinforcement at opening [Mansur (2005)]

Frame-type failures occur when two independent diagonal cracks form, one in each chord member. The chord members behave independently similar to the members in a framed structure, hence the

name frame-type failure. Due to this behavior, each of the chord members requires independent treatment. The design processes for this type of failure using the free body diagram of a beam opening shown in Figure 2.3. The applied factored moment, M_u at the center of the opening is resisted by the bending mechanism provided by the couple formed by the compressive and tensile stress resultants, N_u . Therefore,

$$(N_u)_t = \frac{M_u}{\left(d - \frac{a}{2}\right)} = -(N_u)_b \quad (2.5)$$

Where d is the effective depth of the beam, a is the depth of the equivalent rectangular stress block, and the subscripts t and b denote the top and bottom chord members respectively. The total applied shear, V_u , can be distributed to both chord members based on their cross-sectional areas. Thus,

$$(V_u)_t = V_u \left[\frac{A_t}{A_t + A_b} \right] \quad (2.6)$$

$$(V_u)_b = V_u - (V_u)_t \quad (2.7)$$

Therefore, knowing the shear and axial forces, both chord members can be independently designed for shear following the same procedure as that for solid beams with axial compression for the chord and axial tension for the bottom chord.

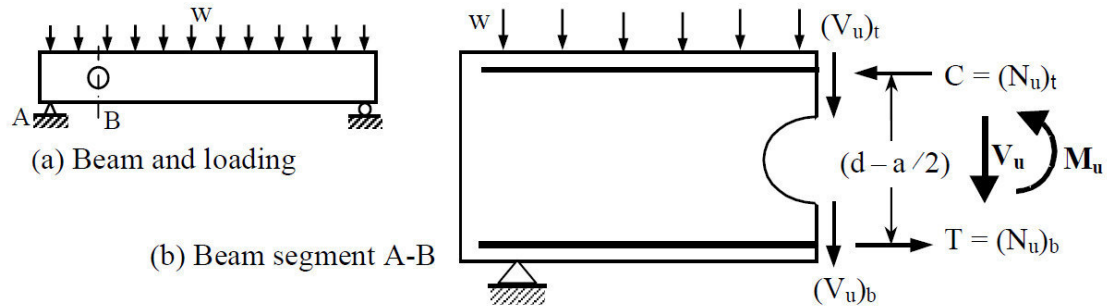


Figure 2.3: Free body diagram at opening [Mansur (2005)]

2.1.2 Beams with Large Openings

There are three main approaches available for the analysis of beams with large openings at collapse. These consist of limit analysis, the plasticity truss method, and the strut and tie method. In a work by Mansur et al. (1984) the authors outlined the use of limit analysis to be able to predict the ultimate strength of a simply supported beam with a large opening subjected to a point load a given distance "x" from the end support. According to the method, collapse of a structure will occur if it is possible to find a distribution of internal actions such that the conditions of equilibrium, yield and mechanism of collapse are satisfied simultaneously. Equilibrium conditions were derived using Figure 2.4. The yield conditions were obtained using strain compatibility. Consistent with experimental observations, the assumed mechanism for collapse consisted of four hinges in the chord members with one at each corner of the opening. Finally, a solution for the ultimate strength is obtained for a simply supported beam with a point load using the virtual work equation. The complete outline of this ultimate strength model for RC beams with large openings subjected to a point load is presented in Mansur et al. (1984).

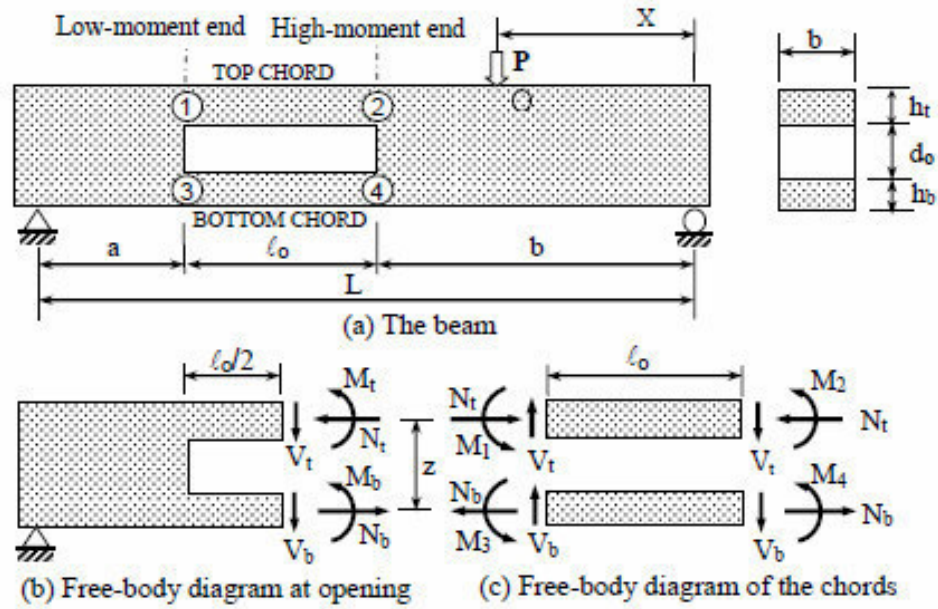


Figure 2.4: Beam with large opening under bending and shear [Mansur (2006)]

The plasticity truss model approach was proposed by the Architectural Institute of Japan (AIJ 1994). This approach assumes that the load in beams with large openings is primarily transferred by a truss model as shown in Figure 2.5. Figure 2.5 also shows the typical reinforcement arrangement suggested for a beam with openings. In this case the top and bottom chord members are equal in depth and the distance between the top and bottom longitudinal reinforcement is d_{vs} . AIJ has suggested that the vertical stirrups be provided uniformly throughout the chord members for a distance equal to $d_{vs} \cot \phi_s$ on each side of the opening, where ϕ_s is the angle of inclination of the compression concrete struts in each chord member. Given that the vertical stirrups yield and the shear force carried by each truss mechanism in the chord member is $bd_{vs}\rho_v f_{yv} \cot \phi_s$ then the shear capacity of the beam is

$$V_u = 2bd_{vs}\rho_v f_{yv} \cot \phi_s \quad (2.8)$$

where

$$\cot \varphi_s = \sqrt{\frac{\nu f'_c}{\rho_v f_{yv}}} - 1 \leq 2 \text{ and } \rho_v f_{yv} \leq \nu f'_c$$

In which b is the width of the section, ρ_v is the shear reinforcement ratio of the stirrups, f_{yv} is the yield strength of the stirrups, f'_c is the compressive strength of the concrete, and ν is the effectiveness factor for the compressive strength of concrete given by $\nu = 0.7 - \frac{f'_c}{200}$. The required force in the longitudinal reinforcement near the opening in each chord member is given by

$$T_{sn} = A_{sn} f_y = \frac{V_u l_o}{2 d_{vs}} \quad (2.9)$$

And away from the opening by

$$T_{sf} = A_{sf} f_y = \frac{V_u (l_o + d_{vs} \cot \varphi_s)}{2 d_{vs}} \quad (2.10)$$

In which A_{sn} and A_{sf} are the area of the longitudinal reinforcement in each chord member near and away from the opening.

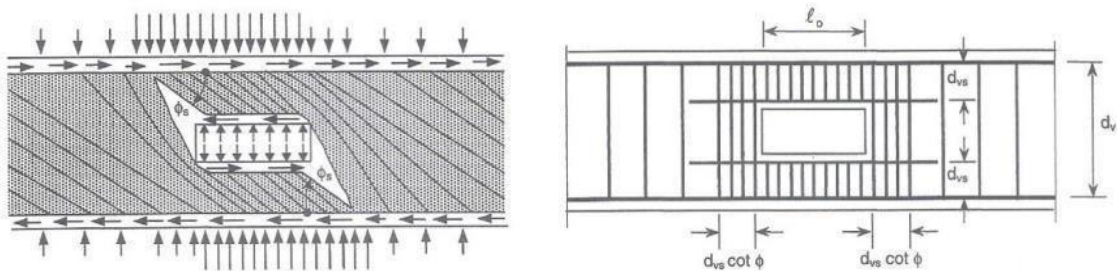


Figure 2.5: Left: Truss action, Right: Arrangement of reinforcement [AIJ 1994]

The design for ultimate strength of simply supported reinforced concrete beams with a large opening is analyzed by Mansur (2006) and a step by step procedure is proposed. Looking at Figure 2.4 it is noted that this is a statically indeterminate case to the third degree and three more equations are needed to solve for the remaining unknown actions. If the beam has identically reinforced chord members, then the moments at the two ends of each chord member are numerically the same at plastic collapse. Hence, $M_1 = M_2$ and $M_3 = M_4$ and since the contraflexure points occur at the middle of the chords this results in $M_t = M_b = 0$. Also, the three equilibrium equations relating to the original six unknowns are: $M_t + M_b + Nz = M_m$, $N_t + N_b = 0$ and $V_t + V_b = V_m$, where V_m and M_m are the applied shear and moment respectively. Finally, if the total shear is proportioned between the two chord members then the problem could turn into a statically determinate one. The following steps are given by Mansur for design and are very briefly stated here:

Step 1: Determine the longitudinal reinforcement for the compression chord by first assuming that the beam has no opening.

Step 2: Determine the shear force carried by the compression chord given by the equation $(V_u)_t = \frac{2(M_u)_{t,2}}{l_0}$.

Step 3: Determine the moments and forces at critical sections and design the tension chord.

2.1.3 Deep Beams with Openings

This section is dedicated to the work conducted on the design and behavior of deep beams with openings. It is included because there is a considerable amount of work performed on Deep Beams with Opening in literature and it was deemed appropriate to mention. Haque et al. (1986)

conducted a photo-elastic investigation (method used to find the stress distribution in a material) on the stress distribution of deep beams with openings. It was concluded that the effect of a web opening was more critical in shallower beams than in the deeper beams. The corner of openings was also identified as sources of critical diagonal tension. Finally, the authors recommend that openings should be located away from the loaded quadrants of high shear zones or zones directly between the path of the load and the support to obtain a higher beam strength.

Campione et al. (2012) studied the influence of a circular opening on deep RC beams with low shear span to depth ratio. Twenty-four small scale RC deep beams with and without openings were tested under a four-point load. Tests revealed that if the opening is placed within the shear span the load carrying capacity is reduced by 18-30% and the use of vertical stirrups only helps increase the load capacity back by about 20%. On the other hand, if the opening is placed in the mid span the beam is not affected. In another study, Yang et al. (2008) investigated how different configurations of web openings in continuous concrete deep beams affected the strength of the beam. Twenty-two RC deep beams with openings were tested. The location of the opening and the shear span to depth ratios were varied. The most notable conclusion stated that the inclined web reinforcement proved to be the most effective form for reducing deflections of the continuous deep beams having opening within interior shear spans. Furthermore, the inclined web reinforcement was seen to reduce the width of the diagonal cracks.

Mansur et al. (1984) conducted an experimental program in which 12 reinforced fiber concrete deep beams with rectangular openings were tested. The variables of this testing program included the volume fraction of fibers, opening location, shear span to effective depth ratio and the amount

of web reinforcement. Some of the significant results include the discovery that the effect of an opening on the strength of the deep beam depends mainly on the amount of which the natural load path joining the loading and support reaction points is interrupted. Also, any degree of web reinforcement was found to help in the delayed formation of and widening of cracks. Shanmugam et al. (1988) conducted a very similar experiment where nine fiber RC beams were tested. There was an interest in studying the effect of the position of the openings and the shear span to effective depth ratio on the strength of the beam. The conclusion that the effect of the opening on the behavior of the beam depends primarily on the extent to which it intercepts the natural load path and the location at which this interception occurs was further validated.

Many of the studies mentioned above have compared their experimental test results with a theoretical prediction proposed by Kong and Sharp (1972). The structural idealization developed is shown in Figure 2.6. It is anticipated that the load is transmitted mainly by the lower load path ABC and the rest of the load by the upper load path AEC. Based on this, the authors have obtained a semi empirical ultimate strength equation for beams in which the opening interrupts the natural load path

$$\frac{P_u}{2} = C_1 \left[1 - 0.35 \frac{(K_1 + a_1)x}{(K_2 + a_2)D} \right] f_t b (K_2 + a_2) D + \sum \lambda C_2 A \frac{y_1}{D} \sin^2 \alpha_1 \quad (2.11)$$

Where P_u is the ultimate load, K_1 and K_2 are coefficients defining the position of opening, a_1 and a_2 are coefficients defining the opening size, x is the clear shear span, f_t is the cylinder splitting tensile strength of concrete, λ is an empirical coefficient that depends on the type of bars used, A is the area of an individual web as well as main bar, y_1 is the depth at which a typical bar intersects

a potential critical diagonal crack, α_1 is the angle of inclination between a typical bar and potential diagonal crack, $C_1=1.40$ for normal weight concrete, and $C_2 = 130 \text{ N/mm}^2$ for plain round bars and 300 N/mm^2 for deformed bars. The experimental test programs mentioned previously seem to agree that for certain cases of shear span to depth ratios the formula is satisfactory.

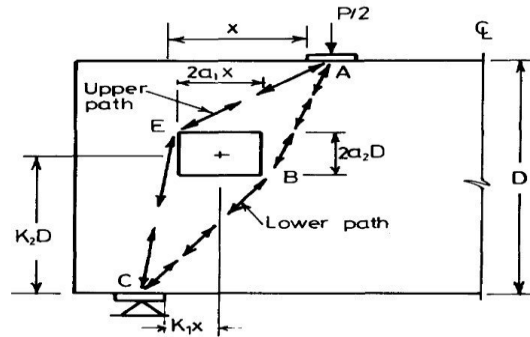


Figure 2.6: Structural idealization of deep beams with openings [Kong and Sharp (1972)]

2.1.4 Externally Strengthened Beams with Openings

The reduction in strength caused by openings in beams has led to many studies on different ways to retrofit the weakened beam. Alam (2005) conducted an experimental study on nine RC beams with large openings. The simply supported beams were tested to failure under the effect of two concentrated loads. The beams with openings were strengthened using two different materials: steel plates and Carbon FRP sheets. The 4 mm thick steel plates were bonded to the beam using a combination of epoxy and steel bolts. The plates were bonded around the opening at both sides of the beam covering both the top and bottom chords and extending 200 mm beyond the vertical edges of the opening. Two layers CFRP was also bonded with epoxy and in the exact same configuration as the steel plates. Alam (2005) concluded that the use of either external

strengthening method was more efficient than simply using internal reinforcement. Furthermore, the use of the steel plates was also more efficient than the CFRP sheets which helped restore the full shear strength of the beam and changed the mode of failure back to a flexural mode rather than a shear mode.

In another experimental study, Mondal et al. (2011) tested 9 beams with openings and used Glass FRP to strengthen and rehabilitate the weakened beams. The simply supported beams were tested under two point loads monotonically to failure. The GFRP of 0.32 mm thickness was applied all around the opening using epoxy adhesive. From this study the authors determined that the GFRP can be used to strengthen and rehabilitate beams with small openings only. Furthermore, the ultimate load carrying capacity was not significantly increased for beams with large openings. A similar study by El-Maaddawy et al. (2012) tested 16 RC beams with web openings strengthened in shear with CFRP composite sheets. The test parameters included the size of the openings and the amount of CFRP sheets used. The simply supported beams were tested under a single monotonically increasing static load. Two CFRP regimes were used for strengthening. The first one consisted of one layer of horizontal CFRP and one vertical layer. The second consisted of one horizontal layer and two vertical layers. The authors concluded that the CFRP significantly improved the shear capacity of the beams but the effectiveness of the CFRP was sensitive to the inclined slope of the lower load path.

The use of FRP rods and ordinary steel bars to strengthen beams with openings was investigated by Pimanmas (2010). The experimental study tested a total of 13 beams with circular and square openings with two different patterns of FRP and steel rod strengthening. The beams had two

openings and were tested under a single point load in the mid span of the beam. From the experimental results the authors concluded that the use of steel bars was an effective in restoring the structural performance of the beam. Furthermore, the FRP rods that were placed diagonally to the beam's axis alongside the opening throughout the entire beam's depth proved to almost fully restore the strength of the beam.

2.2 Cyclically Loaded RC Beams

2.2.1 SMRF Beam Design

This section will provide a brief overview of the specifications necessary to design a SMRF beams. This section was created using National Earthquake Hazards Reduction Program (NEHRP) Technical Brief No.1: Seismic Design of Reinforced Concrete Special Moment Frames: A Guide for Practicing Engineers by Moehle et al. (2008), the ACI Code (2014), and the textbook Reinforced Concrete Mechanics and Design 6th Edition by Wight and MacGregor (2012). SMRFs are used as seismic force-resisting system in buildings and all their components (i.e. beams, columns, etc.) are specially detailed and proportioned to resist the flexural, axial, and shearing actions that occur due to the sways of building through multiple displacement cycles during strong earthquake shaking. Due to this demand, there are certain objectives/requirements that need to be satisfied to ensure that the SMRF system behaves in a ductile manner:

1. Achieve a strong-column/weak-beam design that spreads inelastic response over several stories
2. Avoid shear failure

3. Provide detailing that enable ductile flexural response in yielding regions

The necessity to conform to a strong-column/weak beam design principle is due to need to distribute the drift over several stories of the building. This is done by having the columns act as a rigidly stiff spine where ideally no inelastic deformation occurs. If the columns are weak the drift will be concentrated in a few stories and might create a story mechanism as depicted in Figure 2.7. Therefore, the ideal case occurs where a beam or intermediate mechanism occurs. The way in which ACI 318 complies with the principle of strong-column/weak-beam is by requiring that the sum of column strengths exceed the sum of beam strength at each beam column connection of an SMRF by a factor of 1.2 (ACI Section 21.6.2.2).

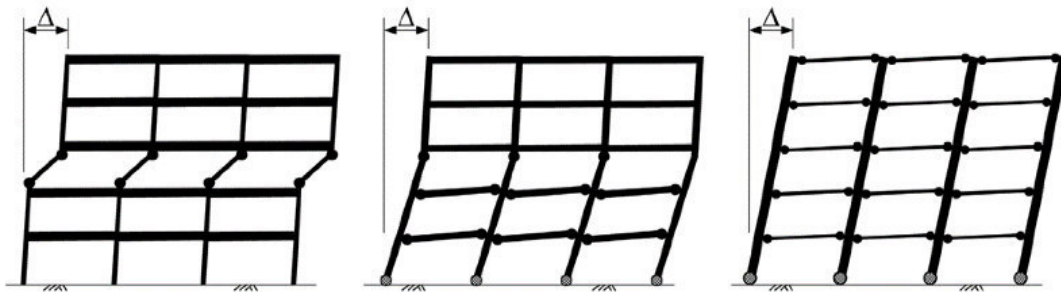


Figure 2.7: Left: story mechanism, Middle: intermediate mechanism, Right: beam mechanism [Moehle 2008]

Shear failure is avoided because it is a sudden and brittle type of failure that leads to rapid loss of lateral strength and axial load carrying capacity. The intended response of SMRFs are to be ductile and yield in flexure. This is done through identifying regions that will undergo flexural yielding, design them for code-required moment strengths, and then calculate design shears based on equilibrium assuming the flexural yielding regions develop probable moment strengths. Detailing of for ductile behavior is based on a few principles. First, confinement of concrete is an important

detailing consideration due to compressive strain capacity of concrete being tremendously benefited. The hoops provide the confinement by encasing the concrete and preventing the bulging of the of the core concrete as it is loaded in compression and therefore, leads to an increased strain capacity. To provide this confinement, the hoops must encase the entire cross section and must be closed by 135° hooks embedded in the core. This will ensure that the hooks remain intact even during the cyclic loading and continue to provide confinement. The hoops should be closely spaced for confinement to be effective and will also help to prevent the buckling of longitudinal reinforcement. Sufficient shear reinforcement is also necessary as ACI 318 requires that the contribution of shear resistance of the concrete be completely ignored and all the shear force is resisted by the shear reinforcement. Special consideration must also be taken to avoid anchorage or splice failures. Thus, bars anchored in exterior joints must develop yield strength by using hooks located at the far side of the joint.

The inelastic action in SMRF is intended to be mainly concentrated in the form of flexural yielding of the beams. These beam sections are designed such that the flexural strength is at least equal to the factored design moment i.e. $\phi M_n \geq M_u$. ACI 318 Section 18.6.2 also places some geometric restriction on flexural members of SMRF namely

- Span to depth ration shall be $l_n \geq 4d$ to avoid deep beam action
- The width, b_w , shall not be less than
 - 0.3 times the depth of the beam
 - 10 in.
 - Not more than the width of the supporting member

After the beam is proportioned, the plastic moment strengths of the beam are determined using the material and cross sectional properties. The probable moment strength, M_{pr} , is calculated by using $1.25f_y$. This is because the average yield strength of a reinforcing steel is typically greater than that of the reported f_y and the longitudinal reinforcement will likely go into strain hardening. The probable moment strength is used in ACI 318 to ensure that the shear strengths of beams exceed the shears that equilibrate flexural hinging at the ends of the beam. Furthermore, the flexural reinforcement must satisfy the requirement outlined in Figure 2.8 and outlined in ACI Section 18.6.3.1.

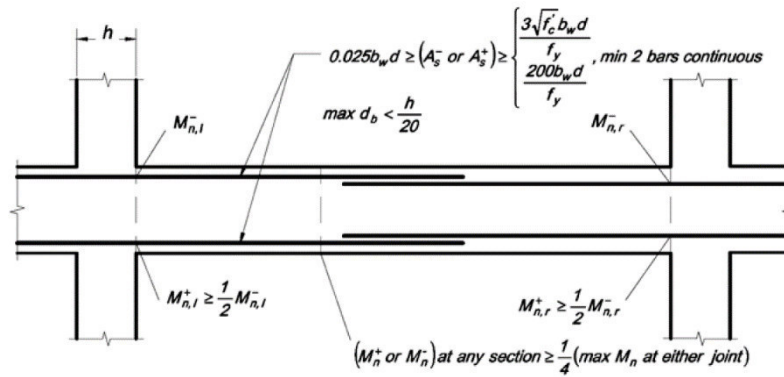


Figure 2.8: Beam flexural reinforcement requirements [Moehle 2008]

Furthermore, the yielding of the beams should be restricted primarily certain lengths of the beam located normally at the beam column connection. This will typically occur if the beam is relatively short and/or the gravity loads are relatively low compared to the seismic forces or if

$$M_{pr+} + M_{pr-} \geq w_u l_n^2 / 2 \quad (2.12)$$

where

$$M_{pr} = 1.25f_y A_s \left(d - \frac{a}{2} \right) \quad (2.13)$$

The yielding of main longitudinal reinforcement are the limits of on the moment capacity that can be developed at the ends of the beam. Therefore, the design shear forces, V_e , are derived from the factored dead and live loads plus the shears due to hinging at the two ends of the beam for the frame swaying to the right or left as shown in Figure 2.9. ACI Section 18.6.5 states that beams be designed for the sum of

$$V_{sway} = \frac{M_{pr^+} + M_{pr^-}}{l_n} \quad (2.14)$$

$$V_g = \frac{w_u l_n}{2} \quad (2.15)$$

$$V_e = V_g \pm V_{sway} \quad (2.16)$$

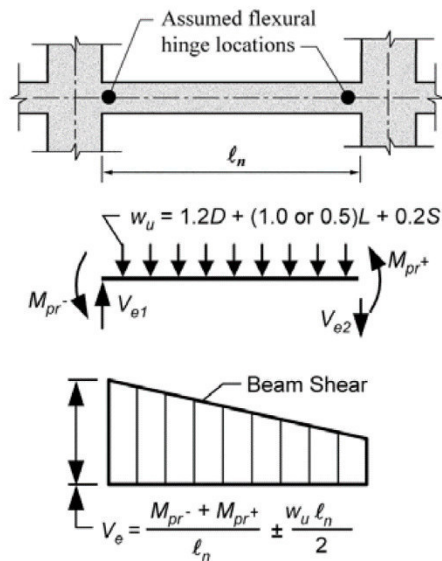


Figure 2.9: Design beam shear based on probable moment strengths combined with factored gravity loads [Moehle 2008]

This will typically result in a conservatively high estimate of the design shears which then allows for the design of the beams transverse reinforcement. Furthermore, SMRF beams can then be divided into three different zones for hoops and stirrup placement: the zones where plastic hinging is to occur, zones where there are lap splices of longitudinal reinforcement, and all other sections. Due to high shear demand around the expected hinging zone at each end of the beam closely spaced hoops are to be placed over a length equal to $2h$ for the face of the supports and in areas where flexural yielding is expected anywhere along the beam span. Additionally, if flexural yielding is expected anywhere along the beam span other than the end of the beam, hoops must also extend $2h$ on both sides of that yielding location. Figure 2.10 shows the requirements of hoop spacing in zones previously mentioned.

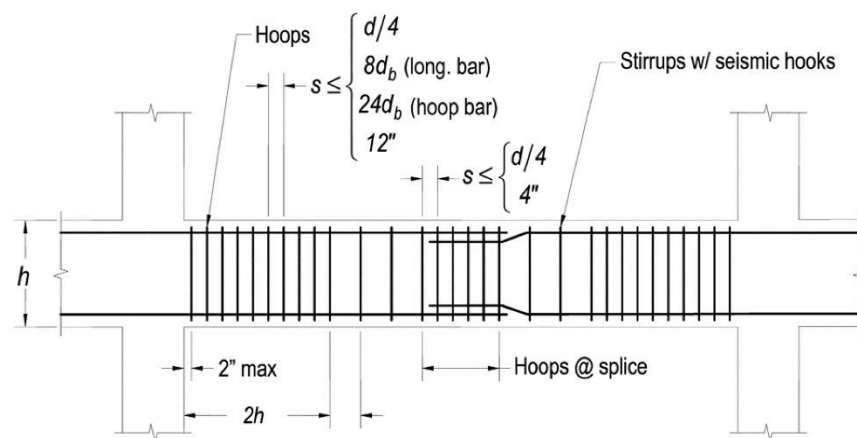


Figure 2.10: Hoop and stirrup location and spacing requirement [Moehle 2008] *Note the minimum spacing of 12" has been reduced to 6" in ACI 318-14

Hoop reinforcement can be made of one or more closed hoops or it may be constructed of typical beam stirrups with seismic hooks at each end closed with crossties having 135° and 90° hooks at opposite ends. ACI 318 specifies that a seismic hook on a stirrup, hoop, or crosstie is a bend not

less than 135° with a six-diameter extension that engages the longitudinal reinforcement and projects into the confined concrete in the interior of the stirrup or hoop (Figure 2.12). Therefore, the shear design requirements in the end zones are

$$\phi V_s \geq V_e \tag{2.17}$$

$$\phi = 0.75$$

And everywhere else it is done using the conventional design equation $\phi(V_s + V_c) \geq V_e$.

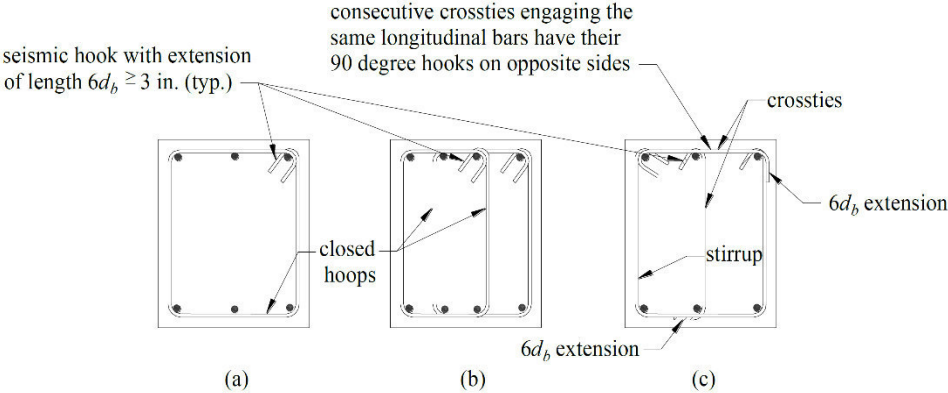


Figure 2.11: Hoop configurations (a) single closed hoop, (b) overlapping hoops, (c) stirrups with crossties [Visnjic 2014]

2.2.2 Experimental Investigations on Cyclically Loaded RC Beams

In seismically active areas, the behavior of RC beams must be evaluated for reversed cyclic loading in the inelastic deformation range in which components deteriorate in both strength and stiffness.

During the past fifty years, numerous experimental studies have evaluated the hysteretic response

of commonly used RC flexural members subjected to large cyclic deformation reversals. The following will review a small portion of the cyclic experimental investigations RC beams.

Popov et al. (1972) conducted reversed cyclic testing on three beams to study the effects of the high shear forces on the deformation, strength, stiffness, and energy dissipation capacity of flexural members. The specimens were 78 in. long, 15 in. wide by 29 in. high. All beam specimens had six #9 longitudinal rebars top and bottom. The main variable of the testing program was the shear reinforcement which consisted of either #3 bars spaced at 4.5 in., #4 bar spaced at 6 in., and #4 spaced at 3 in. The specimens were constructed as cantilevered T-beams where cyclic loading was applied to the tip of the beam. Two beams were reported to fail in shear and the last one failed by premature fracture of the longitudinal reinforcing bar. Notable conclusions drawn from this investigation include the benefit of confinement to reach large curvature and rotation ductility; the slippage of the longitudinal reinforcement may lead to a decrease in stiffness; shear resistance is increased with a decrease in hoop spacing; when the composite action of the concrete and ties deteriorates (truss action), the shear is carried predominately by the dowel action of the main reinforcement; large shear-type deformations lead to pronounced pinching of the hysteresis loops and lead to a decrease in the ability to dissipate energy.

Nine RC cantilever beam tests were reported in Krawinkler and Popov (1973). Slender rectangular beams, T-beams, and short rectangular beams were investigated. The cross-section of the beams was either 9 in. wide by 16 in. high or 15 in. wide by 29 in. high. The length and reinforcement details was varied. Load was applied at the tip of the beam using a hydraulic jack. The rectangular slender beams and the T-beams failed in flexure by crushing of the concrete cover and inelastic

buckling of the main reinforcement. The short beams failed in shear regardless of the amount of shear reinforcement. Notable conclusions include: the ductility is increased if it is possible to restrain the buckling of the main longitudinal reinforcement using closer spaced ties or larger bar sizes; slippage of the reinforcement at the anchor zone can significantly decrease the stiffness; addition of a floor slab increases the strength of the specimen and should be considered in the design and analysis of moment resistant frames; the deterioration in stiffness of flexural members after first reloading in successive cycles of the same displacement amplitude is caused predominately by additional shear deformation; and shear is carried by dowel action of the main reinforcement when the truss action deteriorates.

Ma et al. (1976) conducted an experimental investigation into the behavior of critical regions in beams of RC ductile moment-resisting space frames. Nine cantilever beams constructed to half scale of an original 20-story ductile moment frame were tested. The beams were 9 in. wide by 16 in. high and 38.5 or 62.5 in. long. The beams contained four #6 rebars at the top and either four #6 or three #5 bars at the bottom. The variables of the test included the bottom reinforcement, the slab on the specimens, supplementary ties, shear span, and loading histories. The experimental setup was identical to that reported in Popov et al. (1972) where the loading actuator was attached to the tip of the cantilever beam. Failure modes encountered were predominately buckling of the longitudinal reinforcement. One T-beam suffered from a separation of the slab from the beam stem that led to a significant drop in strength and was believed to be the result of the placement of the top longitudinal bars. Important conclusions derived from this study include: the addition of a T-beam will increase the moment capacity of the beam in one direction due to the slab reinforcement; the addition of supplementary ties increases the energy dissipation by 74%; and

greater amounts of energy can be dissipated by subjecting the beam to loading reversals of gradually increasing amplitude than by subjecting it directly to loading reversals of large amplitude.

Brown and Jirsa (1971) tested twelve RC cantilever beams to investigate the effect of load history on the strength, ductility, and mode of failure of the beams. The beams were attached to a reaction block and the load was applied at the tip. The cross-section of the specimens was 6 in. wide by 8 in. high. The main test variables included the loading history, the amount of top and bottom longitudinal reinforcement (#8 or #6), and the stirrup spacing. The mode of failure of the beams was the gradual deterioration near the support and marked by large shear deformations. Notable conclusions of the study state that closer stirrup spacing is beneficial to energy absorbing capacity; deformation of the steel in the anchorage zone contributed greatly to the total deformation; and reduction in the shear span or increase in the shear forces on the beam reduced the number of cycles to failure.

Fenwick and Fong (1979) reported the testing of five RC cantilever beams subjected to cyclic loading. The shear stress level was the main variable being investigated where the span to depth ratio was changed between all specimens. The beams were 7.87 in. wide and 19.69 in. high with five 20 mm. top bars and five 20 or 16 mm. bottom bars. Beams were cantilevered off a common anchor block and tested by applying cyclic loading at the tip. Failure was observed by excessive cracking and spalling of cracking at the hinging zone. The results of the tests indicate that shear in the plastic hinge zones has a pronounced effect on the behavior of the beams. Namely when

the shear stress level increases the performance decreases. It was also noted that all beams grew appreciably in length under cyclic loading.

Hwang and Scribner (1984) tested eleven RC cantilever beams with two main objectives. The first was to study the effect of variations in beam-tip displacement history on the cyclic response of flexural members. The second was to study the effect of variation of displacement history on the total energy dissipation capacity of members undergoing inelastic cyclic flexure. The rectangular beams were 8 in. wide and 12 in. high with lengths ranging from 25 in. to 39 in. The main longitudinal and transverse reinforcement was also varied among the eleven specimens. The beams were cantilevered from a reaction block and the load was imposed using a hydraulic actuator. Beam specimen strength and stiffness decay was caused primarily from excessive cracking and spalling from the hinging zone and no longitudinal rebar buckling was observed. The study concluded that if the maximum member inflection-point displacement under cyclic reversed loading did not exceed 2% of shear span length, strength degradation in flexural members was not excessive.

Fang et al. (1993) tested fifteen cantilever beams that were 7.87 in. wide and 15.75 in. high. The test variables were the shear span to depth ratio, the amount of main longitudinal reinforcement, and the loading histories. The purpose of the study was to examine the performance of moderately deep high strength concrete beams, the effect of the test variables, and the behavior of the plastic hinge region on moderately deep high strength concrete beams. Beams were anchored to a reaction block and hydraulic actuator loaded the beam cyclically at the tip. The beams could resist cyclic loads up to 3-4 displacement ductility factor. The beams did not appear to be affected by

differences in top and bottom reinforcement. The pinching effect in hysteresis loops was caused by the shear deformations in the plastic hinge zone and was more pronounced in specimens with shear span to depth ratios of 2.5.

Visnjic (2014) and Visnjic et al. (2016) tested two large-scale SMRF beams with the objective to investigate the ACI 318-08 Code provisions for hoop spacing. Both beams were constructed as cantilevers from the same reaction block that was anchored to the strong floor. The load was applied using a hydraulic actuator at the tip of the beam imposing vertical displacement cycles to simulate the deformation reversals occurring during earthquake loading. The beams cross-section (48 in. deep by 30 in. wide), length (13.5 ft.), and longitudinal reinforcement (5 No. 11 top and bottom) were constant among the two beams. The spacing of the transverse reinforcement was the main variable where Beam 1 had a spacing 11 in. and the Beam 2 had hoop spacing of 6 in using #5 bars. For both beams, the main failure mode was that of buckling of longitudinal reinforcement with hinging at the beam near the support. For Beam 1, buckling became apparent during 1.8% drift cycle which led to a critical strength decay at 2.7% drift. Beam 2 buckled at 2.9% drift and the critical strength decay occurred at 3.9% peak drift ratio. It was noted that the reduction in the spacing of the hoops aided in the stability of the longitudinal reinforcement and likely enabled the reinforcement to strain harden. The study produced the changes in hoop spacing in ACI 318-11.

Visnjic (2012) provides a table (Table 2.1) of previously documented experimental tests on flexure-dominant cast in place RC beams. It is noted that the beams are tested as cantilevers protruding from either a reaction block or column and the force is applied transverse to the beam

axis. The table also illustrates the predominant modes of failure and the peak drift ratio right before significant strength loss. Excessive diagonal cracking was the main mode of failure and only one study (Blakely et al. 1975) observed longitudinal rebar buckling as the main mode of failure.

Table 2.1: Previous experimental tests cited by Visnjic (2014) where BF = bond failure; EDC = excessive diagonal cracking; HY = hoop yielding; LRB = longitudinal reinforcement buckling; LRF = longitudinal reinforcement fracture; NF: no failure

Authors	b_w , mm (in.)	h , mm (in.)	M/Vh	ρ_s , %	ρ'_s , %	s_h/d_b	Hoop configuration	θ_{cap}	Failure mode
Popov et al. (1972)	483 (19)	737 (29)	2.7	1.58	1.58	2.7	Single closed hoop	0.045	HY/EDC
Blakeley et al. (1975)	457 (18)	889 (35)	3.9	1.10, 1.03	0.70	5.3	Pair of closed hoops	0.050	LRB/ EDC
Birss (1978)	356 (14)	610 (24)	3.6	1.3	1.3	2.5-5.0 (varied s_h within p.h.)	Pair of closed hoops	0.036 (Unit B1) 0.032 (Unit B2)	NF
Beckingsale (1980)	356 (14)	610 (24)	3.6	1.10, 0.86	0.58, 0.86	2.7-5.4 (varied s_h within p.h.)	Pair of closed hoops	exceeds 0.040 (units B11 and B12) exceeds 0.027(unit B13)	BF (Units B11 & B12) NF (Unit B13)
Paulay and Scarpas (1981)	356 (14)	610 (24)	3.6	0.9	0.9	5.0	Pair of closed hoops	exceeds 0.038	NF (Units 1 & 3) HY (Unit 2)
Restrepo et al. (1990)	300 (11.8)	700 (27.5)	2.7	0.93	0.95	4.3	Single closed hoop	0.036	BF (Unit 5) EDC (Unit 6)
Warcholik and Priestley (1997),	508 (20)	762 (30)	3.5	1.17	1.17	2.8	Closed hoop with vertical cross tie	exceeds 0.028	NF
Warcholik and Priestley (1998a)	508 (20)	762 (30)	3.5	1.17	1.17	2.8	Closed hoop with vertical cross tie	exceeds 0.039	NF
Warcholik and Priestley (1998b)	508 (20)	762 (30)	3.5	0.83	0.83	2.9	Closed hoop with vertical cross tie (specimen HSJ12-4)	exceeds 0.058	NF
Chang et al. (2008)	483 (19), 559 (22)	914 (36)	3.3	0.60 0.67	0.60, 0.67	1.5	Single closed hoop (beams 3 & 4) vertical cross tie (beam 3)	0.055, 0.071	LRF (Beam 3) NF (Beam 4)

2.3 Strut and Tie Modeling

2.3.1 STM Development and Research

A strut-and-tie model (STM) idealizes the complex flow of stresses as compressive and tensile axial elements of a truss. Before STM was used, discontinuous regions were typically designed using empirical equations (Tuchscherer 2014). The earliest evidence of the use of truss modeling can be observed in Wilhelm Ritter (1899) who developed a truss mechanism to represent the behavior of transverse reinforcement within an RC beam. Next, Morsh (1902) refined this model by representing diagonal forces in the truss model with a compression field. With the development of other models that considered the contribution of shear strength, truss modeling fell out of favor for a period of time in North America (Brown 2006). STMs became prominent through the works of Marti (1985) and Schlaich et al. (1987) who both presented modeling approaches for their use in discontinuous regions. Afterward, the STM approach was adopted to codes such as the Canadian CSA Standard in 1984, AASHTO in 1989, and in ACI in 2002. The American Concrete Institute *Building Code Requirements for Structural Concrete* (ACI 318) does not include explicit design procedures for RC beams with web openings, but the design of discontinuous regions using STMs is permitted. As an opening is a discontinuous region it was appropriate to do an investigation on the research performed using this design procedure.

The work conducted on STMs has investigated topics such as the process of determining the appropriate efficiency factors of struts and nodes, the optimum truss model for structural elements, and the validation of the truss models. Typical structural elements of interest designed using STMs are deep beams, deep beams with openings, corbels, pile caps, footing, dapped-end beams, and

anchorage zones. Martin (2007) provides an extensive overview of the development of STM, including several design examples, and addresses opportunities of improvement on STM specifically within the AASHTO LRFD Code. They concluded that there is a lack of research and agreement between codes concerning the serviceability requirements based STM, provide recommendations for modification of design equations, and propose research in other areas where the AASHTO LRFD code for STM.

Tuchscherer et al. (2012) tested 37 RC deep beams which were at a larger scale than had been previously reported in literature. The purpose of the study was to assess the accuracy and conservatism of the STM provisions of ACI 318. The main variable of the testing sequence included: stirrup distribution, width and length of load and support plates, the quantity of web reinforcement, and the depths of the members. The beams were tested in two phases. First, they were loaded near one support corresponding to the appropriate shear span ratio. After the shear failure occurred the failed portion was repaired and the test was conducted at the other end of the support. Through the experimental results, recommendations were provided for improvements to ACI 318-11 STM provisions.

Tuchscherer (2014) made a comparison with design procedures of deep beams designed using ACI 318-71 using empirically derived equations and ACI 318-11 using STM. The paper mentions that STM procedure remains a source of confusion for many design professionals who are more inclined to continue using previous design methods. Through the study of 438 deep beam shear tests from literature, the author analyzed differences between both design procedures. It was concluded that the capacities calculated with both provisions were statically similar but the average

of the capacities of ACI 318-99 is increasingly un-conservative as the specimen's cross-sectional area increases. This was due to the design procedure being empirical whereas the STM procedure will always give a lower bound solution provided the structural element is designed properly.

Ley et al. (2007) validated the use of STM as a design method by conducting experimental tests of dapped end beams with openings. The first phase of the experiments was conducted by five individual graduate students each tasked with designing the specimen using a different STM using ACI 2005. The test specimens were small scale (1:10.5), tested under three-point load, and one of the specimens were tested with no reinforcement. Each of the graduate student groups conducted and FEM analysis of the specimen to first determine the elastic stress field and then modeled their individual STM. While the models varied substantially, all the models developed resulted in test loads greater than that of the factored loads. Therefore, it was concluded that STM can provide a safe, lower bound, design. Furthermore, the teams of designers found it most efficient and beneficial to use two overlapping models to distribute the reinforcement. Finally, it was noted that while the STM does give a reliably safe design it is not able to predict ultimate loads or failure.

Design by STM can be a time-consuming process where several iterations of truss models might be needed along with many detailed calculations. To remedy this shortcoming there has been a development in software to aid in the visualization and design procedure of STM. Kuchma and Tjhin (2001) and Tjhin and Kuchma (2007) introduced their design program Computer Aided Strut and Tie (CAST). The program offers a user-friendly graphical user interface capable of performing both design and load deformation analysis. Additionally, Yun (1999) and Yun (2000) developed a nonlinear STM approach and created an analysis and design tool using

Fortran. The interactive computer graphics program developed claimed to considerably reduce design time by providing an iterative tool for possible revisions. Salem and Maekawa (2006) used a refined version of the nonlinear STM approach from Yun (2000) and develop their program with the similar conclusions about the practicality of its use.

The obtainment of the optimum truss model has also been thoroughly investigated. Liang et al. (2002) and Kwak and Noh (2006) both used topology optimization to produce an optimum truss design for various structural components. Topology optimization iterates through underutilized elements of the structure and eliminates them until the best truss model is achieved. Perrera and Vique (2009) used genetic algorithms as their optimization technique. Genetic algorithms generate an initial random population then evolve iteratively new, increasingly better populations from the previous ones until a solution is reached. Hu et al. (2014) also developed a technique that uses the principal of minimum strain energy to quantify the differences between different truss models and produce a more efficient design.

2.3.2 ACI STM Design

The following section focuses on the design of STM specifically with in the ACI Code. Focus will be placed on the procedure taken and the design of the individual elements. This section was written with the aid of the textbook Reinforced Concrete Mechanics and Design 6th Edition by Wight and MacGregor (2012) and ACI 318-14.

A structural member can be subdivided into regions classified as either B-regions or D-regions. B-regions are those portions in a structural member in which typical Bernoulli's beam theory applies (i.e., plane sections remain plane and the strain distribution is linear). D-regions are regions with discontinuities where plane-strain assumptions are no longer valid (e.g., holes or abrupt changes in cross sectional area or statical discontinuities (i.e. concentrated loads or reactions)).

To determine the boundary between a B- and a D-region it is necessary to determine when the stress distribution once again becomes linear by using St. Venant's principle. St. Venant's principle states that the stress due to an axial load and bending approach a linear distribution at a distance of approximately equal to the overall height of the member, h , away from the discontinuity. Therefore, a discontinuity is assumed to extend a distance h from the section where statical or geometric discontinuity occurs. Figure 2.12 provide an example of how to determine the extent of D-regions.

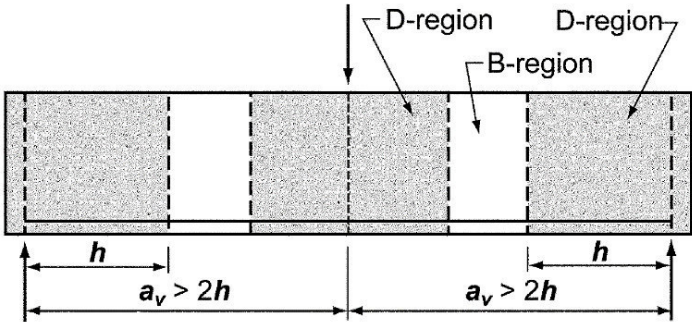


Figure 2.12: B- and D-regions [ACI 318-14]

Once the section of a D-region has been identified, the STM can be used to design these discontinuous regions. A STM has three major components: concrete compressive struts, reinforcing steel tension ties, and the concrete nodes. A STM must satisfy the following

- It represents a system of forces that is in equilibrium with the given set of loads.
- The factored member forces at every section in the strut, ties, and nodal zones do not exceed the corresponding design member strengths for the same sections.
- The structure must have sufficient ductility to distribute the forces within the assumed truss model.

If these conditions are met the STM will satisfy the lower bound theory of plasticity and therefore the capacity of the STM will always be less than or equal to the capacity of the structure. The concrete struts represent the compressive stress fields and depending on how the compressive stress field behaves within the D-region the strut might take on different shapes such as prismatic or bottle-shaped. A prismatic strut is typically used to model the compressive stress block of a beam element and have uniform cross section. A bottle shape strut occurs when there is a well-defined geometric condition at the ends but is generally unconfined at the center. Struts have effective crushing strengths that are proportional to the compressive strength of the concrete. This effective strength is dependent on load duration effects, tensile strains that transverse the strut and crack struts. The ACI Code Section 23.4 presents the nominal compressive strength of a strut as:

$$F_{ns} = f_{ce}A_c \quad (2.18)$$

Where the subscript n refers to nominal condition, s refers to strut and A_c is the cross-sectional area at the end of the strut. f_{ce} is defined as

$$f_{ce} = 0.85\beta_s f'_c \quad (2.19)$$

β_s values are provided by ACI and are shown in Table 2.2. Primarily depending on the type of strut present in the D-region β_s varies from 0.6-1.0.

Table 2.2: Strut coefficient factors β_s

Strut geometry and location	Reinforcement crossing a strut	β_s	
Struts with uniform cross-sectional area along length	NA	1.0	(a)
Struts located in a region of a member where the width of the compressed concrete at midlength of the strut can spread laterally (bottle-shaped struts)	Satisfying 23.5	0.75	(b)
	Not Satisfying 23.5	0.60λ	(c)
Struts located in tension members or the tension zones of members	NA	0.40	(d)
All other cases	NA	0.60λ	(e)

A tie represents one of several layers of reinforcement in the same direction as expected tensile stresses occur. Despite concrete having a small amount of tensile capacity this is normally neglected and all the tensile stress is taken by the steel. ACI 318 provides the nominal strength of a tie to be:

$$F_{nt} = A_{ts}f_y + A_{tp}(f_{se} + \Delta f_p) \quad (2.20)$$

The terms containing a subscript p refer to cases where prestressed ties are being utilized and all terms with a subscript t refer to ties and f_y is the yielding stress of the reinforcement. Furthermore, ACI 318 requires that the axis of the tie to coincide with the axis of the reinforcement and in the layout of the STM the tie consist of the reinforcement and a prism of concrete that encases the tie. This concrete prism is used to determine the effective width of the tie and there are restrictions placed by ACI:

$$w_{t,max} = \frac{F_{nt}}{(f_{ce}b)} \quad (2.21)$$

The idealized prism of concrete only serves to establish the nodal zones and it does not resist any tensile forces. It is important to note that the ties may fail due to lack of properly detailed anchorage since failure to do so would not allow the tensile capacity of the tie to fully develop.

The last major component of an STM are nodes and nodal zones. Nodes are conceptually idealized as pinned joints and they occur at the intersection between ties and struts. A nodal zone can either be hydrostatic or non-hydrostatic. The condition for a hydrostatic node is that all the stresses on each of the face of the nodes are equal and perpendicular which would ensure no shearing stresses to act on the face of the node. This is typically impractical and non-hydrostatic forces are sometimes used with the condition that the ratio of the maximum stress and the minimum stress be less than 2 according to Schlaich et al. (1987). Furthermore, nodal zones can be subdivided into several parts, each of which is assumed to transfer a particular component of the load through the nodal for ease of layout. The strength of a nodal zone is dependent of the concrete similarly to struts as these are assumed to fail by crushing. This strength is determined based on the type of

node. ACI recognizes three types of nodes: CCC, CCT, and CTT nodes. The C and T correspond to compressive strut and tension tie respectively. ACI Code Section 23.9.1 limits the effective concrete strength, f_{ce} , for nodal zone as:

$$F_{nn} = f_{ce}A_n \quad (2.22)$$

where A_n is the area of a face of the node that the strut or tie acts on and f_{ce} is the effective compressive strength of the concrete taken as:

$$f_{ce} = 0.85\beta_n f'_c \quad (2.23)$$

Table 2.3 also provides the values for β_n given by ACI 318. The β_n factor is reduced as the number of ties passing through the nodal zone is increased.

Table 2.3: Nodal zone coefficient factors β_n

Configuration of nodal zone	β_n	
Nodal zone bounded by struts, bearing areas, or both	1.0	(a)
Nodal zone anchoring one tie	0.80	(b)
Nodal zone anchoring two or more ties	0.60	(c)

The design procedure recommended by ACI 318 is provided as the following:

1. Define and isolate each D-region;
2. Compute resultant forces on each D-region boundary;
3. Select a truss model to transfer the resultant forces across the D-region. The axes of the struts and ties, respectively, are chosen to approximately coincide with the axis of the compression and tension fields. The forces in the struts and ties are computed;
4. The effective widths of the struts and nodal zones are determined considering the forces from Steps 3 and effective concrete strengths defined in A.3.2 and A.5.2, and reinforcement is provided for the ties considering the steel strengths in A.4.1. The reinforcement should be anchored in the nodal zone.

2.3.3 Nonlinear Strut and Tie Modeling

Aside from standard code based Strut and Tie Modeling design procedures described in the previous section, there are STM procedures capable of performing nonlinear structural concrete analysis. These are typically conducted using structural analysis software (SAP 2000, OpenSEES, Drain 2DX, etc) and applying material constitutive models to individual truss members of the STM. To et al. (2003a, 2003b, 2005, 2009) developed a nonlinear STM formulation for both Monotonic and Cyclic cases. This work is explained in detail in Chapter 6 where it is applied to analyze the results of the experimental data.

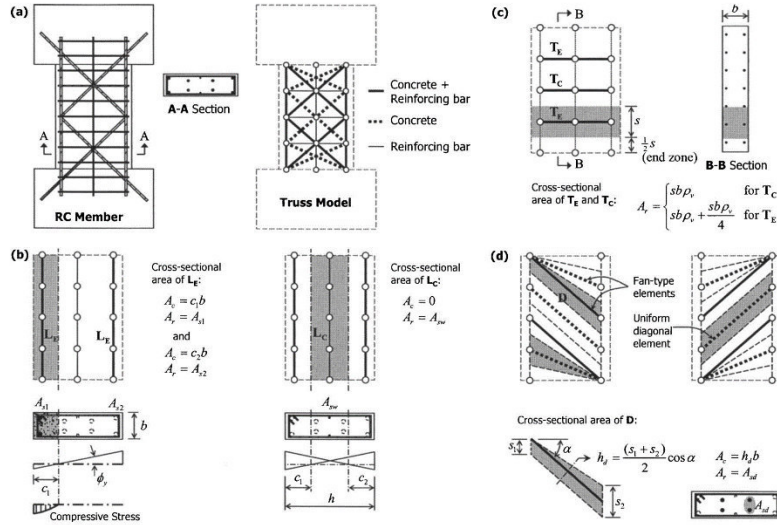


Figure 2.13: Modeling of concrete and reinforcing steel elements [Park and Eom (2007)]

The work by Park and Eom (2007) details a simplified nonlinear analytical method using a truss model. This nonlinear truss model uses longitudinal, transverse, and diagonal truss elements composed of both concrete and reinforcing bars. Figure 2.13 shows an example of how these concrete and steel elements are employed in the modeling procedure and their effective areas. For the longitudinal elements, the concrete area is calculated as $A_c = bc$, where b is the width of the cross section and c is the depth of the compressive zone at the time when the flexural reinforcing bars begin to yield. The areas of the reinforcing bar element at the boundaries are set to the areas of the corresponding longitudinal rebars. The effective compressive strength for the concrete elements was computed using the work by To et al. (2001) where $f_{ce} = \frac{C_u}{A_c}$, C_u is the ultimate resultant compressive force of the concrete in the compressive zone. The effective tensile strength of the concrete was taken to be one-third of the actual tensile strength: $f_{te} = \frac{f_t}{3}$. The transverse elements are represented by reinforcing ties and their effective areas are given by $A_r = sb\rho_v$ for elements at the midspan and $A_r = 5/4sb\rho_v$ for elements at the supports. This is done with the

rational that 50% of the shear resistance occurs in the end zones. Finally, the effective area of the diagonal elements is computed by $A_c = h_d b$ where h_d is the depth of the uniform diagonal element or average depth of the fan type diagonal element. The angle of inclination is restricted based on CEB-FIP requirements where they range from 31 to 59 degrees (To et al. 2001). Figure 2.14 demonstrates the cyclic stress-strain relationships for the concrete and steel materials. The cyclic stress-strain relationship for concrete was derived using a modified model of Mansour et al. (2001). For steel, the model developed by Brown and Jirsa (1971) was used. The nonlinear truss model was then validated by various experimental wall and beam tests from literature, one of which is shown in Figure 2.15. Results indicated that the truss model correctly predicted the overall load-deformation relationship of the test specimens but could not accurately predict buckling and fracture of reinforcement.

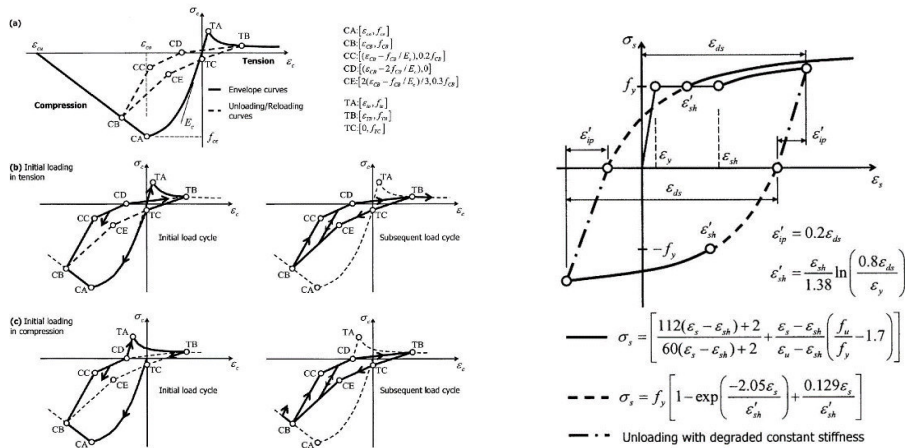


Figure 2.14: Cyclic stress-strain relationship for concrete (left) and steel (right) used in Park and Eom (2007)

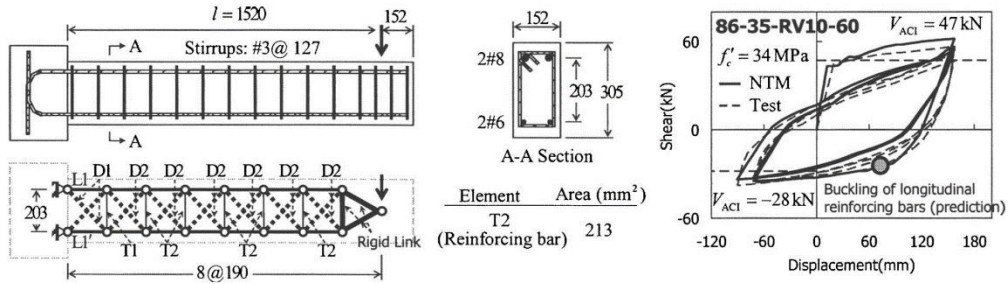


Figure 2.15: Analytical results of a cantilever beam from Park and Eom (2007)

Kim and Mander (1999,2000) developed a cyclic inelastic STM approach to study the behavior of structural concrete members that were subjected to both shear and flexure. A two-point Gauss truss model was used to unify the flexure and shear analysis methods for concrete member including both B- and D- regions. The Cyclic Inelastic Strut-Tie (CIST) model using Drain-2DX showed generally good agreement with experimental test data but the limitations of the model were its inability to predict the gradual loss of anchorage and strength decay because of cyclic loading.

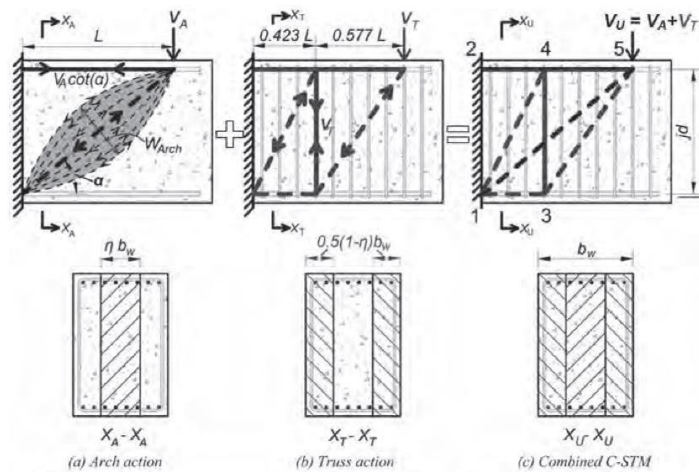


Figure 2.16: Composition of arch and truss action that leads to compatibility strut-and-tie model Scott et al. (2012)

Scott et al. (2012a and 2012b) extended the work by Kim and Mander (1999, 2000) to develop the Compatibility Strut and Tie Model (C-STM). Compatibility truss modeling considers truss member deformations to formulate the shear stiffness of RC beams using strain energy concepts of the analogous beam. The formulation of the C-STM approach is presented in Scott et al. (2012a) and the implementation is provided in Scott et al. (2012b). C-STM analysis combines truss and arch action that contribute to the shear resistance. The modeling approach was designed to aid the practicing engineer using a step by step model formulation and the use of commercially available structural analysis software SAP 2000. Figure 2.16 demonstrates how the truss and arch action are combined to consider the overall structural response and in Table 2.4 provides the truss member axial rigidities. The constitutive material model for steel was chosen to be a bilinear stress-strain curve with a 3% strain hardening ratio. Figure 2.17 shows the material behavior of concrete. Compression softening effect was considered for diagonal struts to take into consideration the reduction in strength due to orthogonal tensile strain. To model the concrete in tension, Karthik and Mander (2011) model was used.

Table 2.4: Elastic truss member axial rigidities for C-STM [Scott et. Al (2012)]

Member	Steel		Concrete		Comments
	E	A	E	A	
2-4	E_s	A_s	E_c	$b.kd$	Tension chord
4-5					
1-3	E_s	A_s'	$\psi_E E_c$	$b.kd$	Compression chord ¹
3-4	E_s	$N_h A_{sh}$	E_c	$(4c + 2d_b) N_h s$	Active hoop steel including tension-stiffening effect ¹
1-5	—	—	E_c	$\frac{0.375\eta b_w j d}{\cos \alpha}$	Concrete strut in arch mechanism
1-4	—	—	E_c	$\frac{0.5(1-\eta) b_w j d}{\sqrt{0.423 + \tan^2 \alpha}}$	Concrete strut in truss mechanism
3-5	—	—	E_c	$\frac{0.5(1-\eta) b_w j d}{\sqrt{0.577 + \tan^2 \alpha}}$	Concrete strut in truss mechanism

$\psi_E =$ strain compatibility coefficient = $\frac{\sqrt{f'_c}$ (psi)}{168(1 - d'/kd)} = $\frac{\sqrt{f'_c}$ (MPa)}{14(1 - d'/kd)}; in lieu of more precise analysis, it is recommended that $\psi_E = 0.6$.

¹ $N_h = \text{int}[L/s - 1]$ is integer part of active hoops in truss mechanism.

Karthik et al. (2016) introduced two improvements to the C-STM model to better represent the overall behavior through failure. These improvements included the implementation of the softened concrete model for diagonal strut members directly into the analysis and the displacement controlled implementation of the analysis. In this study, the authors validated the refined C-STM by comparing it to various experimental results. One such model validation from Braci et al. (2000) is shown in Figure 2.18. The study concluded that satisfactory results could be obtained for both the monotonic and cyclic response of shear critical structures. The improvements that Karthik et al. (2016) proposed enabled the post peak falling branch of the force-deformation response to be captured and predict the failure load and displacement with good accuracy.

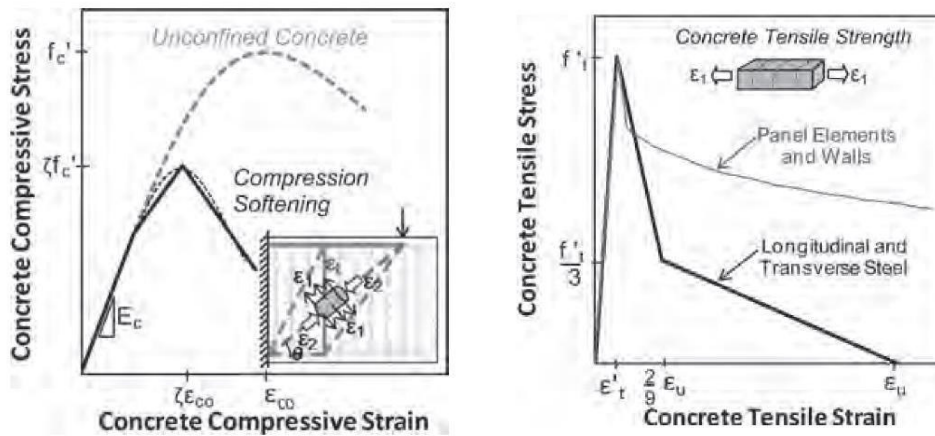


Figure 2.17: Concrete stress-strain behavior for C-STM [Scott et. al. (2012)]

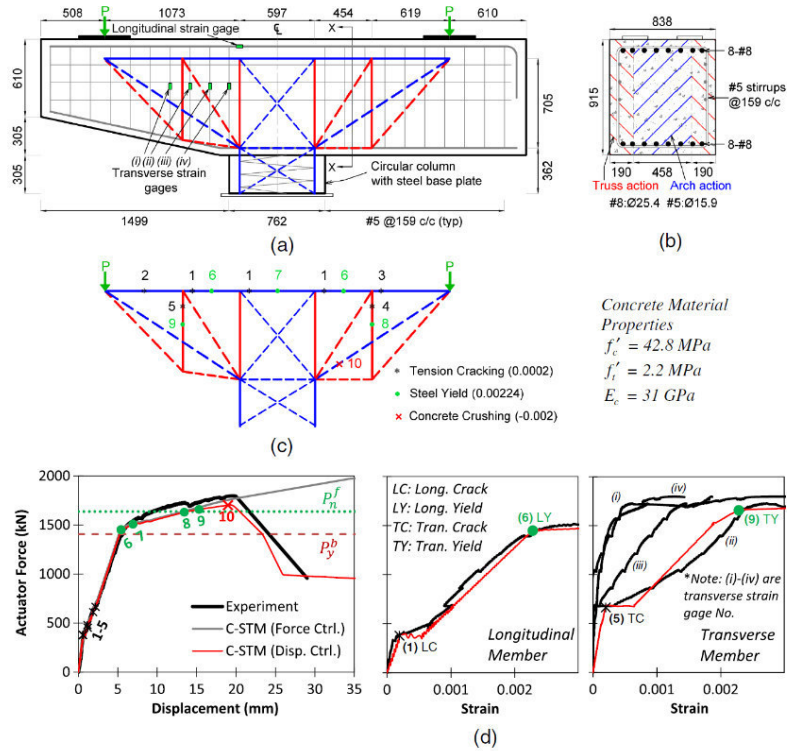


Figure 2.18: Analytical results of C-STM [Karthick et. al. (2016)]

Panagiotou et al. (2012) proposed a 2D nonlinear model using vertical, horizontal, and diagonal truss elements to represent concrete and steel reinforcement. The main objective of the model was to compute the post-cracking plane stress behavior, the lateral force, and the deformation capacity of RC walls. In comparison to other models, this truss model used a parallel angle truss model, accounts for the tension stiffening in the horizontal direction, and accounts for mesh size effects. This work concluded that the nonlinear truss model could compute the post-cracking cyclic force-displacement response of RC walls with significant shear-flexure interaction in their response with reasonable accuracy.

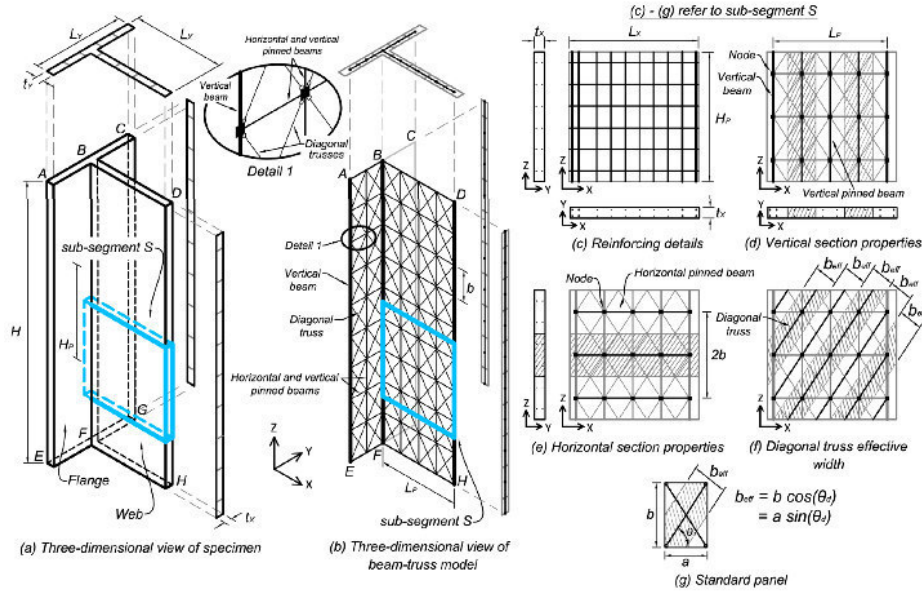


Figure 2.19: Formulation of beam-truss model for a T-shape section wall [Lu and Panagiotou 2013]

Subsequently, Lu and Panagiotou (2013) implemented nonlinear Euler-Bernoulli fiber section beam elements to create a 3D beam truss model (BTM). The modeling approach employs four elements: (1) nonlinear fiber-section Euler-Bernoulli beam elements used in the vertical direction, (2) nonlinear truss elements in the horizontal directions, (3) linear Euler-Bernoulli beam elements used in parallel to the truss elements in the horizontal direction, and (4) nonlinear truss elements in the diagonals of the panels formed by the horizontal and vertical elements. Figure 2.19 shows a schematic of how these elements are applied to a T-shape section wall. The vertical beam elements and horizontal truss elements model the concrete and steel in that section. The concrete truss elements were used to represent the compressive stress fields of concrete. The angle of inclination in the study was restricted to 40-50 degrees. The effective width of the diagonals was computed as $b_{eff} = a \sin(\theta_d)$, where a is the length of a panel. The concrete constitutive model for confined and unconfined concrete and steel elements are shown in Figure 2.20. The nonlinear

analysis program *OpenSees* was used and the material models employed were *ConcretewBeta* and *Steel02*. The model was next validated through various experimental tests and concluded that the BTM computed very satisfactorily the post-cracking cyclic force-displacement response of the three specimens.

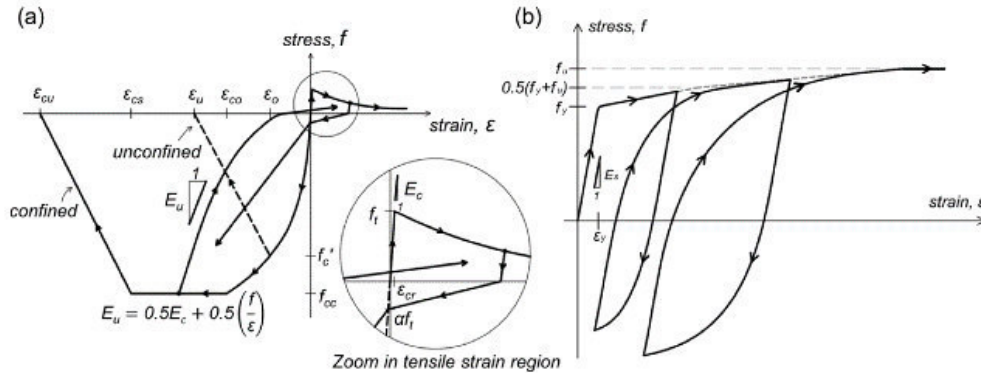


Figure 2.20: Stress-strain relationship for concrete [Lu and Panagiotou (2013)]

Lu et al. 2014 modified the BTM and applied to the model to RC slabs. Five changes were made to the original BTM formulation which includes: (1) the angle of the diagonals is computed based on the shear demand and transverse reinforcement ratio, (2) nonlinear fiber-section Euler-Bernoulli beam elements are used in both the vertical and horizontal directions (3) all vertical beams except those at the ends of each wall segment and all horizontal beam elements are pinned in the direction parallel to the length of the wall segment, (4) the computation of the strain normal to the diagonal truss element is improved and (5) the tension strength of the concrete in the horizontal direction is ignored. The changes were implemented and the refined BTM was validated against experimental tests. Some of these results are shown in Figure 2.21. Additional studies have applied the BTM to RC columns (Moharrami et al 2014) and further studies on RC wall and slabs (Lu et al. 2016 and Lu and Panagiotou 2016). These studies further confirmed that

BTM captures the nonlinear response very well and can predict diagonal compression and tension failure modes.

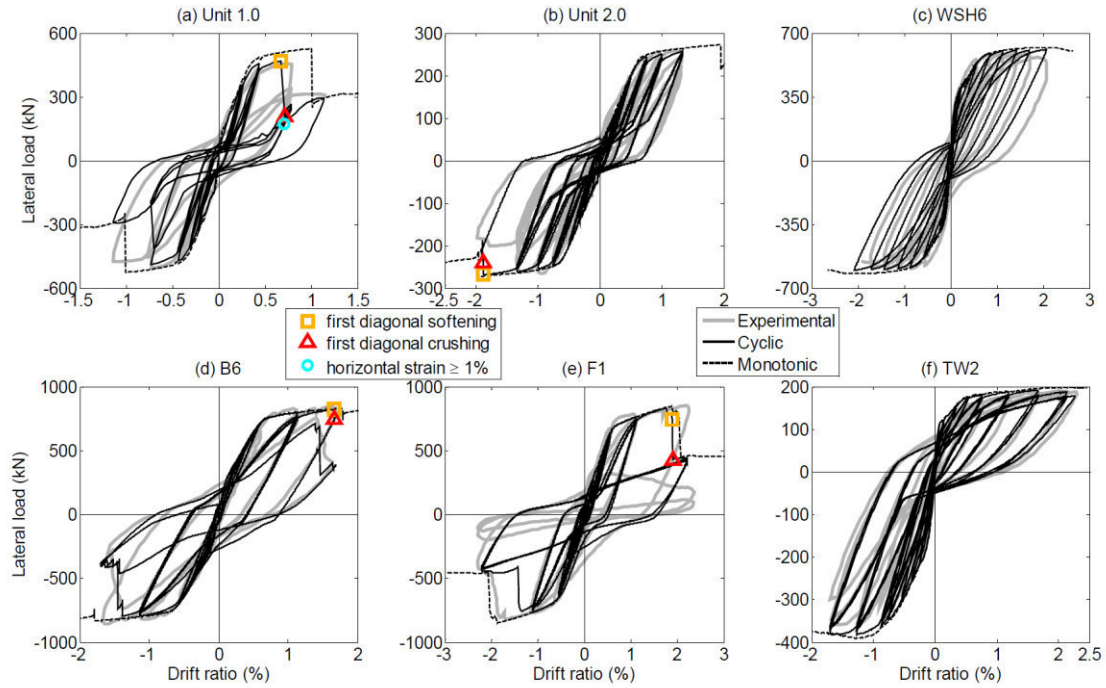


Figure 2.21: Analytical results from beam-truss model [Lu et.al. (2014)]

2.4 Conclusions on Literature Review

This chapter presented a literature review for beams with openings, moment resisting frame beams and strut-and-tie modelling. Based on the literature review on beams with opening it is noted that the experimental investigations conducted thus far have been primarily conducted on small-scale, simply supported, beams tested monotonically to failure. Furthermore, the experimental work on flexure-dominant RC beams have mainly focused on the behavior effects caused by the loading history, the effect of hoop spacing, and the shear span-to-depth ratio. The apparent gap from the

literature is that there is no published experimental data on RC MRF beams with web openings under reverse cyclic loading. The test specimens in this study were large-scale MRF beams that sought to assess the role of introducing rectangular web openings. The nonlinear STM approach can analyze discontinuous shear critical RC structural elements and it is applied to the beam specimens in Chapter 6.

Chapter 3 Specimen Details

3.1 Specimen Design and Test Matrix

The test specimens used in conjunction with the experimental portion of the research program are replicas of MRF beams located in an existing structure in California that were designed in accordance with the recommendations outlined in the ACI Building Code Requirements for Structural Concrete (ACI 318-95) & the Uniform Building Code (UBC 97). Utilizing the benefit of beam symmetry between the columns, the actual test specimens were constructed as half MRF beams (i.e., test specimen length = 50% of the original beam length), as depicted in Figure 3.1. One of the main objectives of the study was to design the specimens at the largest scale feasible while still allowing utilization of standard US rebar sizes. Table 3.1 provides the original and scaled geometry and reinforcement of the specimen along with the actual achieved scaling ratio. The 80% scale was selected such that readily available materials can be used for specimen construction, with good-to-excellent scaling correlation with most reinforcement bars present in the original construction. Note that the effective width of the flange (b_{eff}) was slightly reduced to prevent excessive overhang of the flange during testing.

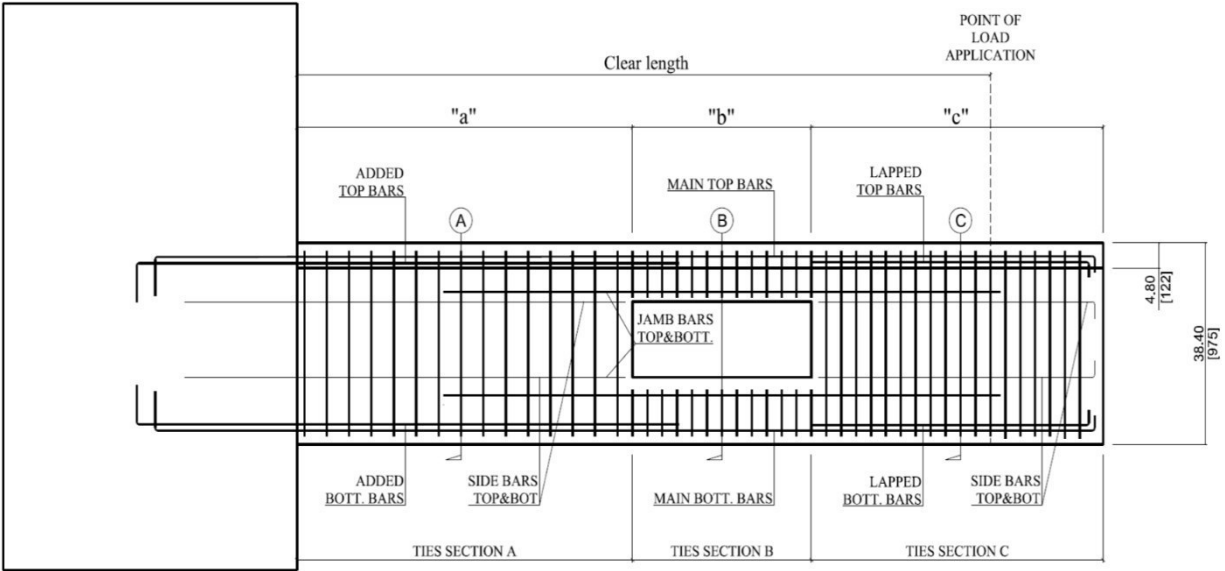


Figure 3.1: Elevation view of generic test specimen with geometry and reinforcement

Table 3.1: Comparison of full-scale and 4/5th scale beam parameters

Parameter [in]	Full Scale		4/5 Scale		Actual Value	Target Value	Ratio
b	30		24		0.8	0.8	1.0
h	48		38.4		0.8	0.8	1.0
t _f	6		4.8		0.8	0.8	1.0
b _{eff}	86		62.4		0.73	0.8	0.91
d _b (1)	#11	1.41	#9	1.13	0.8	0.8	1.0
d _b (2)	#10	1.27	#8	1.0	0.79	0.8	0.98
d _b (3)	#9	1.128	#7	0.88	0.78	0.8	0.97
d _b (4)	#8	1.0	#6	0.75	0.75	0.8	0.94
d _b (5)	#5	0.63	#4	0.5	0.79	0.8	0.99

It is also important to note that the in-situ MRF were single bay frames located in the interior of the building. All material properties were selected based on in-situ material samples, and are presented in detail in Chapter 4.5. The openings in the existing beams were introduced after the original design of the MRF was completed; no accompanying structural analyses and design

information were available. Table 3.2 displays the test matrix for the four specimens hereafter referred to as specimens S1, S2, S3, and S4. The primary test variables included the shear span of the beam (L_s), the inclusion of an opening, and the reinforcement details.

Table 3.2: Test matrix of main beam specimen variables

	Shear Span Ls [ft.]	Opening Present	Beam End Longit. Reinf.: Top/Bot	Beam Opening Jamb Reinf.
S1	11.2	Yes	6#9 + 2#7	4#8 + 2#7
			6#9	
S2	12.4	Yes	12#9	6#9
			8#8	
S3	15.5	Yes	8#9	6#7
			6#8	
S4	10.4	No	6#9 + 2#8	-
			8#8	

3.2 Test Specimen Details

The four beam specimens had consistent cross-sectional geometries: the web was 38.4 in. high and 24 in. wide, and the top slab had a thickness of 4.8 in. and a width of 62.4 in. The length of the specimens ranged from 12 ft. to 17.5 ft. Specimens S1, S2, and S3 were constructed with a rectangular shaped web opening of 38.4 in. long by 14.4 in. high, which represents about 38% of the overall beam depth. Specimen S4 was constructed without a web opening and was used as the control beam to validate the test setup and from which to draw comparisons and differences. The different geometries with respect to specimen length for the four specimens are provided in Figure 3.1 and Table 3.3. As shown in Figure 3.1, each beam is geometrically separated in the three beam regions: (1) region A represents the fixed beam-column interface, (2) region B represents the opening region, and (3) region C represents the beam tip where loading is applied. Along with the

geometric separation, Figure 3.1 also provides the nomenclature for the reinforcing elements. Figure 3.2 allows the comparison of sections A, B, C, for all four specimens. Table 3.3 compares the amount of reinforcement in each section as well as the top, bottom, and transverse reinforcing ratios (ρ_{top} , ρ_{bot} , ρ_{transv}). Figures 3.3-3.6 provide the specific details and section geometries for each beam specimen. Figure 3.7 shows the top view of a typical reaction block and T-beam specimen. The flange was terminated at the tip of the beam to allow the connection of the actuator.

The top and bottom flexural reinforcement of each of the specimens consisted of main U-bars placed along the length of the beam, L-bars to reinforce the portion of the beams with high flexure demands, and additional jamb bars near the top and bottom faces of the rectangular shaped opening. Furthermore, S1 and S2 were furnished with lapped bars at section C, which represents supplemental reinforcement provided at the mid-span of the in-situ RC MRF T-beams. All longitudinal rebar was anchored into the reaction block using development lengths in accordance with ACI 318-11. Shear reinforcement in all beam specimens consisted of full-depth stirrups (No. 4 bars) with seismic hooks. The stirrups were closed with standard cross ties with hooks (135° and 90°) at opposite ends. In addition, at the rectangular openings, both chords were reinforced with small stirrups (No. 4 bars) with seismic hooks.

Table 3.3: Reinforcement details

		S1			S2			S3			S4		
		A	B*	C	A	B*	C	A	B*	C	A	B*	C
TOP	ρ (top)	0.009	0.011	0.017	0.015	0.016	0.023	0.009	0.012	0.007	0.009	—	0.005
	Main	4-#9			6-#9			6-#9			4-#9		
	Added Layer 1	2-#9			—			—			2-#9		
	Added Layer 2	2-#7			6-#9			2-#9			2-#8		
	Jamb	4-#8 + 2-#7			6-#9			6-#7			—		
	Lapped	4-#9			4-#9			—			—		
BOTTOM	ρ (bottom)	0.007	0.011	0.015	0.007	0.012	0.017	0.005	0.009	0.004	0.007	—	0.004
	Main	4-#9			4-#8			4-#8			4-#8		
	Added layer 1	2-#9			2-#8			2-#8			2-#8		
	Added layer 2	—			2-#8			—			2-#8		
	Jamb	4-#8 + 2-#7			6-#9			6-#7			—		
	Lapped	4-#9			4-#9			—			—		
TIES	ρ (transv.)	0.004	0.004	0.006	0.008	0.012	0.012	0.004	0.004	0.002	0.004	—	0.003
	no. sets-size	1-#4@			2-#4@			1-#4@			1-#4@		
	spac'g (in)	4.75	4.75	3.25	4.75	3.25	3.25	4.75	4.5	8.75	4.75	—	6.5

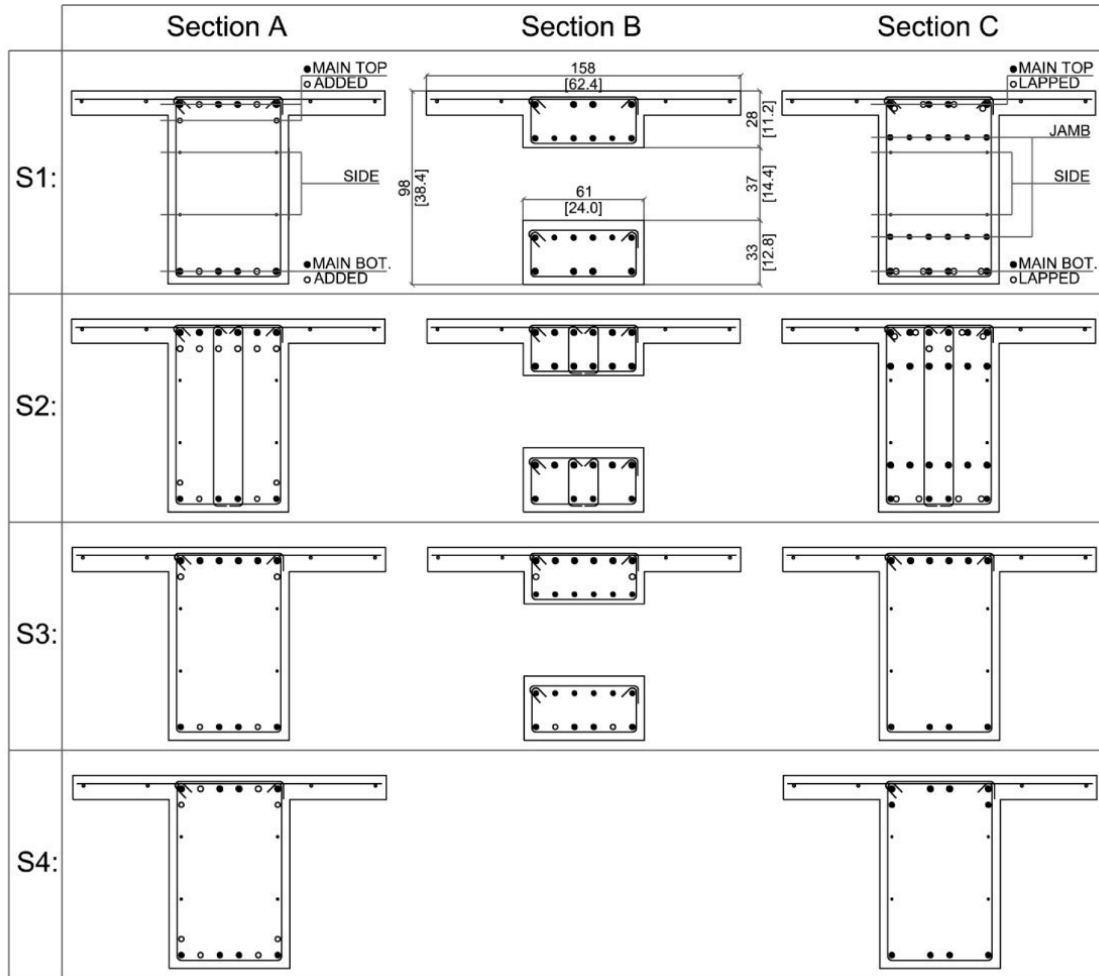


Figure 3.2: General reinforcement description in cross-section of sections A (left), B (center), and C (right). Dimensions in inches and SI units shown in brackets [mm].

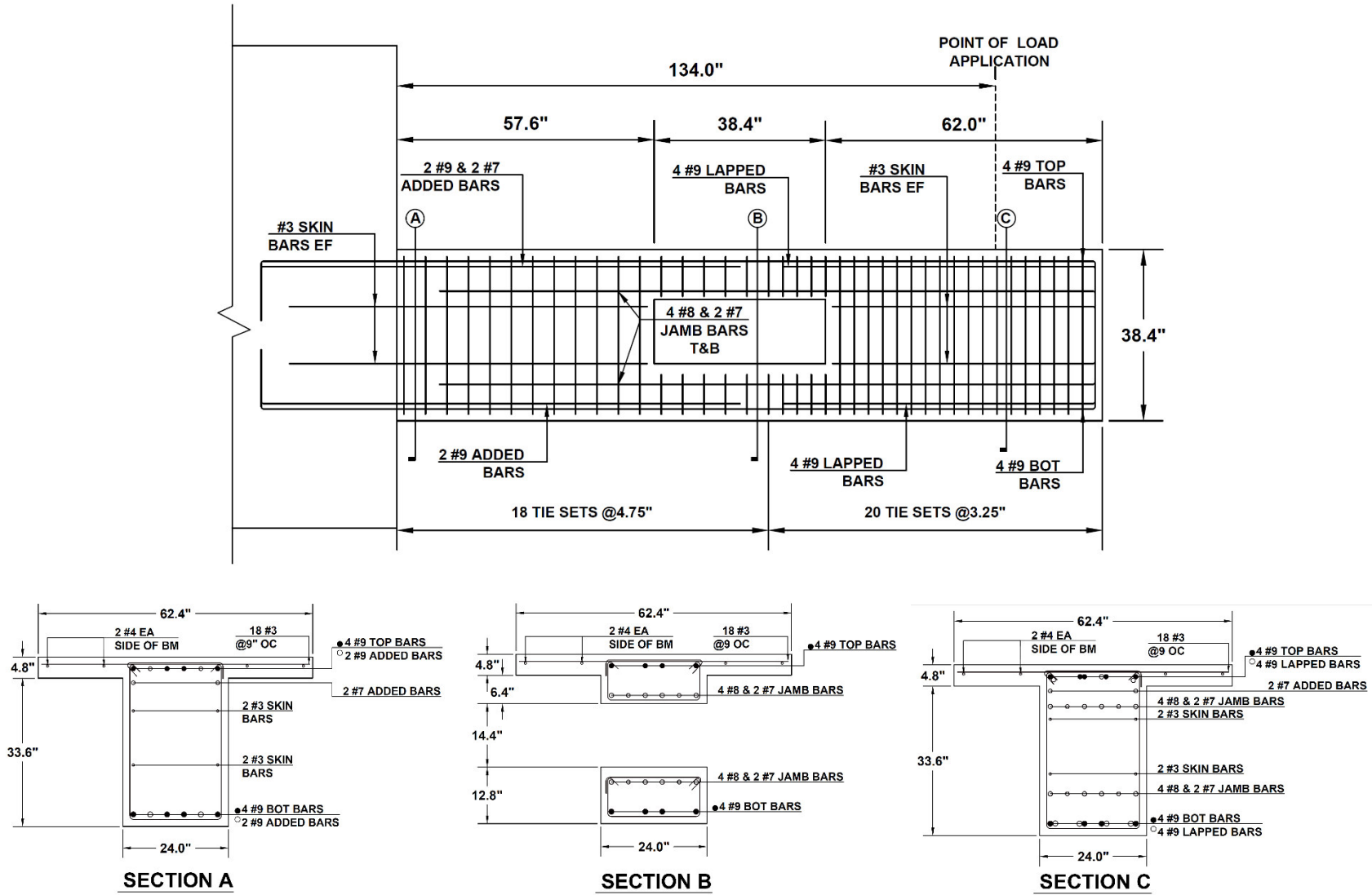


Figure 3.3: Beam elevation geometry and reinforcement details for S1

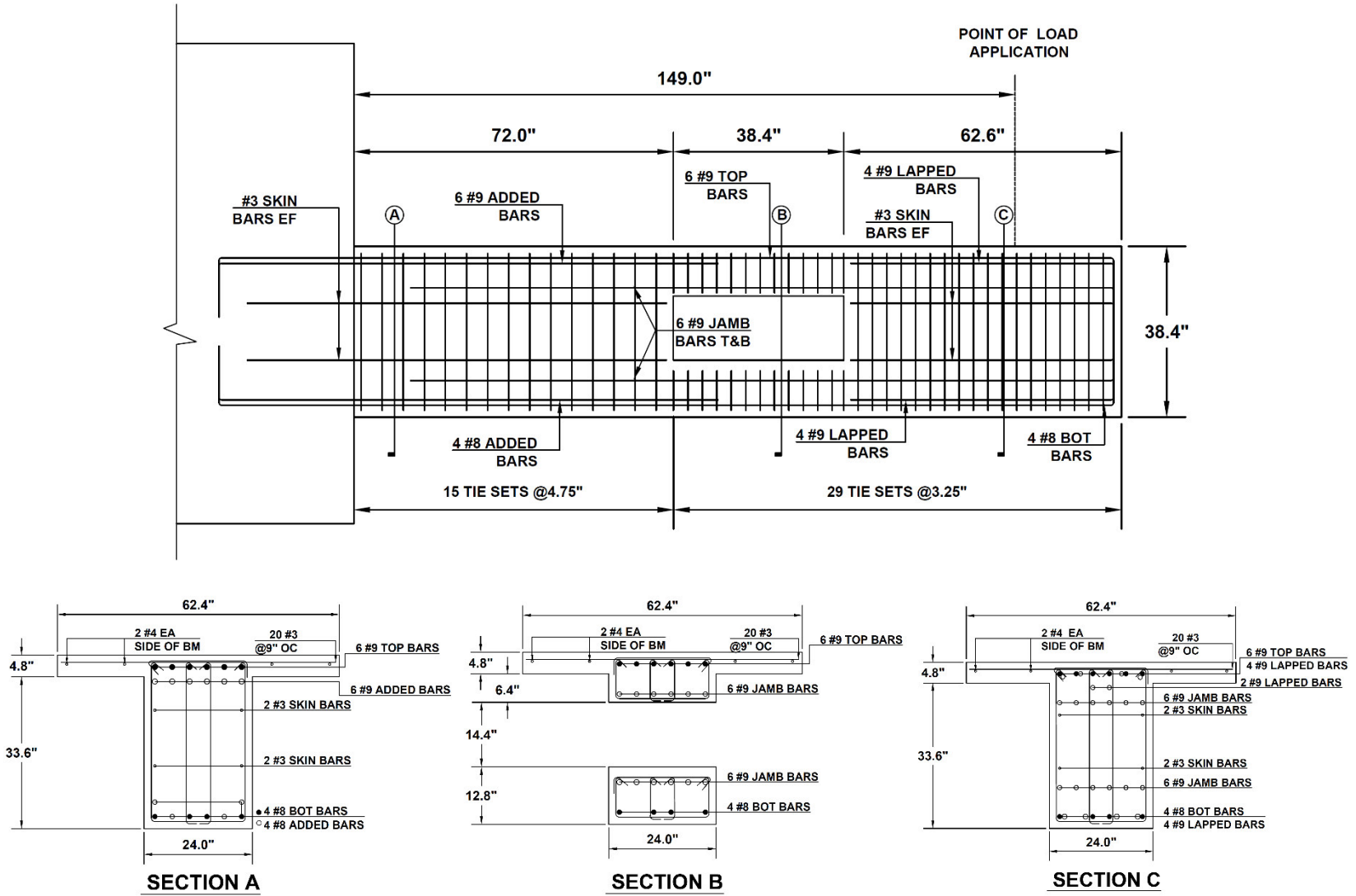


Figure 3.4: Beam elevation geometry and reinforcement details for S2

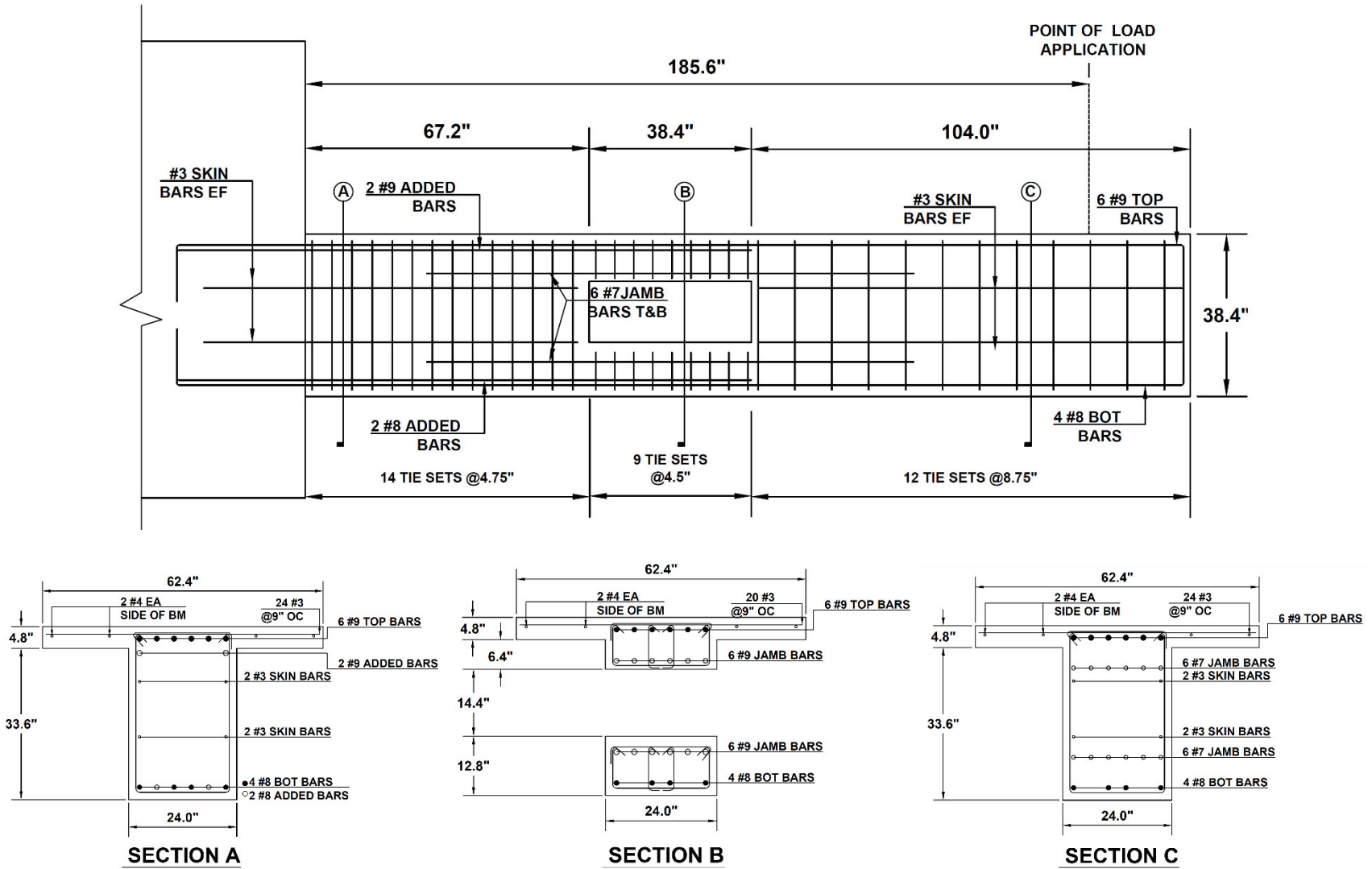


Figure 3.5: Beam elevation geometry and reinforcement details for S3

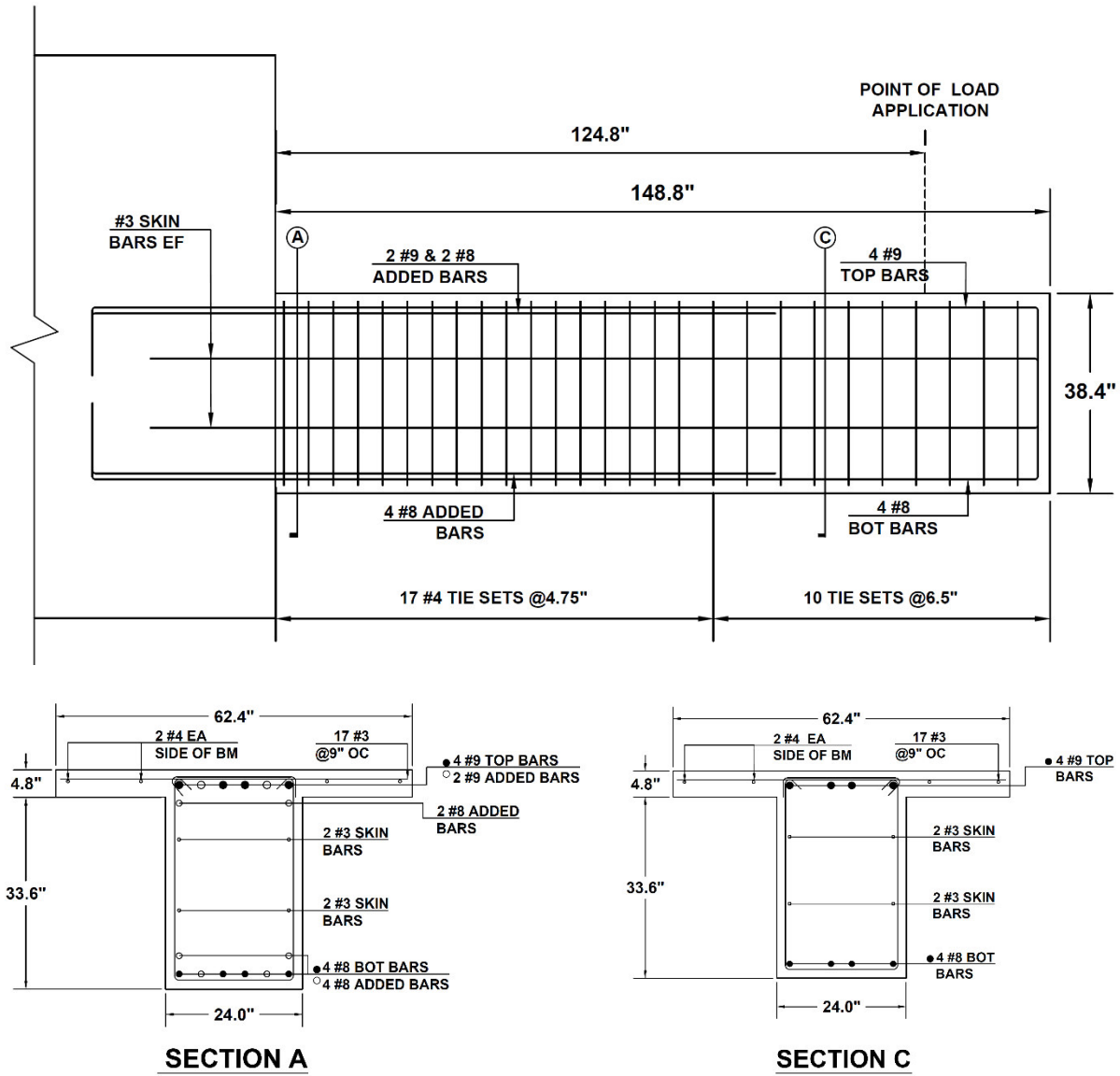


Figure 3.6: Beam elevation geometry and reinforcement details for S4

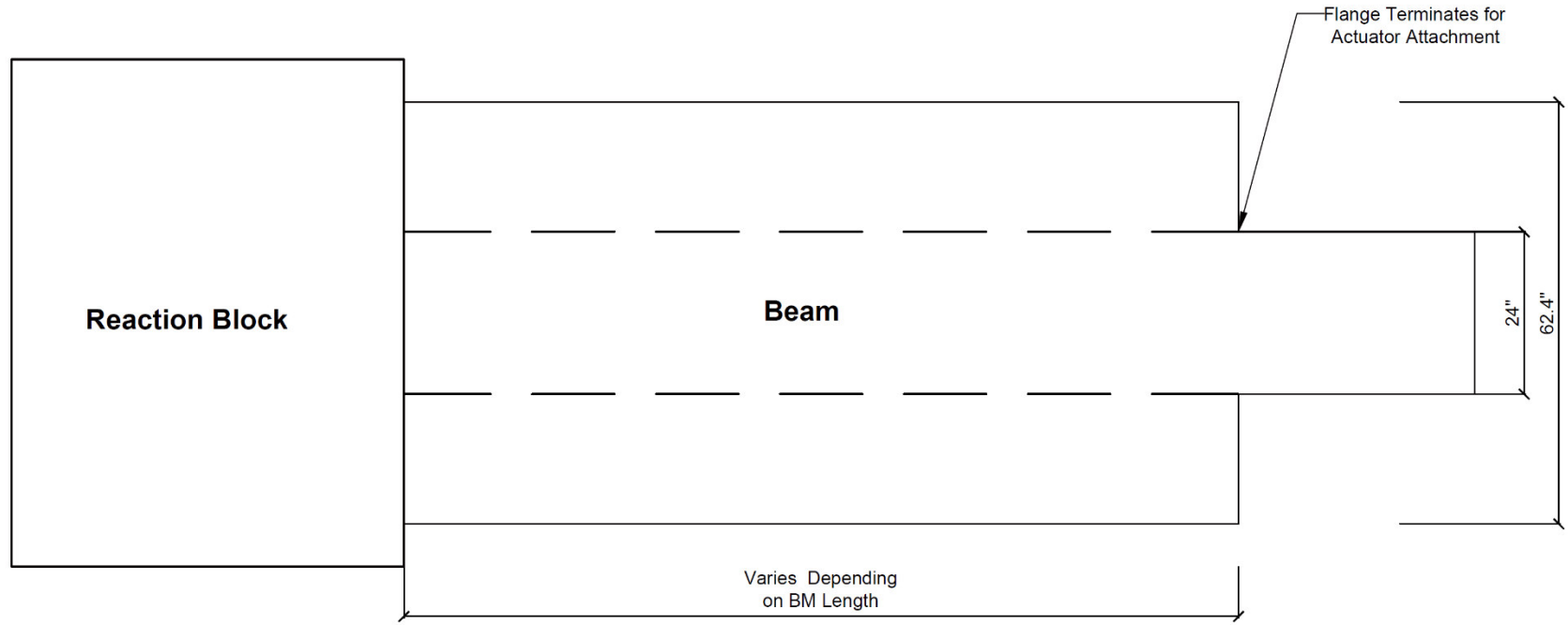


Figure 3.7: Top view of reaction block and beam specimen

Chapter 4 Experimental Program

4.1 Construction

All test specimens were constructed in the UCI Structural Engineering Testing Hall (SETH). The construction of S1 and S4 was conducted between January and March 2013. S2 and S3 were constructed in April and May 2013. It was required that the test specimens be fabricated in a manner which represented the sequenced used in the construction of the in-situ beams, therefore the construction sequence was similar for all beam specimens. Approximately 11 tons of rebar were shipped on Jan 28th, 2013 to the UCI SETH lab and stored in a corrosion protected environment (see Figure 4.1)



Figure 4.1: Rebar delivery to the UCI structural laboratory

The first stages of construction included the reinforcement preparation for the reaction blocks. All stirrups were tied and stored on site for easy assembly (Figure 4.2 and Figure 4.3). Following the preparation work, the peripheral rebar of the reaction block was situated in place

(against the strong wall) and the assembled stirrup rings were lifted via crane into the longitudinal reinforcement. Transverse reaction block reinforcement was spaced at 6 in. Following the reaction block reinforcement, the beam reinforcement was placed simultaneously and the rebar cage was constructed step by step integrating beam and reaction block reinforcement at the respective locations. PVC pipes with diameters of 2.0 in. were placed in the rebar cage to secure the space needed for the anchors into the strong wall and strong floor (Figure 4.5). Independent structural observations were performed for each rebar cage by MTGL Testing Laboratories to ensure reinforcement details complied with the in-situ condition. The completed rebar cages for S1 and S2 are shown in Figure 4.4.

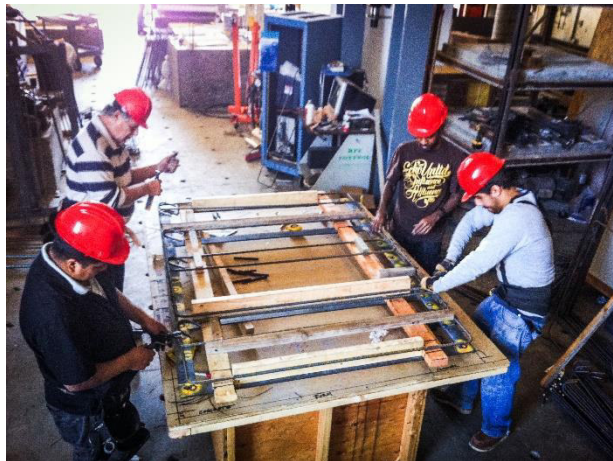


Figure 4.2: Stirrup assembly at the UCI structural lab using a prefabricated mold

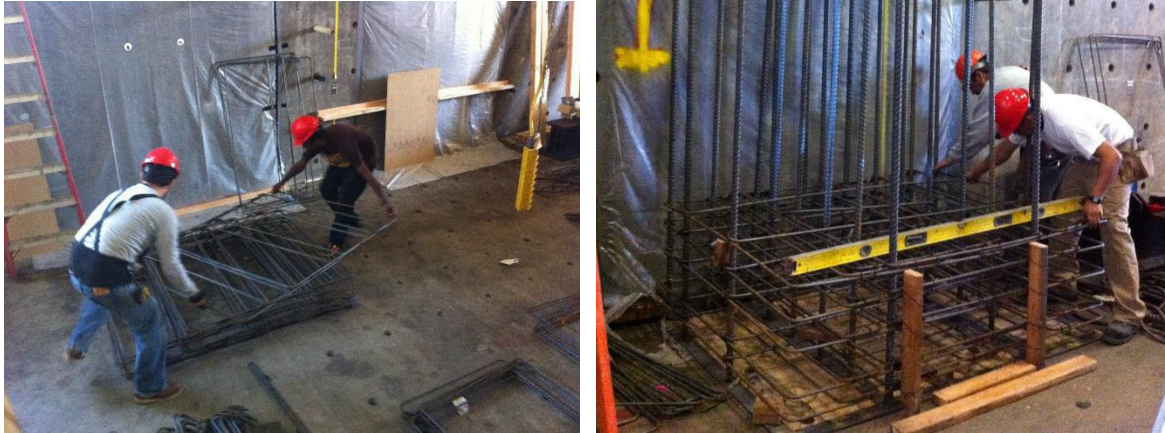


Figure 4.3: Left: Assembly of stirrups for the reaction block stacked in front of the strong wall; Right Construction of the reaction block for S1

The formwork was constructed onsite with reusable panels specifically dimensioned for the geometry of all reaction blocks and beam specimens. $\frac{3}{4}$ in. plywood along with lateral bracing consisting of 2x4s, 4x4s and 2x6s were used to prevent concrete leaking and deformation during concrete placement. Figures 4.4-4.7 show the construction of the formwork and the lateral stabilization thereof. Dywidag rods and hollow metal sections were also used to secure the formwork prior to pouring the concrete (Figure 4.7). The bottom of the cantilevered section was supported using plywood as the bed, and a series of 2x4s spaced at 2 ft. to hold the plywood up. The sides and the flange were also formed using a combination of plywood and 2x4s. Additionally, kickers were also placed at the sides prior to pouring concrete to prevent the formwork from blowing out.



Figure 4.4: Left: Completed rebar cages for S4(left) and S1(right); Right: Formwork panels for the reaction block



Figure 4.5: Left: Top view of reaction block for S1 reinforcement with PVC pipes into strong wall and strong floor; Right: Completed reaction block formwork and construction of beam formwork



Figure 4.6: Almost completed formwork for S4



Figure 4.7: Left: Completed formwork for S1 and view of top slab reinforcement; Middle: Lateral formwork bracing; Right: Formwork around opening of S1

Concrete placement was conducted in 2 stages to create a construction joint between the beam and the top slab to comply with in-situ construction procedure. Concrete placement at day1 consisted of pouring the bottom of the reaction blocks and the beams up to a height of 2 in. below the beam-slab-interface as indicated in Figure 4.8. Each specimen was constructed with its separate concrete truck to prevent a mixing of concrete mixes. Concrete placement was supervised by a certified inspector from MTGL Laboratories.

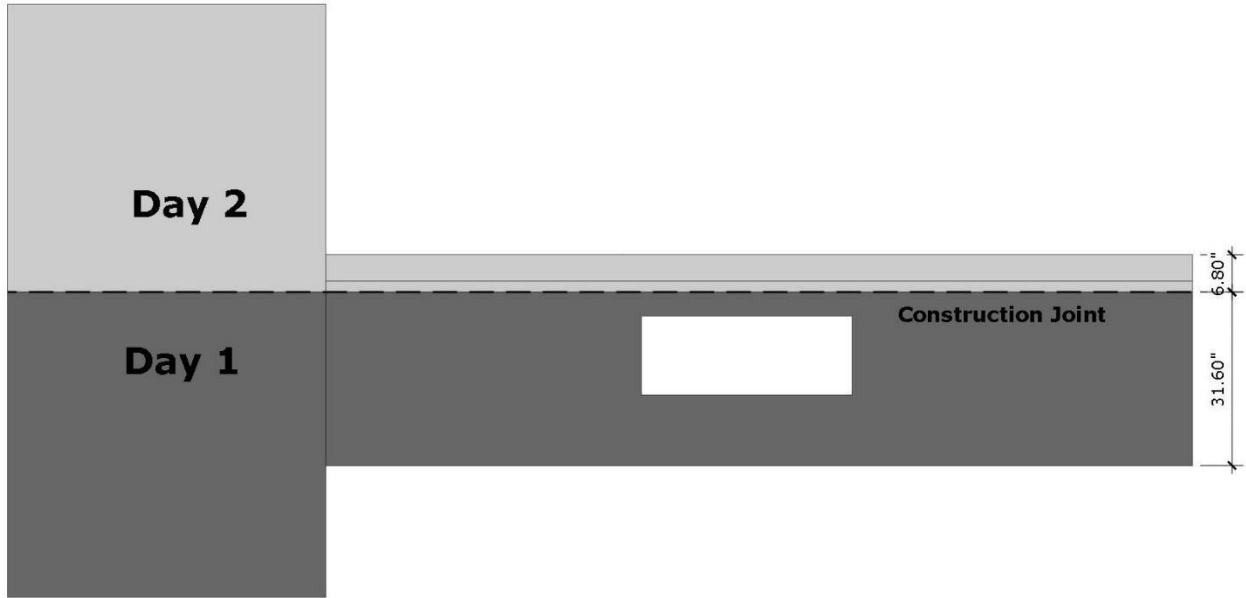


Figure 4.8: Schematic showing typical concrete pouring schedule with construction joint



Figure 4.9: Left: Completion of concrete placement stage 1 (beam and bottom block) of S1; Right: Top slab for S1 is completely poured; Pumper fills up the top of the reaction block

Slump tests were performed simultaneously and concrete cylinder samples were taken from each truck. The concrete surface was left in a rough condition to ensure good adherence of the following concrete layer. The rebar was cleaned with steel brushes and water to prevent concrete from hardening on the steel. Following concrete placement of the slab and the top of the reaction

block, the specimens were covered with plastic sheeting and moistened every day to prevent curing cracks on the top slab. Afterward, the test specimens remained uncovered until the day of testing. Figures 4.10 show the concrete placement and the slab preparation. Figures 4.11 shows the concrete sampling by the structural inspector for consecutive cylinder tests and the conduction of a concrete slump test.

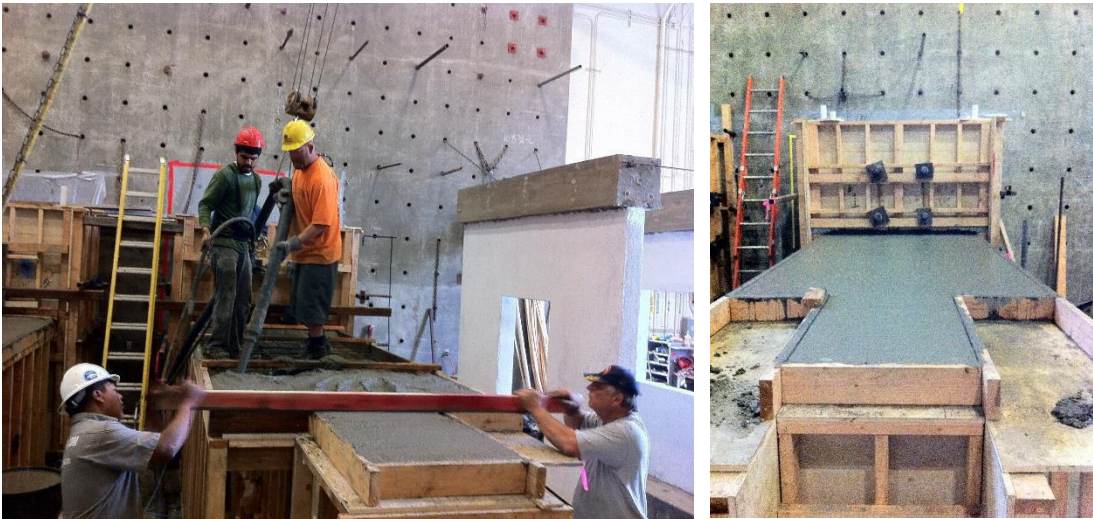


Figure 4.10: Left: Concrete placement of S3 and simultaneous slab finishing; Right: Completed concrete pour of S4



Figure 4.11: Left: Inspector prepares concrete cylinders for strength tests; Middle & Right: Slump tests for concrete in S1 (slump~6.5 in.)

The formwork was removed approximately 7-10 days after concrete placement. The beam specimens were painted with 2 layers of white paint to enhance the visibility of crack development during testing. Additionally, a 6x6 in. grid was applied to each specimen to ease the identification of crack lengths and locations. Figure 4.13 shows the painted test specimen with the grid.

4.2 Test Setup

The cantilever T-beam specimens were tested in a horizontal position at the UCI SETH laboratory. Figure 4.12 shows a typical schematic of the test setup and Figure 4.13 shows an actual photograph of the completed test setup for a typical beam specimen. The following subsections provide more details of the test setup process.

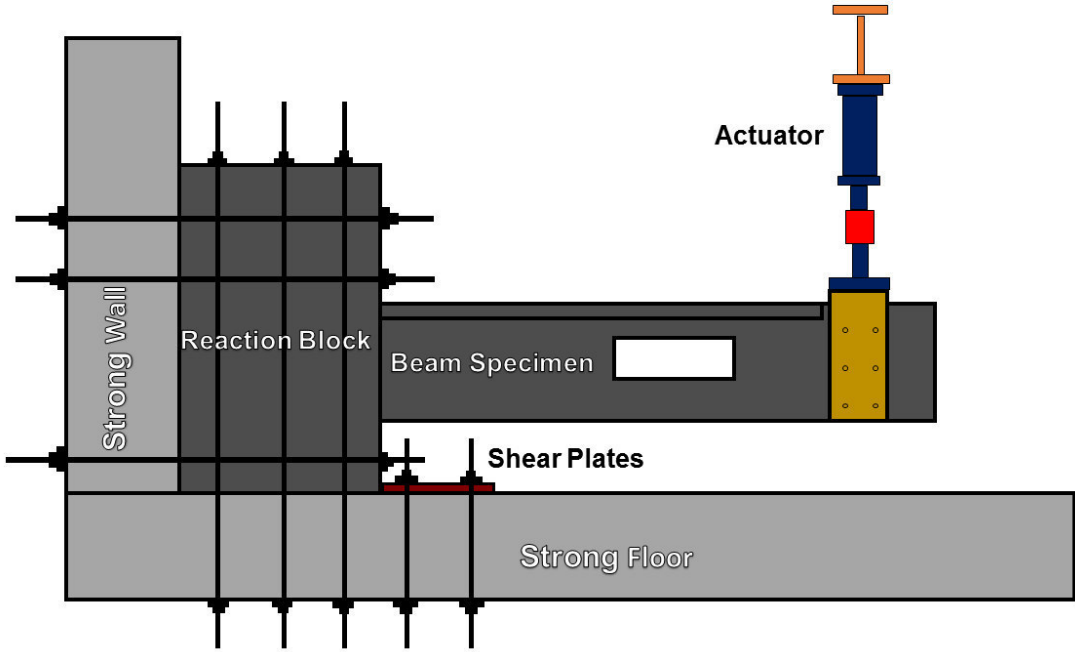


Figure 4.12: Schematic of test setup

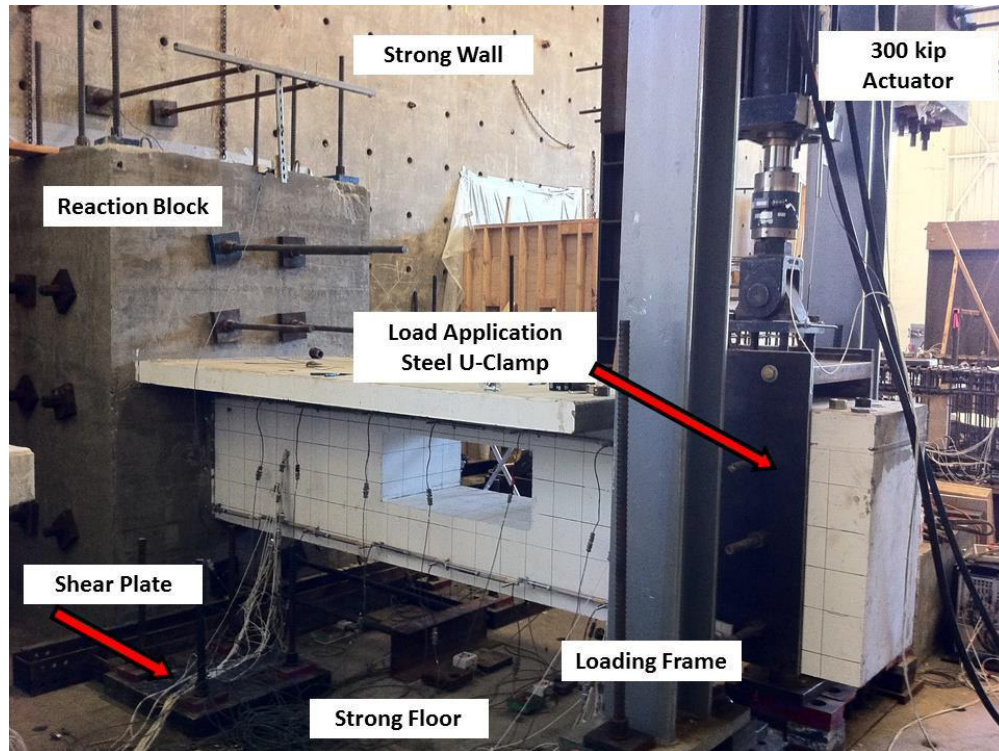


Figure 4.13: Photograph of typical completed test setup

4.2.1 Reaction System

All cantilever beams were anchored in a reaction block with dimensions of approximately 9ft. high, 6ft. wide and 5 ft. long. The reaction block was designed specifically for each test specimen to accommodate the force and moment requirements of the beam end reactions. Additionally, the reaction block dimensions were adjusted to accommodate the floor grid and the point of load application into the beam. The reaction block consisted of a complex system of longitudinal and transverse reinforcement and included an “interior column” with a strongly reinforced system that can simulate the in-situ column condition. The internal column was designed per “weak beam – strong column” principle per ACI 318-11. Figure 4.14 shows the reinforcement details of the

reaction block and Figure 4.15 shows the completed reinforcing cage for the reaction block. The block reinforcement consisted of #9 longitudinal bars all around its circumference and #10 bars in the internal column region. Transverse reinforcement consisted of a stirrup system with additional transverse bars with seismic hooks.

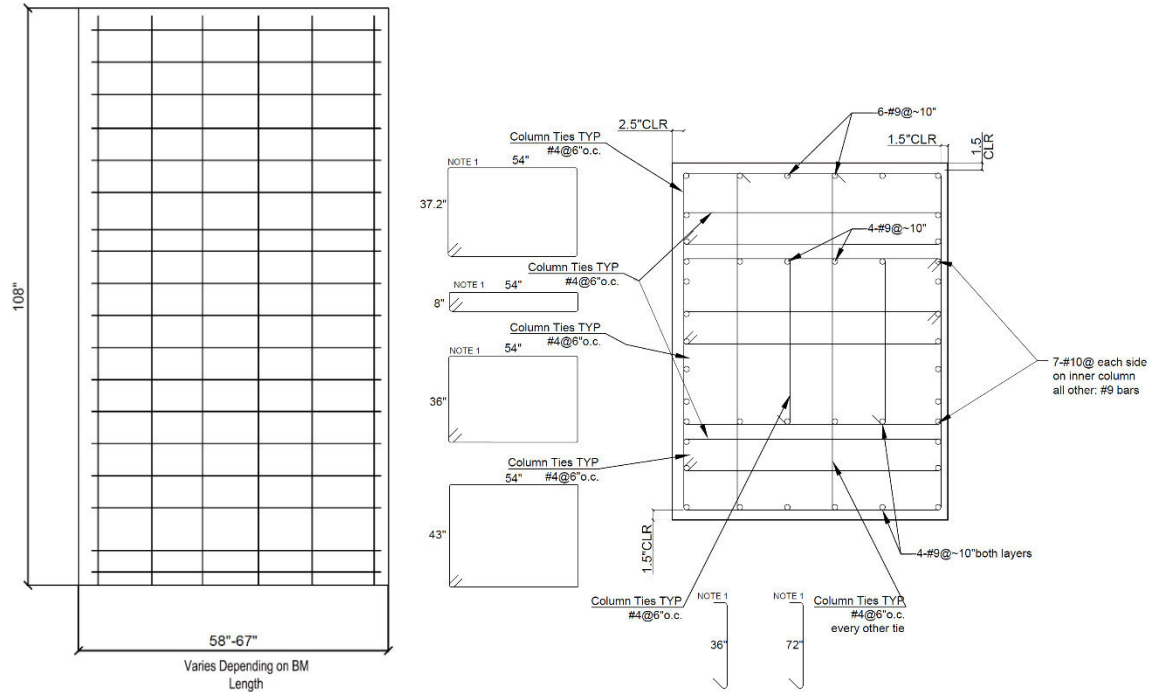


Figure 4.14: Left: Elevation view of reinforcement of the reaction block; Right: Section view of the reaction block demonstrating the reinforcement details



Figure 4.15: Photograph of completed reinforcement for reaction block

The reaction block was anchored in the strong wall via six high-strength post-tensioning anchor bars, i.e., DYWIDAG threaded bars, with diameters of 1-3/8 inches. The DYWIDAG rods passed through holes created by the PVC pipes embedded into the reaction block. Four anchor points were located above the beam and two anchor points were located below the beam. Each DYWIDAG anchor was post-tensioned to approximately 75% of its ultimate strength per anchor onto the block (Figure 4.16). Bolts and steel bearing plates 7x7.5x1.75 in. were used to spread the post-tensioning force over the reaction block. Additionally, the reaction block was anchored to the strong floor in an identical manner using six DYWIDAG bars. Two additional steel shear plates anchored with four post-tensioned rods per plates were installed in front of the block as shown in Figure 4.16 to restrict any rotational movement during uplift

cycles. The reaction block rotation was monitored via external instrumentation. The rotational movement of the block was so insignificant that no corrections to the test data had to be made.

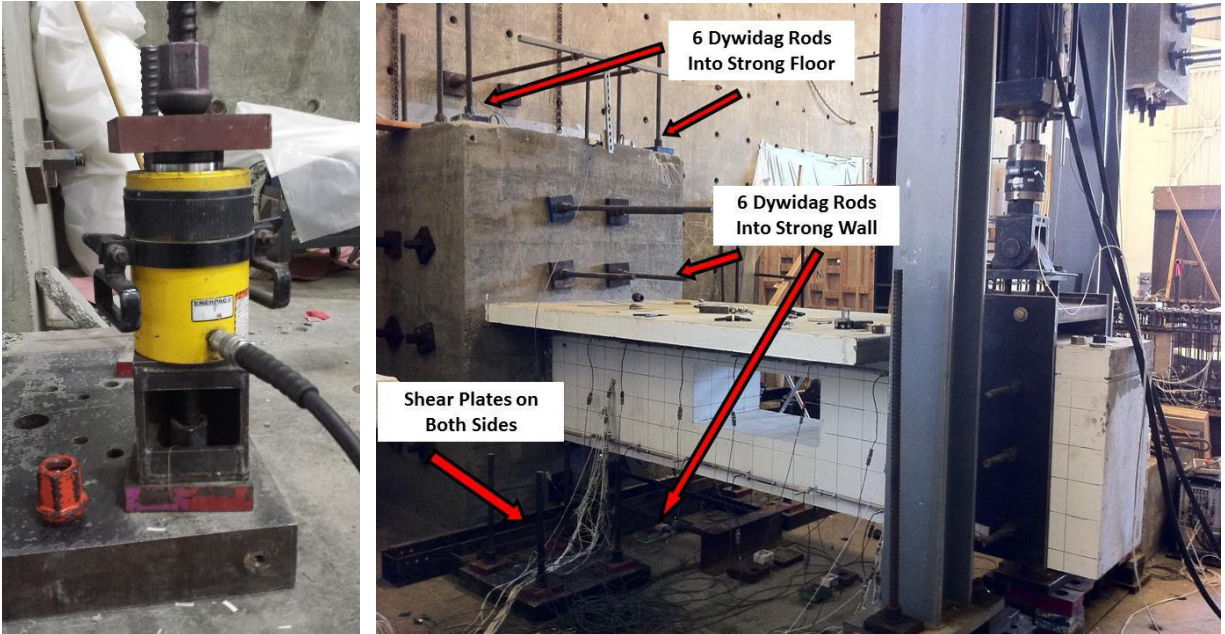


Figure 4.16: Left: Method of post-tensioning of steel anchors; Right: Completed test setup with arrows pointing to anchorage points

4.2.2 Load Application System

A vertical point load was applied at the beam end as shown in Figure 4.17. The point of load application represents the midpoint and inflection point of the full-span-length beam. A hydraulic actuator with a capacity of 300 kips in compression and 270 kips in tension and a +/-12 in. stroke was attached to a loading frame that can withstand a maximum capacity of 270 kips. The single bay steel frame was composed of W10x112 steel section and was 13 ft. high and 7 ft. wide. The reaction frame was elevated from the ground with a combination of steel plates and anchored into the strong floor with eight DYWIDAG rod, post-tensioned to at least 5700 psi. Additional chains

were installed at the top of the frame and tightened into the strong wall and strong floor as shown in Figure 4.17, which provided additional resistance against possible frame rotation.

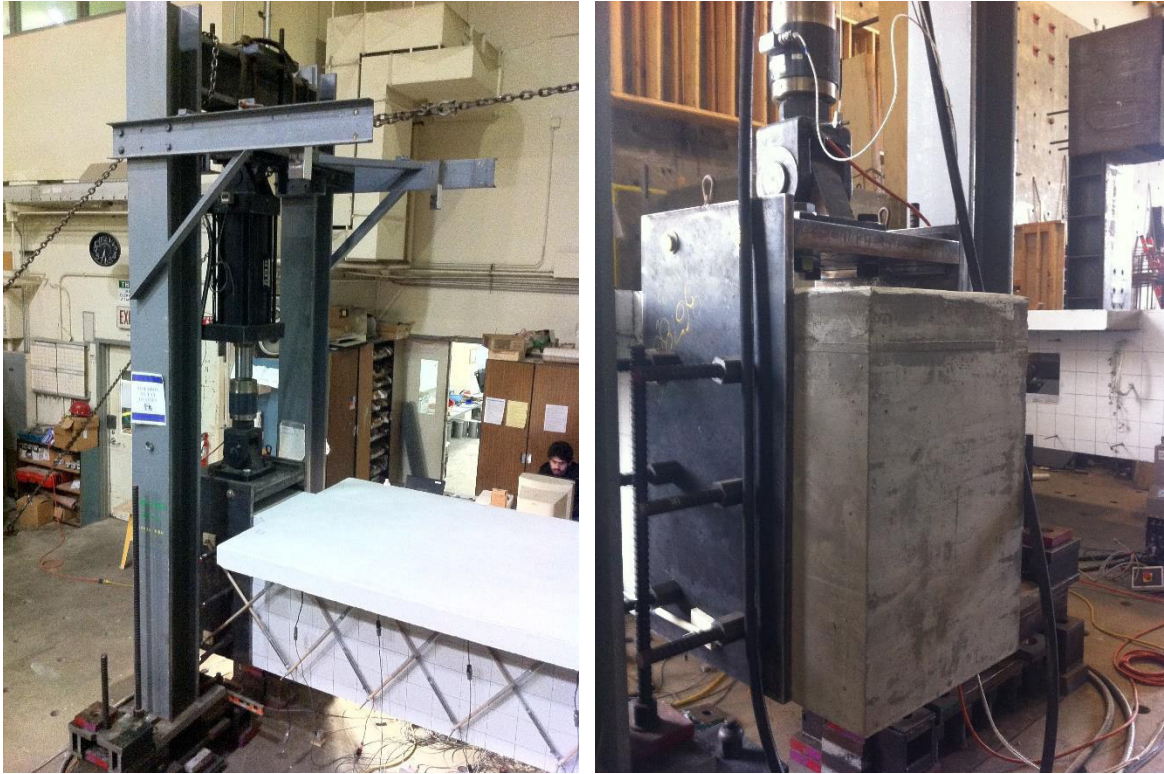


Figure 4.17: Left: Loading frame with actuator, anchors into the strong floor and chains around the top of the beam and into the strong floor; Right: U-plate system at load application point with post-tensioned rods

The load was applied at the beam end via a U-shaped three plate system that embraced the beam from the top and attached the actuator plate directly to the top plate as shown in Figure 4.17. The side plates were 24 in. wide, 46.4 in. high, and 1 in. thick. The side plates were attached to the top plate, 24 in. square and 2 in thick, via high strength bolts and additional supporting welds. The actuator was attached to the top plate via four high-strength bolts, washers, and nuts. The plate system was installed flush along the sides of the beam. Six DYWIDAG rods post-tensioned to 5600 psi were installed through the beam and created a continuous load application profile along

the beam height. The fixity at the end helped to replicate the bending shape of a moment frame beam at the midpoint (i.e. zero curvature at the beam block interface and the moment frame beam center).

4.3 Loading Protocol

The load sequencing of each of the specimens is shown on Figure 4.18 and listed in Table 4.1. In accordance with ASCE/SEI Standard *Seismic Rehabilitation of Existing Buildings* (ASCE/SEI Std. 41-06) and with limited exceptions, three load cycles per displacement increment were applied until the Collapse Prevention (CP) structural performance level was reached; thereafter, two cycles were applied. Testing protocols were developed to capture the anticipated failure mode using the recommendations outlined in C2.8.1 in ASCE Std. 41-06, where theoretical yield displacements were used as reference.

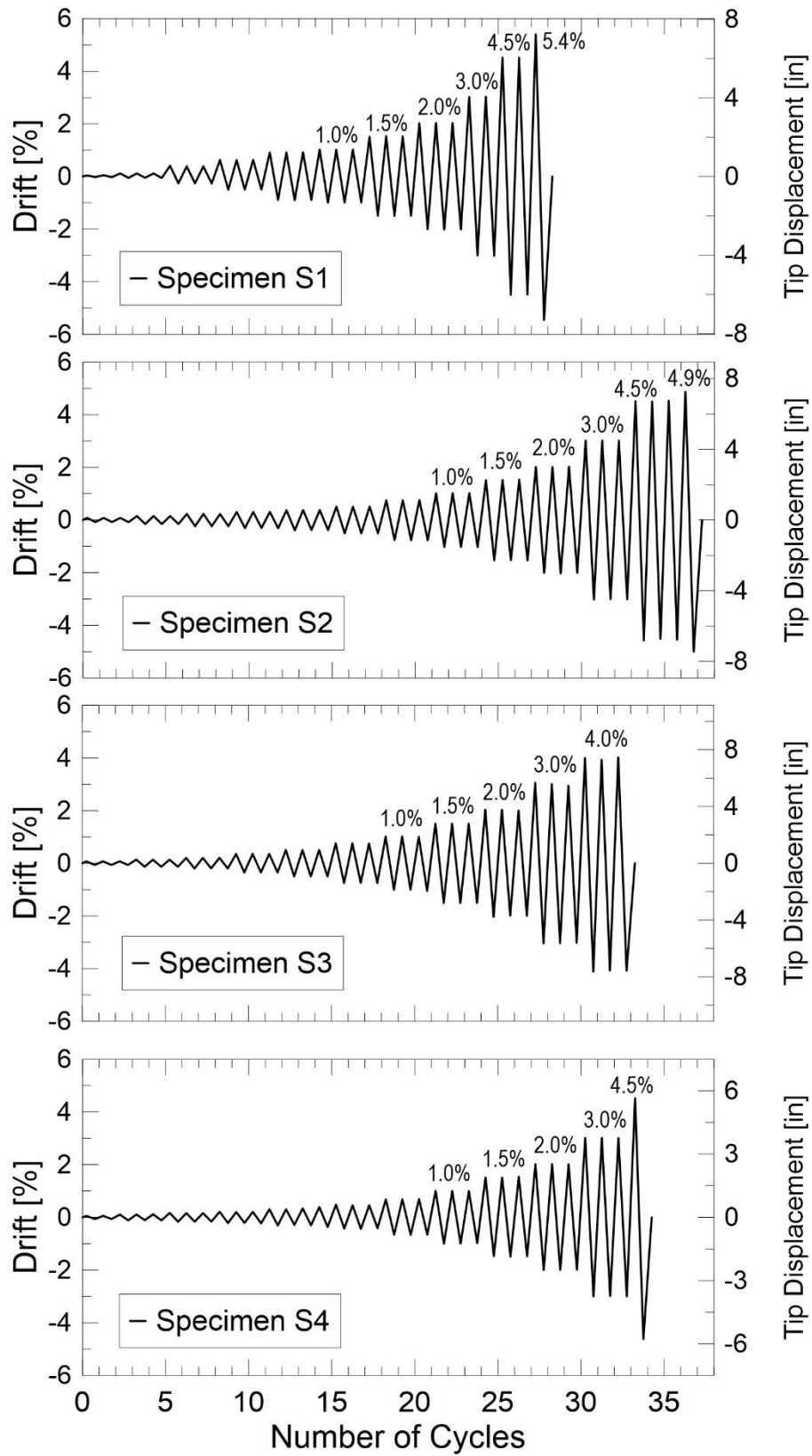



Figure 4.18: Loading sequence for specimens S1 to S4

Table 4.1: Applied load-displacement sequences

		Increasing applied drift levels 												
S1	θ_{down} [%]	0.04%	0.12%	0.41%	0.63%	0.91%	1.0%	1.5%	2.0%	3.0%	4.5%	5.4%		
	Δ_{down} [in]	0.1	0.2	0.5	0.8	1.2	1.4	2.0	2.7	4.0	6.1	7.2		
	μ_{down} [in/in]	0.0	0.1	0.4	0.7	1.0	1.1	1.7	2.2	3.3	5.0	5.9		
	F_{down} [kips]	12.0	32.5	72.5	96.4	127.1	127.7	138.4	145.3	117.3	61.6	34.9		
	F_{up} [kips]	-12.2	-30.9	-64.0	-95.3	-122.4	-120.9	-126.9	-132.5	-107.7	-72.5	-51.7		
S2	θ_{down} [%]	0.08%	0.15%	0.23%	0.30%	0.37%	0.51%	0.75%	1.0%	1.5%	2.0%	3.0%	4.5%	4.9%
	Δ_{down} [in]	0.1	0.2	0.3	0.5	0.6	0.8	1.1	1.5	2.3	3.0	4.5	6.7	7.3
	μ_{down} [in/in]	0.1	0.2	0.2	0.3	0.4	0.5	0.7	1.0	1.5	2.0	3.0	4.5	4.8
	F_{down} [kips]	22.5	37.9	52.2	64.0	74.4	96.9	130.5	163.7	177.3	190.5	203.6	214.9	92.7
	F_{up} [kips]	-34.5	-49.6	-61.5	-71.0	-83.1	-97.5	-120.4	-127.8	-130.6	-137.2	-149.9	-159.1	-110.6
S3	θ_{down} [%]	0.07%	0.14%	0.21%	0.35%	0.50%	0.75%	1.0%	1.5%	2.0%	3.1%	4.0%		
	Δ_{down} [in]	0.1	0.3	0.4	0.7	0.9	1.4	1.9	2.8	3.8	5.7	7.4		
	μ_{down} [in/in]	0.1	0.1	0.2	0.3	0.5	0.7	1.0	1.5	2.0	3.0	3.9		
	F_{down} [kips]	13.7	22.3	29.4	44.9	59.5	79.3	95.0	100.1	105.4	113.7	104.9		
	F_{up} [kips]	-25.5	-32.1	-39.4	-51.4	-63.3	-81.7	-84.4	-84.6	-88.3	-95.6	-97.6		
S4	θ_{down} [%]	0.05%	0.10%	0.17%	0.21%	0.31%	0.39%	0.48%	0.68%	1.0%	1.5%	2.0%	3.0%	4.5%
	Δ_{down} [in]	0.1	0.1	0.2	0.3	0.4	0.5	0.6	0.8	1.3	1.9	2.5	3.8	5.6
	μ_{down} [in/in]	0.1	0.1	0.2	0.2	0.4	0.5	0.6	0.8	1.2	1.8	2.4	3.6	5.3
	F_{down} [kips]	16.7	37.4	50.4	55.5	69.8	80.0	93.6	119.8	148.5	156.0	162.1	170.3	142.2
	F_{up} [kips]	-35.5	-46.2	-60.9	-71.0	-76.9	-97.5	-108.7	-139.6	-145.6	-147.0	-153.6	-165.1	-75.0

4.4 Instrumentation

A total of 52–76 internal and external sensors were installed on the test specimens to monitor beam displacements, rotations and internal strains during the test. The instrumentation consisted of 120-ohm Strain Gauges, Linear Variable Differential Transducers (LVDTs), and String Potentiometers with a displacement range of ± 12.5 in. The internal instrumentation (strain gauges) was installed before or during the construction of the rebar cages. Figure 4.19 shows the installation of a strain on the longitudinal rebar after grinding and cleaning the rebar surface. General purpose strain gauges with gauge lengths of 0.25 in. were manufactured and purchased from Micro Measurements (Vishay) with the respective application chemicals (Conditioners, Neutralizers, and Hardeners). All sensors were covered with special tape to prevent damage from concrete placement or moisture penetration. Connection cables and connectors were soldered to the sensors prior to placing and strain gages were checked for feedback signals at the completion of reinforcement cage construction. Most strain gauges survived the rough process of concrete placement and vibration without any damage; however, some strain gages were found non-functional at the time of test conduction. Given the duplicate placement of each sensor on both sides of the beam, redundant readings can be retained and substituted. Strain gauges installed on selected sets of stirrups to capture possible shear strains across the beam and on top and bottom main longitudinal reinforcement.



Figure 4.19: Left: Strain gauges installed along the longitudinal rebar before cage construction; Right: Strain gauge attached to a #8 bar during installation process

LVDTs and string potentiometers were calibrated before testing, as shown in Figure 4.20 below. Figure 4.20 also shows a photograph of a Celecso String Potentiometer (SP series). The LVDTs were direct current (DC) and were Trans-Tek models 0244-00000, 0245-00000, and 0246-00000. All LVDTs were placed in plastic housing and combined with wooden extension rods to allow a larger span width as well as a protection from concrete spalling and cracking along the beam (Figure 4.21 and 4.22). 3/8 in. diameter threaded rods were embedded transversely through the beam during construction to secure the LVDTs. LVDTs were installed in longitudinal and diagonal configurations on both sides of the beam to measure flexural and shear deformations respectively. The sensors had displacement ranges between +/- 1, +/- 2 and +/- 3 in. displacement and were installed according to where the respective deformations were expected.

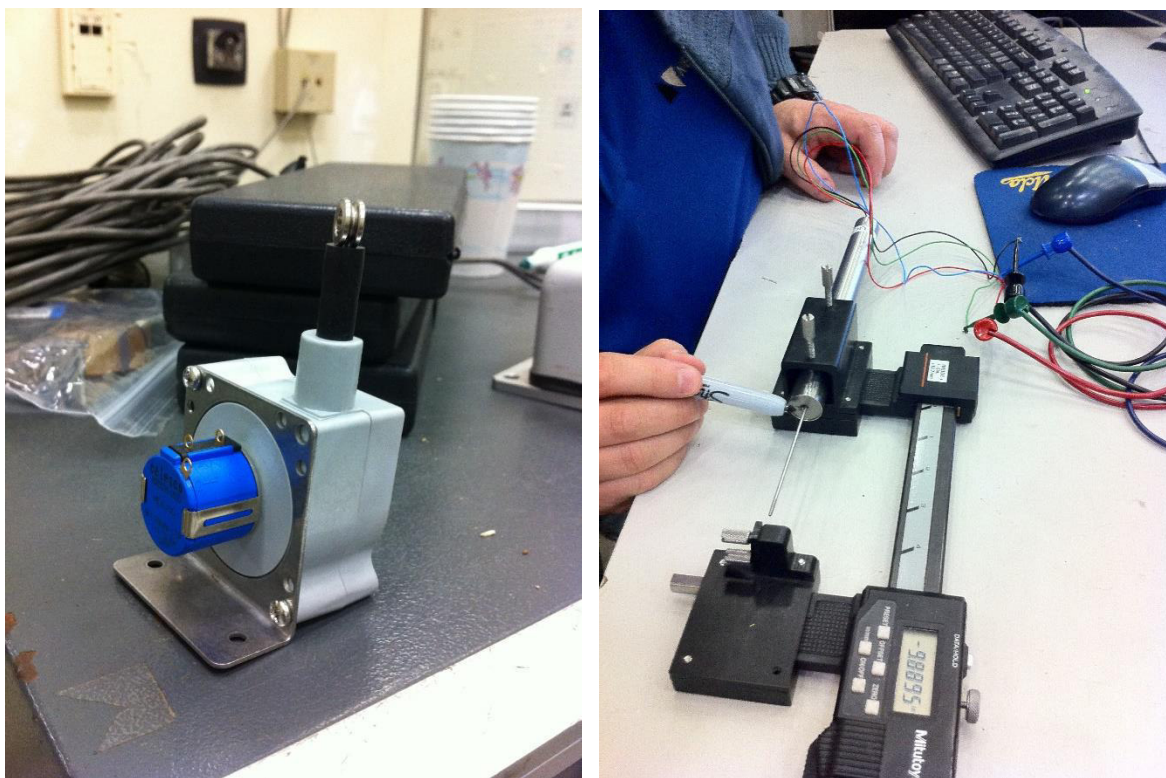


Figure 4.20: Left: String potentiometer sensor before installation; Right: Calibration of LVDT

The string potentiometers installed on the reaction block (below and above the beam) were used to monitor and measure eventual reaction block rotations. For S2 and S6, one of the string pots was damaged and was replaced with an LVDT. The remainder of all string potentiometers were installed below the beam and attached to the strong floor. Those potentiometers yielded the beam deflection curves presented in Chapter 5. Finally, the actuator was fitted with a 300-kip capacity load cell and an external AC LVDT that enabled displacement control. Both the load and displacement of the actuator were also recorded.

Data from all sensors was recorded by a data acquisition system (DAQ). The DAQ system consisted a National Instruments (NI) PXI-1011 chassis, which integrated an NI PXI-8106 controller and between five to seven modules (depending on the number of sensors used). LVDTs

and string potentiometers were plugged into two 32-channel SCXI-1100 modules which were connected SCXI-1300 terminal blocks in the chassis. Furthermore, LVDTs and string pots were externally excited to ten volts with a power supply. The strain gages connected the 8 channel SCXI-1520 module which was in turn connected to the SCXI-1314 terminal block within the chassis. The load and displacement from the actuator were recorded through SCXI-1300 module. A SignalExpress express procedure was used plot the load-deformation and all the sensor data in real-time. The procedure also allowed recording raw and averaged data. Figure 4.23 shows a photograph of the exact location of the external sensors.

Figures 4.24-4.35 show the instrumentation plan of the external and in internal sensors. The strain gauges were installed on the main top and bottom longitudinal reinforcement on both sides of the beam. The LVDTs were installed on 3/8 in. diameter rods that were installed through the beam prior to concrete placement. During the concrete pour, slight movement of all rods occurred which caused the rods to be slightly skewed. Additionally, rods at the tip of the beam were placed after concrete pour due the impediment of the U-steel plate system and had to be installed on the plate itself. It is also noted that one horizontal LVDT was not installed on S2 because of the DYWIDAG rods on the U-plate system.



Figure 4.21: Horizontal LVDTs



Figure 4.22: Diagonal LVDTs

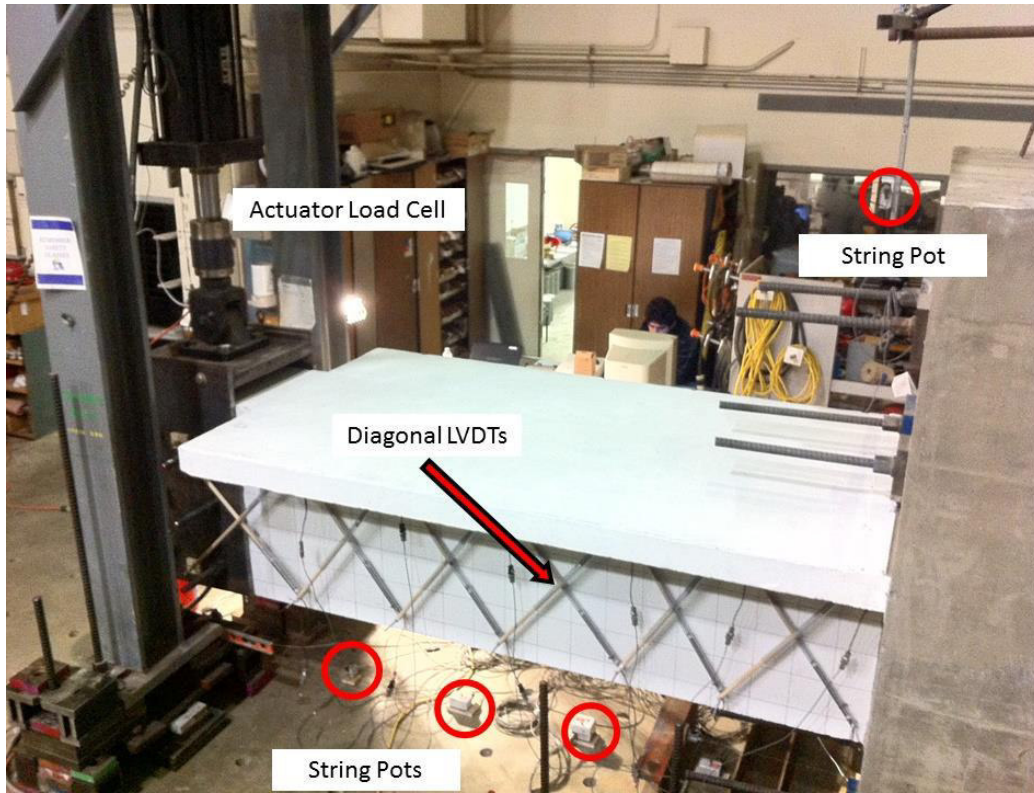


Figure 4.23: Location of external sensors

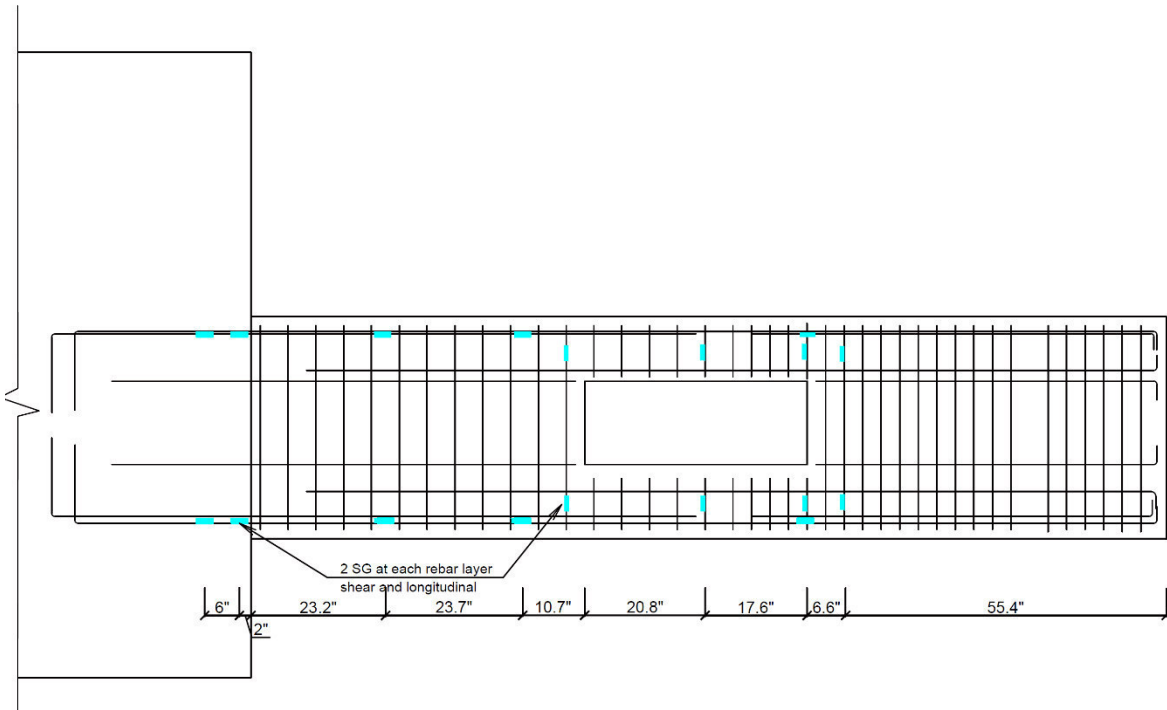


Figure 4.24: Layout of strain gauges on S1

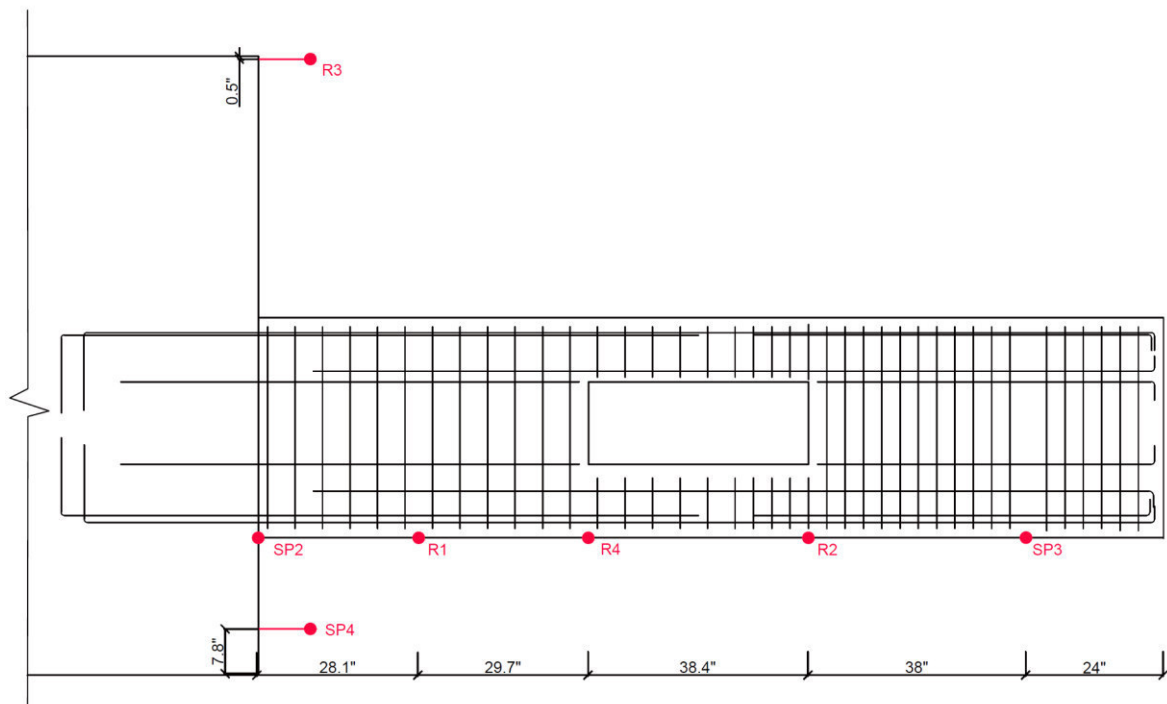


Figure 4.25: Layout of string potentiometers on S1

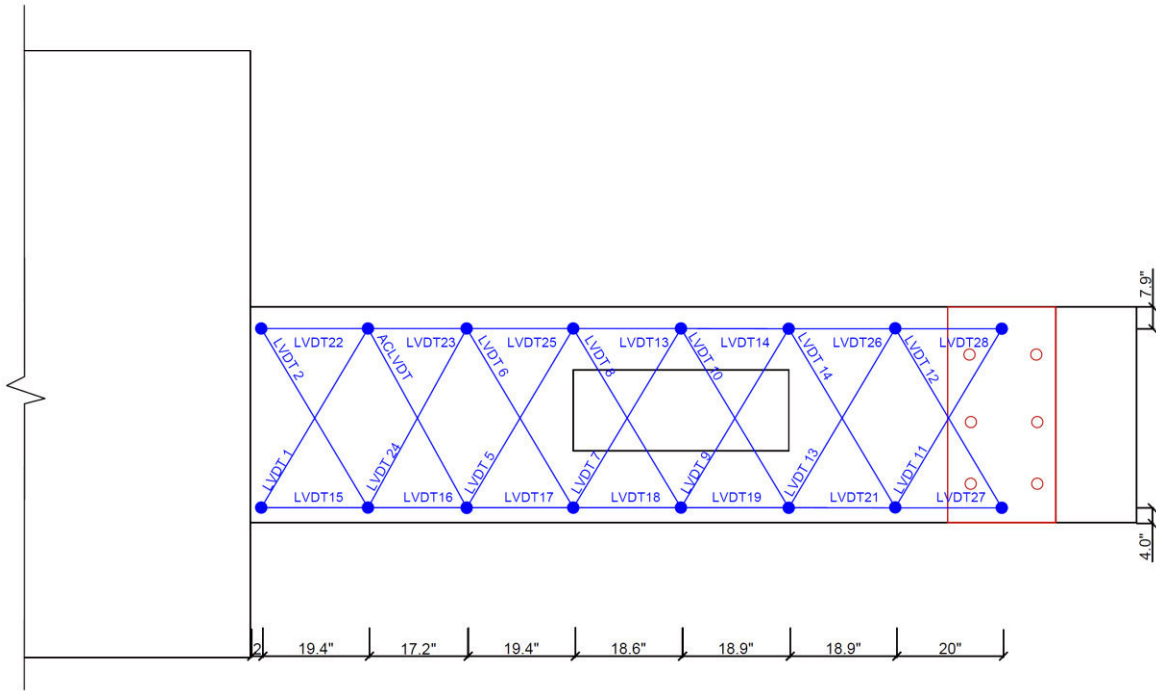


Figure 4.26: Layout of horizontal and diagonal LVDTs on S1

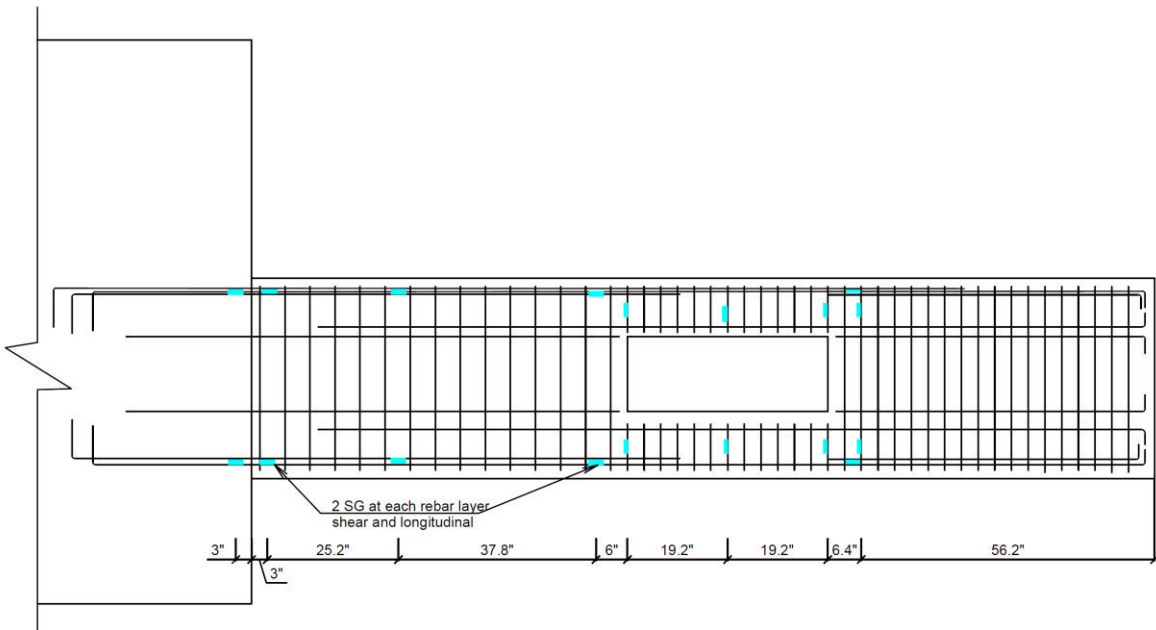


Figure 4.27: Layout of strain gauges on S2

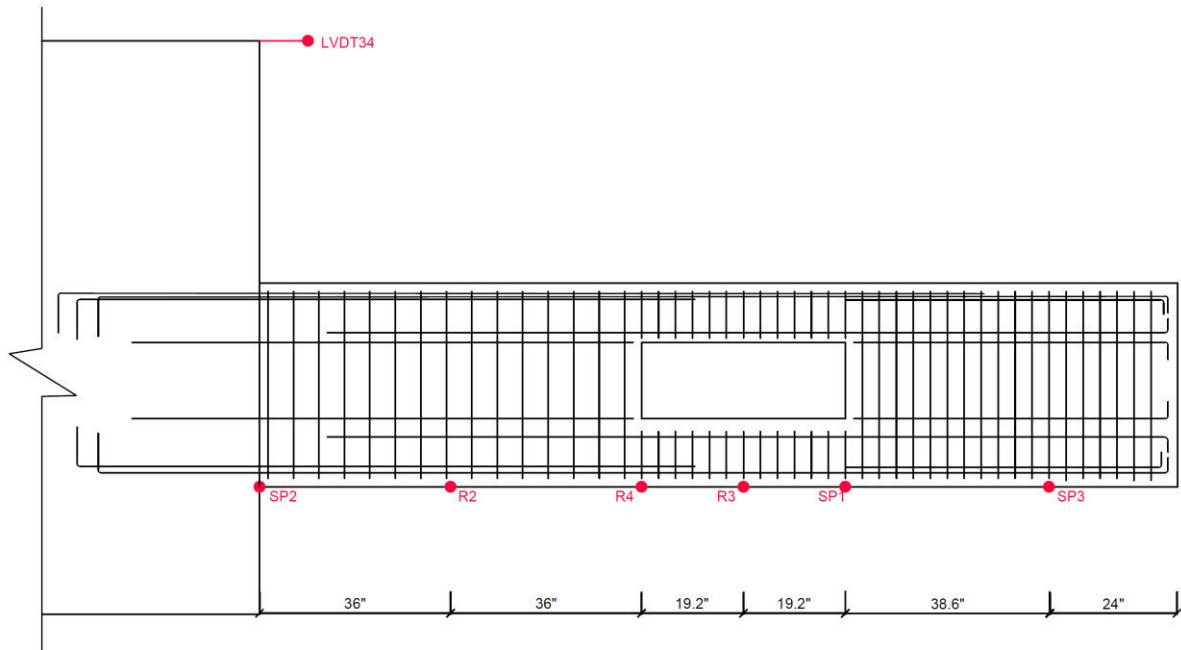


Figure 4.28: Layout of string potentiometers on S2

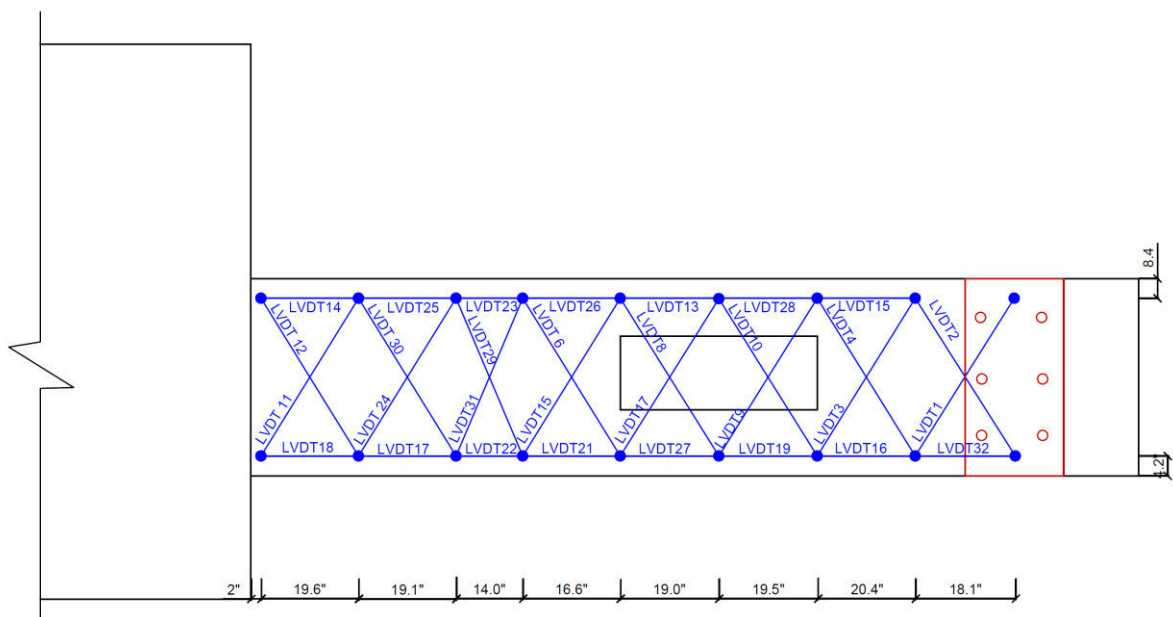


Figure 4.29: Layout of horizontal and diagonal LVDTs on S2

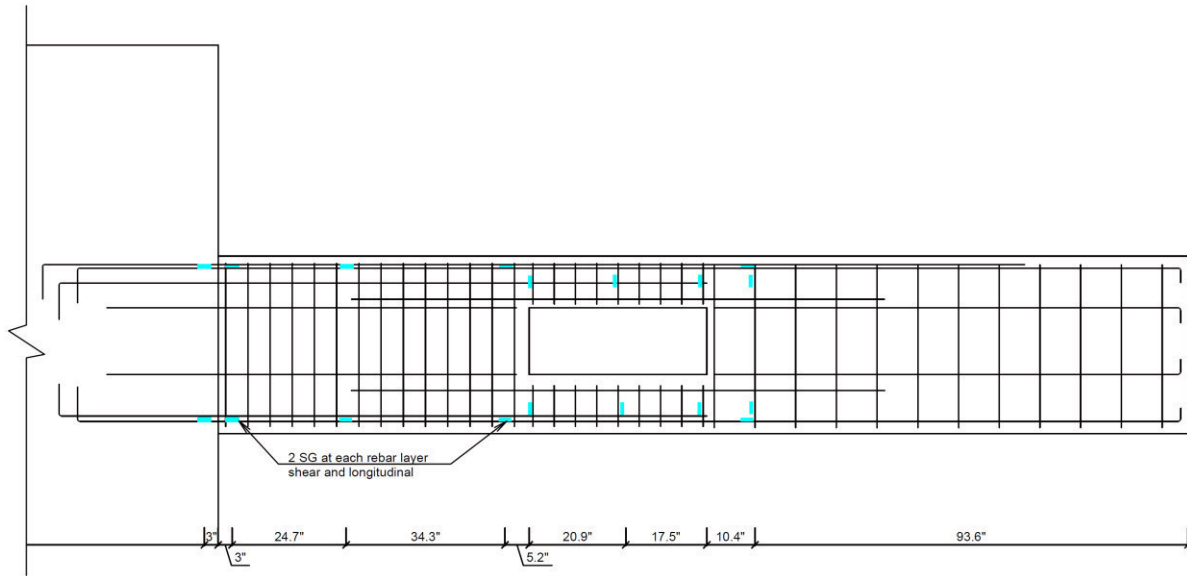


Figure 4.30: Layout of strain gauges on S3

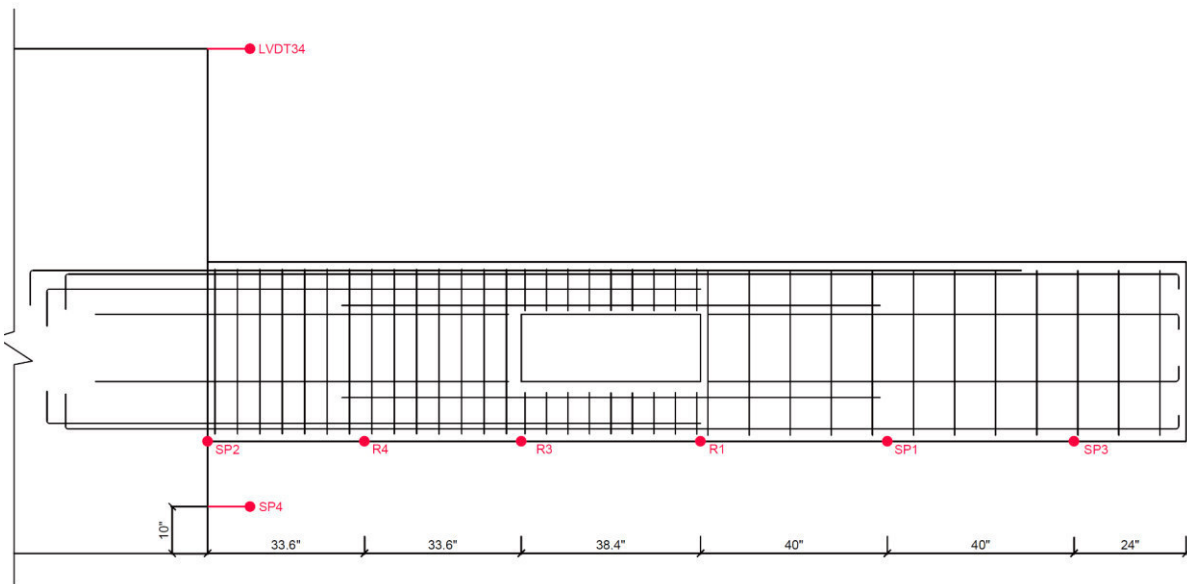


Figure 4.31: Layout of string potentiometers on S3

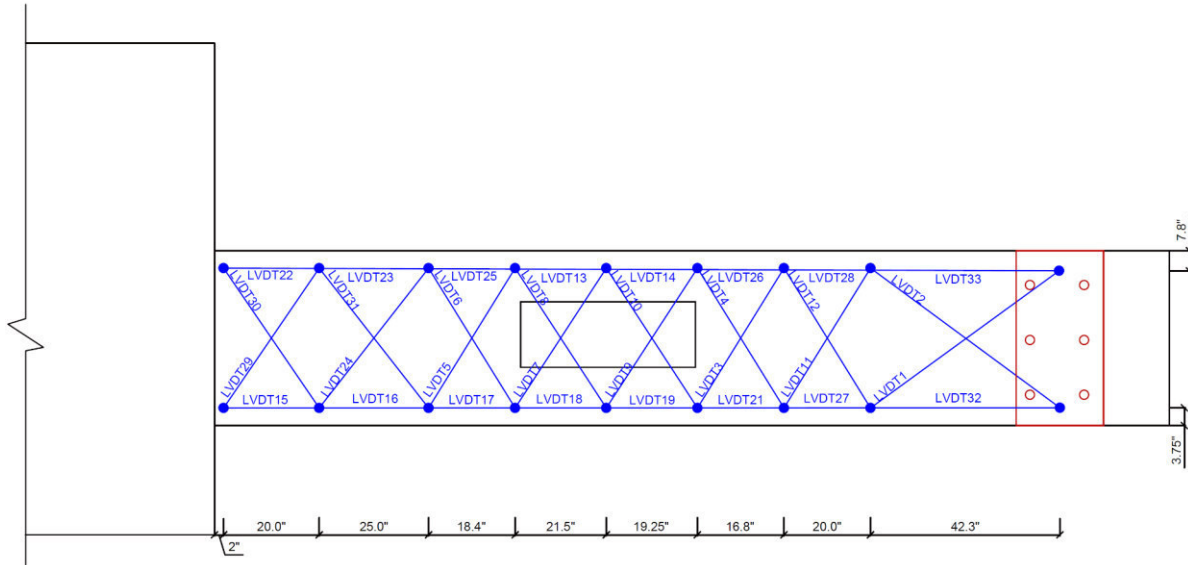


Figure 4.32: Layout of horizontal and diagonal LVDTs on S3

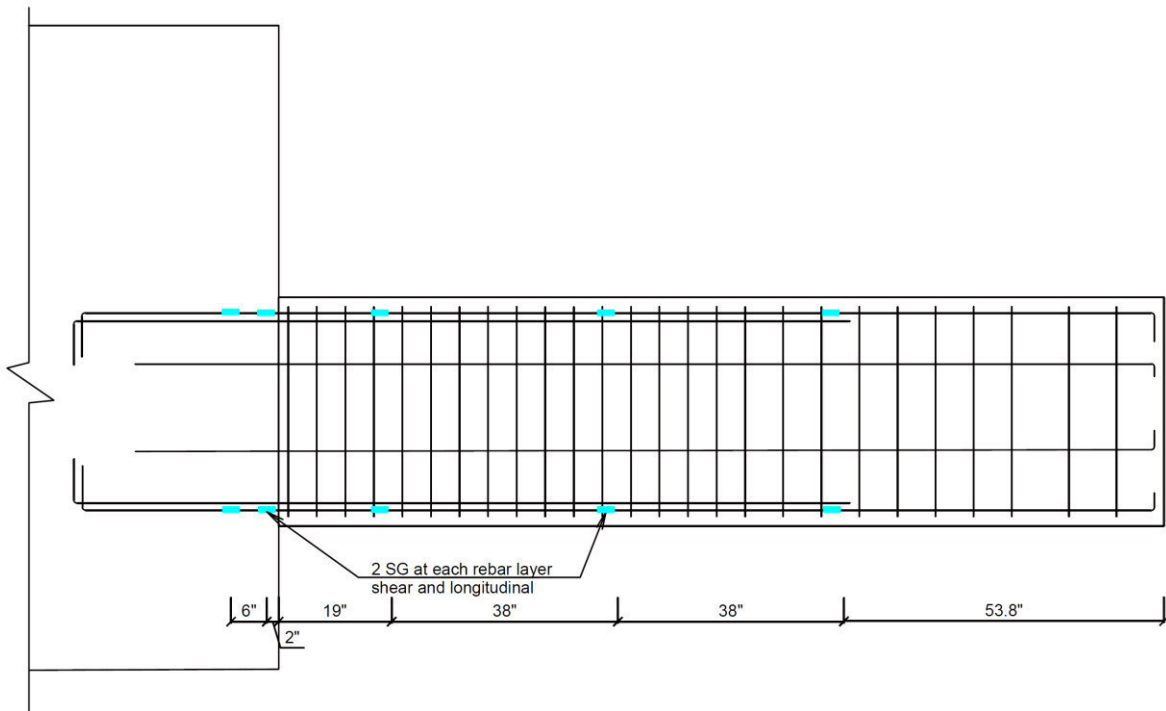


Figure 4.33: Layout of strain gauges on S4

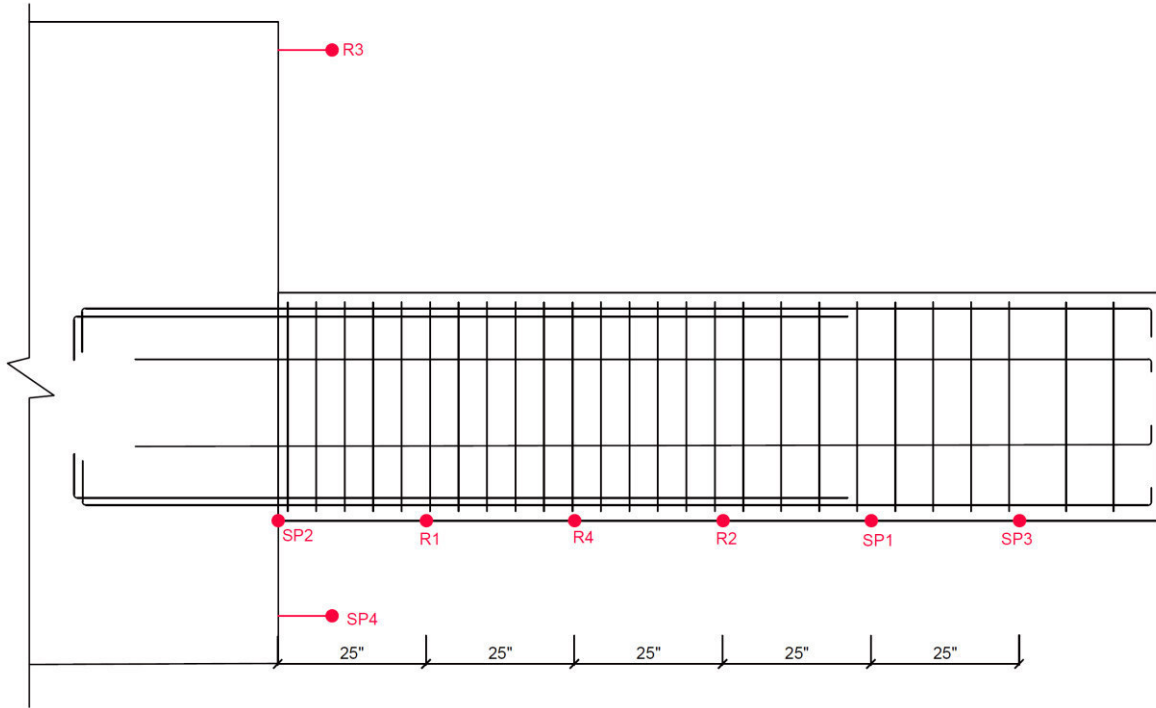


Figure 4.34: Layout of string potentiometers on S4

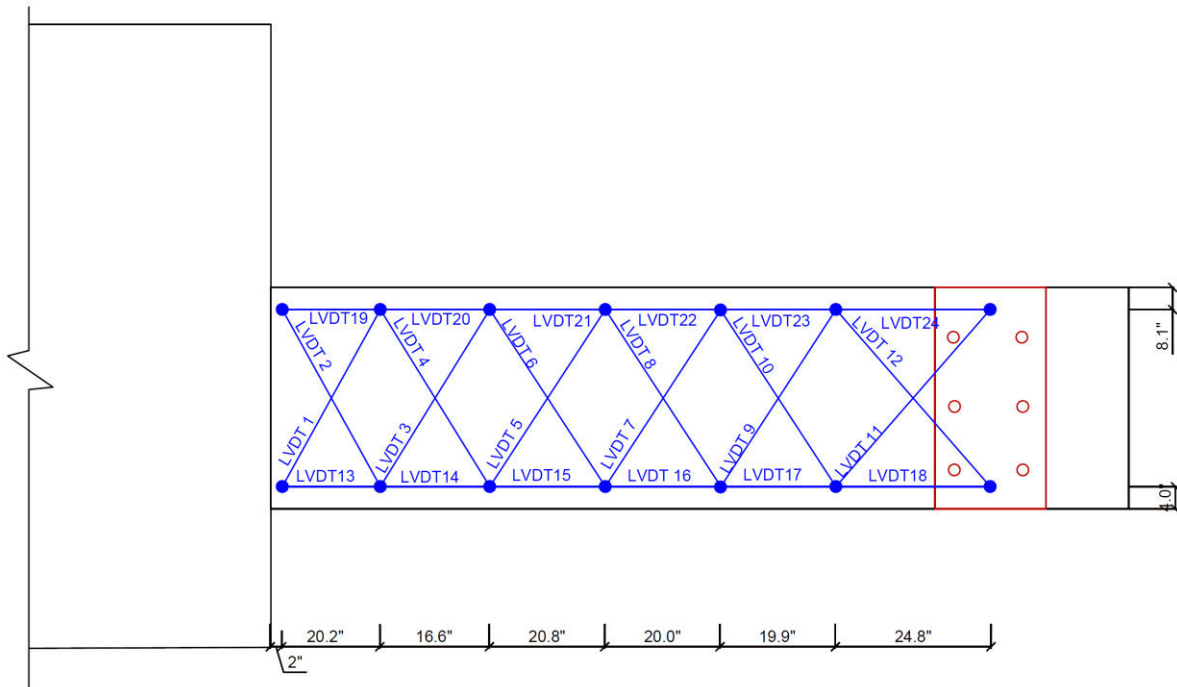


Figure 4.35: Layout of horizontal and diagonal LVDTs on S4

4.5 Material Properties

4.5.1 Concrete

The concrete mix used for the test specimens was intended to provide a compressive strength comparable to the in-situ concrete strength, determined through coring and testing prior to this study. Hereby, the maximum and nominal size, shape, angularity, and surface texture of the aggregate played an important role using samples delivered from the concrete plant. A 6 ksi design mix was developed and suggested by Associated Ready Mix with laboratory data provided prior to testing. The design recipe and the laboratory test results for design mix 19946 are attached in Appendix A. A slump of 5-6 in. was desired for the concrete mix to easily fill the formwork space below the opening. Slump tests on the site revealed concrete slumps between 6 and 7 in. for all specimens. No air voids were observed after formwork removal and confirmed a proper concrete placement. The concrete compressive strength was determined by conducting tests per *ASTM C873 / C873M - 10a "Standard Test Method for Compressive Strength of Concrete Cylinders Cast in Place in Cylindrical Molds"*. Figure 4.11 shows the concrete sampling and slump testing performed by MTGL during concrete placement. Figures 4.36 below show the compressive strength test results for the beams of all specimens over the curing time. The averaged compressive strengths measured at the day of testing are shown in Table 4.2 below. Two concrete cylinders were tested at UCLA's structural laboratory and stress strain curves were back calculated from load deformation data recorded during testing. Figure 4.37 shows the stress strain curves for beams S1 and S4. The E-moduli were back calculated for both specimens and resulted into $E_{S1} = 3401$ ksi and $E_{S4} = 3103$ ksi.

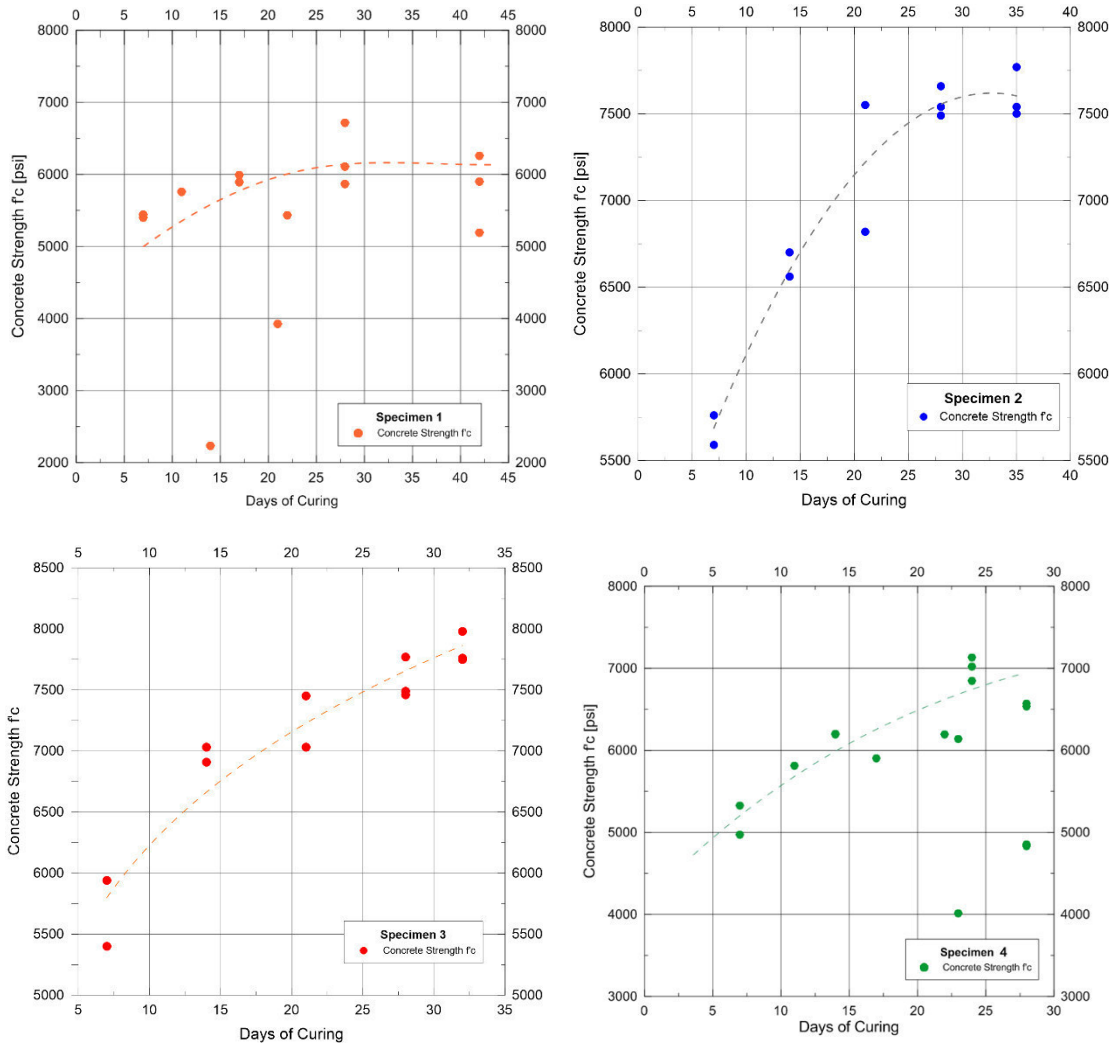


Figure 4.36: Concrete compressive strength development over curing time for S1-S4

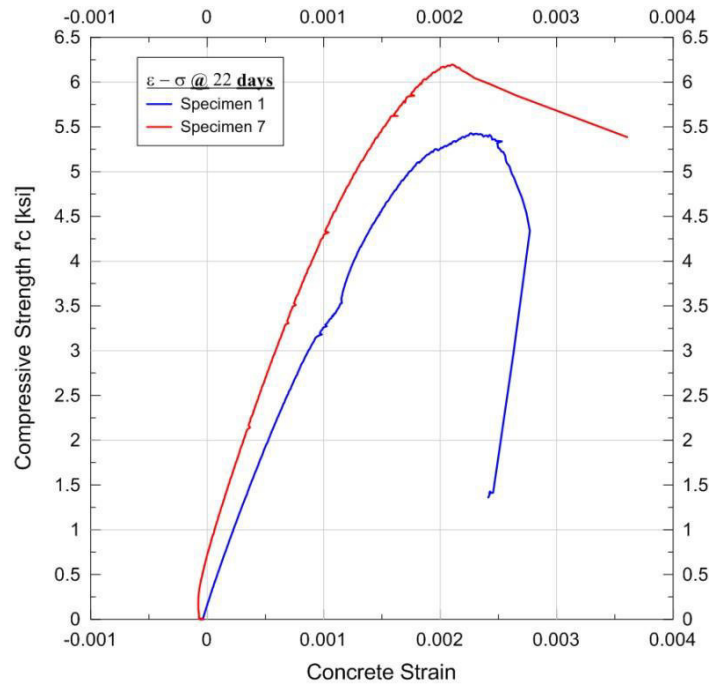


Figure 4.37: Concrete stress strain curves at 22 days of concrete curing for S1 and S4

Table 4.2: Concrete compressive strengths at the day of testing

Specimen	Test Date	Avg. Comp. Strength f'_c [ksi]
1	3/14/2013	7
2	4/03/2013	7.7
3	5/29/2013	7.83
4	6/02/2013	7.6

4.5.2 Steel

The rebar was of Grade 60 or Grade 60/A706 and reached an average yield strength of 66 ksi and an average ultimate tensile strength of about 107 ksi. Additional rebar testing was performed on one sample of each rebar size present in the specimen's beam through UCI and Twining

Laboratories. The results are attached in Appendix A. Figure 4.38 below shows the stress strain relationship obtained for the number 3 rebar. The E moduli for the samples were back-calculated to be 21,695.5 ksi and 20,744.4 ksi for sample 1 and 2 respectively. Unfortunately, stress-strain data were not available for testing performed at Twining Laboratories, however, yield and ultimate stresses can be calculated from the load deformation data shown in Appendix A for the #4 stirrups and the number 7, 8 and 9 longitudinal rebar. The test results are summarized in Table 4.3.

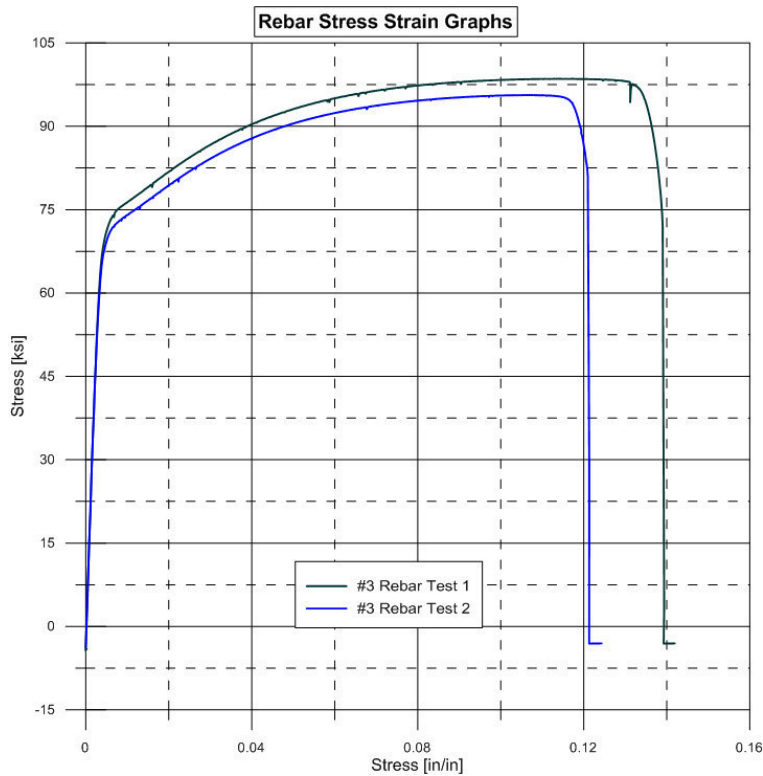


Figure 4.38: Stress strain curves from rebar testing of #3 samples

Table 4.3: Summary table of rebar test results

Rebar #	Area [in²]	Yield Strength [ksi]	Ult. Tensile Strength [ksi]	Elongation [%]
9	1.0	64.3	105.94	16.75
8	0.79	66.5	110.3	20.38
7	0.6	66.7	108.3	19
4	0.2	69.6	108	15.63
3	0.11	65.4/65.6	98.55/95.5	12/14

Chapter 5 Experimental Results

The experimental results presented in this chapter include a description of experimentally observed damage and behavior, hysteretic response, beam deflection profiles, dissipated energy, deflection components, and beam axial elongation.

5.1 Experimentally Observed Damage and Behavior

A schematic of the cracking patterns for each of the test specimens at complete structural failure is depicted in Figure 5.1. Each of the beams developed initial flexure-type cracks at a distance equal to approximately $h/2$ from the beam-column interface, where h is equal to the overall beam height. For specimen S4 (beam with no opening), an alternating succession of flexural and shear cracks originated at the fixed end region and progressively propagated towards the free end. Hereby, flexural cracks always preceded shear cracks. For specimens S1 to S3 (beams with a web opening), early cracking in the area around the opening occurred simultaneously or soon after the development of cracks in the vicinity of the fixed end. However, the strength at which flexural cracking initiated seemed relatively unaffected by the presence of an opening. Although flexural deformations were prevalent, each of the specimens exhibited extensive diagonal cracking along the length of the beam. Wide diagonal cracks within the zones that developed plastic hinges during the cycles preceding failure suggest that shear is an important contributor to the inelastic response.

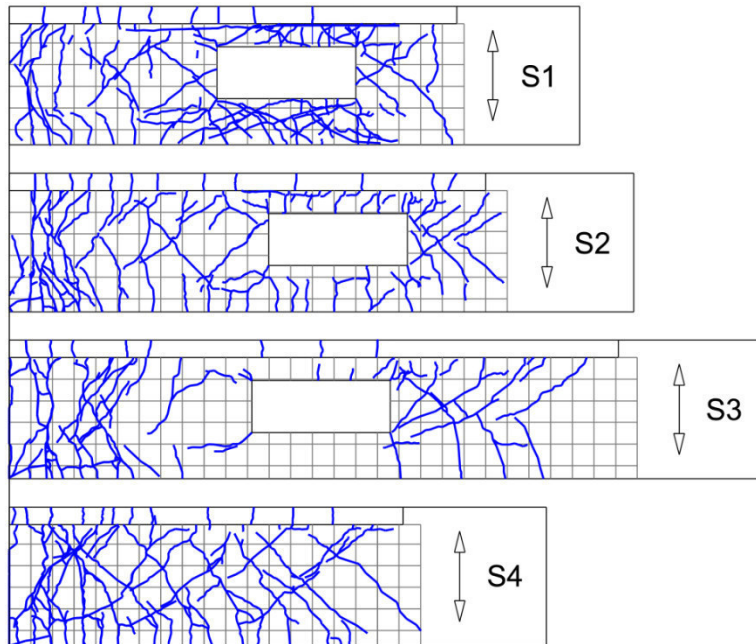


Figure 5.1: Cracking patterns at failure for S1-S4

Photographs of the different failure modes (i.e., crack patterns and hinge development) at selected drift ratios for each of the beam specimens are provided in Figures 5.2-5.31. Load levels corresponding to the development of the first vertical (flexural) and diagonal (shear) cracks are listed in Table 5.1. The earliest cracks (flexural and diagonal) appeared nearly simultaneously for specimens S1 and S2 at 0.12% drift (33 kips) and 0.15% drift (38 kips), respectively, at the corners of the rectangular opening on the side closest to the beam-column connection. Conversely, initial flexural cracks were observed at 0.14% drift (22 kips) for specimen S3 (i.e., the most slender specimen) at the beam-column connection, which were followed soon thereafter by cracks at the corners of the opening that occurred at a drift level of 0.2% (29 kips). Long diagonal tension cracks between the opening and point of load application were observed at drifts levels of 0.6% (96 kips), 0.2% (52 kips), and 0.5% (60 kips), for specimens S1, S2, and S3, respectively.

For each of the specimens, vertical flexural cracks developed at the beam-column interface and widened during the loading cycles greater than 2% drift. During the 2nd cycle at 3% drift for specimen S1 and during the 1st cycle for specimens S2 to S4 at 4% to 4.5% drift, severe crack opening and concrete crushing within the zone of the plastic hinges was observed (i.e., at the opening for S1, and at the beam-column interface for S2 to S4), which was accompanied by spalling of the concrete within the confined core. For specimens S2 and S4, excessive buckling of the bottom longitudinal reinforcement near the fixed end support was observed.

The development of a plastic hinge in the area around the opening (i.e., in the chords) for specimen S1 at 3% drift is shown in Figure 5.3. Important to note, S1 is the only specimen to fail within region B. The short vertical flexural cracks that developed at the faces of both chord members progressively extended deeper and more inclined due to the predominant shear force within the top chord. Bond splitting cracks developed along both the jamb bars and main reinforcement of the bottom chord because of the high compression forces (i.e., bending couple). Moreover, the diagonal and longitudinal cracks within the chords widened substantially during the first load cycle at 3% drift. Cracking patterns within the beam (S1) suggest that the top chord failed primarily by the formation of bi-directional diagonal cracks (i.e., a shear failure), while the bottom chord displayed a predominantly bond splitting failure mode (i.e., an axial compression failure). Inadequate detailing of the steel reinforcement around the opening likely contributed to the failure of specimen S1 within the region around the opening. Even though transverse reinforcement spacing satisfied general ACI recommendations for all beam regions when taking “ d ” as the depth of the solid cross-section, tie spacing calculated per “ d ” of the top and bottom chords would have resulted in closer spacing requirements. In addition to the larger spacing of the tie reinforcement

in the chords, neither the added nor the lapped reinforcing bars fully continued along the length of the chord members, thus creating an abrupt discontinuity of the longitudinal reinforcement near the mid-section of the opening.

The following photographs in section 5.1.1-5.1.4 depict the progression of failure for each beam specimen. Photographs of the observed buckling of the bottom bars in specimens S2 and S4 are shown in Figures 5.15 and Figure 5.31, respectively. In contrast, buckling of the bottom bars was not observed at the plastic hinge that developed in the area of the opening for specimens S1 or at the beam-column interface for specimen S3. For Specimen S1 this performance may be due to the lower moment demand in the opening region and the strong bottom reinforcement (#9 bars) in the bottom chord. Specimen S3 may have potentially experienced buckling if larger drift levels would have been applied, but was not observed up to ultimate capacity. Figure 5.23 shows the exposed bottom bars of S3 at the end of testing which have begun to lose contact with the stirrups. Photographs of S4 indicate that buckling of all rebar occurred (i.e., in the bottom bars, side bars, and top bars). Additionally, the cracking pattern on top of the slab of S1 is shown Figure 5.8. The cracking patterns of the slabs are practically identical in all specimens occurred during downward loading.

The demand-to-capacity ratios in shear and flexure (i.e., V_{peak}/V_u and F_{peak}/F_u) were calculated to characterize the type of structural failure that occurred due to the imposed loading (Table 5.1). Using this simplified analysis, a sufficient safety margin in both flexure and shear at the beam/column interface was computed for the beam of specimen S1, but a strong potential for shear failure in the region of the opening was indicated by the ratio V_{peak}/V_u , which exceeded the 1.0

threshold significantly (i.e., $V_{peak}/V_u = 1.52$). For specimen S2 and using the same simplified approach, sufficient capacity in both flexure and shear around the region of the opening was computed, and the beam was expected to fail due to the development of a plastic hinge at the fixed beam/column connection (i.e., $F_{peak}/F_u = 0.97$ and $V_{peak}/V_u = 1.10$). The demand-to-capacity ratios for specimen S3 were determined to be close to 1.0 in flexure at the fixed end and in shear at the region of the opening, and the beam could theoretically fail at both locations in the respective failure modes. However; given the proximity of the flexural ratios close to the threshold in upward and downward loading at the fixed beam region, failure initiation in flexure is likely. For the beam with no opening (specimen S4), a combined flexure-shear type failure in region A was expected as the ratios of F_{peak}/F_u and V_{peak}/V_u were approximately equal to 0.91. It should be noted that large moments and large shear forces occurred in the area of the rectangular openings in specimens S1, S2, and S3 (fixed connections), which was not the case for most of the experimental studies documented in the literature, where the RC beam specimens were pinned and the openings were located in close proximity to the supports (Nasser et al. 1971, Mansur 1984, Mansur et al. 1985, Mansur and Tan 1984).

Table 5.1: Analytical results summary: (a) Section A (Fixed End); (b) Section B (Opening)

		S1		S2		S3		S4	
		down (+)	up (-)	down (+)	up (-)	down (+)	up (-)	down (+)	up (-)
SECTION A (fixed-end)	M_y [kip-ft]	1415	1143	2050	1131	1523	897	1459	1128
	ϕ_y [1/ft]	1.0E-03	9.2E-04	1.1E-03	9.2E-04	1.0E-03	9.0E-04	1.1E-03	9.2E-04
	M_{yc} [kip-ft]	1286	1071	2019	1048	1425	833	1313	1081
	M_u [kip-ft]	2251	1791	3064	1910	2321	1489	2290	1900
	ϕ_u [1/ft]	5.8E-02	6.8E-02	4.5E-02	6.5E-02	5.0E-02	5.8E-02	5.2E-02	5.7E-02
	F_u [kips]	202	160	247	154	150	96	220	183
	V_n [kips]	344	354	523	544	343	356	335	339
	$V_n @ V_c=0$ [kips]	197	203	383	398	197	204	197	199
	F_{peak} [kips]	147	133	218	161	115	102	172	167
	V_{peak} [kips]	162	118	235	144	135	82	187	153
	F_{peak}/F_u	0.73	0.83	0.88	1.04	0.77	1.06	0.78	0.92
V_{peak}/V_n	0.82	0.58	0.61	0.36	0.68	0.40	0.95	0.77	
SECTION B (opening)	M_y [kip-ft]	1342	1286	1822	1308	1605	1038		
	ϕ_y [1/ft]	1.1E-03	9.4E-04	1.1E-03	9.5E-04	1.1E-03	9.2E-04		
	M_{yc} [kip-ft]	1546	1546	2160	1703	1886	1331		
	M_u [kip-ft]	2293	2192	3119	2418	2579	1926		
	ϕ_u [1/ft]	5.4E-02	6.4E-02	7.2E-02	6.7E-02	5.2E-02	6.2E-02		
	F_u [kips]	436	449	598	495	295	234		
	$V_{n,t} @ V_c=0$ [kips]	46	56	133	165	48	60		
	$V_{n,b} @ V_c=0$ [kips]	54	58	156	169	57	61		
	$V_{n,total}$ [kips]	99	114	289	334	105	122		
	F_{peak} [kips]	147	133	218	161	115	102		
	V_{peak} [kips]	154	125	226	153	127	90		
	F_{peak}/F_u	0.30	0.29	0.34	0.32	0.37	0.44		
	$V_{peak}/V_{n,total}$	1.56	1.10	0.78	0.46	1.20	0.74		

5.1.1 Specimen 1



Figure 5.2: Crack pattern at 2.0% drift for S1



Figure 5.3: Crack pattern at 3.0% drift for S1



Figure 5.4: Crack pattern at 4.5% drift for S1



Figure 5.5: Crack pattern at 6.0% drift for S1



Figure 5.6: Left: Widening of flexural cracks at 3.0% drift; Right: Crack were approximately 5/8-1.0-inch wide



Figure 5.7: View of opening region on both sides of beam during 6.0% drift



Figure 5.8: Cracking pattern on top of slab of S1

5.1.2 Specimen 2



Figure 5.9: Crack pattern at 2.0% drift for S2

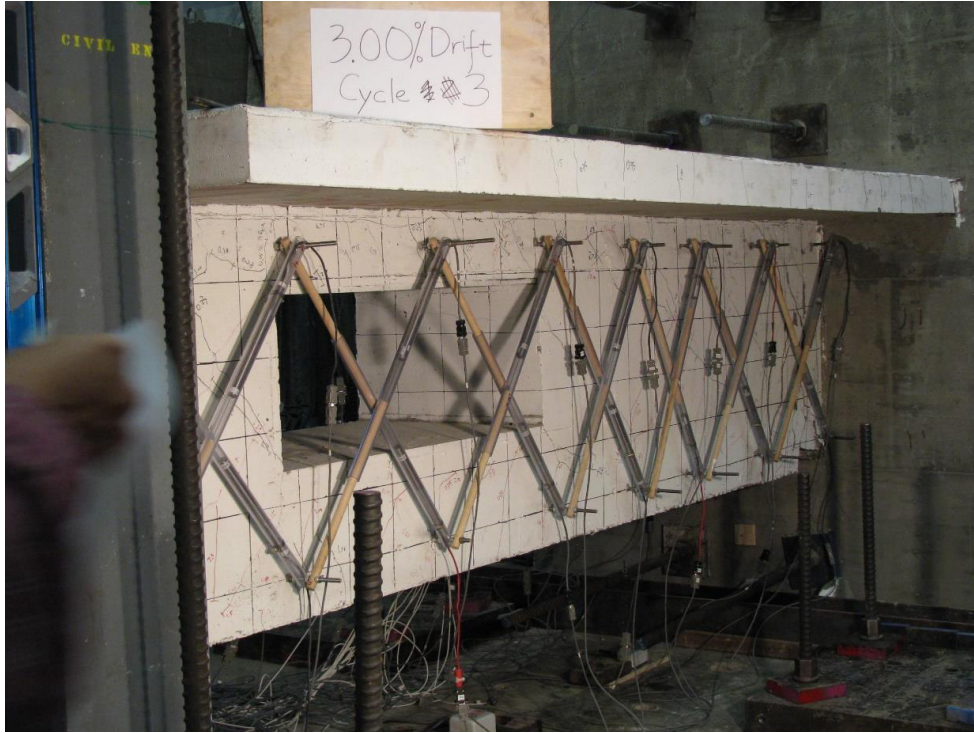


Figure 5.10: Crack pattern at 3.0% drift for S2



Figure 5.11: Crack pattern at 4.5% drift for S2



Figure 5.12: Crack pattern at 5.0% drift for S2



Figure 5.13: Cracking pattern at the fixed end at 2.0% drift on both sides of beam

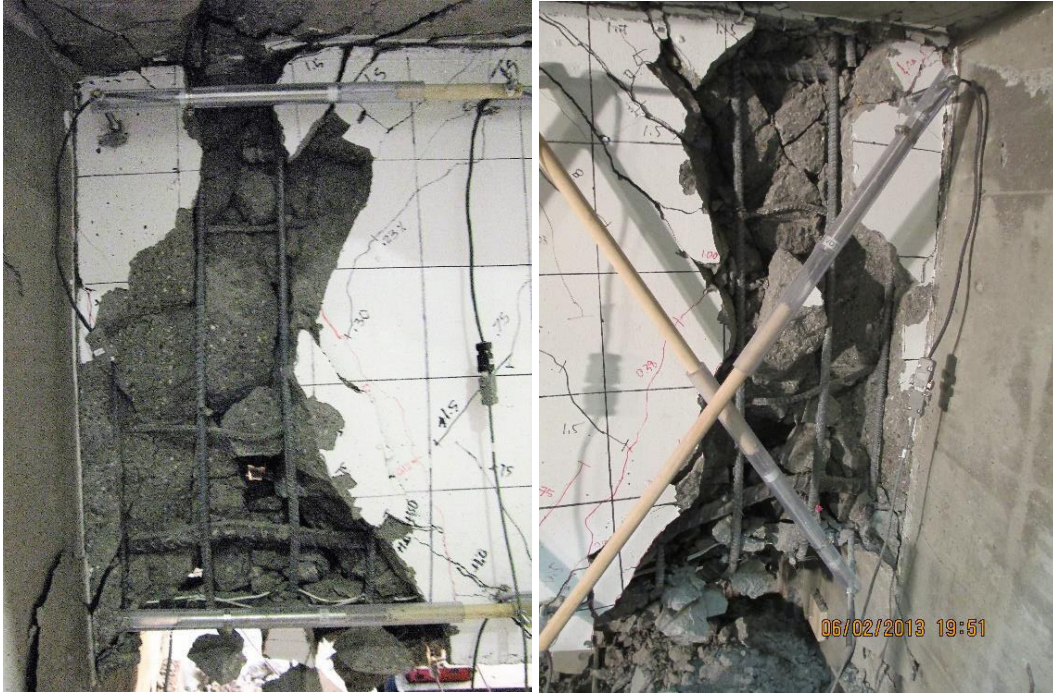


Figure 5.14: Plastic hinge region at both sides of beam for S2

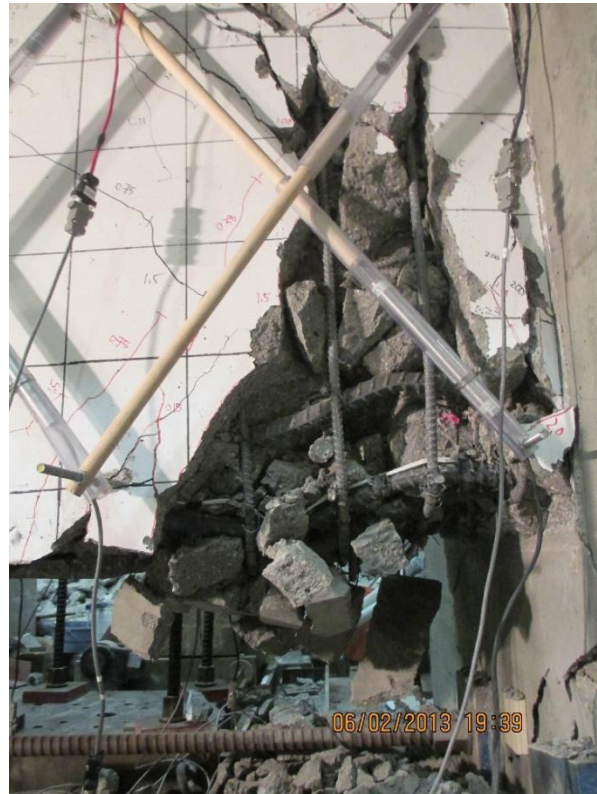


Figure 5.15: Buckling of bottom bars for S2



Figure 5.16: Opening region of S2 at end of test

5.1.3 Specimen 3

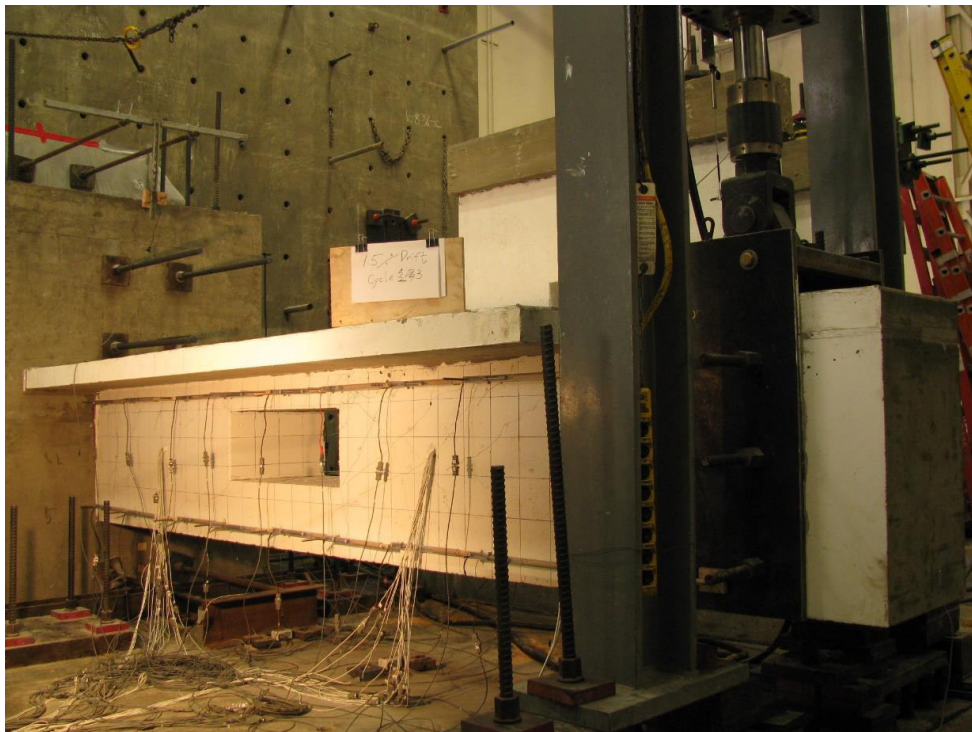


Figure 5.17: Crack pattern at 1.5% for S3

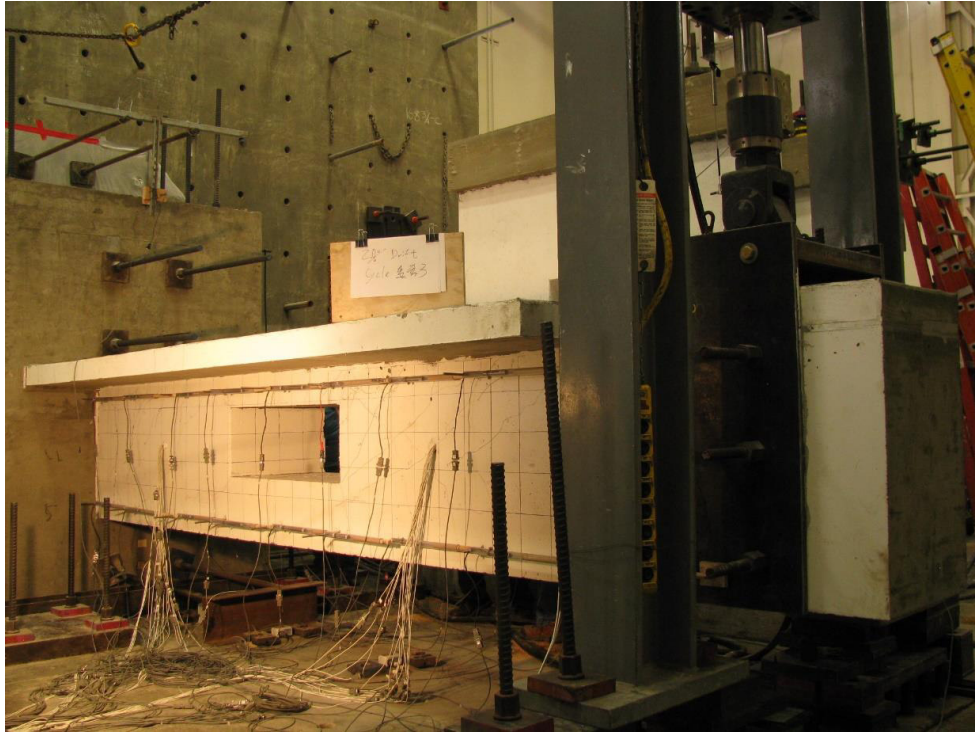


Figure 5.18: Crack pattern at 2.0% drift for S3

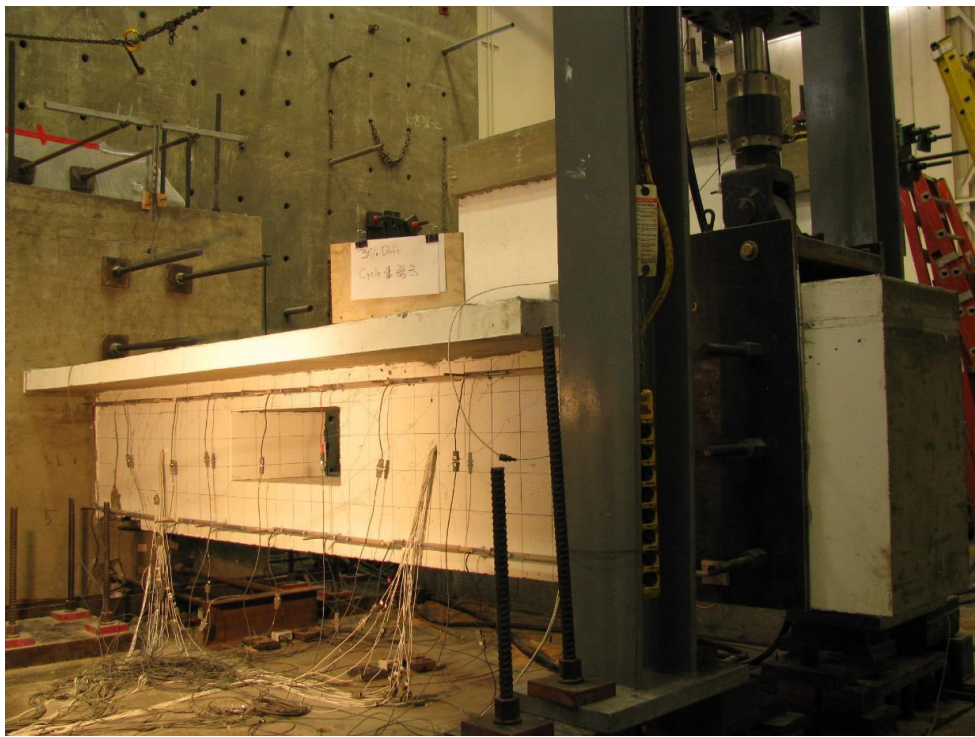


Figure 5.19: Crack pattern at 3.0% drift for S3

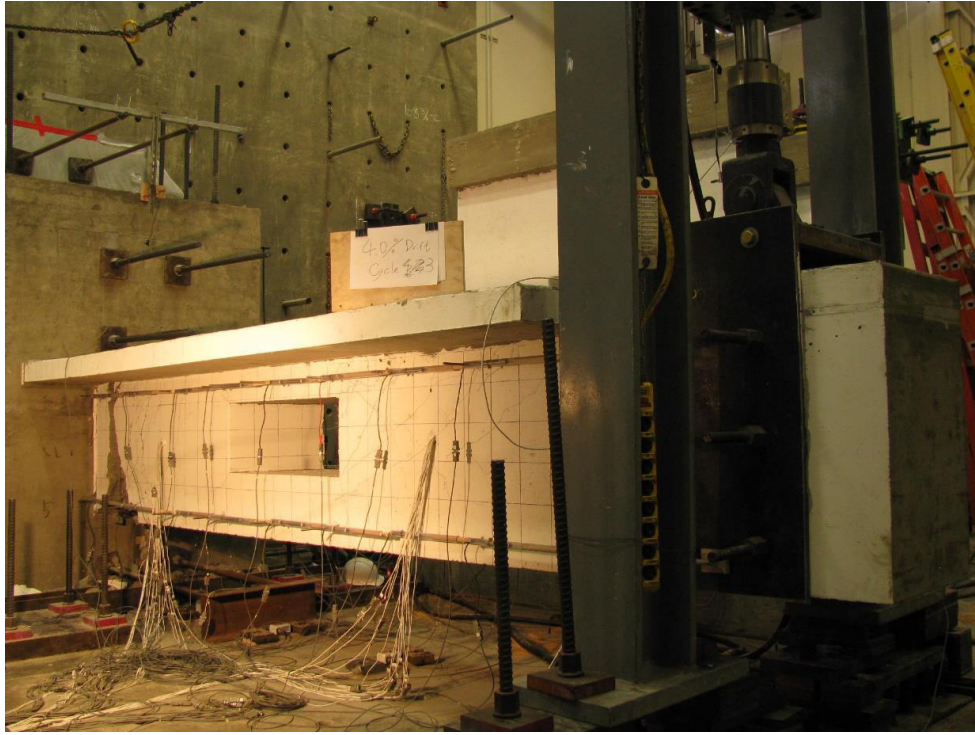


Figure 5.20: Crack pattern at 4.0% drift for S3



Figure 5.21: Cracking pattern at the fixed end at 3.0% drift on both sides of beam



Figure 5.22: Plastic hinge region at both sides of beam for S3



Figure 5.23: Exposed bottom longitudinal reinforcement at end of test for S3

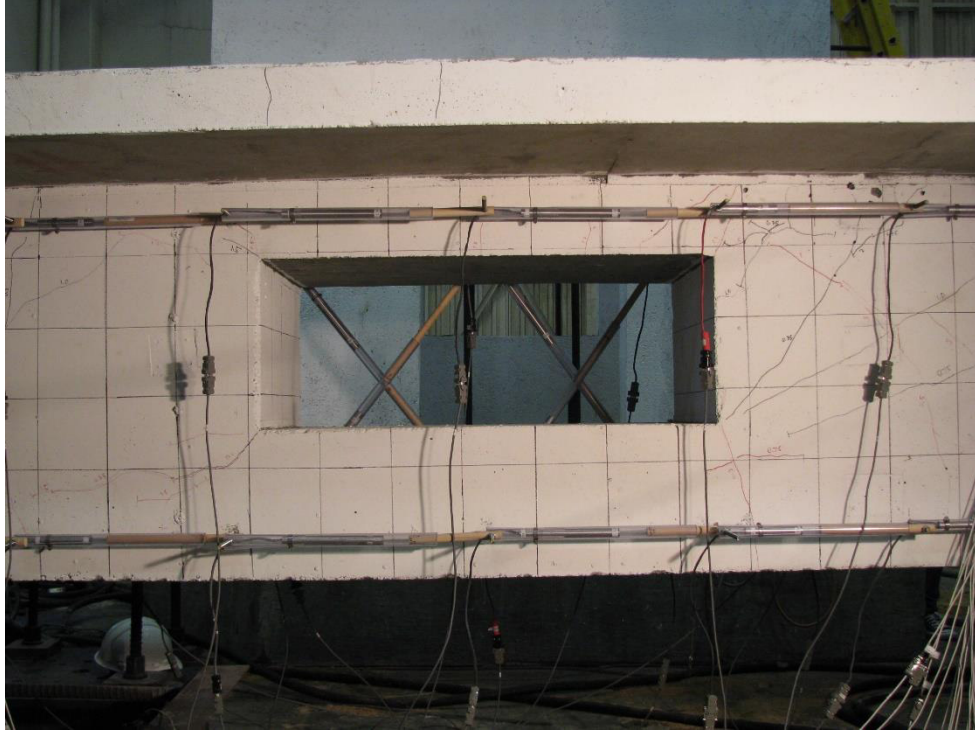


Figure 5.24: Opening region of S3 at end of test

5.1.4 Specimen 4

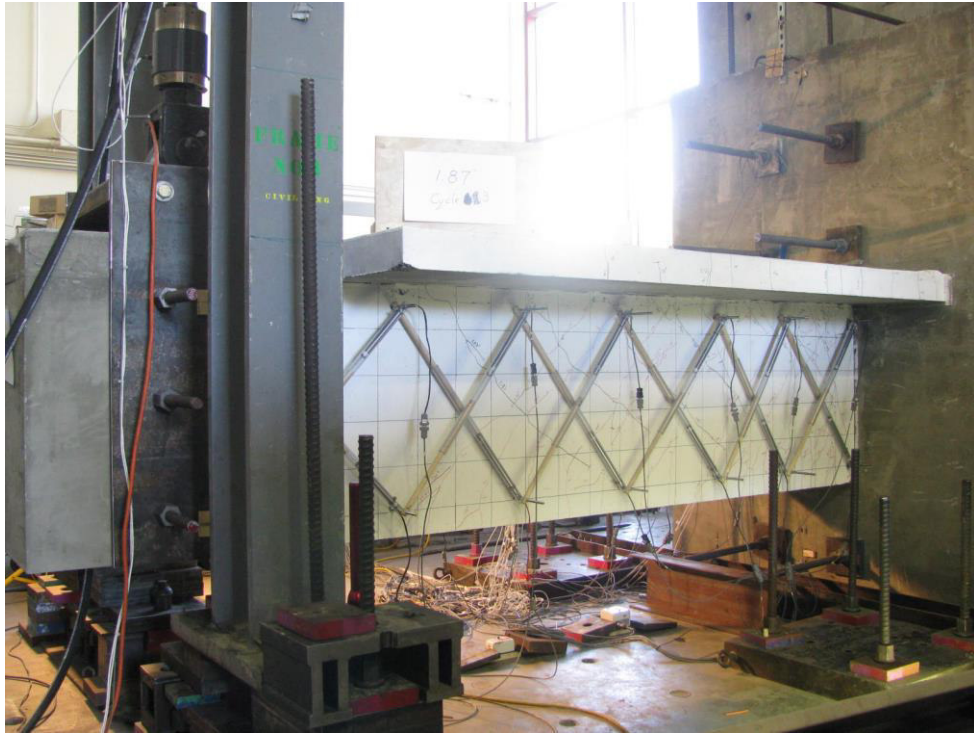


Figure 5.25: Crack pattern at 1.5% drift for S4

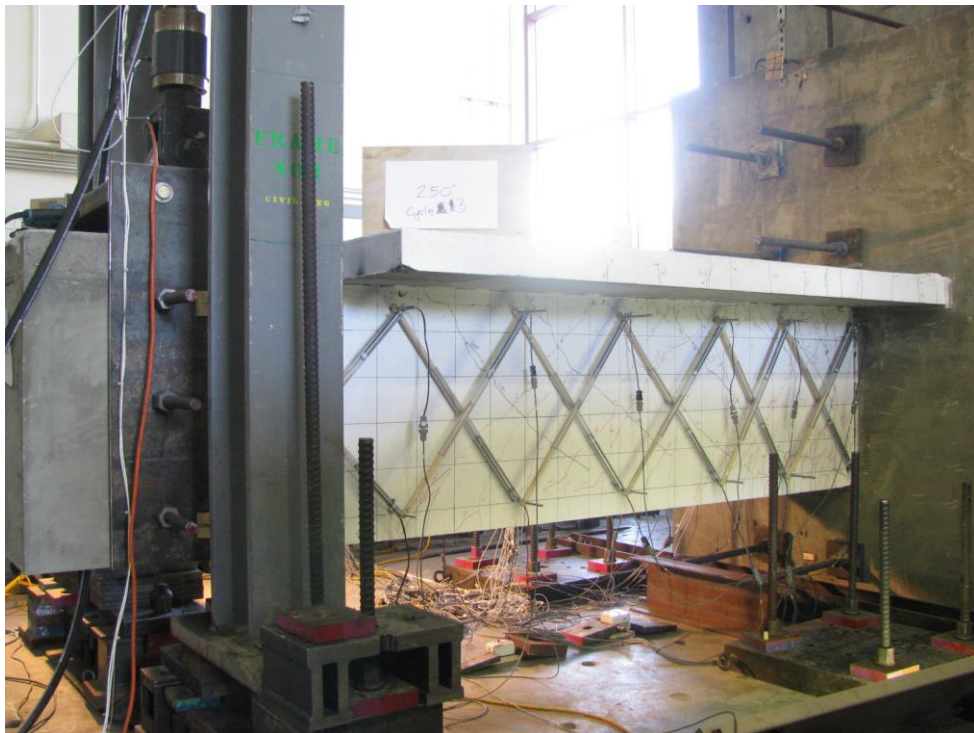


Figure 5.26: Crack pattern at 2.0% drift for S4

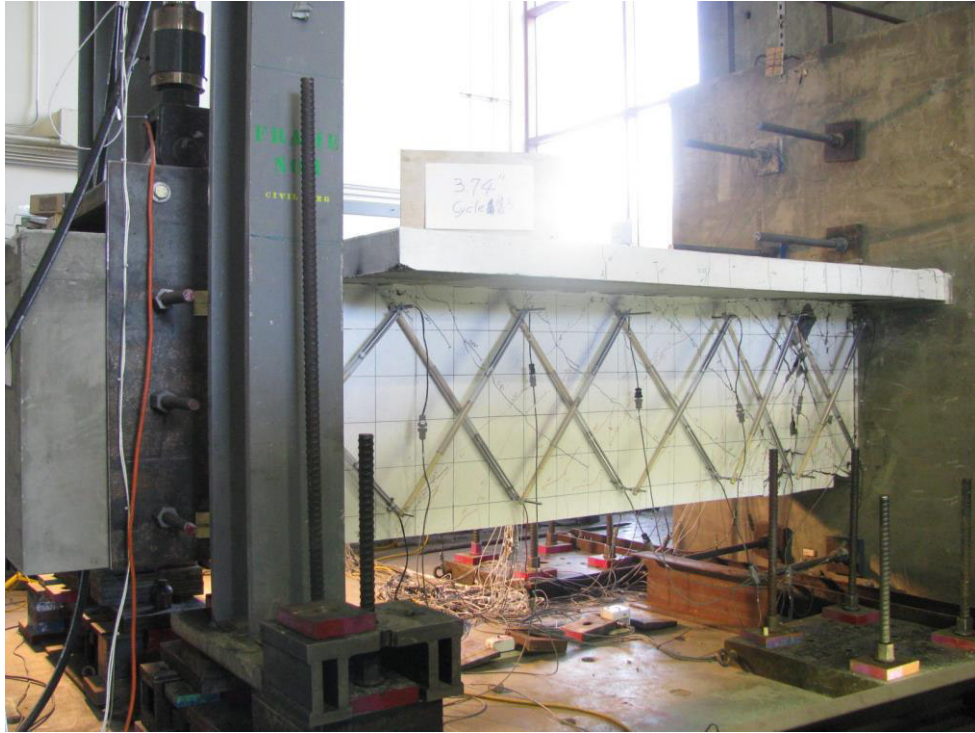


Figure 5.27: Crack pattern at 3.0% for S4

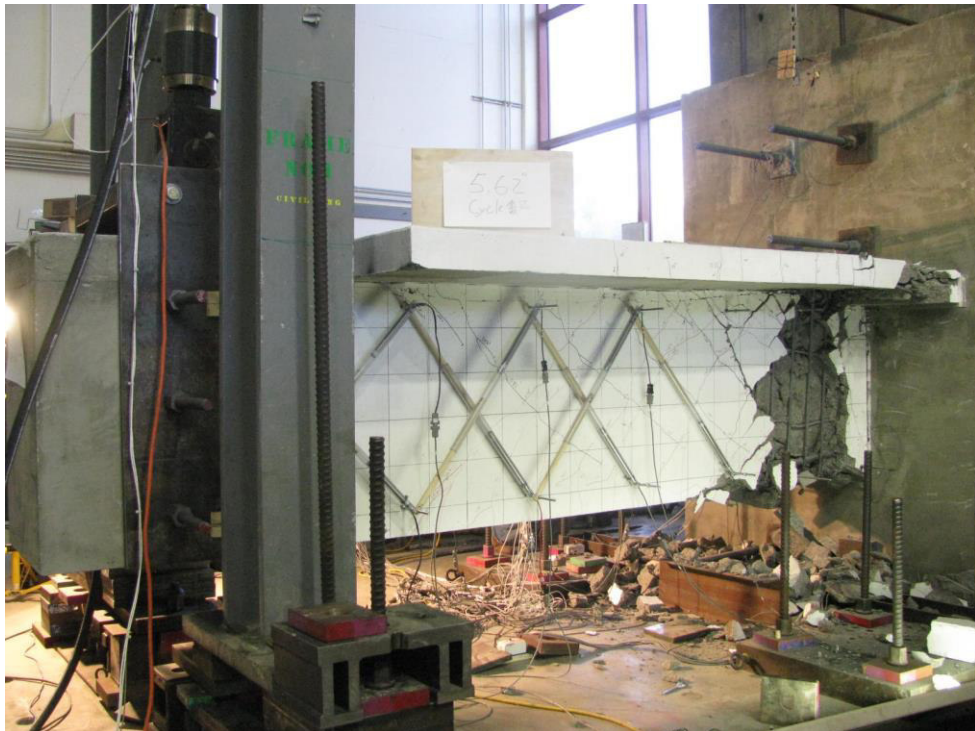


Figure 5.28: Crack pattern at 4.0% drift for S4



Figure 5.29: Cracking pattern at the fixed end at 3.0% drift on both sides of beam



Figure 5.30: Plastic hinge region at both sides of beam for S4



Figure 5.31: Buckling of bottom bars for S4

5.2 Summary of Test Results

The hysteretic response of each of the specimens is presented in Table 5.2. Flexural and diagonal shear cracking strengths ($F_{cr,f}$ and $F_{cr,s}$) were estimated from video documentation recorded during the testing, while strengths and displacements at yield (F_y and Δ_y) were selected based on the point of first substantial stiffness change within the cyclic envelope. Peak strengths and corresponding displacements (F_{peak} and Δ_{peak}) were defined based on the point of ultimate strength and were used to determine the ductility capacity (μ) of each specimen. The yield stiffness (k_y) was calculated as the ratio between the yield load and yield displacement. The stiffness (k_h) described the segment of the load-displacement curve between yield and ultimate capacity, and the stiffness (k_{pp}) is the post peak stiffness corresponding to the softening branch of the envelope. The shear stress at peak load was evaluated using a shear stress level factor Fang et al. (1993): $\alpha_c = V_{max}/(b_w d \sqrt{f'_c})$, where V_{max} is the maximum shear developed within each of the specimens, b_w is the width of the beam's web, d is the effective depth, and f'_c is the average concrete compressive strength at the time of testing. Moment-to-shear ratios at the support and at the area of the opening are labeled (M_s/V_s) and (M_o/V_o), respectively.

Table 5.2: Experimental hysteresis results

	S1		S2		S3		S4	
	Down (+)	Up (-)	Down (+)	Up (-)	Down (+)	Up (-)	Down (+)	Up (-)
$F_{cr,f}$ [kips]	32.5	30.9	37.9	49.6	22.3	32.1	16.7	35.5
$F_{cr,s}$ [kips]	96.4	95.3	52.2	61.5	79.3	81.7	50.4	60.9
F_y [kips]	127.1	122.4	163.7	120.4	95.0	81.7	148.5	139.6
Δ_y [in]	1.2	1.2	1.5	1.1	1.9	1.4	1.3	0.8
F_{peak} [kips]	145.3	132.5	214.9	159.1	113.7	97.6	170.3	165.1
Δ_{peak} [in]	2.7	2.7	6.7	6.8	5.7	7.6	3.8	3.7
$\mu=\Delta_{peak}/\Delta_y$ [in/in]	2.2	2.3	4.5	6.0	3.0	5.5	3.0	4.6
$k_y=F_y/\Delta_y$ [kips/in]	104.0	102.9	108.4	106.5	50.3	58.6	118.3	169.4
$k_h=(F_{peak}-F_y)/(\Delta_{peak}-\Delta_y)$ [kips/in]	12.2	6.7	9.8	6.8	5.0	2.5	8.7	8.7
k_{pp} [kips/in]	-24.4	-17.5	-227.5	-76.1	-5.0	-	-15.0	-44.6
$\beta=k_h/k_y$	0.12	0.07	0.09	0.06	0.10	0.04	0.07	0.05
M_y [kips-ft]	1511.5	1274.3	2143.8	1384.3	1636.2	1095.8	1633.5	1363.5
θ_y [%]	0.91%	0.89%	1.01%	0.76%	1.02%	0.75%	1.01%	0.66%
M_{peak} [kips-ft]	1714.7	1386.9	2779.8	1864.1	1926.4	1341.7	1860.1	1629.0
θ_{peak} [%]	2.03%	2.01%	4.51%	4.57%	3.06%	4.12%	3.02%	3.00%
αc	2.2	1.6	3.3	2.0	1.8	1.0	2.7	2.2
M_s/V_s [in]	129	140	145	156	174	205	121	130
M_o/V_o [in]	79	83	81	84	118	131	-	-

5.3 Boundary Condition: Rotation of Reaction Blocks

The measurements from the instrumentation located at the top and bottom of the reaction block are displayed in the Figures 5.32-5.35. Due to the damage of a string potentiometer, only one sensor was utilized for S2. The data below was clipped at the moment in which the sensor was disconnected to remove erroneous data recorded afterward. The spalling of the concrete typically caused the removal of the bottom sensor in order to avoid damage. The measured displacements were typically in the order of 10^{-3} in. and therefore their contribution of the beams overall displacement was deemed negligible.

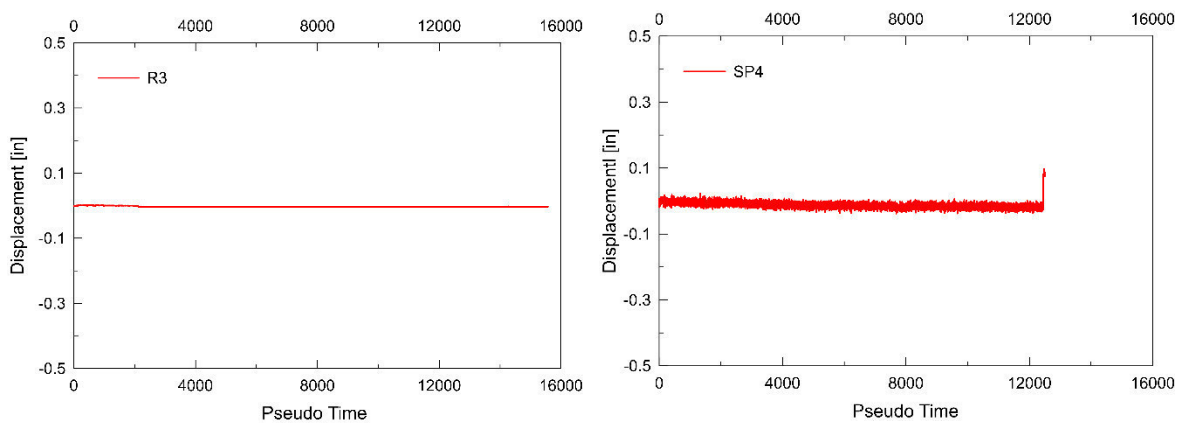


Figure 5.32: Time histories of string potentiometers used to measure the rotation of the reaction block for S1

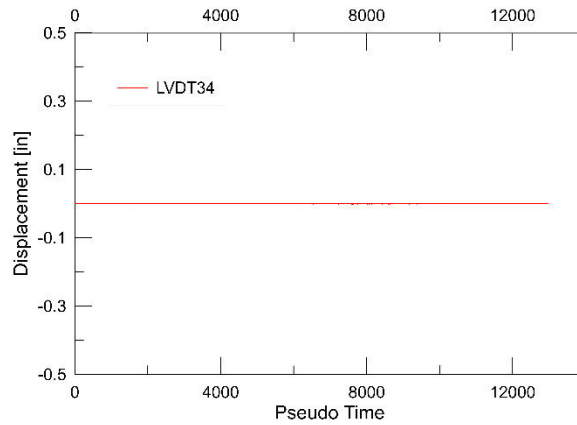


Figure 5.33: Time histories of string potentiometers used to measure the rotation of the reaction block for S2

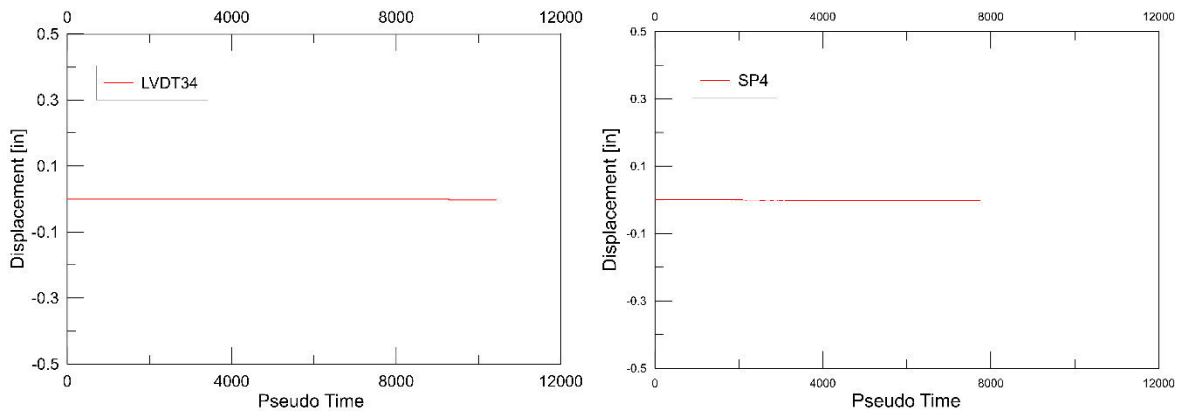


Figure 5.34: Time histories of string potentiometers used to measure the rotation of the reaction block for S3

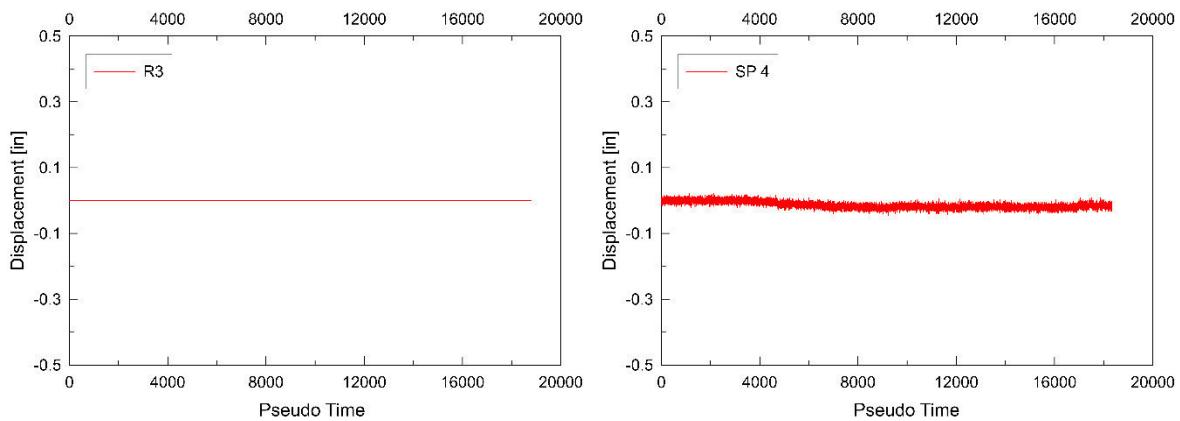


Figure 5.35: Time histories of string potentiometers used to measure the rotation of the reaction block for S4

5.4 Load versus Tip Displacement

The hysteretic response of each of the specimens is listed in Table 5.2 and shown in Figures 5.36-5.39 (for shear-displacement). The load–displacement relationships ($P - \Delta$) are presented in terms of shear force vs. displacements to account properly for the self-weight of the beams and to enable a general comparison with the limits of shear capacity, as determined from the results of the cross-sectional analyses provided in Table 5.1. The applied loading can be extracted by subtracting the self-weight of the beams (i.e., 14 kips, 15.5 kips, 19 kips, and 14.3 kips for specimens S1 to S4, respectively). On Figures 5.36-5.39, positive values of load (i.e., shear) and deformation correspond to the downward loading direction (i.e., slab in tension), while negative values correspond to upward loading (i.e., slab in compression). Cyclic envelopes were established using the peak points from the first loading cycle at each displacement level which have been plotted together in Figure 5.40. For specimen S1, a maximum load of 145 kips was achieved in the downward loading direction at 2.7 in. of displacement (2% drift), and the beam experienced a predominantly shear and bond-slip type of failure at the chord members above and below the web opening. Furthermore, specimen S1 exhibited the lowest displacement ductility (2.2 in/in) among all the specimens in the test series, and experienced the most substantial degradation of post-peak stiffness and strength. Maximum shear capacities at the opening region ($V_{n,B}$) were reached halfway through the test in downward direction and at maximum load in upward direction as shown in Figure 5.36,

Conversely, the best performance among all four specimens was demonstrated by specimen S2, which was the most heavily reinforced beam of the series. That is, specimen S2 achieved the highest yield load equal to 164 kips at 1.5 in downward displacement, which was 29%, 72%, and

10% greater than F_y for S1, S3, and S4, respectively. With only one exception, S2 also reached the greatest peak strength in both loading directions (i.e., 215 kips at 6.7 in. of downward displacement and 159 kips at 6.8 in. of upward displacement), which was 48%, 89%, and 26% greater than F_{peak} measured for S1, S3, and S4, respectively, for loading in the downward direction. S2 displayed the largest displacement ductility of 4.5 in./in. and 6.0 in./in. in downward and upward loading direction, respectively, and failed at the beam column interface while maintaining complete structural integrity within the opening region. It is important to reiterate that the reinforcement at the fixed end (region A) and at the opening (region B) of specimen S2 was significantly higher compared to specimens S1, S3 and S4. That is, the top longitudinal reinforcement ratio for S2 in region A was 63% to 72% greater than those for S1, S3, and S4, and 28% to 43% greater for region B. The bottom longitudinal reinforcement ratio was approximately equal to that of specimens S1 and S4 in region A, but 37% bigger than S3. Along the opening, S2's bottom longitudinal reinforcement was 13% and 39% higher when compared to S1 and S3, respectively. The transverse reinforcement ratio for S2 was 100% greater at region A and 177 % to 192% greater at region B than those of the other specimens. As indicated in Figure 5.37, shear capacities are significantly larger than shear forces reached during testing, and fall outside of the figure limits.

Specimen S3, characterized as the most flexible specimen in the test series, manifested the weakest performance with respect to strength capacities. S3 achieved yield forces of 95 kips and 82 kips in downward and upward loading directions at displacement levels of 1.9 in. and 1.4 in., respectively. The measured yield force for S3 was approximately 25% to 42% lower when compared to S1, S2, and S4. Peak strengths of only 114 kips and 98 kips were recorded for S3 at

displacements of 5.7 in. and 7.6 in. respectively, which were about 22% to 47% lower than those exhibited in the other specimens. This type of performance, however, was somewhat expected as S3 had the lowest yield stiffness (k_y) and the longest shear span of all the specimens in the test series (i.e., 39%, 25%, and 49% longer than S1, S2, and S4, respectively). Furthermore, S3 was constructed with the lowest combined longitudinal reinforcement ratio (i.e., $\rho_{top} + \rho_{bottom}$) at the fixed end (i.e., 7%, 35%, and 12% lower than S1, S2, and S4, respectively), and experienced classical plastic hinge failure at the beam-column interface with only limited cracking around the opening. The displacement ductility was calculated to be 3.0 in./in. and 5.0 in./in. in the downward and upward loading direction, respectively. Nevertheless, out of all test specimens, the largest displacement ductility was observed for S2 and S3 in upward loading direction. Shear strengths (V_n) in both directions exceeded the applied loading by approximately 70%.

For specimen S4 (i.e., beam with no opening), the beam experienced consistent behavior in both loading directions, i.e., downward and upward yield and peak capacities are similar. Yielding was observed at 149 kips and 140 kips at corresponding displacement levels of 1.3 and 0.83 in., and peak forces were reached at 170 kips and 165 kips at displacement levels of 3.8 and 3.8 in., respectively, in the downward and upward directions. The contribution of the top slab to the overall performance of specimen S4 after it yielded was found to be minimal. Available shear capacities in both directions exceeded the peak load reached during testing, however shear capacities in downward loading direction were only 17% larger than the max shear force reached with the applied loading.

Strength deterioration in the cyclic envelope beyond the peak strength (i.e., post-peak negative stiffness branch) was more pronounced in specimens S1 and S2. The assessment of strength deterioration for specimen S3 was restricted to only one displacement level past peak, as the experimental setup reached its maximum displacement range. However, significant cyclic degradation occurred during repeated cycles at the first post-peak drift level in the downward loading direction of S3, which indicated that strength loss was initiated and increasing deterioration was to be expected thereafter. In general, a considerably greater post-peak decay is displayed for non-symmetrically reinforced specimens in the loading direction corresponding to their larger reinforcement ratio, as also noticed by Fang et al. (1993). This can be observed for specimens S2 and S3, which have greater differences between the top and bottom reinforcement amounts and show a much larger drop in stiffness at small drift ratios in the upward loading direction.

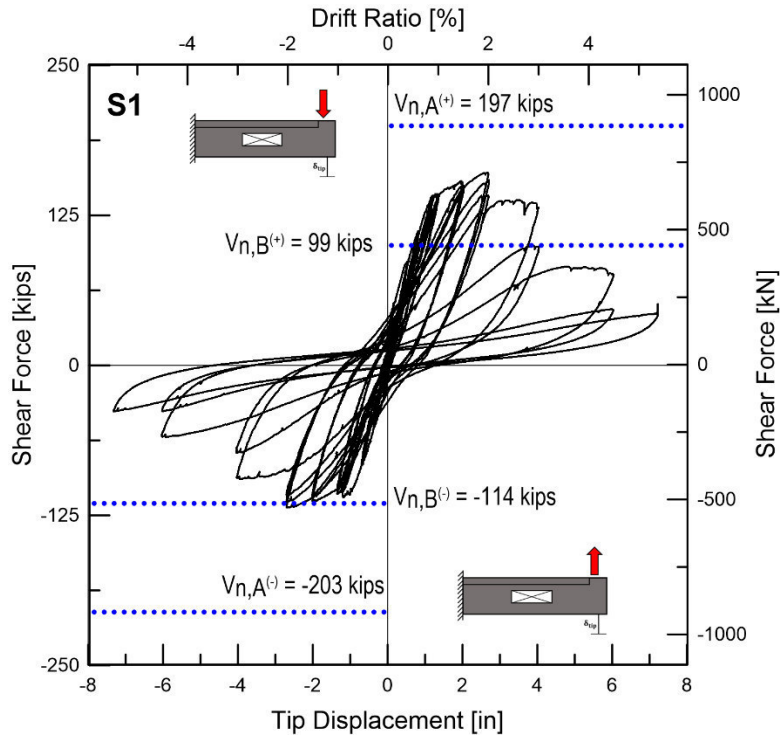


Figure 5.36: Load (shear)-displacement relationship specimens S1

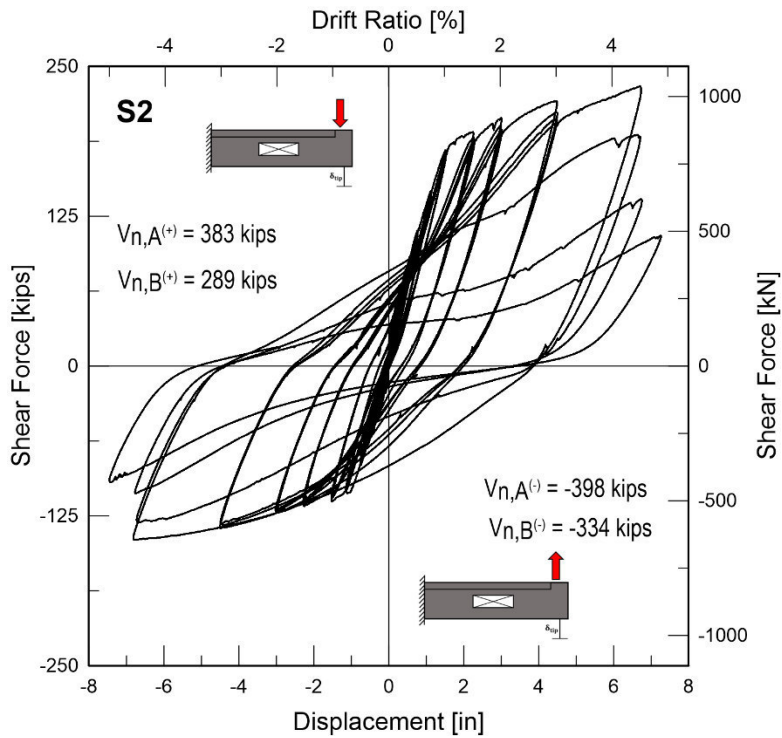


Figure 5.37: Load (shear)-displacement relationship specimens S2

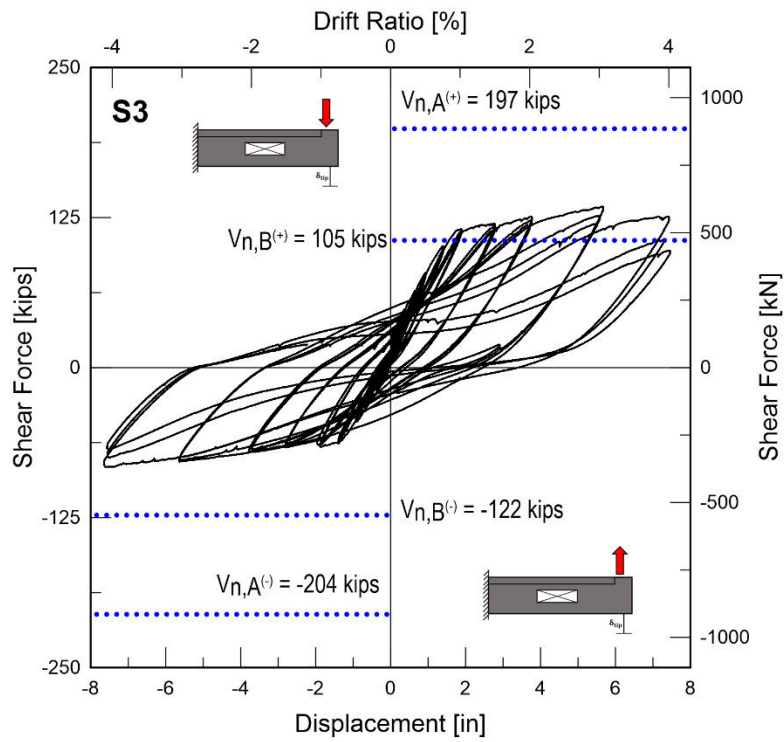


Figure 5.38: Load (shear)-displacement relationship specimens S3

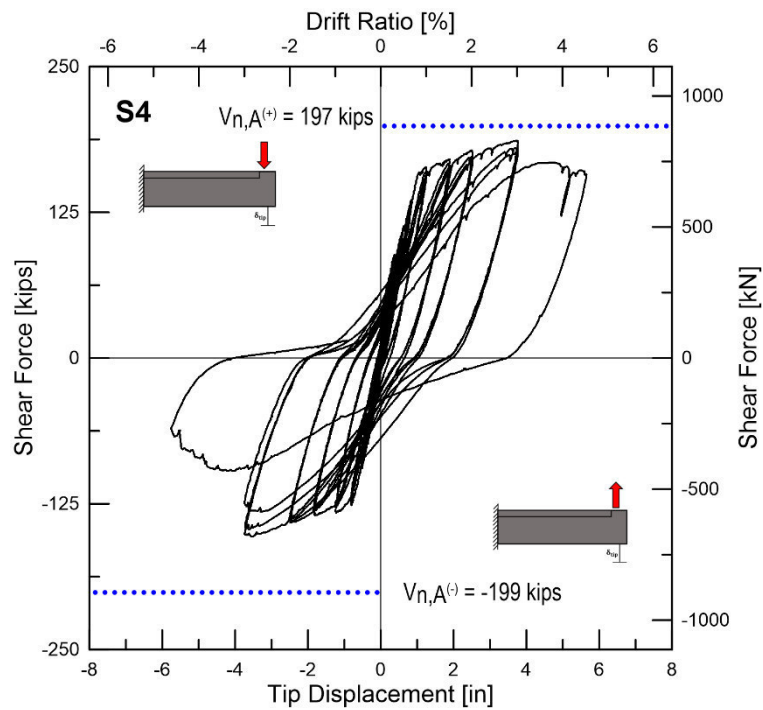


Figure 5.39: Load (shear)-displacement relationship specimens S4

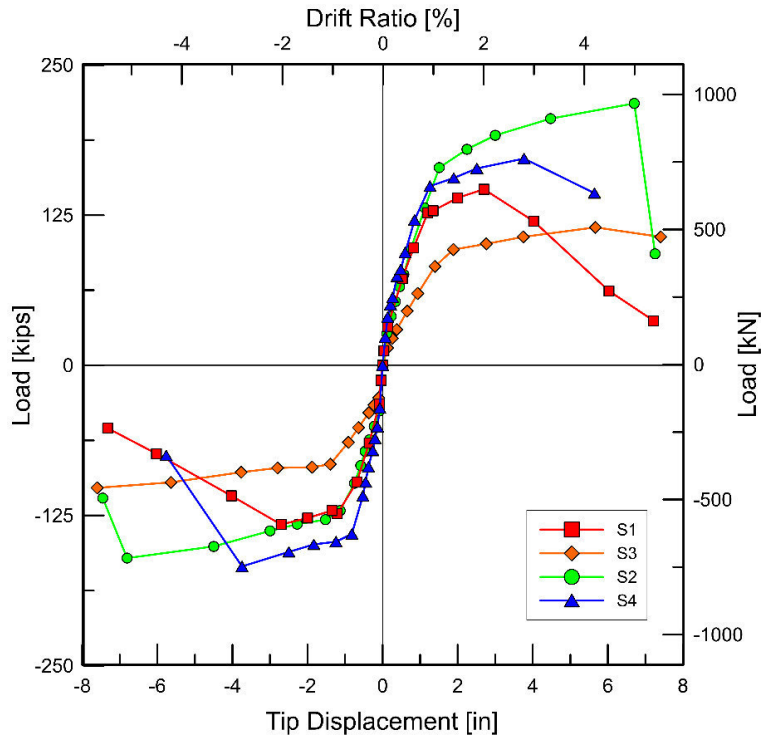


Figure 5.40: Load-displacement backbone curve for all beams

5.5 Moment Rotation Relationships

Monotonic moment-curvature ($M - \phi$) relationships of the solid cross-section at the fixed end (i.e., section A) and at the mid-span (i.e., opening at section B) in both loading directions are depicted in Figure 5.41. The sectional analyses were performed with the commercial software XTRACT (v3.08) considering only flexural deformations due to monotonic loading, and, thus, deformations resulting from shear, fixed-end rotations and cyclic deterioration were not accounted for. The $M - \phi$ relationships were derived using as-tested material properties. Mander et al. (1988) formulations were used to model the unconfined and confined concrete materials. The strains associated with compression yield, peak strength, crushing and spalling of the unconfined cover concrete were assigned as 0.0014, 0.002, 0.004 and 0.006, respectively. The tensile strength

of concrete was estimated as the modulus of rupture, in accordance with Eq. 19.2.3.1 in ACI 318-14. A parabolic strain hardening model was used for the reinforcing steel, assuming a hardening onset strain value of 0.012 and a failure strain equal to the corresponding experimental percent elongation at failure. The $M - \phi$ relationships at region B were determined under the assumption that the beam cross-section rotated as one solid beam (i.e., '*plane sections remain plane*' assumption). Thus, bending moments at the opening were assumed to be resisted by a tension-compression couple in the chords. To facilitate the $M - \phi$ analysis of the top and bottom chords as one coherent cross-section, the chords were connected by two vertical strips of unconfined concrete cover material (i.e. 1.6 in.) on each side of the opening.

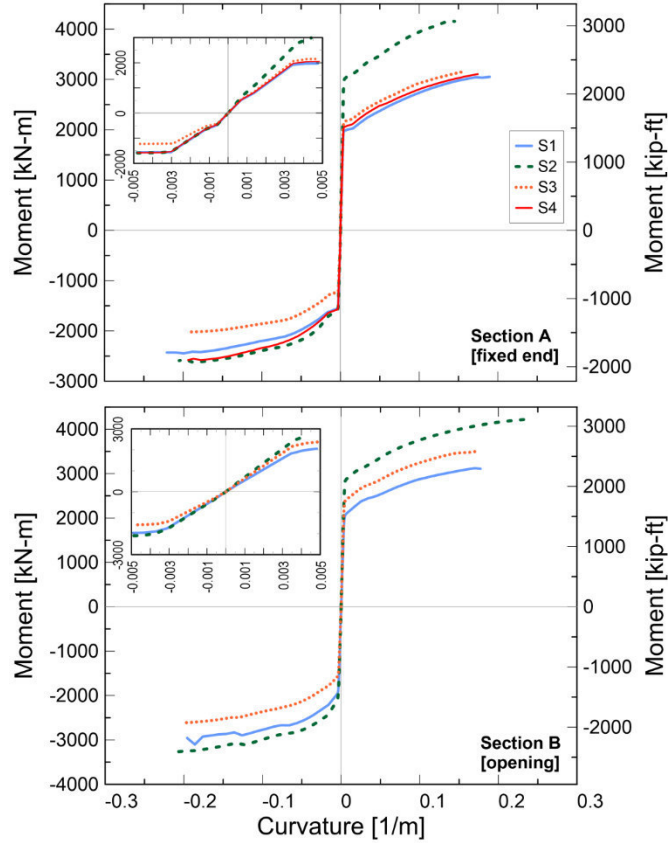


Figure 5.41: Monotonic moment-curvature ($M - \phi$) relationships: (a) at section A (fixed end), and (b) at section B (opening)

A summary of the results from the analytical determinations of the moment-curvature ($M - \phi$) relationships and shear capacities for sections A and B are presented in Table 5.2. The cyclic yield moment capacities, M_{yc} , were estimated using the relationship proposed by Fenwick (1983), as shown in Eq. 5.1, which assumes that the internal lever arm following the first complete inelastic load cycle is equal to the distance between the centroids of the tension and compression steel reinforcement (i.e., $d - d'$):

$$M_{yc} = A_s f_y (d - d') \quad (5.1)$$

In Eq. 5.1, A_s is the total area of the steel reinforcement in flexure, and f_y is the corresponding yield strength. The force F_u represents the theoretical load required to develop the ultimate moment (M_u) at the fixed end of the beam, and was computed by dividing M_u by the shear span (L_s). Force and shear capacities are compared to the maximum (peak) force and shear loads measured during testing (F_{peak} and V_{peak}). The maximum shear force was computed by adding the self-weight of the beam (W) to the applied load: $V_{peak} = F_{peak} + W$. As noted previously, the flexural and shear capacity values do not account for the degradation of cyclic strength.

The flexural capacities (M_u) of the perforated beams (i.e., specimens S1 to S3) in the region of the rectangular opening were determined to be similar to the flexural capacities in the solid region of the beams, as the chord members above and below the opening had greater depths than the height of ultimate compression stress block (typically referred to as “ a ”) formed at M_u . Therefore, the flexural resistance at the opening was sufficiently provided by the internal tension-compression ($T - C$) couple. The small divergences observed in M_u are attributed to differences in reinforcement ratios between sections A and B . Except for the condition when the loading was applied in a downward direction to specimen S4, the available shear capacity at the fixed end section (section A) of each of the specimens was sufficient to allow the development of full flexural capacity (i.e., $V_n > F_u$) even when $V_c = 0$.

The moment–rotation ($M - \theta$) relationships for each of the specimens along with critical benchmark values for monotonic yield and ultimate moments at section A ($M_{y,A}$ and $M_{u,A}$, respectively) are depicted in Figures 5.42-5.45. For comparison, the idealized component response

curve defined by ASCE 41-06, which implicitly incorporates cyclic strength and stiffness degradation, is also presented in Figures 5.42-5.45. The probable moment (M_{pr}) of each specimen, which corresponds to the peak moment strength within the ASCE 41-06 envelope, was calculated according to R18.6.5 in the commentary to ACI 318-14 using the nominal unconfined compression strength of concrete (i.e., $f'_c = 6$ ksi) and the nominal yield strength of the reinforcing steel multiplied by an over-strength factor of 1.25 (i.e., $1.25*f_y = 75$ ksi). The yield moments and corresponding rotations were determined from the moment-curvature analyses, and the “expected” material properties were replaced by measured material properties. To obtain envelop parameters prior to and after yielding, as well as after peak, the beam behavior was assumed to be governed by flexure. Two strain-hardening slopes were evaluated, i.e., at 5% and 10% of the elastic stiffness, k_y . Except for specimen S1, each of the beam specimens demonstrated very good agreement between the test data and the proposed numerical modeling curve, as expected given the typical SMRF failure and in-situ material properties. Specimen S2 exhibited slightly greater ultimate capacities, which is a result of the reinforcement ductility. Specimen 1 has less capacity than predicted by ASCE 41-06 as combined shear and flexural failure modes dominate the specimen behavior and hinging in the opening region led to ultimate failure. A softening branch between Life-Safety and Collapse Prevention Levels was considered to account for component degradation beyond the probable moment capacity.

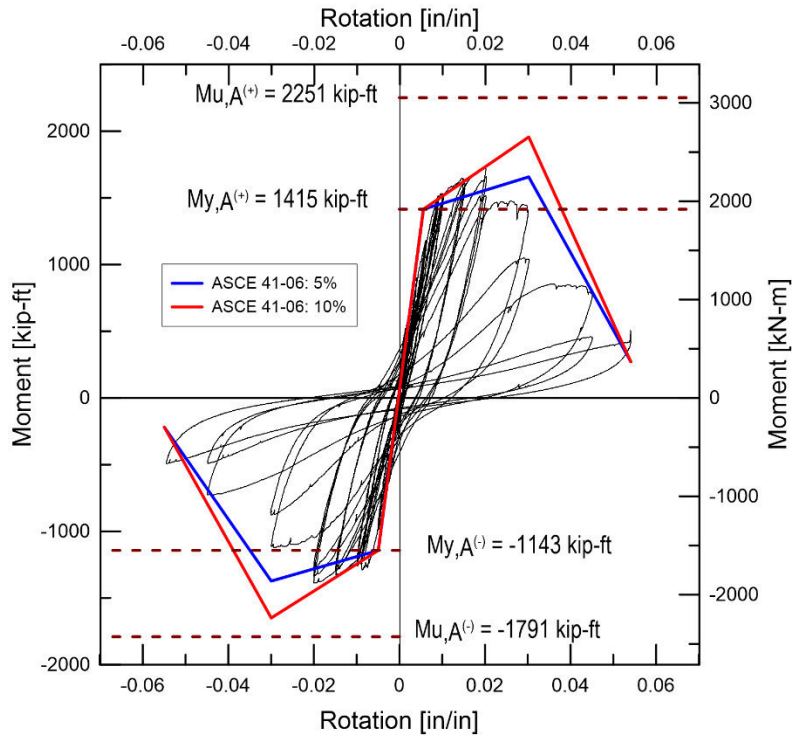


Figure 5.42: Moment-rotation relationships specimens S1

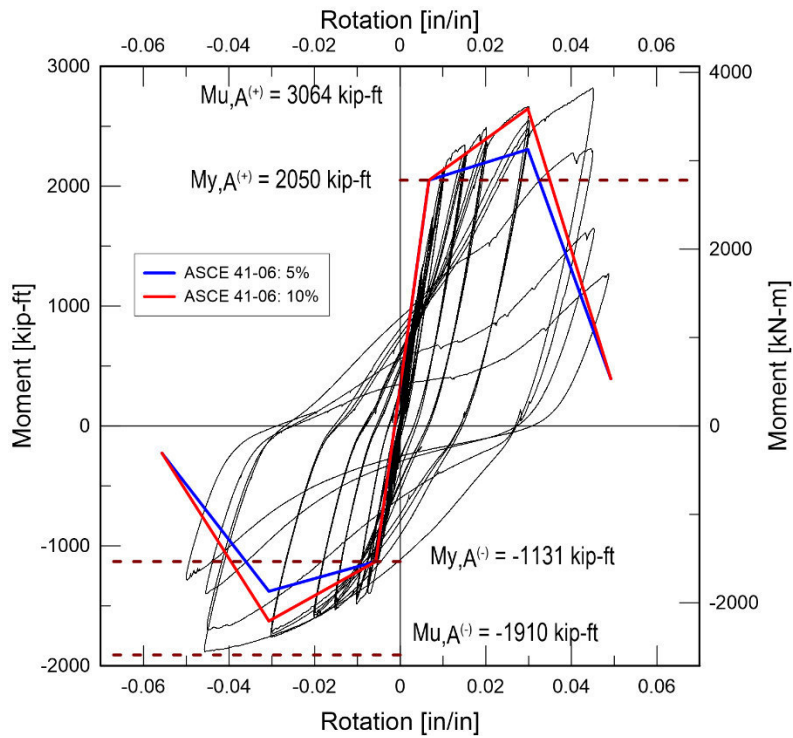


Figure 5.43: Moment-rotation relationships specimens S2

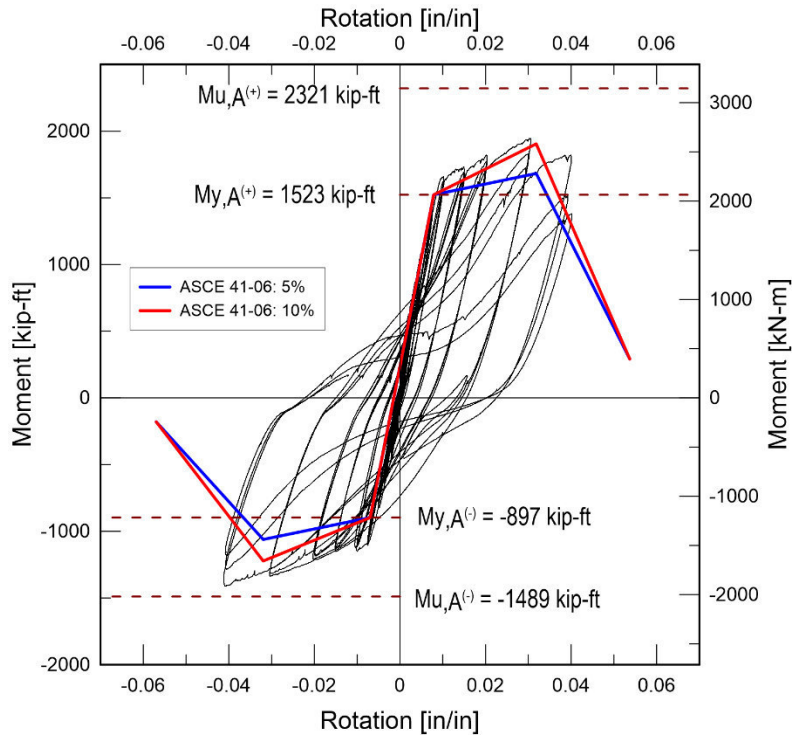


Figure 5.44: Moment-rotation relationships specimens S3

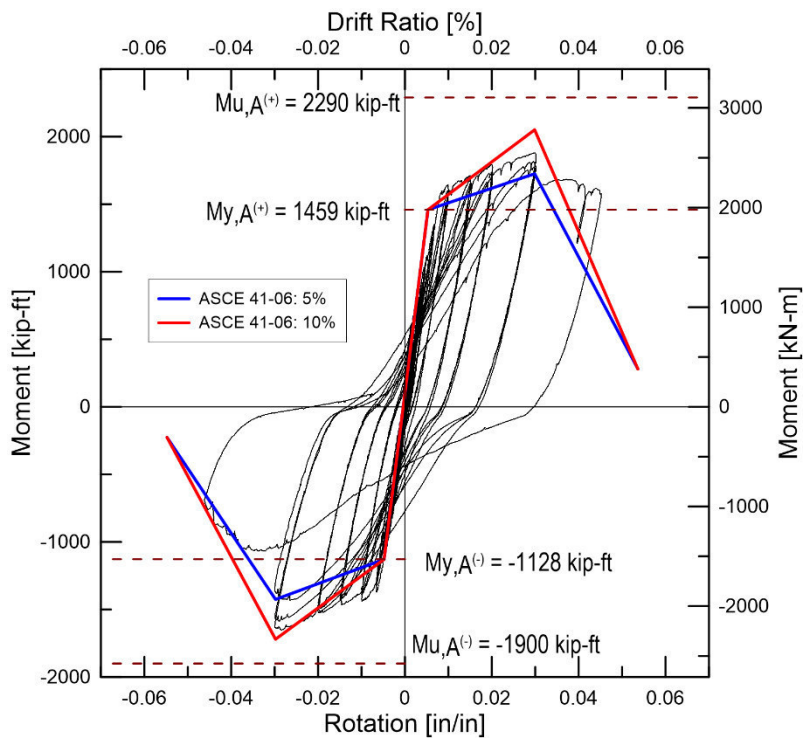


Figure 5.45: Moment-rotation relationships specimens S4

5.6 Beam Deflection Profiles

Figures 5.46-5.49 below were created using the string potentiometers located underneath the beam. The sensor data represents the complete deflection profile during the different displacement levels of the experiment. In these profiles, total displacements were determined at maximum lateral displacement during the first cycle under both positive and negative loadings. The separate markers on each of the lines represent the location of the sensor for that beam specimen.

As the figures demonstrate, the profiles for all beam specimens were consistently linear up to approximately 3% drift. Afterward, the deflection profiles are effected by the plastic hinging that occurred at the support or at the opening. This is most clearly observed for the deflection profile of S1 at 3% drift where the sensors located at the opening capture the same behavior observed in Figure 5.46. It is important to note that the deflection profile for S2 and S3 were practically identical to that of S4 despite the presence of an opening.

During cycles where concrete debris from the spalling began to occur, sensors needed to be removed to prevent damage. This typically occurred at the beam support and therefore, the sensor at the support (i.e., at 0 in.) was removed for S2, S3, and S4. Values for the sensor were assumed to be 0 in. of displacement to create the profiles post sensor removal. Additionally, for tests of S2 and S3, the sensor SP1 (Figures 4.28 and 4.31) began to malfunction at approximately 1% drift in the upward loading cycle. The values for this sensor were interpolated which was deemed appropriate due to the observed deflection and lack of damage in that location.

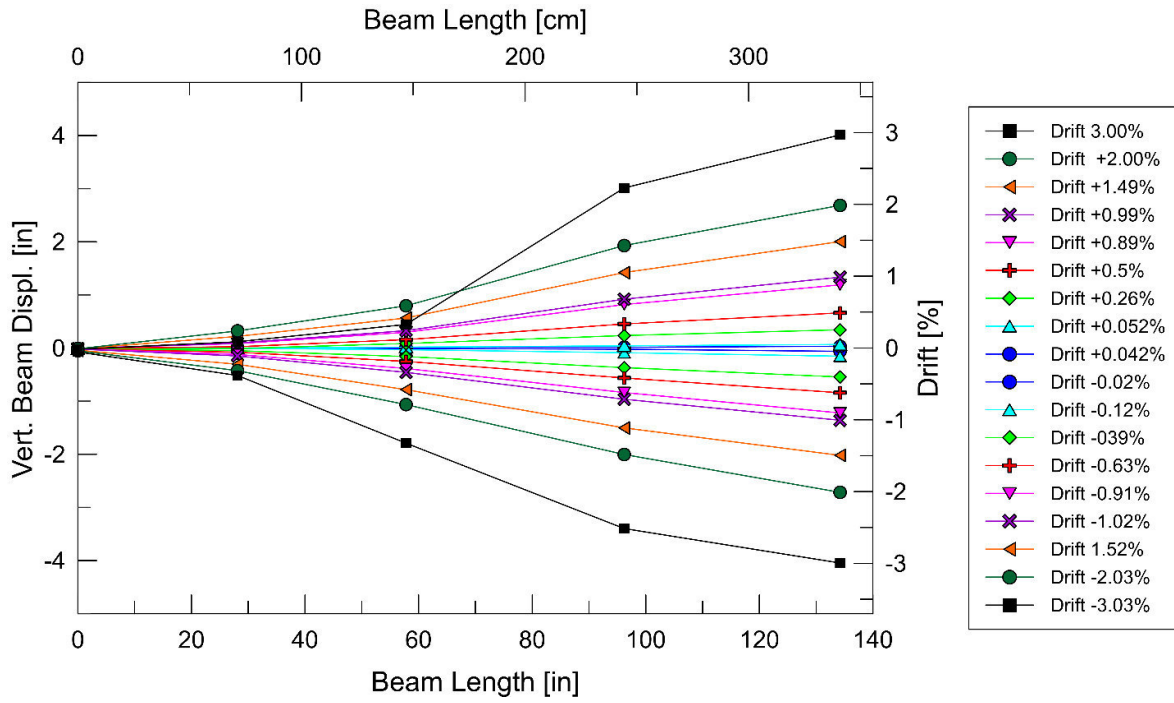


Figure 5.46: Beam deflection profile for S1

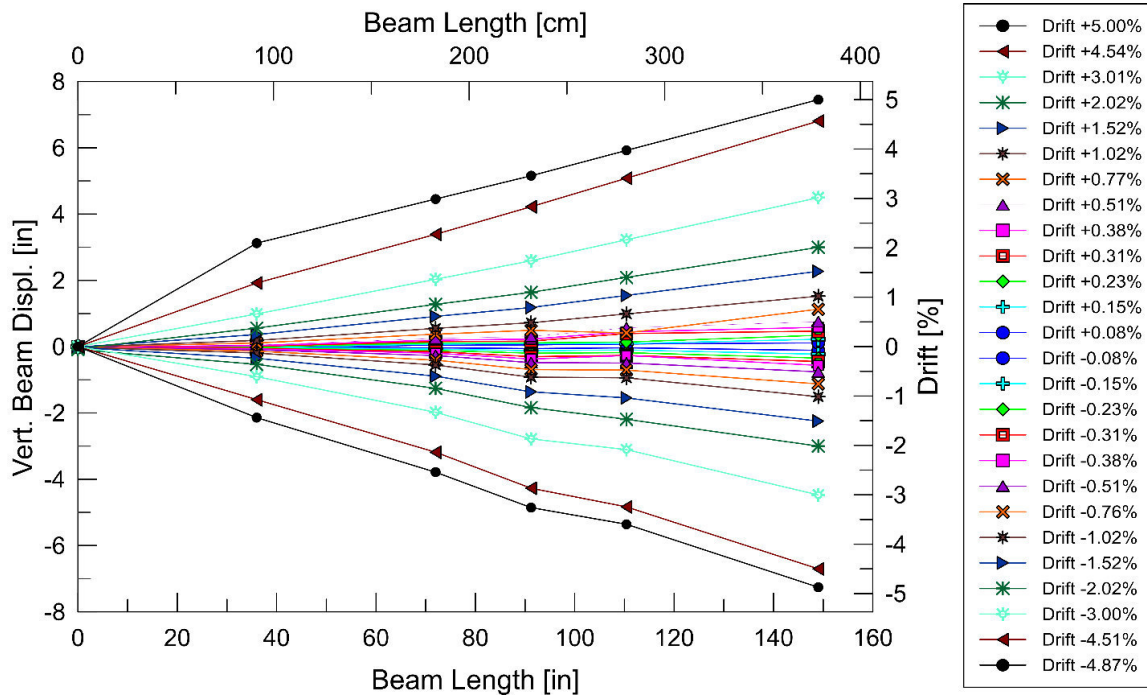


Figure 5.47: Beam deflection profile for S2

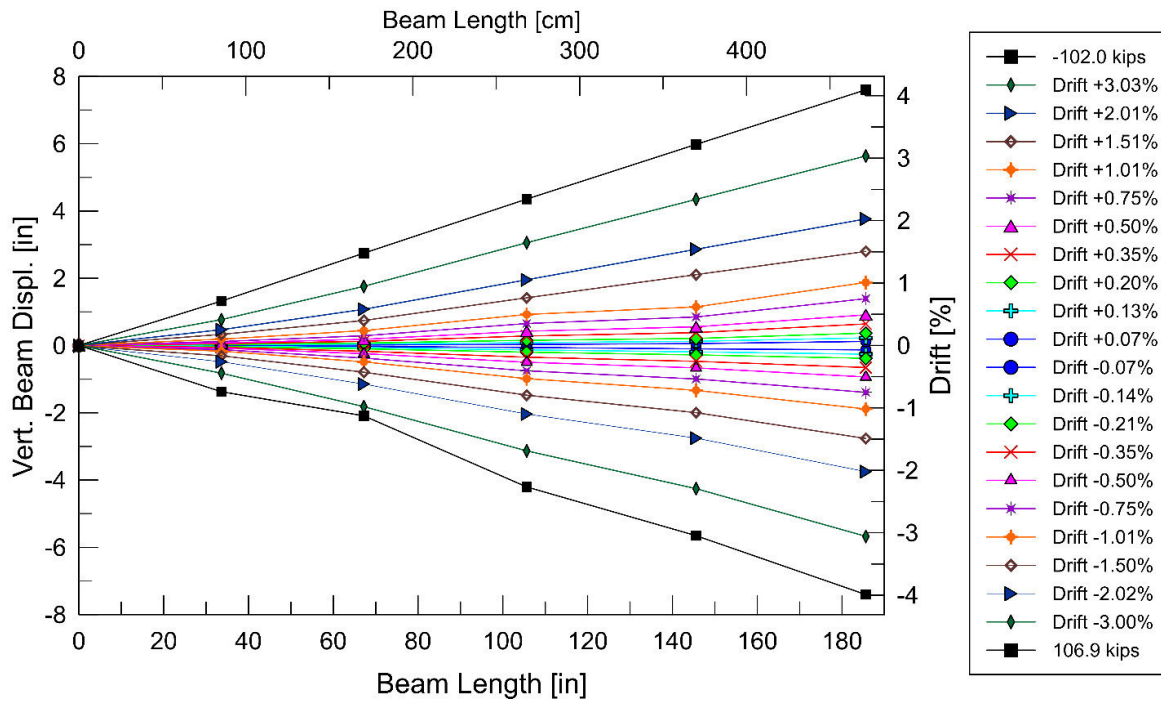


Figure 5.48: Beam deflection profile for S3

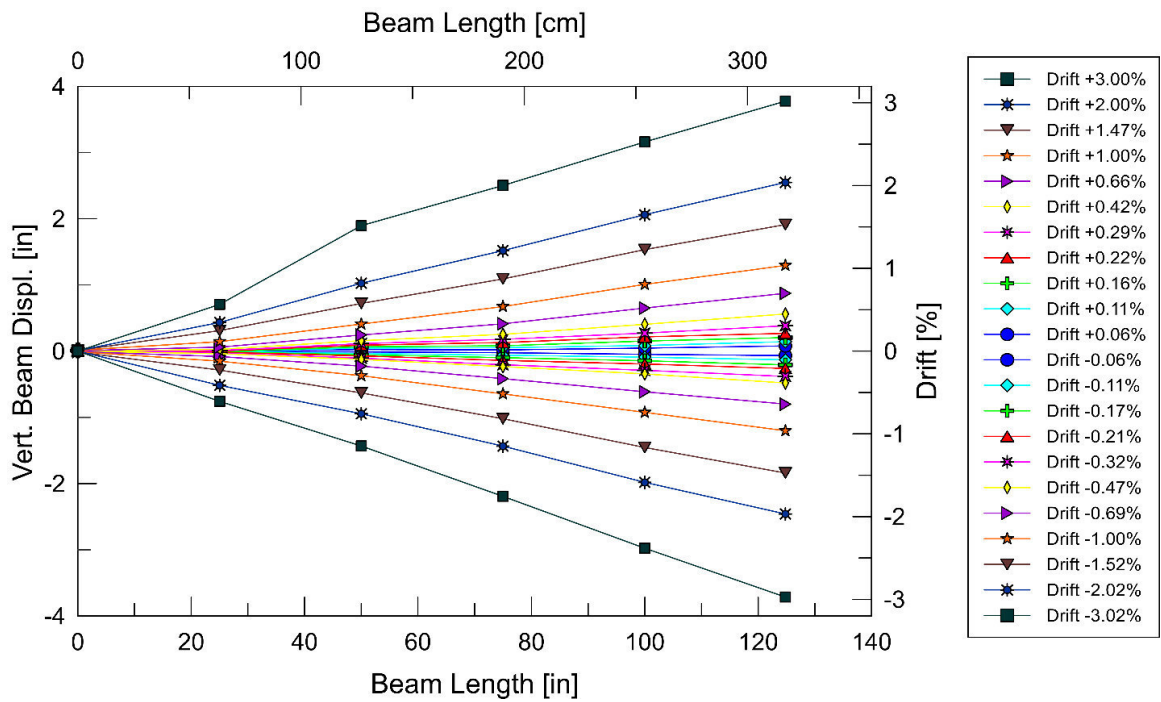


Figure 5.49: Beam deflection profile for S4

5.7 Dissipated Energy

The history of normalized cumulative hysteretic energy (NHE) dissipation of all test specimens is presented in Figure 5.50. The cumulative NHE at a given cycle (i) was computed as the summation of the dissipated hysteretic energies (HE) of all current and preceding cycles and is normalized by twice the elastic strain energy as described by Eq. 5.2, where HE_i is defined as the energy dissipated during the i th cycle, determined from the area enclosed by the corresponding hysteretic loop, and NHE_i is the normalized cumulative dissipated energy up to the i th cycle.

$$NHE_i = \frac{\sum_{j=1}^{j=i} HE_j}{2(\frac{1}{2}F_y\Delta_y)} = \frac{HE_1+HE_2+\dots+HE_i}{2(\frac{1}{2}F_y\Delta_y)} \quad (5.2)$$

The normalized cumulative energy reached at yield was 1.0, 1.9, 1.7 and 2.1 for specimens S1 through S4, respectively. Normalized energy dissipated at peak capacity accumulated to 8.5, 40.4, 19.4 and 22.0 for specimens S1 to S4, respectively. Both Figures indicate that that cumulative energy dissipation for specimens S2 and S4 progressed relatively similarly, and more cycling was needed to reach the same level of dissipation as in Specimens S1 and S3 (Figure 5.50 right). Specimen S1 shows a typical plateau (Figure 5.50 left) associated with the reduction of loop sizes in repeated loading cycles, while S2 – S4 show consistent increase as loops experience much less reduction in size. As the post yield loading protocols for all specimens are relatively similar, specimen S1's reduced capacity is likely associated with the plastic hinge development (@ >2% drift) around the opening.

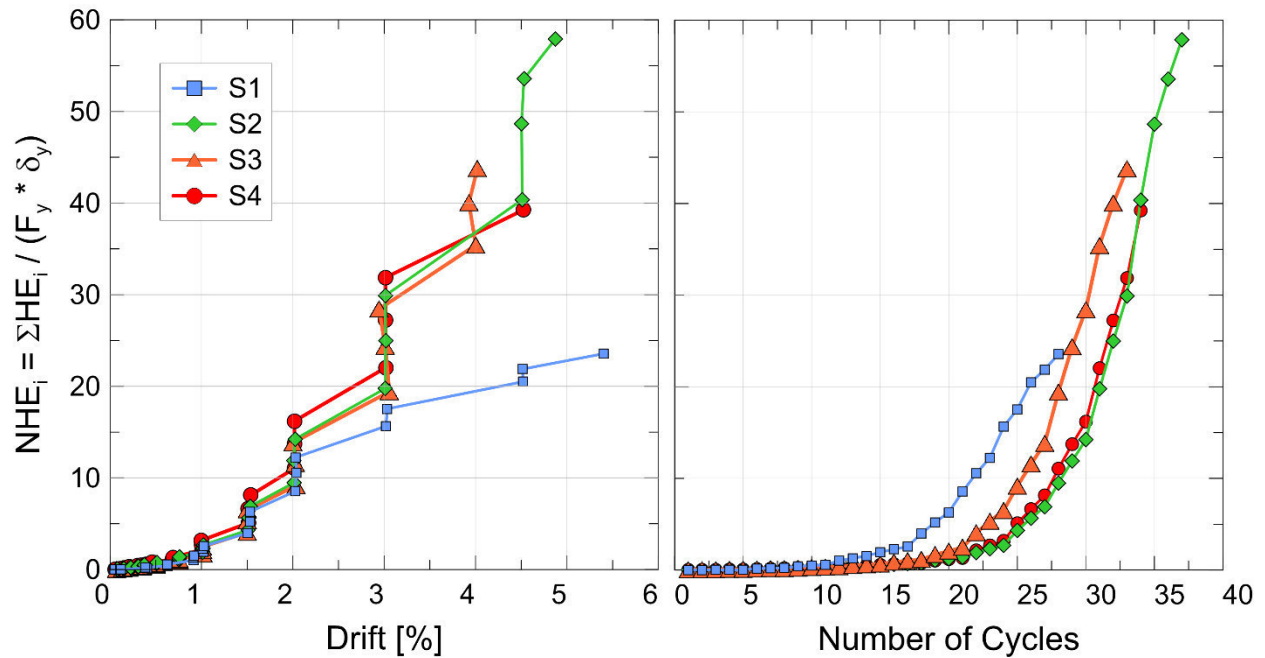


Figure 5.50: Cumulative normalized hysteretic energy (NHE) dissipation

5.8 Deflection Components

Following Massone and Wallace (2004) the contributions of shear and flexural displacements to the overall beam deformation were studied using the external LVDT instrumentation. Hereby additional deformations resulting from block rotation, reinforcement elongation and bond deterioration were considered in the analysis. Specifically, bar extension at the beam-column interface was calculated from the measurements of local strains on the top and bottom main longitudinal reinforcement anchored into the joint as described by Massone et al. (2009). A triangular strain distribution is assumed along the embedment length of the reinforcing bars, with maximum strain at the beam-column interface and zero strain at a distance equal to the development length of the rebar. The axial strains were integrated to obtain cumulative axial

displacements (extension) of the top and bottom main bars within the reaction block, thus, the corresponding rebar extension was obtained as the area of the triangular strain distribution.

$$u_{ext} = \frac{\varepsilon \cdot l_d}{2} \quad (5.3)$$

Where u_{ext} is the rebar extension and l_d is the development length calculated according to ACI 18-11 section 12.5.2 for bars in tension terminating in a standard block. The associated interface rotation was computed as the ratio of the difference in axial displacement between top and bottom bars divided by the distance between their centroids.

$$\theta_{ext} = \frac{u_{ext,top} - u_{ext,bot}}{h} \quad (5.4)$$

The corresponding vertical deflection at the section of load application was then estimated by multiplying the rotation at the beam-column interface by the shear span of the beams.

$$\Delta_{ext_{tip}} = \theta_{ext} \cdot L_s \quad (5.5)$$

In addition to Massone et al. (2009), an alternative empirical approach proposed by Elwood and Moehle (2003) was considered to estimate the deflection component associated with bond slip:

$$\Delta_{sl} = L d_b f_y \phi_y / 8u \quad (5.6)$$

where L is the clear length of the beam specimen, d_b is the diameter of the main longitudinal reinforcement, ϕ_y is the curvature at first yield at the beam-column interface, obtained from the section analysis performed with XTRACT, and u is the bond stress between the longitudinal reinforcement and the concrete in the reaction block, which can be estimated as:

$$u = 6\sqrt{f'_c}, \text{ with } f'_c \text{ in psi.}$$

Figure 5.51 displays the discretization of the beam in segments used to determine shear and flexural components due to vertical loading. Each segment contains two longitudinal and two diagonal LVDTs. The shear displacement at the right end of the i^{th} segment due to the deformation of the i^{th} segment can be expressed as

$$\Delta s_{i,i} = \frac{(\ell_{i,1} + \ell_{i,2})}{2} \frac{(s_{i,1} + s_{i,2})}{2h} \quad (5.7)$$

where $\ell_{i,1}$ and $\ell_{i,2}$ are the undeformed lengths of the two diagonal LVDTs within the i th beam segment, $s_{i,1}$ and $s_{i,2}$ are their respective displacement readings, and h is the vertical distance measured between the centroids of the longitudinal LVDTs. The total cumulative shear displacement at the end of each i^{th} beam segment can be summed up using the cumulative shear displacements from all preceding and current segments.

$$\Delta s_i = \sum_{j=1}^i \Delta s_{j,j} = \Delta s_{1,1} + \Delta s_{2,2} + \dots + \Delta s_{(i-1),(i-1)} + \Delta s_{i,i} \quad (5.8)$$

Consequently, the total contribution of shear to the vertical displacement at the point of load application (i.e. tip displacement) can be expressed as:

$$\Delta S_{tip} = \sum_{j=1}^n \Delta S_{j,j} = \Delta S_{1,1} + \Delta S_{2,2} + \cdots + \Delta S_{i,i} + \cdots + \Delta S_{n,n} \quad (5.9)$$

where n is the total number of segments in which the beam is divided via the layout of LVDTs.

Similarly, flexural displacements at the right end of the i^{th} beam segment due to the deformation of the i^{th} segment only can be written as:

$$\Delta f_{i,i} = \theta_i(\alpha_i L_i) \quad (5.10)$$

with:

$$\theta_i = \frac{(d_{i,1} - d_{i,2})}{h} \quad (5.11)$$

where θ_i is the average rotation of the i^{th} beam segment (positive in the clockwise direction), α is a coefficient that defines the location of the center of rotation of the i^{th} segment with respect to the segment's right end (assumed as $\alpha = 0.5$), L_i is the length of the i^{th} beam segment, $d_{i,1}$ and $d_{i,2}$ are the displacement readings of the top and bottom longitudinal LVDTs of the i^{th} beam segment, respectively, and h is the vertical distance measured between the centroids of the longitudinal LVDTs. Total flexural displacement at the right end of the i^{th} beam segment:

$$\Delta f_i = \sum_{j=1}^i \theta_j(\alpha_j L_j + L_{j-i}) = \theta_1(\alpha_1 L_1 + L_{1-i}) + \theta_2(\alpha_2 L_2 + L_{2-i}) + \cdots + \theta_i(\alpha_i L_i + L_{i-i}) \quad (5.12)$$

where L_{j-i} is the distance between the right end of segment j and the right end of segment i (i.e. $L_{i-i} = 0$). Total flexural displacement contribution at the point of load application (i.e., tip displacement) can be obtained as

$$\Delta f_{tip} = \sum_{j=1}^n \Delta f_{tip_j} = \sum_{j=1}^n \theta_j (\alpha_j L_j + L_{j-n}) = \theta_1 (\alpha_1 L_1 + L_{1-n}) + \dots + \theta_i (\alpha_i L_i + L_{i-n}) + \dots + \theta_n (\alpha_n L_n) \quad (5.13)$$

where Δf_{tip_j} is the contribution of the j^{th} segment to the total flexural “tip” displacement, and n is the total number of segments.

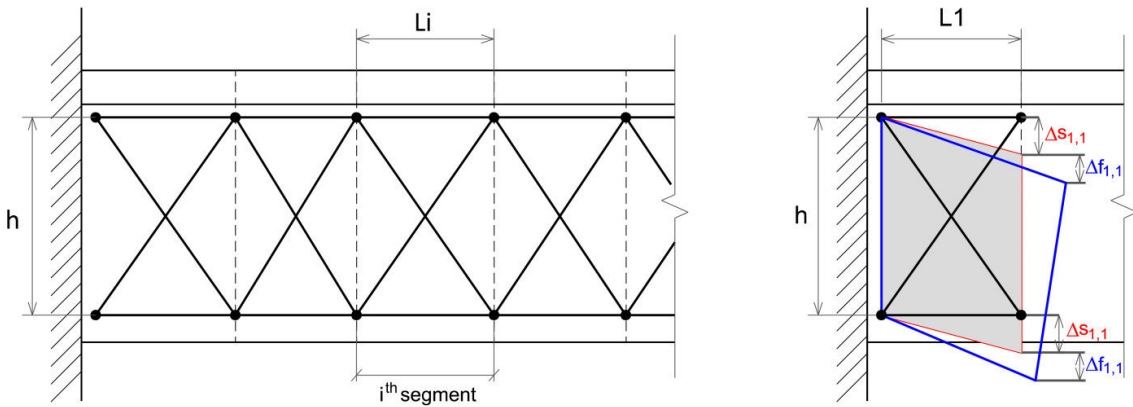


Figure 5.51: Schematic of beam segments used to analyze shear and flexural deformations

Table 5.3 summarizes the individual deformation components at various drift ratios. Δ_f , Δ_s , and Δ_{sl} correspond to flexure, shear, and bond slip contributions to the overall vertical deflection, respectively. Data outliers shown as dash are related to sensors located within or adjacent to the hinging region that contain reading with uncertainties or were disconnected during the test (e.g. when severe spalling occurred). A comparison of all deformation components indicates that the contribution of flexural deformations to the tip displacement dominates all other deformation

modes. However, it can also be recognized that shear-type deformations have an important effect on the structural response of the specimens, which is consistent with the crack patterns described in the previous section. In general, the contribution of shear deformations is considerably more pronounced for the specimens with web openings, suggesting that shear deformations should be accounted for when modeling the nonlinear response of MRF beams with openings.

$P-\Delta_f$ and $P-\Delta_s$ component hysteresis loops using accumulated displacements at the beam tip (i.e. at the point of load application) are depicted in Figures 5.52-5.59. Both graphs indicate that most of the energy is dissipated in the form of inelastic flexural deformations, while shear deformations are the main cause behind the characteristic pinching of the hysteresis loops. It should be noticed that the shape of the shear deformation loops is characterized by a reduced initial loading stiffness, which is associated with open flexure and diagonal cracks on both sides of the beam due to previous load reversals, and, consequently, shear being resisted exclusively by dowel action of the longitudinal reinforcement. When cracks start to close, the contribution of concrete and transverse reinforcement to resist shear increases progressively and consequently shear stiffness rises. It can also be observed that shear deformations increase substantially with the number of cycles, even for cycles of the same displacement level, as previously described by Krawinkler and Popov (1973).

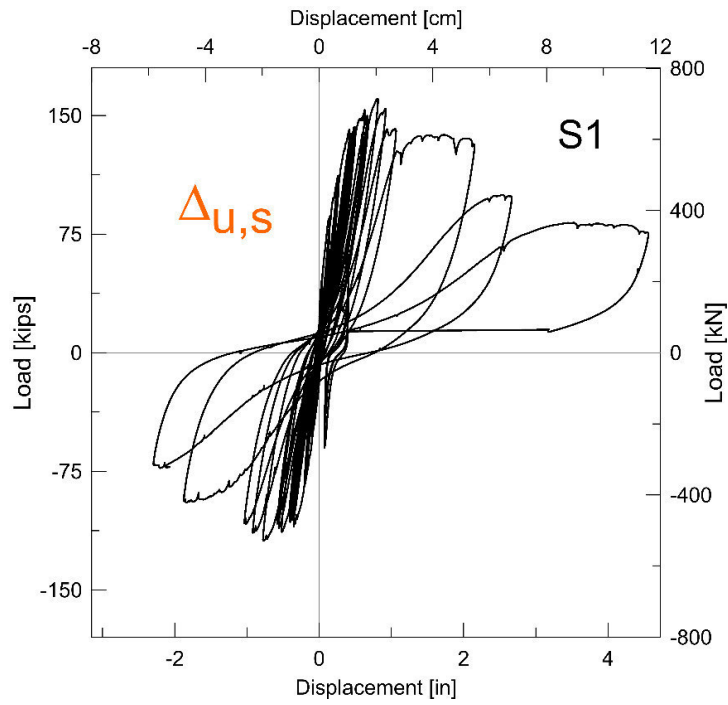


Figure 5.52: Load vs. shear displacement for specimen S1

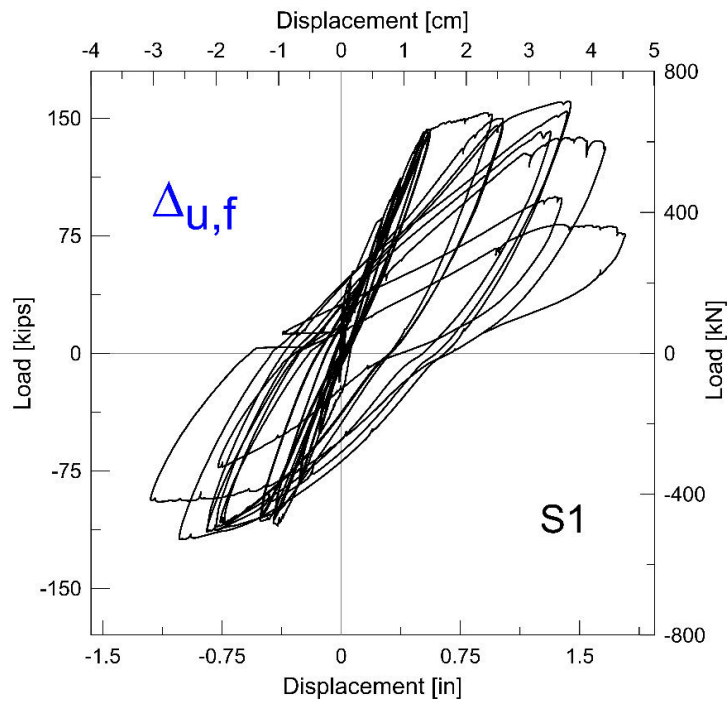


Figure 5.53: Load vs. flexural displacement for specimen S1

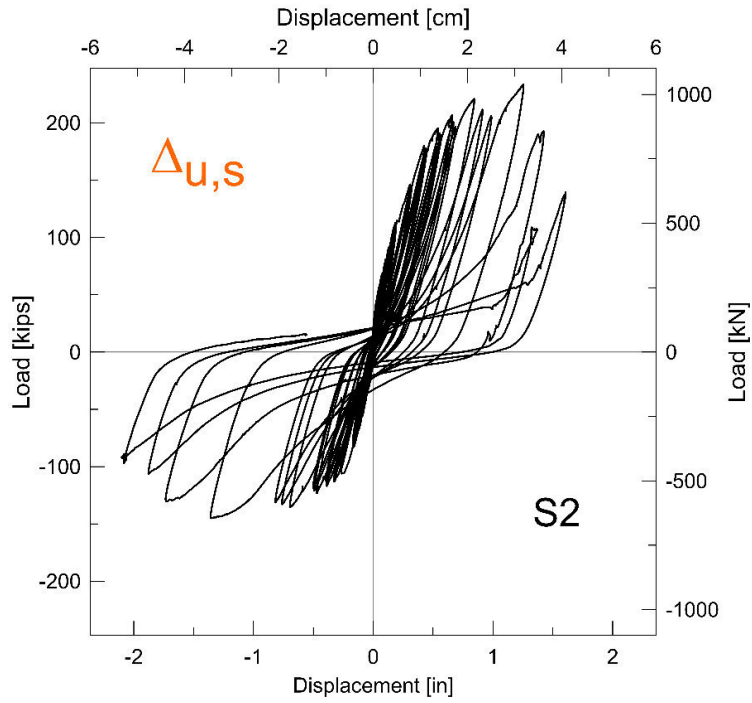


Figure 5.54: Load vs. shear displacement for specimen S2

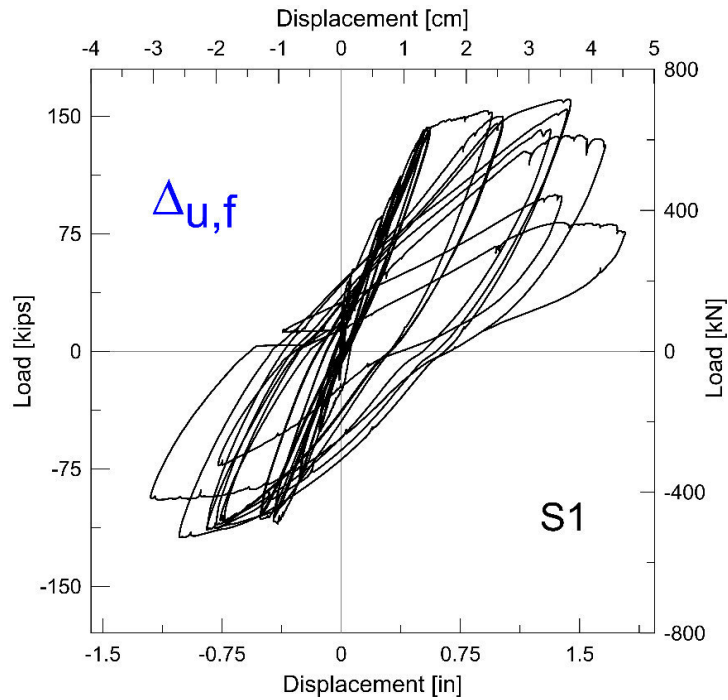


Figure 5.55: Load vs. flexural displacement for specimen S2

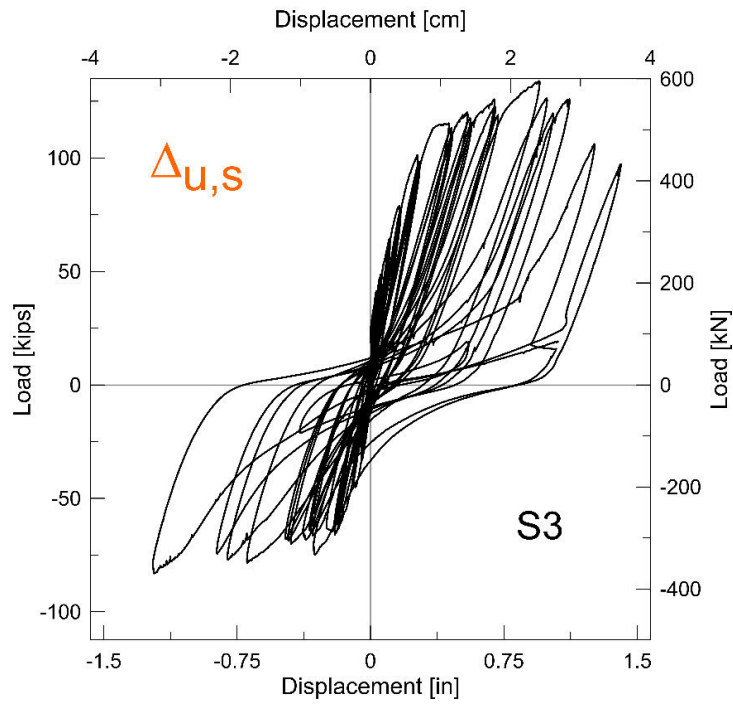


Figure 5.56: Load vs. shear displacement for specimen S3

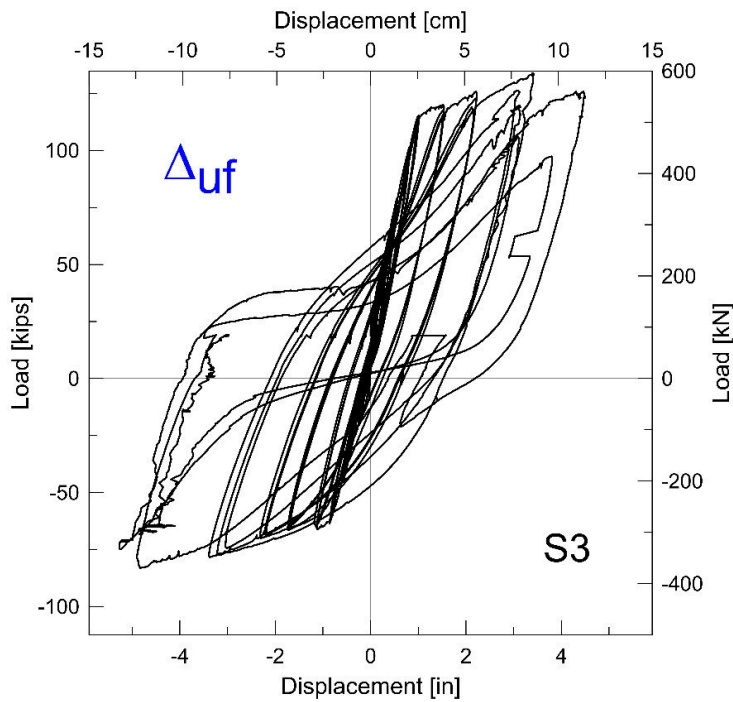


Figure 5.57: Load vs. flexural displacement for specimen S3

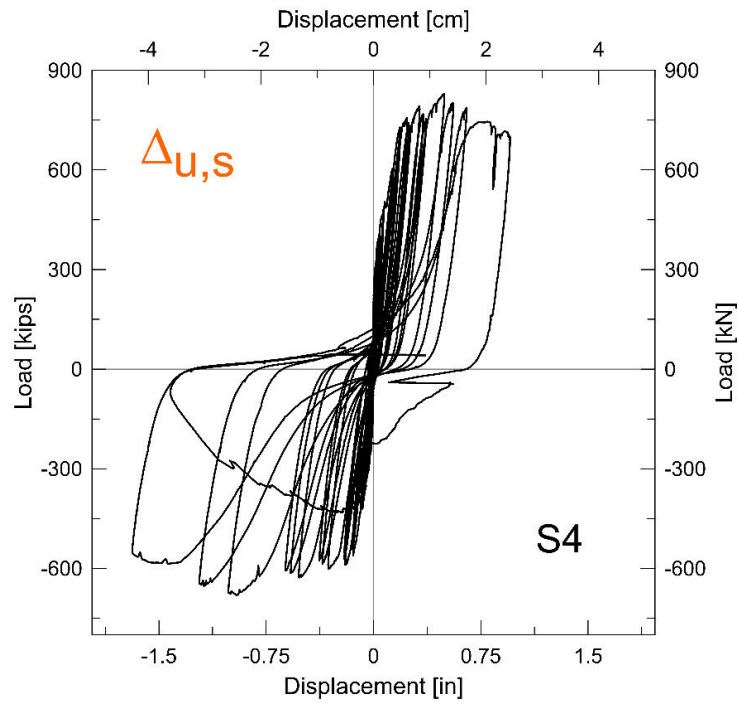


Figure 5.58: Load vs. shear displacement for specimen S4

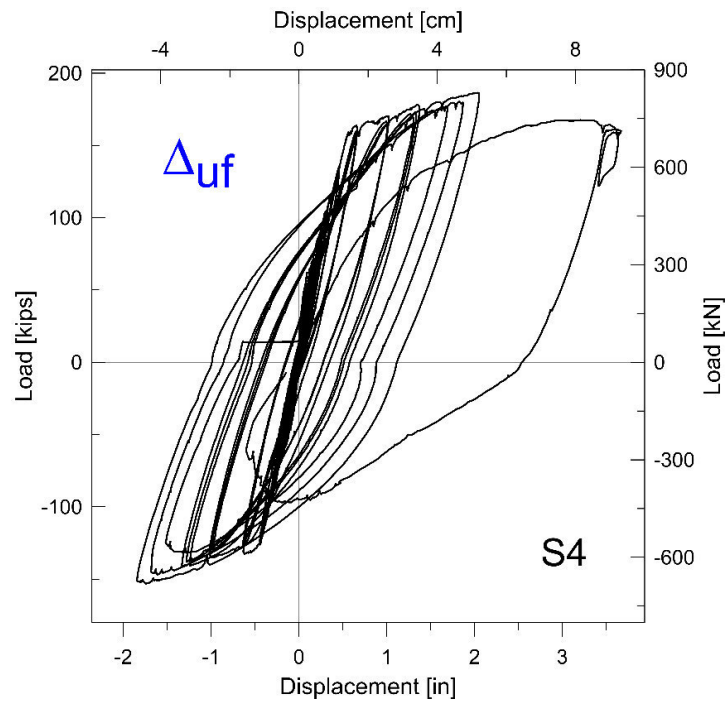


Figure 5.59: Load vs. flexural displacement for specimen S4

Table 5.3: Flexural, shear and bond slip displacement components

			S1				S2				S3				S4			
			down (+)		up (-)		down (+)		up (-)		down (+)		up (-)		down (+)		up (-)	
0.4% DRIFT	Δ_f	[in]/[%]	0.3	48%	-0.1	38%	0.3	47%	-0.3	52%	0.4	60%	-0.4	67%	0.3	54%	-0.3	59%
	Δ_s	[in]/[%]	0.2	28%	-0.1	25%	0.1	23%	-0.1	21%	0.1	16%	0.0	7%	0.0	9%	-0.1	13%
	Δ_{ext}	[in]/[%]	0.1	12%	0.0	12%	0.1	11%	-0.1	13%	0.1	8%	0.0	4%	0.1	12%	-0.1	15%
	Δ_{total}	[in]/[%]	0.5	100%	-0.3	100%	0.6	100%	-0.6	100%	0.7	100%	-0.6	100%	0.5	100%	-0.5	100%
1% DRIFT	Δ_f	[in]/[%]	0.6	41%	-0.5	38%	0.7	44%	-0.9	57%	1.0	54%	-1.1	60%	0.7	53%	-0.6	51%
	Δ_s	[in]/[%]	0.5	36%	-0.4	30%	0.4	28%	-0.3	21%	0.4	23%	-0.2	11%	0.2	15%	-0.2	16%
	Δ_{ext}	[in]/[%]	0.1	4%	0.0	2%	0.1	5%	-0.4	24%	0.1	4%	-0.1	4%	0.1	4%	0.0	4%
	Δ_{total}	[in]/[%]	1.4	100%	-1.3	100%	1.5	100%	-1.5	100%	1.9	100%	-1.9	100%	1.3	100%	-1.2	100%
1.5% DRIFT	Δ_f	[in]/[%]	0.9	47%	-0.8	42%	1.1	50%	-1.3	56%	1.5	55%	-1.7	62%	1.0	54%	-1.0	56%
	Δ_s	[in]/[%]	0.6	31%	-0.5	26%	0.5	24%	-0.4	17%	0.5	20%	-0.3	12%	0.2	12%	-0.3	17%
	Δ_{ext}	[in]/[%]	0.1	3%	-0.1	4%	-	-	-	-	0.1	2%	-0.1	3%	0.1	3%	-0.1	3%
	Δ_{total}	[in]/[%]	2.0	100%	-2.0	100%	2.3	100%	-2.3	100%	2.8	100%	-2.8	100%	1.9	100%	-1.8	100%
2% DRIFT	Δ_f	[in]/[%]	1.4	53%	-1.0	38%	1.5	51%	-1.7	55%	2.2	59%	-2.3	61%	1.4	54%	-1.3	53%
	Δ_s	[in]/[%]	0.8	30%	-0.8	29%	0.7	22%	-0.5	16%	0.7	18%	-0.4	12%	0.3	13%	-0.5	21%
	Δ_{ext}	[in]/[%]	0.1	2%	-0.1	4%	-	-	-	-	0.0	1%	-0.1	2%	-	-	-	-
	Δ_{total}	[in]/[%]	2.7	100%	-2.7	100%	3.0	100%	-3.0	100%	3.8	100%	-3.8	100%	2.5	100%	-2.5	100%
3% DRIFT	Δ_f	[in]/[%]	1.7	41%	-1.2	30%	2.4	54%	-2.5	55%	3.4	60%	-3.4	60%	2.1	55%	-1.8	49%
	Δ_s	[in]/[%]	2.2	53%	-1.9	47%	0.8	19%	-0.7	15%	1.0	17%	-0.7	12%	0.5	13%	-1.0	27%
	Δ_{ext}	[in]/[%]	0.0	1%	-0.1	2%	-	-	-	-	0.0	0%	-0.1	1%	-	-	-	-
	Δ_{total}	[in]/[%]	4.0	100%	-4.0	100%	4.5	100%	-4.5	100%	5.7	100%	-5.7	100%	3.8	100%	-3.7	100%
4.0-4.5% DR.	Δ_f	[in]/[%]	-	-	-	-	3.6	53%	-3.6	53%	4.5	60%	-4.9	64%	3.5	61%	-0.6	10%
	Δ_s	[in]/[%]	-	-	-	-	1.3	19%	-1.4	20%	1.1	15%	-1.2	16%	1.0	17%	-1.1	19%
	Δ_{ext}	[in]/[%]	0.0	1%	-0.1	1%	-	-	-	-	0.0	0%	0.0	0%	-	-	-	-
	Δ_{total}	[in]/[%]	6.1	100%	-6.0	100%	6.7	100%	-6.8	100%	7.4	100%	-7.6	100%	5.6	100%	-5.8	100%

5.9 Beam Axial Elongation

Plots of the axial elongation versus the applied beam rotation for all four beam specimens are provided in Figures 5.60-5.63. The plots were created using longitudinal LVDTs that spanned the length of the beam. Furthermore, they show the measured elongation along the centerline of the beam by taking the average of the sum of the displacements measured by the top longitudinal LVDTs and the sum of the measured displacements of the bottom longitudinal LVDTs. The plots were clipped at the time of which sensors were removed due to the initiation of plastic hinging. The axial growth mainly concentrated within approximately one member depth from the beam-column interface for all beam specimens. For S1, the opening region also contributed a large portion of the axial deformation which was not the case for the other beams with an opening. S2 and S3's axial growth concentrated around sections near the support similar to S4, the beam without an opening. The disproportionate amount of axial growth in the upward loading direction is attributed to the unsymmetrical reinforcement and geometry of the test specimens.

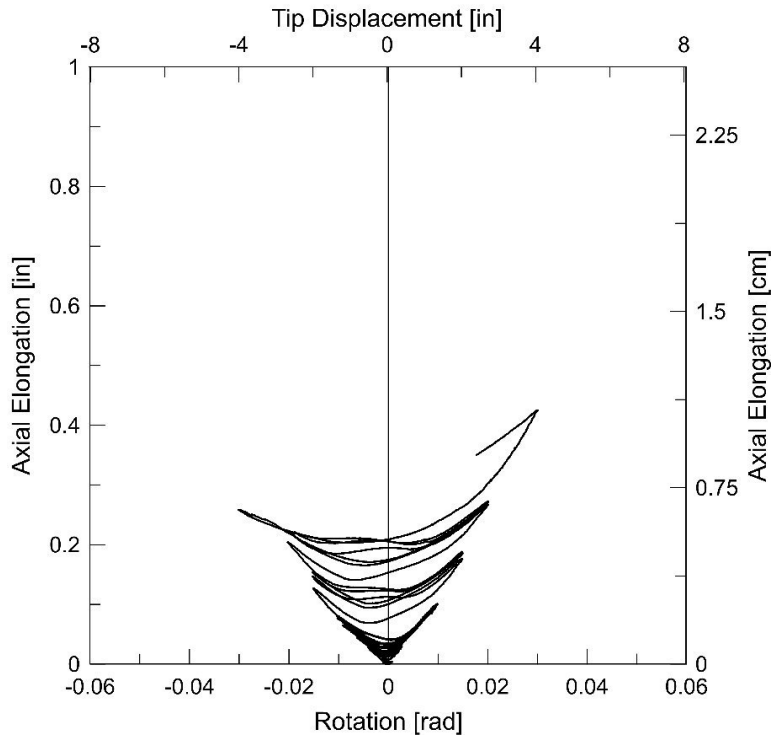


Figure 5.60: Axial deformation for S1

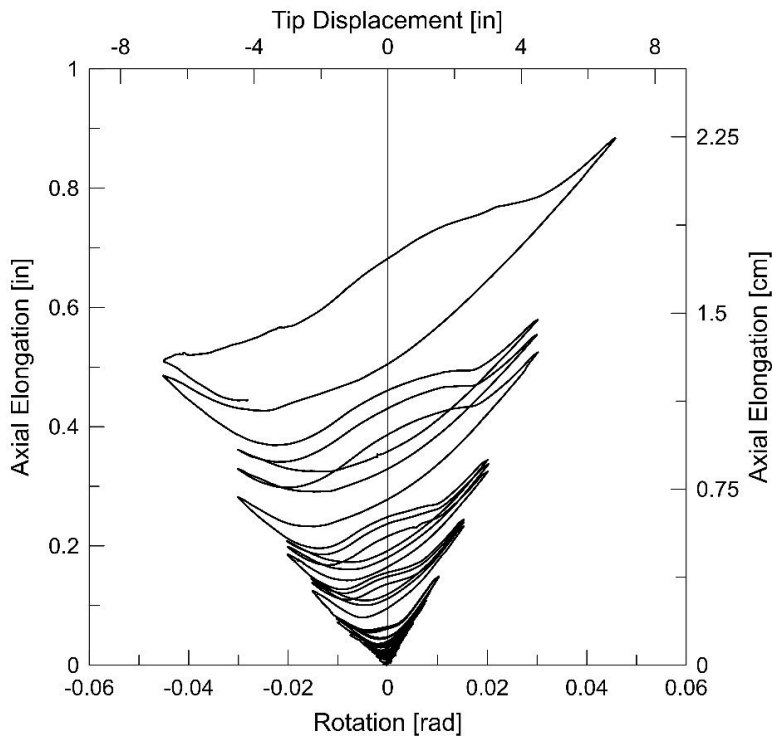


Figure 5.61: Axial deformation for S2

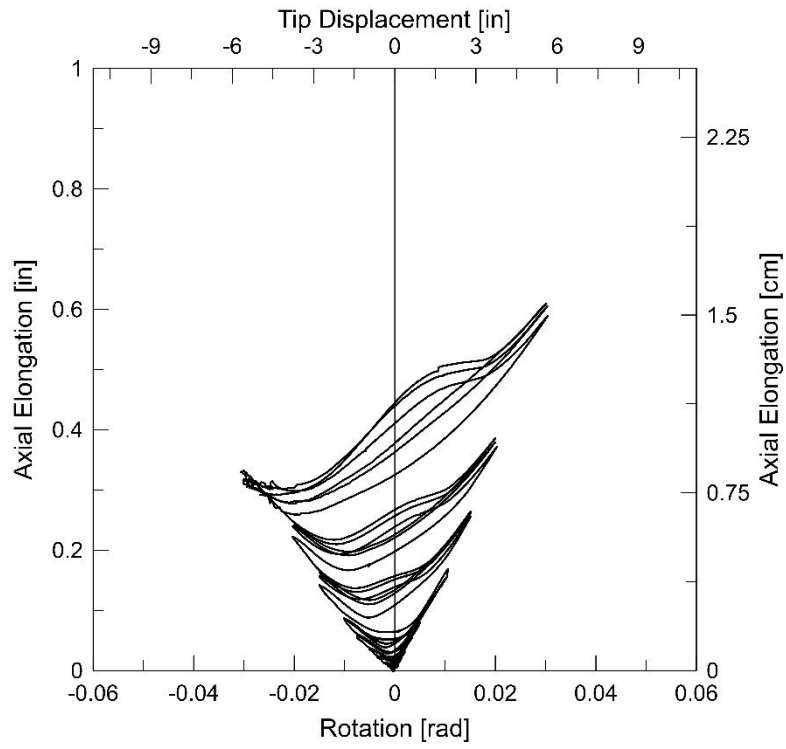


Figure 5.62: Axial deformation for S3

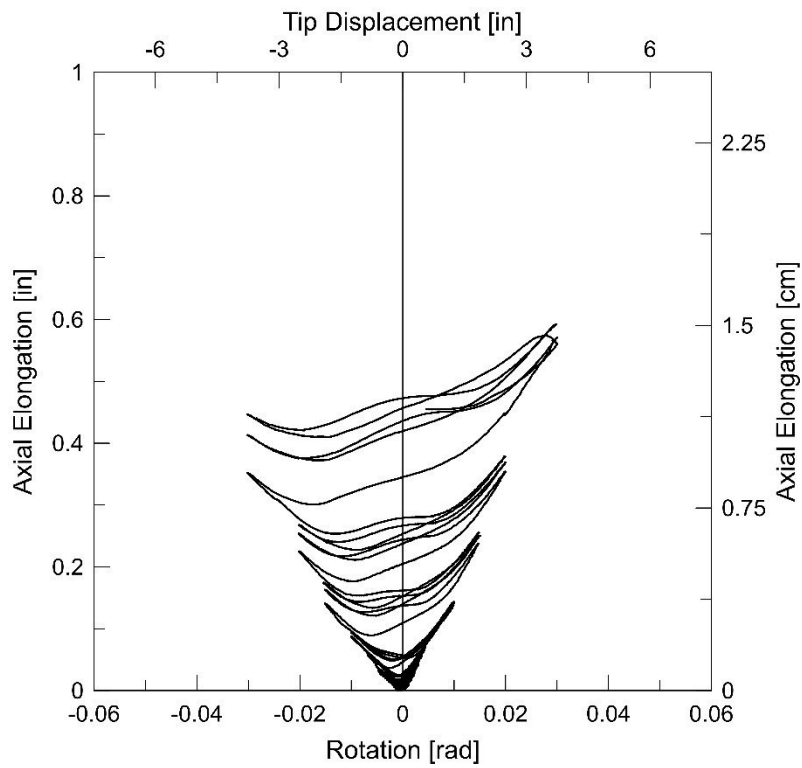


Figure 5.63: Axial deformation for S4

Chapter 6 Nonlinear Strut and Tie Modelling

A nonlinear strut and tie model was used to analyze the load-deformation behavior of the beam specimens. The method for calculating the effective strengths and areas is presented for both monotonic and cyclic analysis cases and follows the procedure proposed by To (2005). The development of the truss models is explained and the results of one monotonic and two cyclic truss models are compared to experimental results. Finally, a variation of the steel material is applied to the cyclic models to better capture the hysteretic response.

6.1 Strut and Tie Model Formulation

To (2005) outlines a model formulation for the truss elements used in both B- and D-regions, the appropriate positioning of the model elements, the stress-strain material models for concrete and reinforcing steel, the effective strength of the model elements, and the concrete tension carrying capacity associated with the tension stiffening effect. The model formulation is validated with various structural systems and their results are proven to give accurate results of the nonlinear behavior of the structure. It is important to emphasize that the primary objective of this STM formulation was to develop a procedure for a computer based STM that could be used by practicing engineers as a structural concrete analysis tool. The aim was not to capture the structural behavior at a microscopic level nor was it intended to predict all possible structural failures in detail.

6.1.1 Monotonic Model Formulation

To (2005) developed two modelling procedures using the nonlinear program Drain 2DX. The first model formulation is monotonic and used primarily to perform a push-over analysis. The second is a model formulation aimed at predicting the hysteretic response of a structural system. The monotonic procedure consists of six different model element types as illustrated in Figure 6.1.

- Type 1 element: represents flexural compression zones in B-regions
- Type 2 element: represents flexural tension zones in B-regions
- Type 3 element: represents diagonal concrete struts in B-regions
- Type 4 element: represents transverse reinforcement ties in B-regions
- Type 5 element: represents concrete mass in D-regions
- Type 6 element: represents rebar ties in D-regions

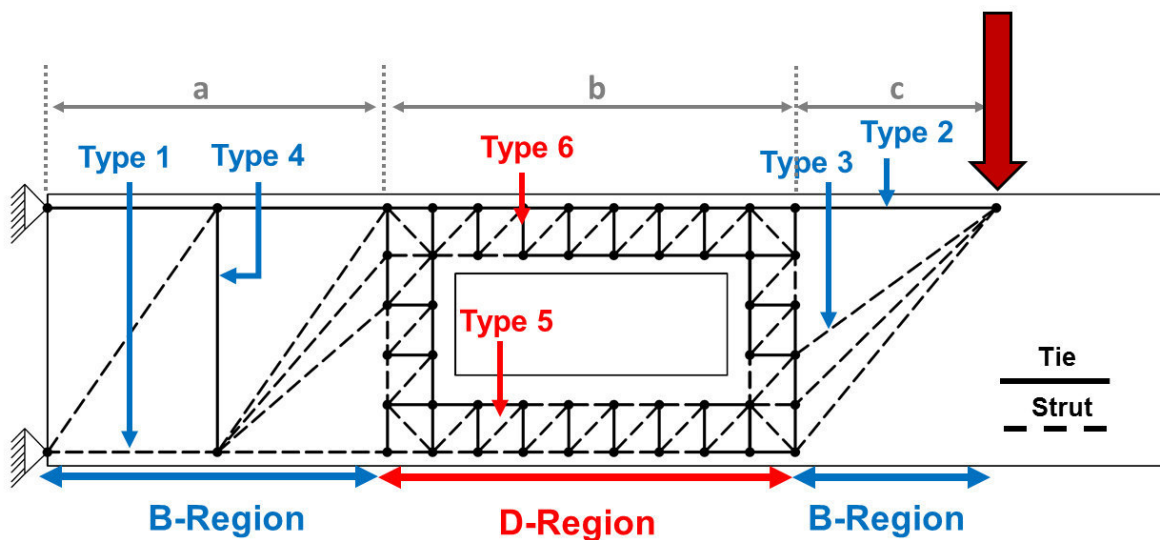


Figure 6.1: Discretization of B- and D-regions along with element types in monotonic STM

The Type 1 elements are located at the compression centroid and the Type 2 elements are located at the tension centroid which are measured at the serviceability limit states. These limit states are defined as rebar yielding or the extreme compression fiber reaching a compressive strain of 0.002, whichever occurs first. The position of Type 3 elements is dictated to ensure that the angle of the diagonal concrete struts and the member longitudinal axis is between $31^\circ \leq \theta \leq 59^\circ$ as recommended by CEB-FIP (1978). Type 5 and 6 elements were positioned at the centroids of the force paths developed at the ultimate limit states in D-regions.

6.1.1.1 Type 1 Element - Monotonic

The Type 1 element is composed of a concrete strut and a rebar strut arranged in parallel. For the concrete strut, a quad-linear curve replicating the curvilinear model of Kent and Park (1971) was used to represent the material stress-strain relationship (Figure 6.3). The ascending branch reaches its full strength at a strain of 0.002 for both confined and unconfined concrete and the slope of the descending branch is determined by the strain ε_{50} . ε_{50} represents the strain at which the material model losses 50% of its maximum compressive strength. Furthermore, the model assumes that concrete has a residual strength corresponding to 20% of its concrete cylinder strength (f'_c). ε_{50} is calculated in the following manner:

$$\varepsilon_{50} = \frac{3 + 0.2f'_c}{145 f'_c - 1000} + \frac{3}{4}p'' \sqrt{\frac{b_o}{s}} \quad (f'_c \text{ in MPa}) \quad (6.1)$$

$$p'' = \frac{2(b_o + D_o)A_{vs}}{b_o D_o s} \quad (6.2)$$

Where ε_{50} is the strain value at $0.5f_d$, p'' is the volumetric ratio of transverse reinforcement, s is the spacing between transverse reinforcement, b_o is the width of the concrete core, and D_o is the depth of the concrete core (Figure 6.2). The elastic modulus of concrete is also utilized to define the ascending branch of the curve and this is taken as:

$$E_c = 9500(f'_c + 8)^{1/3} \text{ (MPa)} \quad (6.3)$$

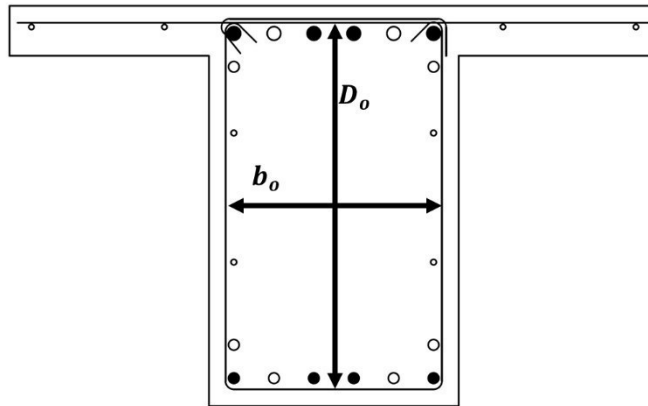


Figure 6.2: Width and depth of concrete core

The effective area for a concrete strut in a Type 1 element is defined as the area between the neutral axis depth and the width of the section. The effective compressive strength is computed using maximum compressive force, $C_{c(\max)}$, and the effective area of the concrete strut:

$$A_{cs} = c \cdot b_w \text{ for rectangular sections} \quad (6.4)$$

$$f_d = \frac{C_{c(\max)}}{A_{cs}} \quad (6.5)$$

The effective area and strength of the rebar strut in a Type 1 element is defined as:

$$A_{rs} = A'_s \quad (6.6)$$

$$f_{cy} = f_y \quad (6.7)$$

Where A'_s is the main flexural compression reinforcement and f_y is the yield strength of the reinforcement. The stress-strain behavior of the reinforcement steel struts was characterized by using a bilinear curve shown in Figure 6.3. A strain hardening of 5% was utilized in B-regions and 2.5% in D-regions.

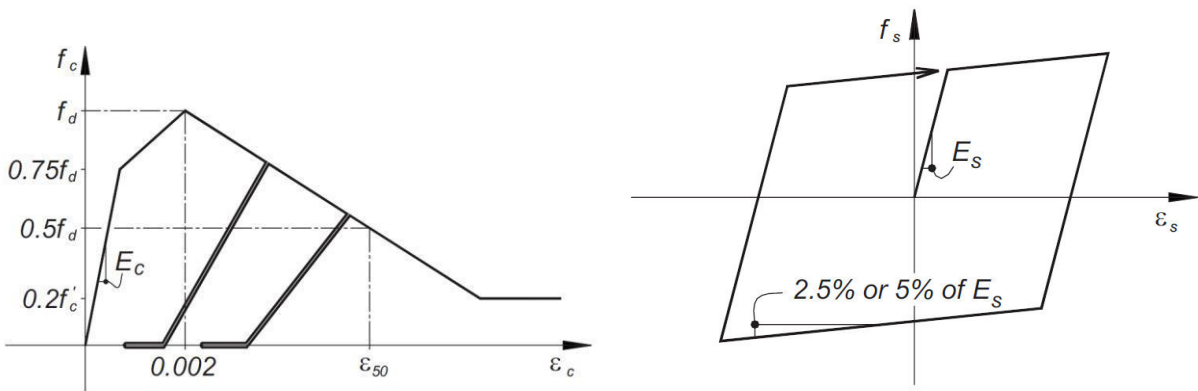


Figure 6.3: Stress-Strain relationship for concrete (left) and steel (right) [To (2005)]

6.1.1.2 Type 2 Element - Monotonic

The Type 2 element is composed of a concrete tie and a rebar tie arranged in parallel. For the concrete ties, a trilinear curve was used to represent the material response. The ascending branch is defined using the elastic modulus of concrete defined previously. The descending branch and the residual tensile strength was defined using Prakhya and Morley (1990) tension stiffening model. For the reinforcement, the tension branch of the bilinear curve described previously was

used using the same elastic modulus and strain hardening ratio. The effective area of a concrete tie is defined as follows

$$A_{ct} = \frac{A_g - A_{cs}}{2} \quad (6.8)$$

According to To (2005), this equation was utilized due to its satisfactory comparisons with the experimentally recorded un-cracked member stiffness. For the effective strength of concrete, a procedure first proposed by Somayaji and Shah (1981) and later modified by Chan et al. (1992) was adopted. For the cases where there is no solution to the algorithm described previously, the effective tensile strength is then evaluated by dividing the total concrete tension force by the concrete tie area, A_{ct} :

$$f_{dt} = \frac{D_r \cdot b_w \cdot f'_t}{4 \cdot A_{ct}} \quad (6.9)$$

$$f'_t = 0.6\sqrt{f'_c} \text{ [NZS 3101 (1995)]} \quad (6.10)$$

The effective area and strength for the rebar tension ties are defined as

$$A_{rt} = A_s \quad (6.11)$$

$$f_{sy} = f_y \quad (6.12)$$

6.1.1.3 Type 3 Element - Monotonic

The Type 3 element is comprised of diagonal concrete struts representing the diagonal concrete mass located in beams and columns. The concrete stress-strain curve of Figure 6.3 is used to describe Type 3 elements. The effective area and strengths are as follows:

$$A_{cs} = h_p \cdot b_o \quad (6.13)$$

Where h_p is the perpendicular distance between the diagonal strut members and:

$$f_d = v f'_c \quad (6.14)$$

$$v = 0.7 - \frac{f'_c}{200} \geq 0.5 \text{ (} f'_c \text{ in MPa)} \quad (6.15)$$

This equation was proposed by Nielsen et al. (1978) and is also recommended by the Eurocode (1992)

6.1.1.4 Type 4 Element - Monotonic

The Type 4 element consists of transverse rebar ties aimed to replicate the transverse reinforcement in beams and columns. The material response of Type 4 element is represented by the tension branch of the bilinear curve of Figure 6.3. The effective strength is calculated as follows:

$$f_{vy} = f_y \quad (6.16)$$

The effective area:

$$A_v = \frac{V_n}{f_{vy}} \quad (6.17)$$

$$V_n = V_s + V_c + V_p \quad (6.18)$$

Where V_s is the shear strength contribution of the transverse reinforcement, V_c is the shear strength contribution of the concrete, and V_p is the force component in the direction of applied shear arising from the prestressing or externally applied action. For the shear strength of the reinforcement the following equation was utilized which takes into consideration the angle of the concrete struts, θ

$$V_s = \frac{d_v}{s \tan \theta} A_{vs} f_{vy} \quad (6.19)$$

Where A_{vs} is the total area of transverse reinforcement in a layer in the direction of the shear force and d_v is the effective section depth. For the concrete contribution, the modified compression field theory by Vecchio and Collins (1986) was used. The concrete shear strength is calculated as:

$$V_c = \beta \sqrt{f'_c} A_{ve} \quad (6.20)$$

$$\beta = \frac{0.33 \cot \theta}{1 + \sqrt{500 \varepsilon_1}} \leq \frac{0.18}{0.3 + \left[\frac{7200 \varepsilon_1}{35} \right]} \quad (6.21)$$

$$\varepsilon_1 = \varepsilon_s + \left[\varepsilon_s + 0.002 \left(1 - \sqrt{1 - \nu (\tan \theta + \cot \theta (0.8 + 170 \varepsilon_1))} \right) \right] \cot \theta^2 \quad (6.22)$$

$$\nu = \frac{V_s + V_c - V_p}{A_{ve} f'_c} \quad (6.23)$$

$$A_{ve} = 0.8 A_g \quad (6.24)$$

Where A_{ve} is the effective shear area, ε_1 is the average principal tensile strain in diagonal concrete, and v is the total shear stress resisted by concrete and transverse reinforcement. A trial and error computation procedure was described in To (2005). The reinforcement tensile strain was taken to be 0.002.

6.1.1.5 Type 5 Element - Monotonic

The model Type 5 element is composed of a concrete strut representing the compressed concrete mass in D-regions. The material behavior is depicted using the quad-linear curve in Figure 6.3. The effective area was calculated by multiplying the effective strut depth parallel to the plane of the model layout by the strut width orthogonal to the plane of the model layout. The strut width was measured by the average distance between adjacent concrete struts. The effective depth was taken as the concrete core width, which was assessed as $0.8 b_w$ where b_w is the total width of the structural component. The effective strength is taken as

$$f_d = \phi_e f'_c \quad (6.25)$$

Where ϕ_e is a strength efficiency factor. A value of 0.51 was recommended by To (2005).

6.1.1.6 Type 6 Element - Monotonic

The Type 6 Element is composed of rebar ties meant to model the reinforcement in D-regions. The tension branch of the bilinear curve shown in Figure 6.3 is used to describe the material

characteristics. A strain hardening ratio of 2.5% was utilized. The actual rebar area and material yield strength were also used as the effective area and effective yield strength.

6.1.2 Cyclic Model Formulation

The STM formulation used to capture the hysteretic response due to cyclic loading is described in this section. The model element types in the cyclic formulation are:

- Type 1 element: represents the concrete struts in the flexural zone in B-regions
- Type 2 element: represents the diagonal concrete struts in B-regions
- Type 3 element: represents transverse reinforcement ties in B-regions
- Type 4 element: represents concrete struts in D-regions
- Type 5 element: represents reinforcing ties in D-regions

6.1.2.1 Type 1 Element - Cyclic

The material characteristics of the Type 1 element were derived using the work conducted by Tjokrodimuljo (1985) who tested 17 RC prisms under reversed cyclic axial loads to investigate the hysteretic response of concrete and reinforcement in the flexural zone of beams and columns. Using the experimental results of Tjokrodimuljo (1985), To (2005) suggested the use of a uniaxial fiber model that consists of 3 elements arranged in parallel: a concrete strut, a concrete tie, and a rebar strut-tie. It was important to capture both the contact stress effect and the tension stiffening in the tie reinforcement observed in these results. Therefore, a concrete tie with an elastic-perfectly plastic material stress-strain relationship was implemented (Figure 6.4). The cyclic response of

the concrete strut was replicated using the Kent and Park (1971) model and the bilinear elasto-plastic curve for steel was used with a recommended strain hardening ratio of 5% (Figure 6.3). The effective area of the concrete strut was identical to the concrete strut used in the monotonic case and the effective area was calculated as follows:

$$f_d = 0.85 \frac{C_{c(\max)}}{A_{cs}} \quad (6.26)$$

The effective area of the concrete tie is the same as the concrete strut and the effective strength representing the contact stress and the tension stiffening is computed as:

$$f_{cont} = 0.05 f_d \quad (6.27)$$

$$f_{ts} = 0.5 f_{dt} \quad (6.28)$$

Where f_{dt} is the effective tensile strength of the concrete. The effective area and effective strength of the rebar strut-tie representing the flexural reinforcement are calculated as follows:

$$A_{s-t} = \phi_r A_s \quad (6.29)$$

$$f_{s-t} = f_y \quad (6.30)$$

Where $\phi_r = 0.75$, based on satisfactory comparisons between analysis results and experimental data

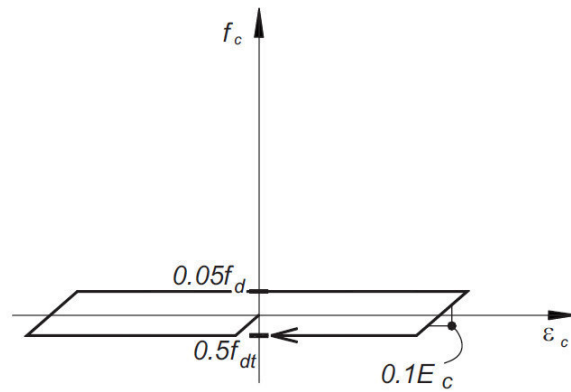


Figure 6.4: Stress-strain curve for a concrete tie [To (2005)]

6.1.2.2 Type 2 Element - Cyclic

The Type 2 Element was intended to represent the diagonal mass of concrete in beams and it is composed of a concrete strut and a concrete tie. The inclined angle of the diagonal concrete struts was taken as $31^\circ \leq \theta \leq 59^\circ$ in accordance with CEB-FIB (1978). The effective area of the concrete strut is identical to that of the monotonic case and the effective strength was:

$$f_d = 0.85v f'_c \quad (6.31)$$

$$v = 0.7 - \frac{f'_c}{200} \geq 0.5 \text{ (} f'_c \text{ in MPa)} \quad (6.32)$$

6.1.2.3 Type 3 Element - Cyclic

The Type 3 element is composed of a rebar tie representing the transverse reinforcement in beams and columns. The bilinear stress-strain curve of Figure 6.3 was used to describe Type 3 elements. The effective area and strength are identical to that of the monotonic case.

6.1.2.4 Type 4 Element - Cyclic

The Type 4 element was used to represent the mobilized mass of concrete in structural D-regions and is composed of a concrete strut and a concrete tie. The computation of the effective area and strength of the concrete strut is identical to that of the monotonic case. The parameters of the concrete tie in this element are the same as in the previously discussed elements.

6.1.2.5 Type 5 Element- Cyclic

The Type 5 element consists of a rebar tie to represent the reinforcement in structural D-regions. The same stress-strain relationship from Figure 6.3 is used in Type 5 elements. The actual reinforcement area and yield strength are adopted as the effective area and effective strength of the rebar tie.

6.2 Monotonic STM Results

The monotonic STM formulation described in the previous section was applied to all specimens to assess how well the model could predict the cyclic envelope. The first step in creating an STM was to determine the flow of forces that will translate to axial compressive strut and axial tension tie members. The literature review conducted on STMs aided in understanding how to both formulate a truss model and how the opening affected the force path of the beam specimens. Wight and MacGregor (2012) state that the crack pattern from the test specimens can aid in formulating an STM and the layout of the ties should correspond to a practical reinforcement layout. Therefore, the cracking patterns recorded during testing aided in formulating the truss models. Furthermore,

Figure 6.5 shows how an opening affects the force path for a beam according to Muttoni et al. (1996) who also state that the main concern with the introduction of an opening is the transmission of the shear force. Figure 6.5 shows two cases where the shear force is transferred by the compression chord (left) or the tension chord (right).

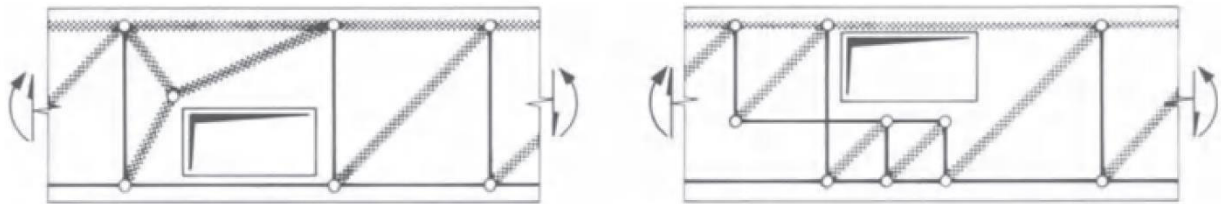


Figure 6.5: Resultant forces in openings [Muttoni et al. (1996)]

Additionally, Cook and Mitchell (1988) created an STM to design a uniformly loaded T-beam with an opening. The opening was located close to the support and placed just under the flange of the beam. The effect of the opening to the flow of forces in the beam is shown in Figure 6.6 where the uniform field of diagonal compression is interrupted and leads to high shear stress in the section. The higher shear stress dictates a necessity to increase the number of stirrups in opening region. A vertical tension tie is provided to lift the shear force to the top of the beam to make use of the full depth of the section beyond the opening (i.e. near the support). Finally, the lifted force is taken to the support by the means of a diagonal compression strut. The STM design was compared with an experimental test. The crack pattern on the bottom chord confirmed the steeper inclination compression field due to the high shear stress. Mansur and Tan (1999) also provided an example of an STM for a simply supported beam with a large rectangular opening with point loads shown in Figure 6.7. Using these example STMs as reference initial monotonic STMs were developed. The STMs are shown in Figures 6.10-6.12 were intended to capture the general flow

of forces from the previously mentioned STM examples. The results are shown in Figure 6.13 and these STMs produced unfavorable results in which the strength and stiffness was greatly underestimated.

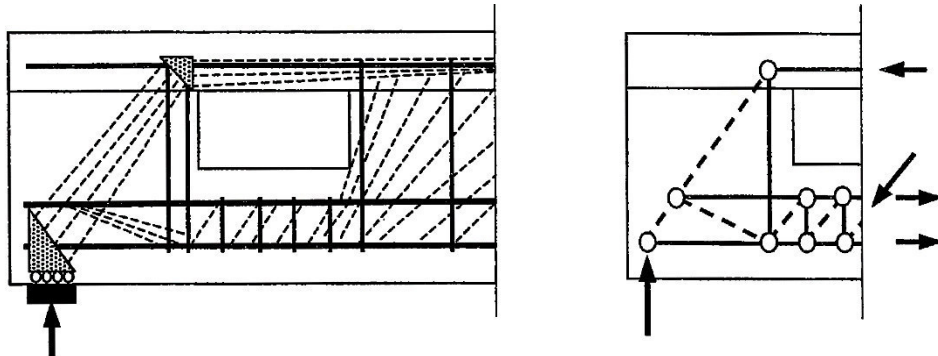


Figure 6.6: STM for a T-beam with an opening [Cook and Mitchell (1988)]

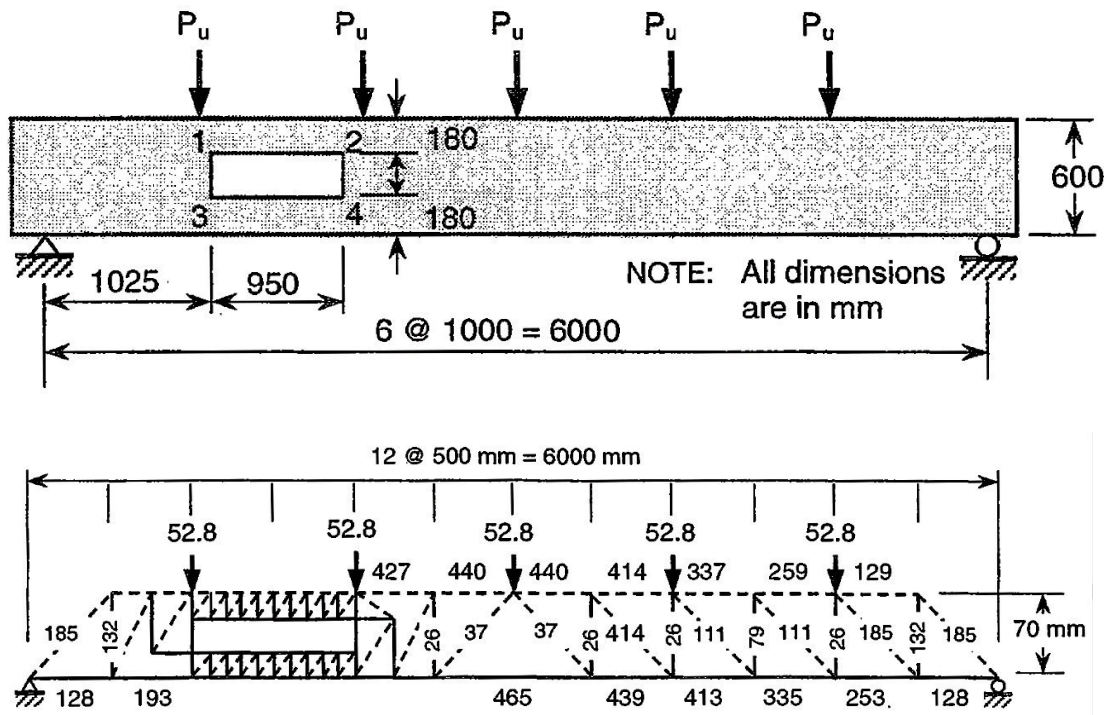
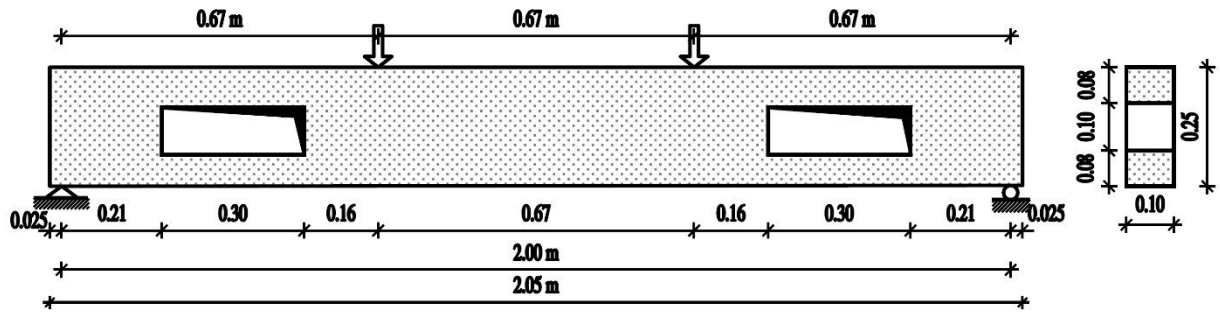


Figure 6.7: STM formulation for a simply supported beam with an opening and point loads [Mansur and Tan (1999)]

Figure 6.8 shows the STM formulated by El-Dermerdash et al. (2014) which incorporates a small truss around the opening. Utilizing this proposed force path for a beam with an opening an STM was developed that yielded appropriate results. The STMs for each beam specimen is presented in Figures 6.14-6.17 where the struts are represented with dashed lines and the ties are represented with solid lines. The area and reinforcement of the flanges of the slab were disregarded and only a rectangular section of 38.4 in. high and 24 in. width was considered. The beams were subdivided in the same manner described in Chapter 3 with three sections, “*a*”, “*b*”, and “*c*” (Figure 6.1). The opening section, *b*, was considered to be a D-region where Type 5 and 6 elements were utilized. Type 1-4 elements were utilized in sections *a* and *c*. S4 was modeled entirely as a B-region and only Type 1-4 elements were used. The effective strengths and areas of the strut and tie members used in the STMs are provided in Tables 6.1-6.4. The computer program *OpenSees* was used to perform the pushover analysis. The material model used for the concrete elements was *Concrete02*. *Steel01* was used to represent the steel elements. As shown in Figure 6.9, *Steel01* is a bilinear curve that requires as inputs the yield strength, initial elastic stiffness, and the strain hardening ratio. For *Concrete02*, the required inputs are the compressive strength, crushing strength, the ratio between unloading slope at the crushing strain, the tensile strength, and the tension softening stiffness.



(a) Concrete dimensions and location of opening.

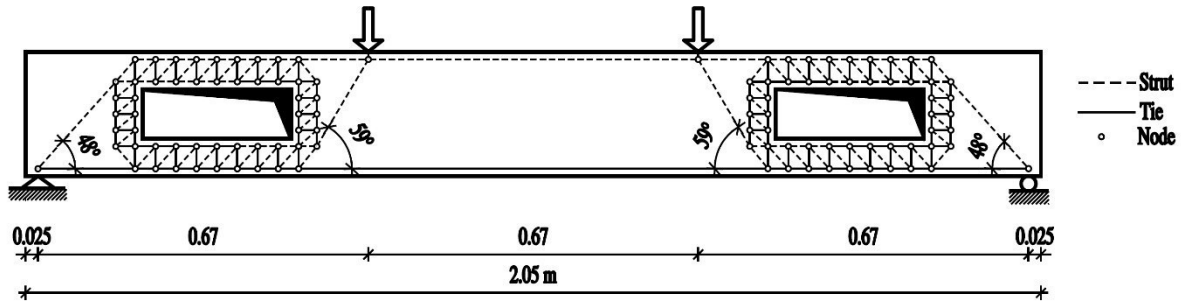


Figure 6.8: STM of a simply supported beam with two opening [El-Dermerdash et al. (2014)]

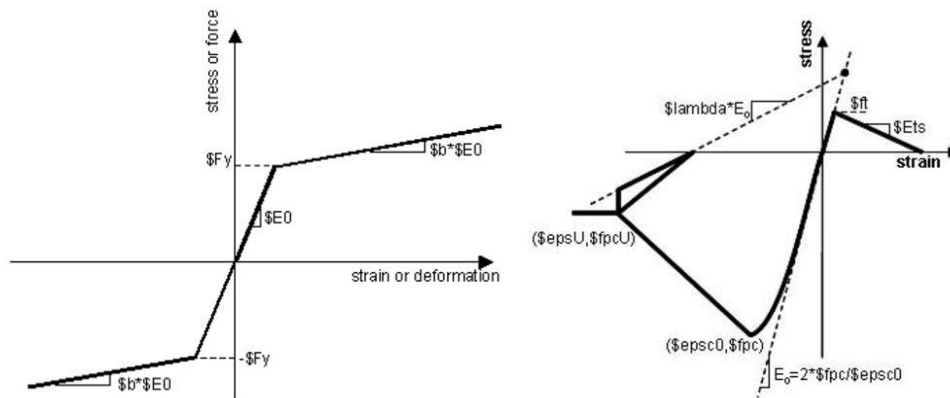


Figure 6.9: Stress-strain relationship for Steel01 (left) and Concrete02 (right)

The monotonic analytical results for all beam specimens are provided in Figures 6.18-6.21. The monotonic response envelope for S1 demonstrates satisfactory agreement with the initial stiffness and yield strength. In the downward loading direction, the predicted yield strength was 5.2% lower

than actual yield force. In the upward loading direction, the predicted yield strength was 1.6% lower than the actual yield force. The model failed to predict the ultimate strength of the beam specimen due to the material models used. The steel elements representing the top and bottom longitudinal reinforcement and the transverse reinforcement at the mid-section of the opening yielded initially. Subsequently, the longitudinal reinforcement at the support yielded. These results agree with the strain gauge data from the test.

The results for S2 indicated that the yield strengths and initial stiffness were not in good agreement but did capture the general behavior post-yield in the upward loading direction. The predicted yield strength in downward loading direction was 11.4% less than actual yield strength. The predicted yield strength in the upward loading direction was 20.4% greater than the actual yield strength. The top and bottom longitudinal reinforcement and the transverse reinforcement at the opening were the elements that yielded and dictated the beam's overall yield strength. No elements at the opening reached their respective yield strengths which contradicts the strain gauge data.

The results from the monotonic analysis of S3 demonstrate good agreement with the initial stiffness and yield strengths in both loading directions. The post-peak stiffness in the downward loading direction was also captured satisfactorily. The predicted yield strength in the downward loading direction was 6% greater than that of the actual yield strength. Furthermore, the analytical yield strength of the upward loading direction was 23.3% greater than that of the actual yield strength. The analytical yielding strength was dictated predominately by the yielding of the top and bottom longitudinal reinforcement and the transverse reinforcement at the opening. Yielding also occurred at the longitudinal reinforcement at the support. The strain gauge reading from the

experiment indicate that no yielding of the transverse reinforcement occurred and yielding only occurred in the longitudinal reinforcement.

The analytical STM results for S4 show that the initial stiffness is in good agreement with the experimental results. The predicted yield point in upward loading direction was 0.21% greater than the experimental yield point. Furthermore, the analytical yield point in the downward loading position was 21.6% lower than the experimental yield point. The longitudinal reinforcement near the support and all the vertical ties were shown to yield in the STM results. The strain gauges on the longitudinal reinforcement are consistent with the areas of yielding from the STM.

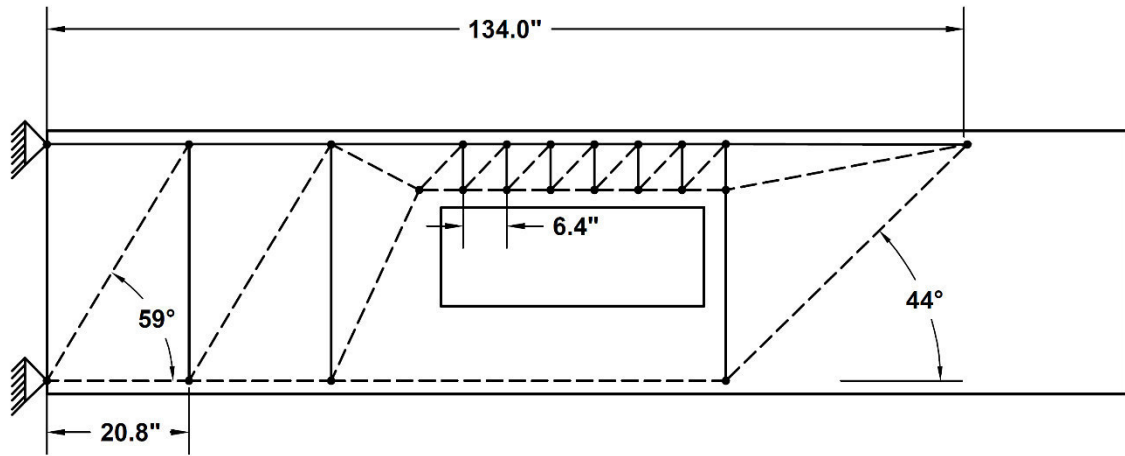


Figure 6.10: Monotonic STM for S1 trial 1

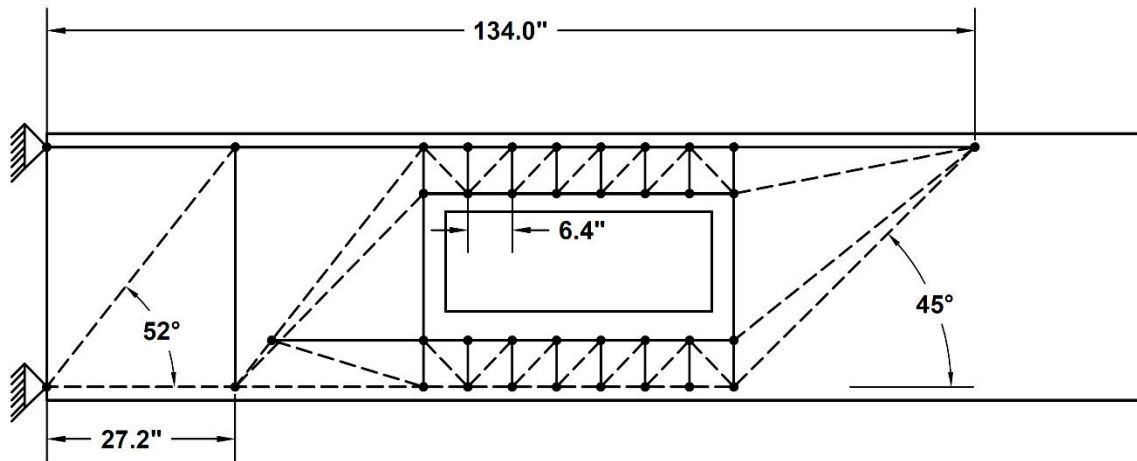


Figure 6.11: Monotonic STM for S1 trail 2

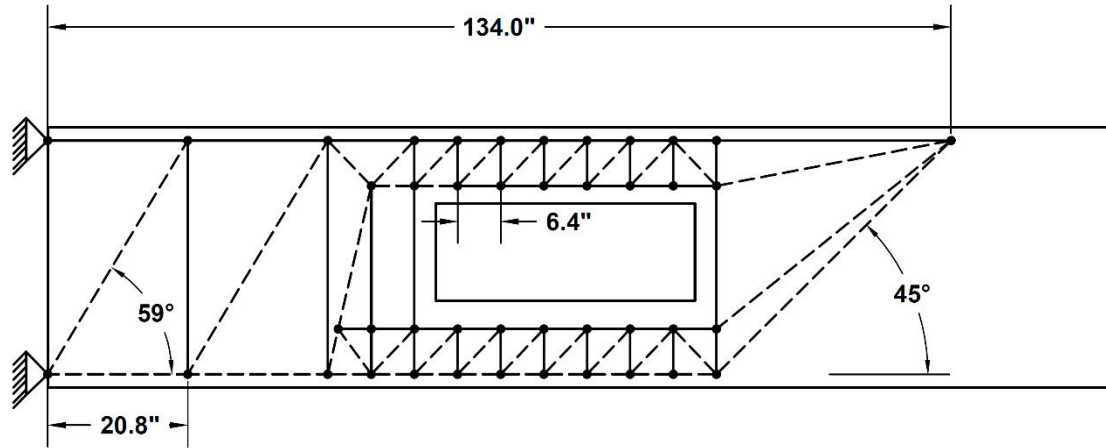


Figure 6.12: Monotonic STM for S1 trail 3

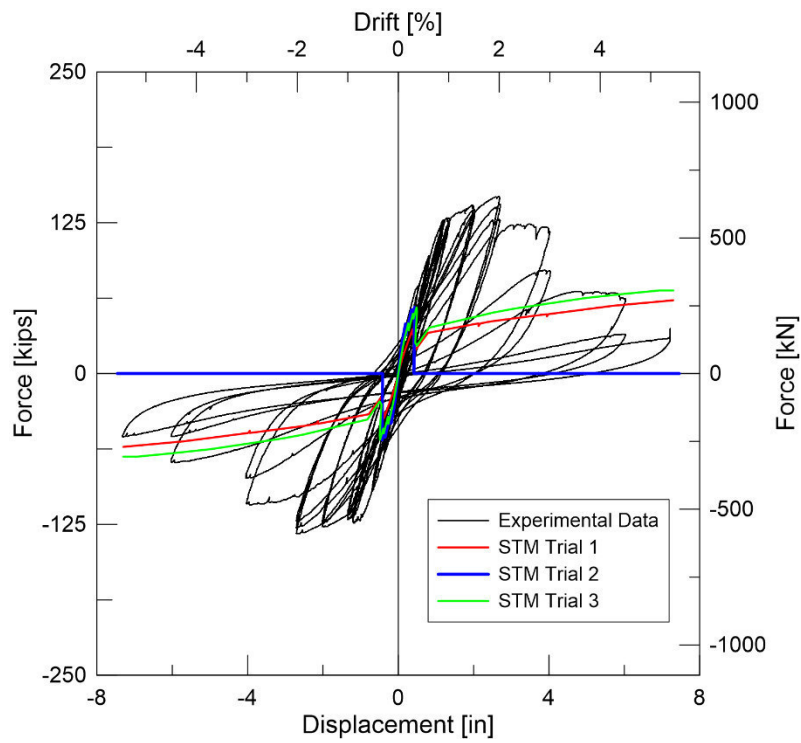


Figure 6.13: Monotonic analytical results for S1 trials 1-3

Table 6.1: Monotonic STM properties for S1

Model Elements	S1					
	A (Bm.-Col. Joint/B-Region)		B (Opening/D-Region)		C (Bm. End/B-Region)	
	Area [in ²]	Strength [ksi]	Area [in ²]	Strength [ksi]	Area [in ²]	Strength [ksi]
Type 1-Concrete Struts	99.3	$0.56f'_c$	-	-	-	-
Type 1-Rebar Struts	6.0	f_y	-	-	-	-
Type 2-Concrete Ties	503.3	$0.46f'_t$	-	-	489.5	$0.5f'_t$
Type 2-Rebar Ties	7.2	f_y	-	-	9.2	f_y
Type 3-Concrete Struts	410.0	$0.5f'_c$	-	-	510.0	$0.5f'_c$
Type 4-Rebar Ties	2.4	f_y	-	-	3.75	f_y
Type 5-Concrete Struts	-	-	122.9	$0.51f_c$	-	-
Type 6-Rebar Ties	-	-	A_s	f_y	-	-

Table 6.2: Monotonic STM properties for S2

Model Elements	S2					
	A (Bm.-Col. Joint/B-Region)		B (Opening/D-Region)		C (Bm. End/B-Region)	
	Area [in ²]	Strength [ksi]	Area [in ²]	Strength [ksi]	Area [in ²]	Strength [ksi]
Type 1-Concrete Struts	167.6	$0.57f'_c$	-	-	-	-
Type 1-Rebar Struts	6.3	f_y	-	-	-	-
Type 2-Concrete Ties	469.2	$0.49f'_t$	-	-	469.2	$0.49f'_t$
Type 2-Rebar Ties	12.0	f_y	-	-	12.0	f_y
Type 3-Concrete Struts	478.6	$0.5f'_c$	-	-	462.1	$0.5f'_c$
Type 4-Rebar Ties	5.3	f_y	-	-	7.12	f_y
Type 5-Concrete Struts	-	-	122.9	$0.51f_c$	-	-
Type 6-Rebar Ties	-	-	A_s	f_y	-	-

Table 6.3: Monotonic STM properties for S3

Model Elements	S3					
	A (Bm.-Col. Joint/B-Region)		B (Opening/D-Region)		C (Bm. End/B-Region)	
	Area [in ²]	Strength [ksi]	Area [in ²]	Strength [ksi]	Area [in ²]	Strength [ksi]
Type 1-Concrete Struts	109.5	$0.56f'_c$	-	-	82.14	$0.56f'_c$
Type 1-Rebar Struts	4.7	f_y	-	-	3.2	f_y
Type 2-Concrete Ties	498.2	$0.49f'_t$	-	-	511.9	$0.45f'_t$
Type 2-Rebar Ties	8.0	f_y	-	-	6.0	f_y
Type 3-Concrete Struts	460.2	$0.5f'_c$	-	-	513.2	$0.5f'_c$
Type 4-Rebar Ties	2.58	f_y	-	-	1.83	f_y
Type 5-Concrete Struts	-	-	122.9	$0.51f_c$	-	-
Type 6-Rebar Ties	-	-	A_s	f_y	-	-

Table 6.4: Monotonic STM properties for S1

S4		
Model Elements	Area [in ²]	Strength [ksi]
Type 1-Concrete Struts	109.7	$0.59f'_c$
Type 1-Rebar Struts	6.32	f_y
Type 2-Concrete Ties	410.0	$0.61f'_t$
Type 2-Rebar Ties	7.58/3.16	f_y
Type 3-Concrete Struts	439.3	$0.5f'_c$
Type 4-Rebar Ties	2.87/2.14	f_y

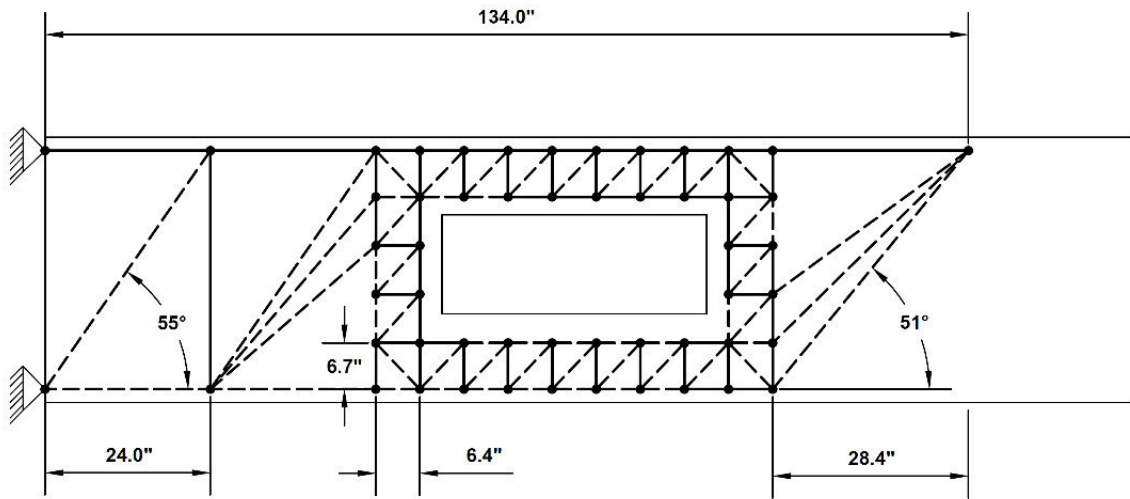


Figure 6.14: Monotonic STM for S1

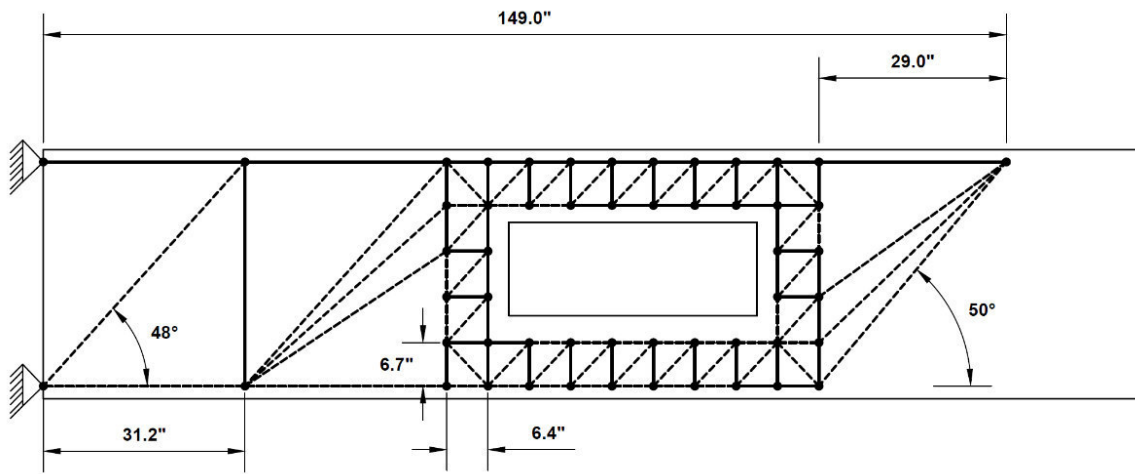


Figure 6.15: Monotonic STM for S2

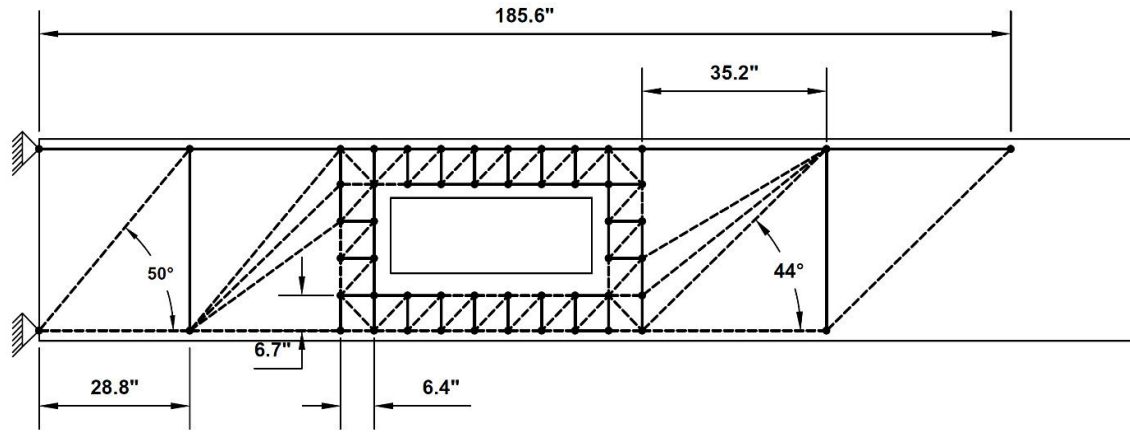


Figure 6.16: Monotonic STM for S3

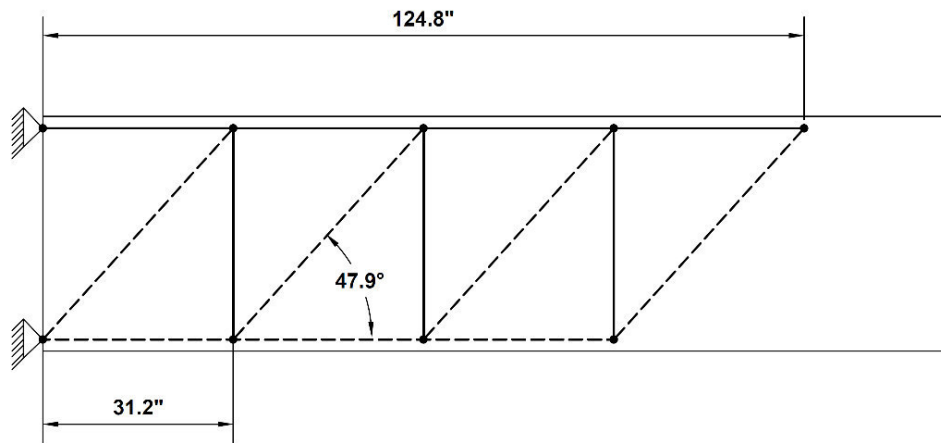


Figure 6.17: Monotonic STM for S4

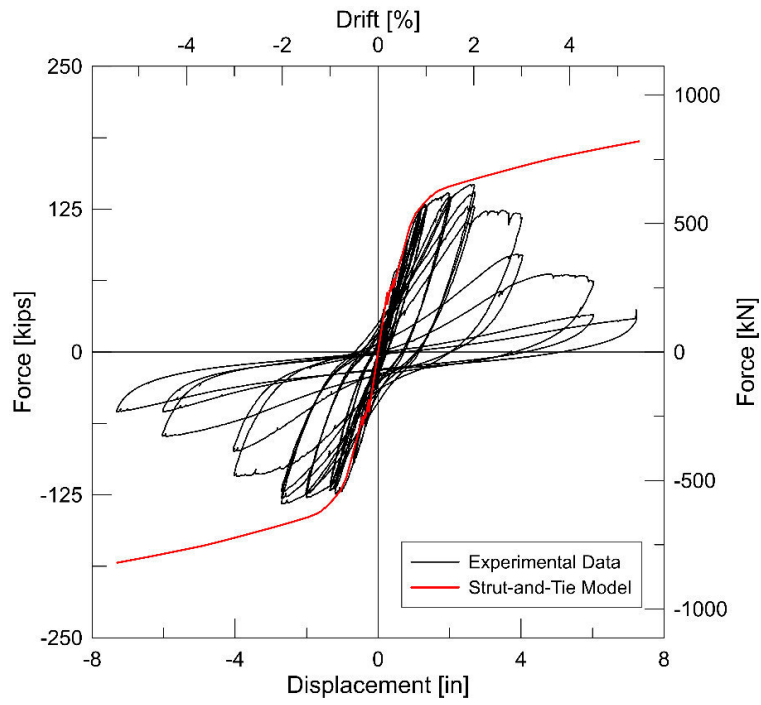


Figure 6.18: Monotonic analytical results for S1

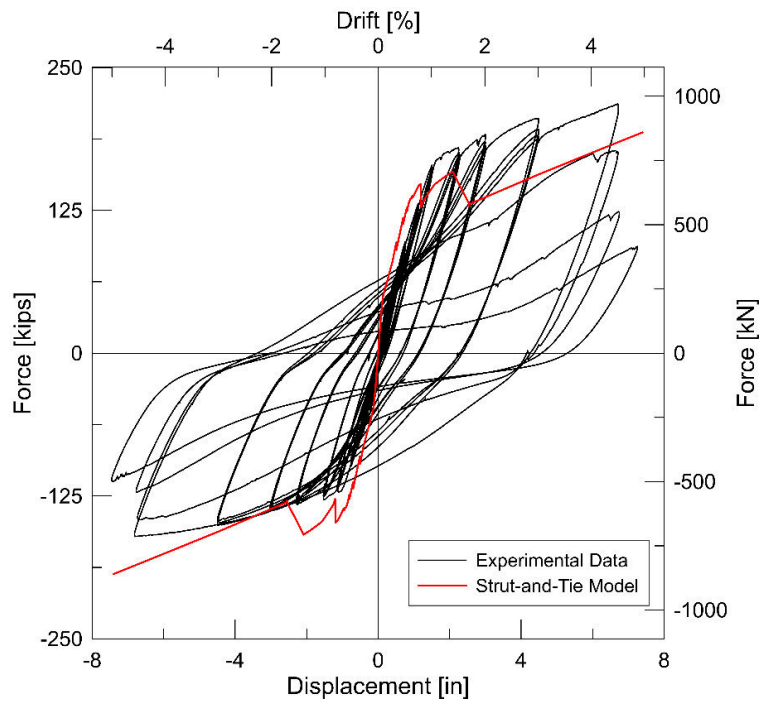


Figure 6.19: Monotonic analytical results for S2

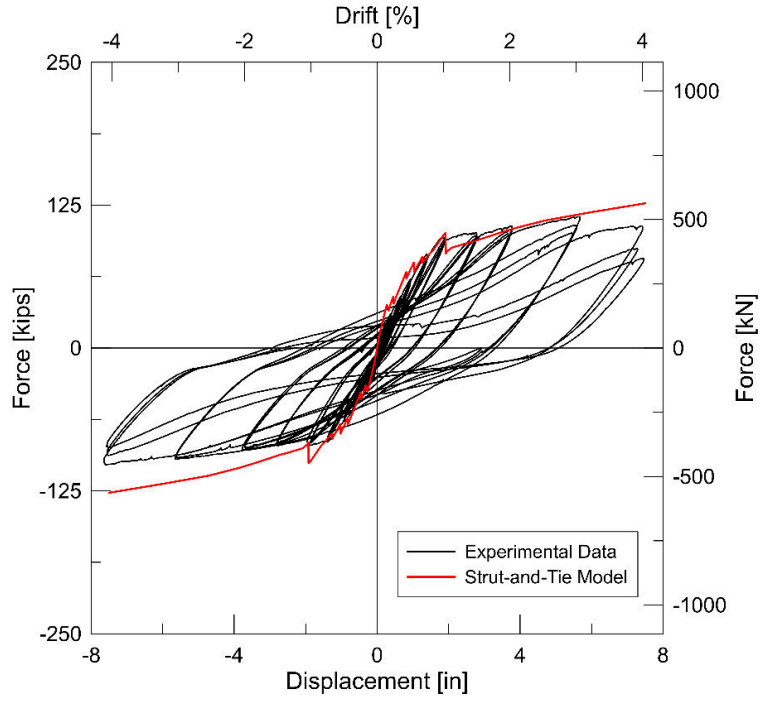


Figure 6.20: Monotonic analytical results for S3

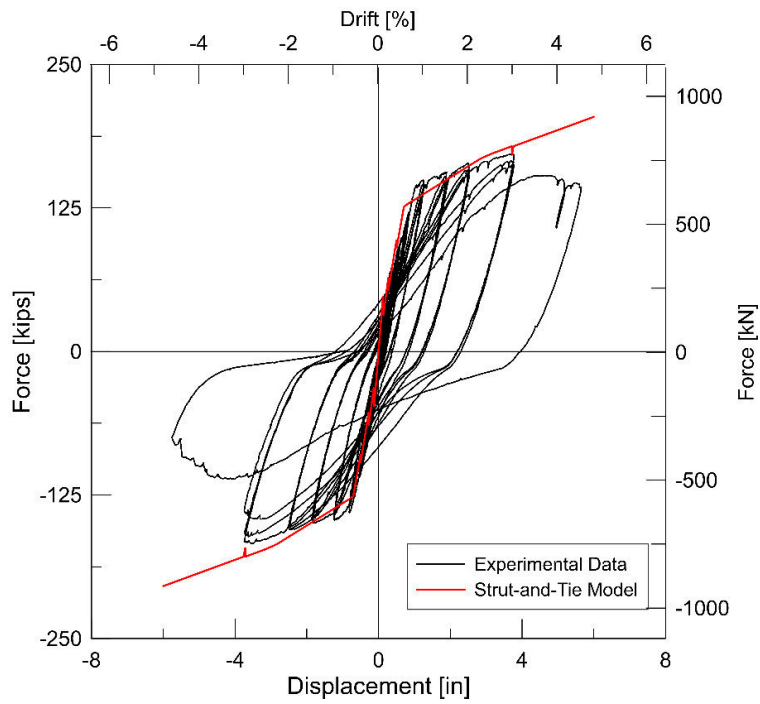


Figure 6.21: Monotonic analytical results for S4

6.3 Cyclic STM Results

6.3.1 Cyclic STM 1

The cyclic STM formulation proposed by To (2005) was used to predict the load versus tip displacement relationship for all beam specimens. The development for the cyclic STM was investigated concurrently with the monotonic case. The initial iteration of STM developed for S1 is shown in Figure 6.24 with the corresponding results shown in Figure 6.25. The model utilized a truss at the top and bottom chords of the opening. The results of the first truss model demonstrated severely low strength and stiffness which prompted the formulation of another cyclic STM.

The final version of the cyclic truss model utilized the same concept from the monotonic truss model with a small truss bordering the opening which resulted in improved behavior. The opening region, b , was the only section to be considered a D-region as demonstrated by Figure 6.22. S4 was considered to be a B-region entirely and only incorporated elements 1-3. The respective truss model for each specimen is provided in Figures 6.26-6.29. The height and width of the bays of the truss around the opening are consistent in all beam specimens. The properties of the individual elements of each model are provided in Tables 6.5-6.8. The material models *Concrete02* was used for all concrete elements. For the concrete ties, the material model *ElasticPP* was utilized to replicate the behavior of the “contact stress” and “tension stiffening” effects. The elastic material requires two strain data points and a stiffness as inputs as shown in Figure 6.23. *Steel01* was used for all steel ties in the cyclic STMs.

The analytical hysteretic response for all specimens is shown in Figures 6.30-6.33. The analytical hysteretic response generated using the cyclic STM for S4 compared well with the experimental data particularly with the initial upward loading stiffness and the post-yield behavior of the downward loading direction. The strength of the specimen past yield was overestimated in the negative quadrant and the initial stiffness in the positive quadrant was also greater than the experimental results. The predicted yield strength in the positive loading direction was 8.0% less than the experimental results. In the opposite direction, the predicted yield force was 9.8% greater. The individual member elements of the STM demonstrate yielding in the steel elements at the first bay of the truss.

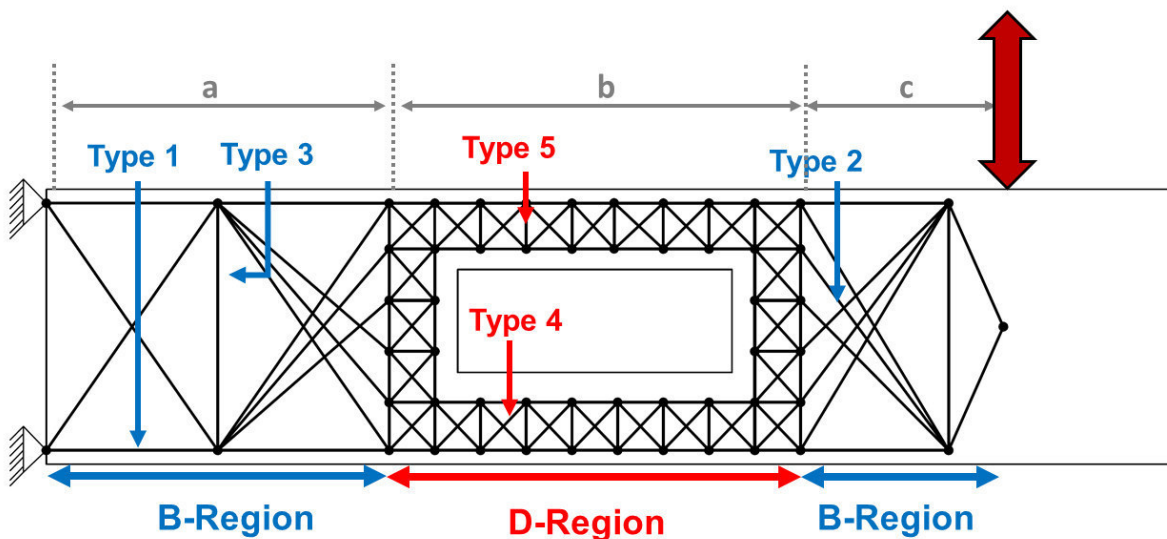


Figure 6.22: Discretization of B- and D-regions along with element types in cyclic STM

The analytical hysteretic response for S1-S3, the beams with openings, showed satisfactory yielding strength and initial stiffness. The predicted yield strength in the downward loading direction of S1-S3 was 6.1%, 15.3%, and 8.6% greater than that of the actual results, respectively. For the upward loading direction, the predicted yield strength for S1 and S3 were 11.4% and 12.8%

less than the actual yield strength, respectively. For S2, the analytical yield strength was 5.5% greater than the experimental results. The analytical stiffness past yield also matches well with for S2 and S3. Furthermore, S1 does not capture the rapid strength degradation that occurred past peak load. The response of the individual truss members for S1-S3 demonstrate similar behavior. The steel ties at the first bay of section a of the truss all yielded. Additionally, a few of the tie elements in the opening section yielded as well. The main model deficiency observed in all analytical results was that the strength and cyclic degradation was not captured. This was a conclusion of To (2005), where it is attributed to the material models chosen at the time. This issue is addressed by using a different steel material in Section 6.3.3.

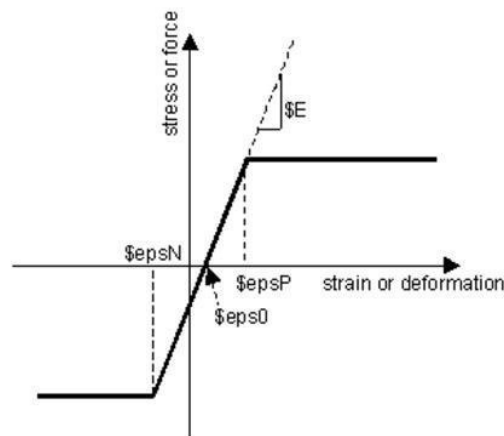


Figure 6.23: Stress-strain relationship for *ElasticPP* material in *OpenSees*

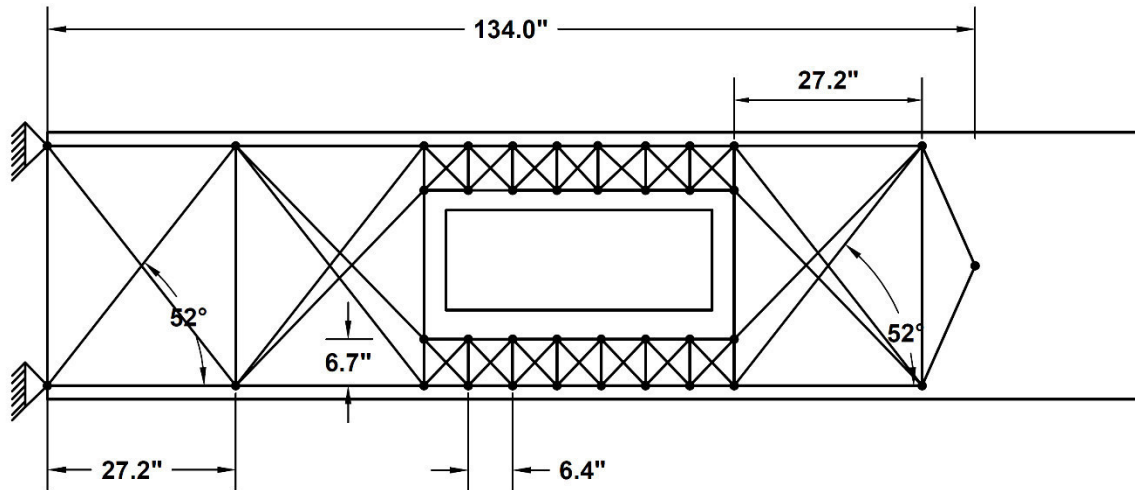


Figure 6.24: Cyclic STM 1 for S1 trial 1

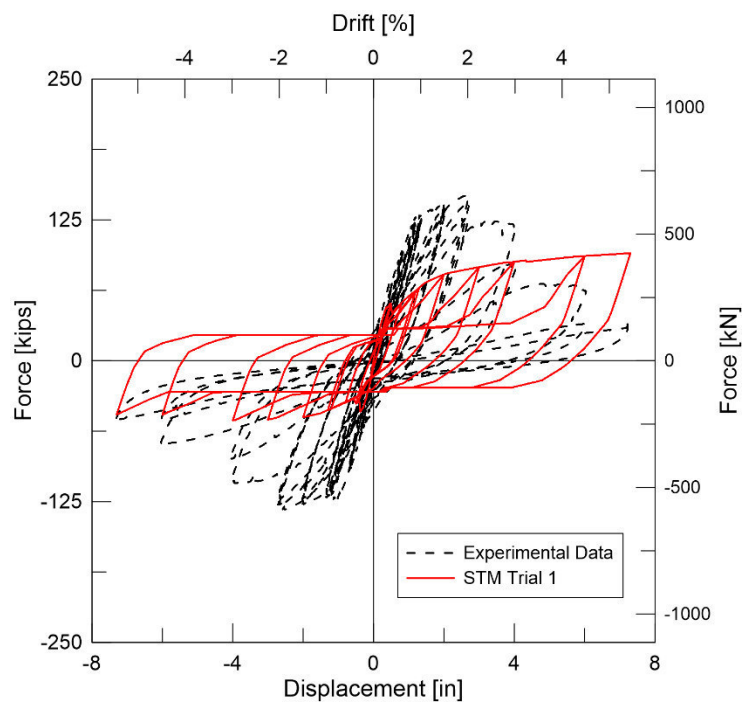


Figure 6.25: Cyclic analytical results for trial 1 of S1

Table 6.5: Cyclic STM properties for S1

S1							
		A (Bm.-Col. Joint/B-Region)		B (Opening/D-Region)		C (Bm. End/B-Region)	
Model Elements	Area [in ²]	Strength [ksi]	Area [in ²]	Strength [ksi]	Area [in ²]	Strength [ksi]	
Type 1-Concrete Struts	99.3	$0.48f'_c$	-	-	126.8	$0.48f'_c$	
Type 1-Concrete Ties	99.3	$f_{cont} = 0.024f'_c$ $f_{ts} = 0.23f'_t$	-	-	126.8	$f_{cont} = 0.024f'_c$ $f_{ts} = 0.23f'_t$	
Type 1-Rebar Strut-Ties	$0.75A_s$	f_y	-	-	$0.75A_s$	f_y	
Type 2-Concrete Struts	410.0	$0.425f'_c$	-	-	412.5	$0.425f'_c$	
Type 2-Concrete Ties	410.0	$f_{cont} = 0.021f'_c$ $f_{ts} = 0.23f'_t$	-	-	412.5	$f_{cont} = 0.021f'_c$ $f_{ts} = 0.23f'_t$	
Type 3-Rebar Ties	2.6	f_y	-	-	3.3	f_y	
Type 4-Concrete Struts	-	-	122.9	$0.51f'_c$	-	-	
Type 4-Concrete Ties	-	-	122.9	$f_{cont} = 0.026f'_c$ $f_{ts} = 0.23f'_t$	-	-	
Type 5-Rebar Ties	-	-	A_s	f_y	-	-	

Table 6.6: Cyclic STM properties for S2

S2						
A (Bm.-Col. Joint/B-Region)		B (Opening/D-Region)		C (Bm. End/B-Region)		
Model Elements	Area [in ²]	Strength [ksi]	Area [in ²]	Strength [ksi]	Area [in ²]	Strength [ksi]
Type 1-Concrete Struts	167.6	$0.48f'_c$	-	-	167.6	$0.48f'_c$
Type 1-Concrete Ties	167.6	$f_{cont} = 0.024f'_c$ $f_{ts} = 0.25f'_t$	-	-	167.6	$f_{cont} = 0.024f'_c$ $f_{ts} = 0.25f'_t$
Type 1-Rebar Strut-Ties	$0.75A_s$	f_y	-	-	$0.75A_s$	f_y
Type 2-Concrete Struts	478.6	$0.425f'_c$	-	-	373.3	$0.425f'_c$
Type 2-Concrete Ties	478.6	$f_{cont} = 0.021f'_c$ $f_{ts} = 0.25f'_t$	-	-	373.3	$f_{cont} = 0.021f'_c$ $f_{ts} = 0.25f'_t$
Type 3-Rebar Ties	5.3	f_y	-	-	7.12	f_y
Type 4-Concrete Struts	-	-	122.9	$0.51f'_c$	-	-
Type 4-Concrete Ties	-	-	122.9	$f_{cont} = 0.026f'_c$ $f_{ts} = 0.25f'_t$	-	-
Type 5-Rebar Ties	-	-	A_s	f_y	-	-

Table 6.7: Cyclic STM properties for S3

S3						
A (Bm.-Col. Joint/B-Region)		B (Opening/D-Region)		C (Bm. End/B-Region)		
Model Elements	Area [in ²]	Strength [ksi]	Area [in ²]	Strength [ksi]	Area [in ²]	Strength [ksi]
Type 1-Concrete Struts	109.5	$0.48f'_c$	-	-	82.1	$0.48f'_c$
Type 1-Concrete Ties	109.5	$f_{cont} = 0.024f'_c$ $f_{ts} = 0.23f'_t$	-	-	82.1	$f_{cont} = 0.024f'_c$ $f_{ts} = 0.23f'_t$
Type 1-Rebar Strut-Ties	$0.75A_s$	f_y	-	-	$0.75A_s$	f_y
Type 2-Concrete Struts	488.4	$0.425f'_c$	-	-	496.4	$0.425f'_c$
Type 2-Concrete Ties	488.4	$f_{cont} = 0.021f'_c$ $f_{ts} = 0.23f'_t$	-	-	496.4	$f_{cont} = 0.021f'_c$ $f_{ts} = 0.23f'_t$
Type 3-Rebar Ties	2.58	f_y	-	-	1.83	f_y
Type 4-Concrete Struts	-	-	122.9	$0.51f'_c$	-	-
Type 4-Concrete Ties	-	-	122.9	$f_{cont} = 0.026f'_c$ $f_{ts} = 0.23f'_t$	-	-
Type 5-Rebar Ties	-	-	A_s	f_y	-	-

Table 6.8: Cyclic STM properties for S4

S4		
Model Elements	Area [in²]	Strength [ksi]
Type 1-Concrete Struts	109.7	$0.5f'_c$
Type 1-Concrete Ties	109.7	$f_{cont} = 0.025f'_c$ $f_{ts} = 0.29f'_t$
Type 1-Rebar Strut-Ties	$0.75A_s$	f_y
Type 2-Concrete Struts	457.4	$0.425f'_c$
Type 2-Concrete Ties	457.4	$f_{cont} = 0.021f'_c$ $f_{ts} = 0.29f'_t$
Type 3-Rebar Ties	2.54/1.89	f_y

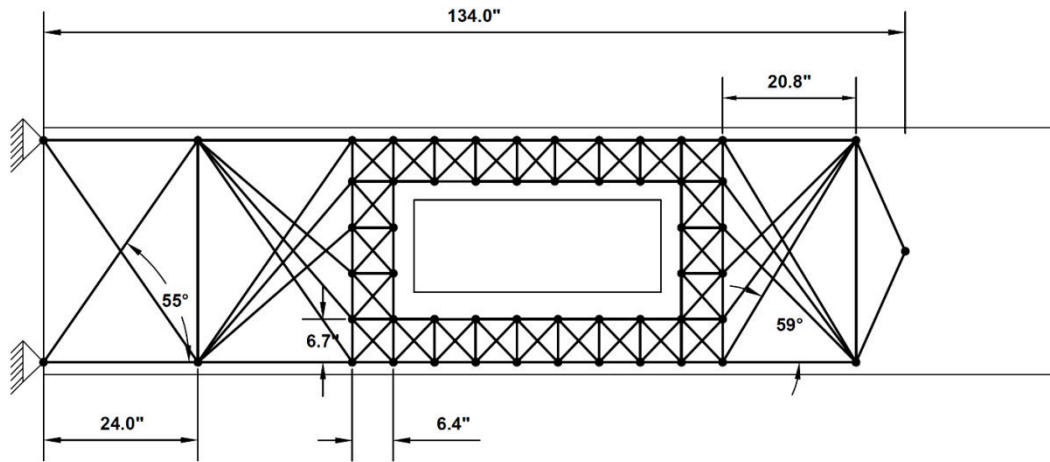


Figure 6.26: Cyclic STM 1 for S1

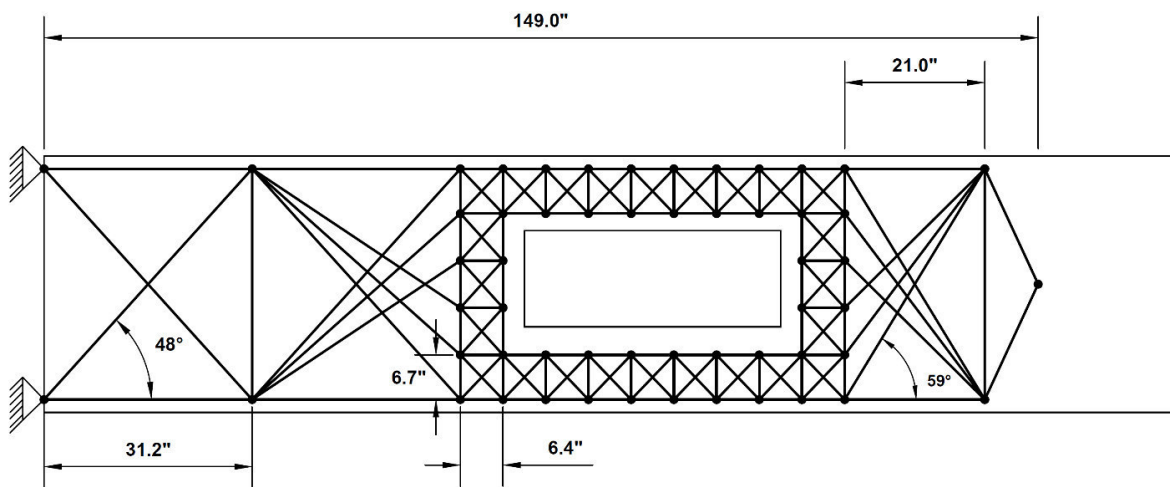


Figure 6.27: Cyclic STM 1 for S2

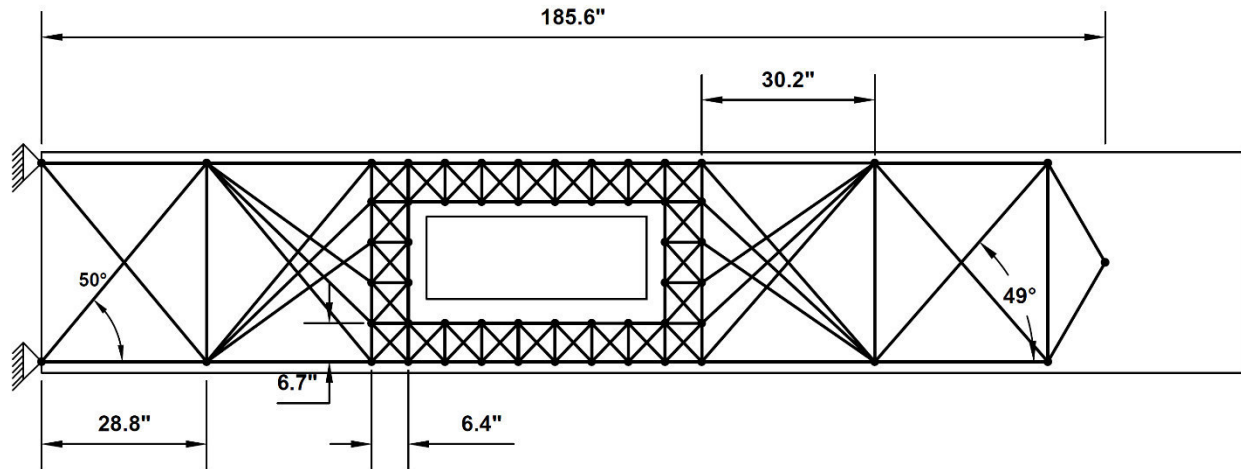


Figure 6.28: Cyclic STM 1 for S3

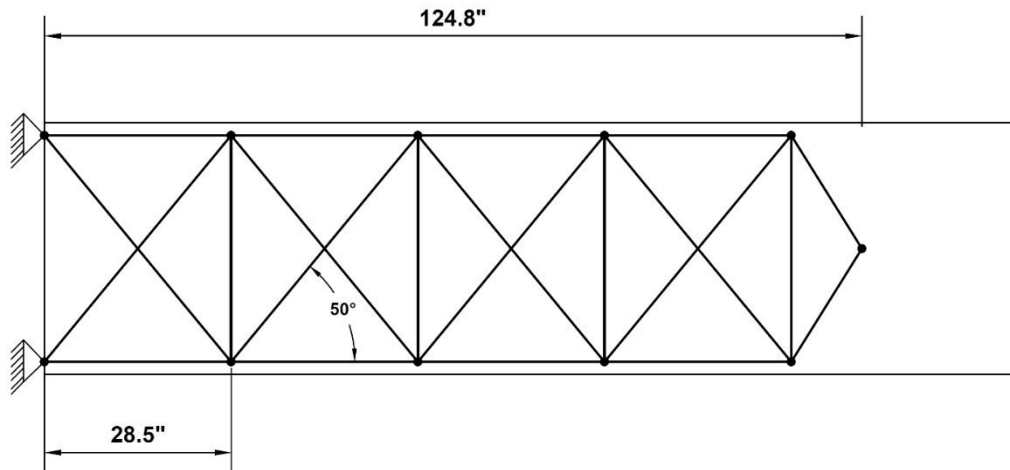


Figure 6.29: Cyclic STM 1 for S4

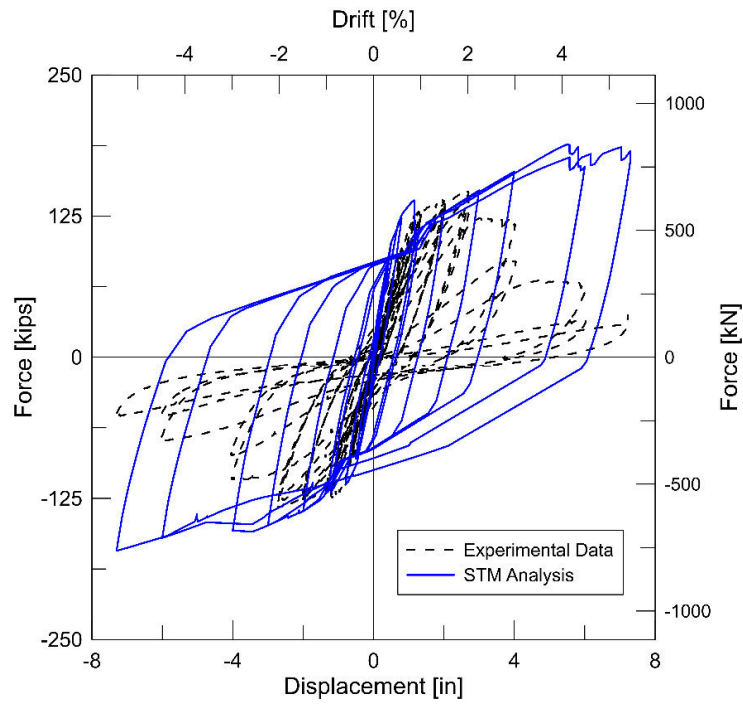


Figure 6.30: Cyclic analytical results for STM 1 of S1

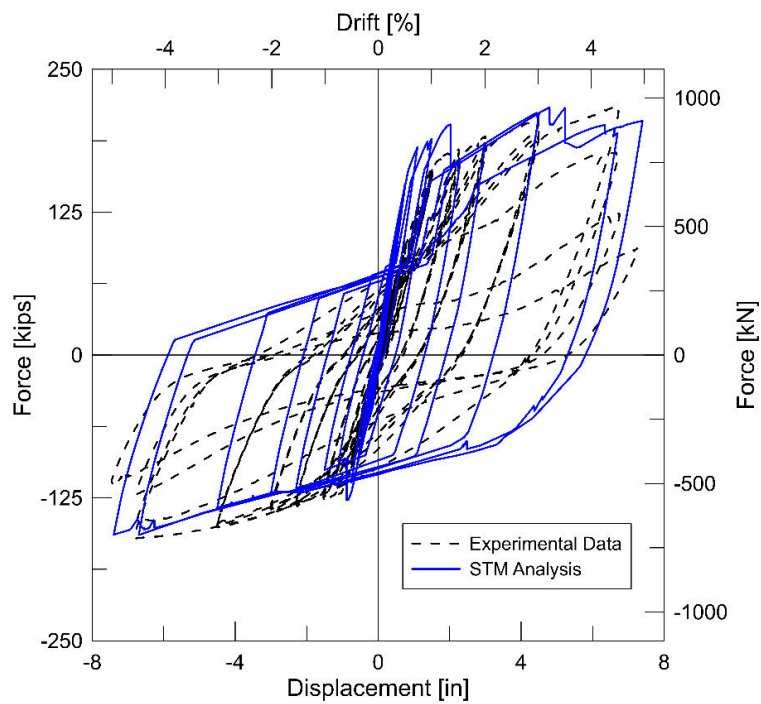


Figure 6.31: Cyclic analytical results for STM 1 of S2

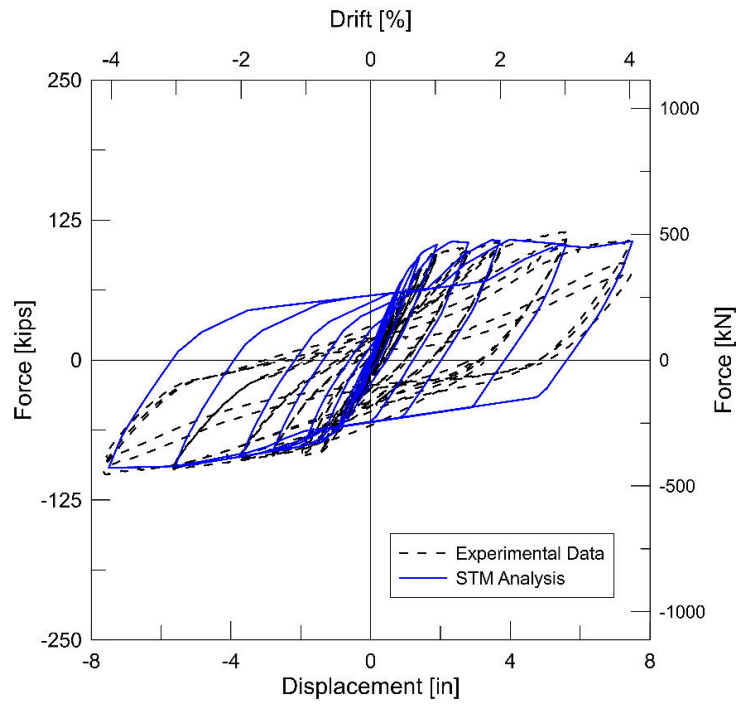


Figure 6.32: Cyclic analytical results for STM 1 of S3

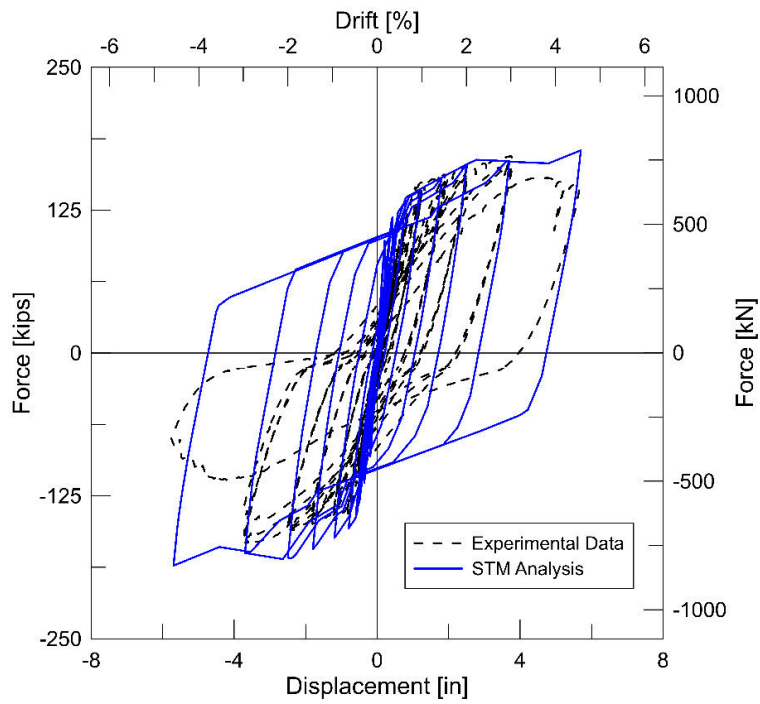


Figure 6.33: Cyclic analytical results for STM 1 of S4

6.3.2 Cyclic STM 2

An additional truss model was created for the beams with an opening with the objective to better represent the experimental results. The new truss model contains a small truss in the top and bottom chords of the opening and spanned sections a and c (Figure 6.34). The truss at the sides of the opening were removed in comparison to STM 1. The rationale for doing this comes from the jamb reinforcement in all beams with openings. The analytical results demonstrated that the truss model overestimated the strength of the beam by a significant amount (Figure 6.35). The additional strength was likely because the jamb reinforcement did not anchor into the reaction block as modelled by the additional pin supports. Therefore, the top and bottom truss was removed from section c and from the bay closest to the support of section a . This final version of the second truss model for S1-S3 is shown in Figures 6.36-6.38. The STM effective material properties were identical to those of the first model. The effective areas also remained constant except for the diagonal struts which were affected depending on the change of the inclination angle.

The results from the analytical hysteric response of the second cyclic model are shown in Figures 6.39-6.41. The results show a better initial stiffness response in comparison to STM 1 especially in the downward loading direction. For comparison, the two models are plotted together with the experimental data in Figures 6.42-6.44. Additionally, the yield strength is also estimated satisfactorily for all beam specimens. In the positive loading direction, the yield force for S1 is 1% less, for S2 0.12% less and for S3 it is 10% greater than that of the experimental results. In the opposite loading direction, the analytical results show that the predicted yield strength for S1 was 4.7% less, for S2 12.2% less and for S3 9.3% less than that of the experimental results. The response of the individual truss members shows that most of the longitudinal ties at section a

yielded. For S3, there was no yielding of the ties at the opening section. For S1 and S2 the ties at the opening closer to the support yielded.

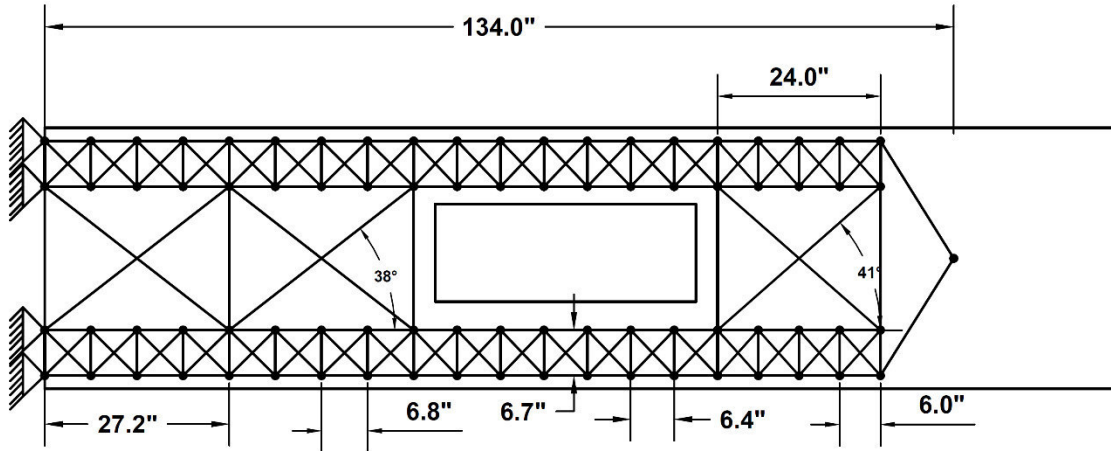


Figure 6.34: Cyclic STM 2 for S1 trial 1

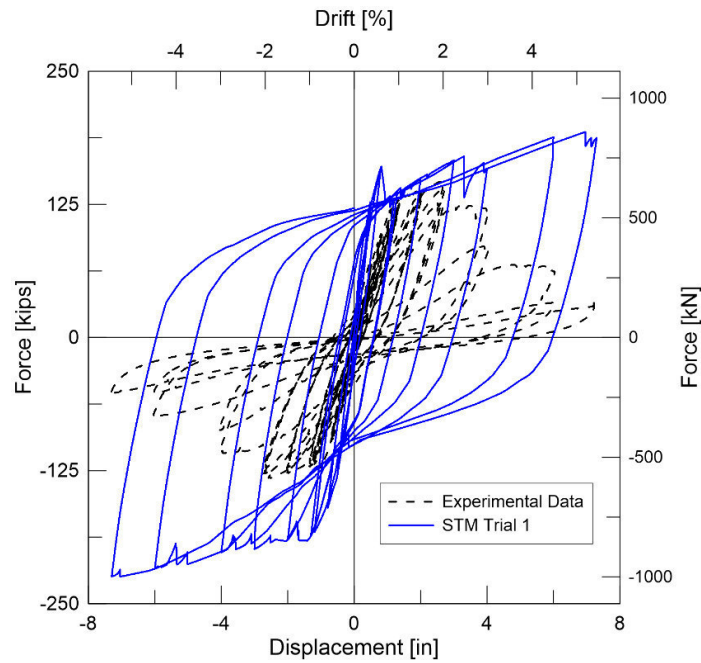


Figure 6.35: Cyclic analytical results for trial 1 of S1

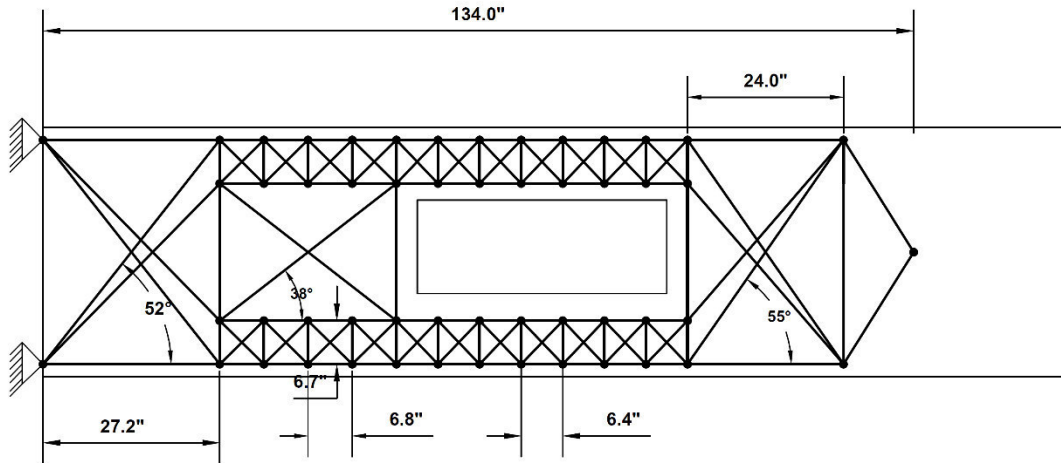


Figure 6.36: Cyclic STM 2 for S1

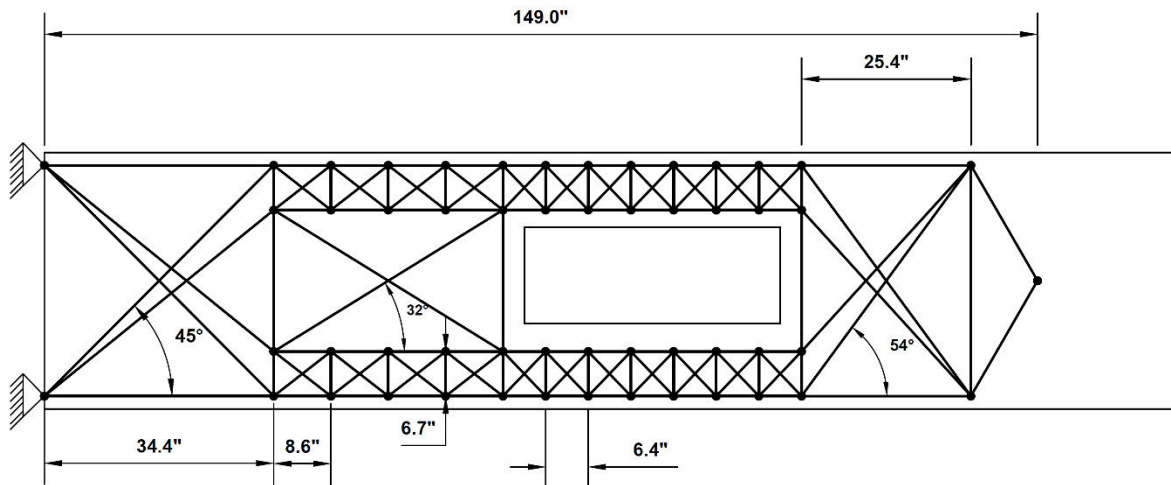


Figure 6.37: Cyclic STM 2 for S2

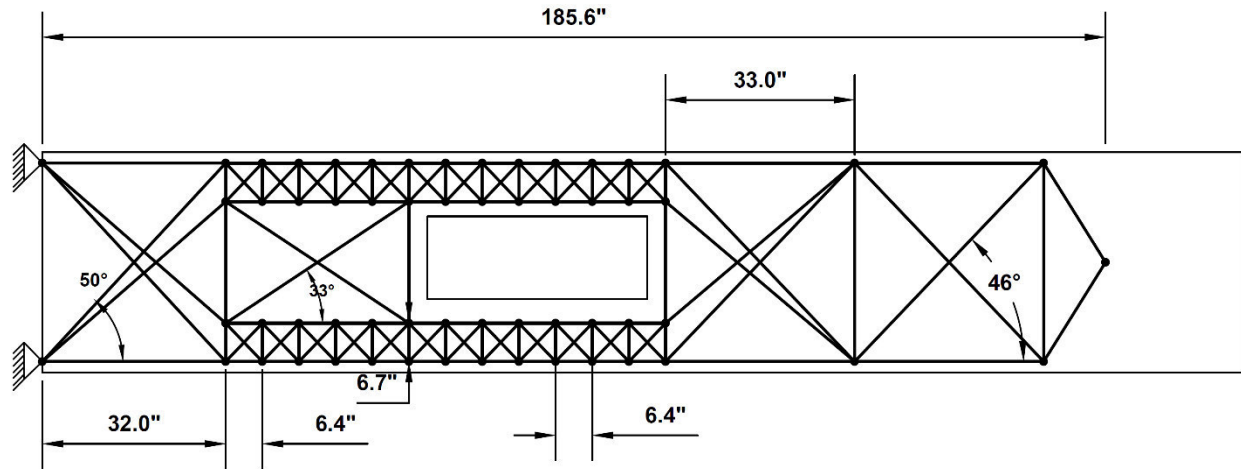


Figure 6.38: Cyclic STM 2 for S3

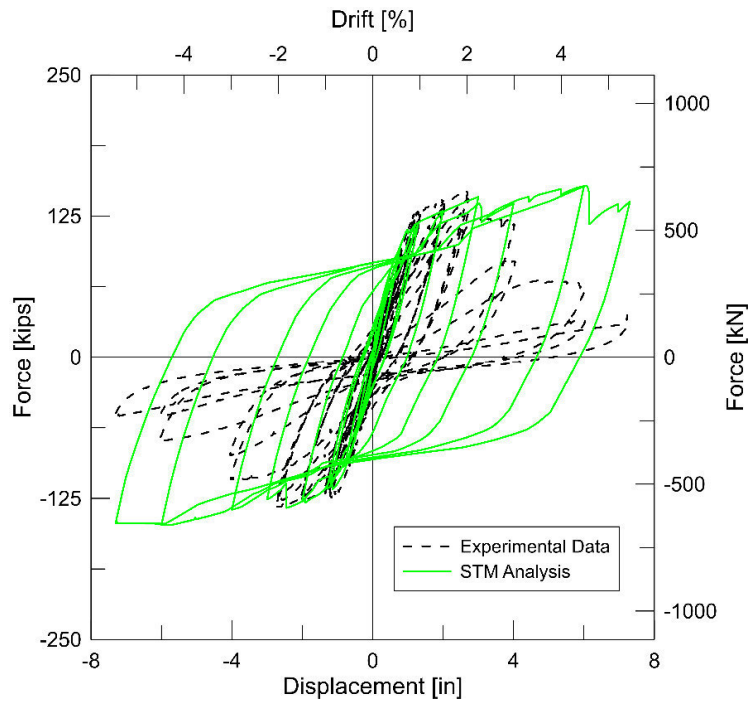


Figure 6.39: Cyclic analytical results for STM 2 of S1

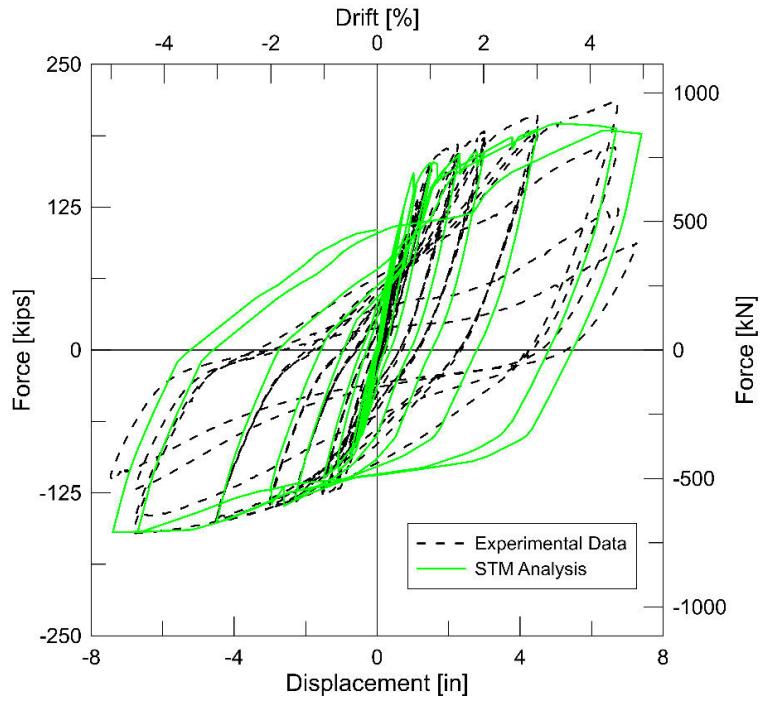


Figure 6.40: Cyclic analytical results for STM 2 of S2

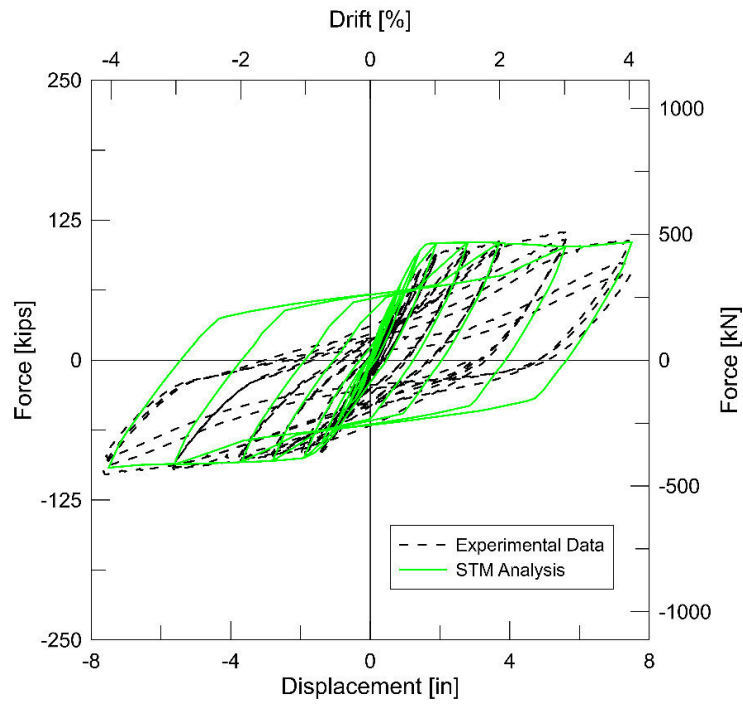


Figure 6.41: Cyclic analytical results for STM 2 of S3

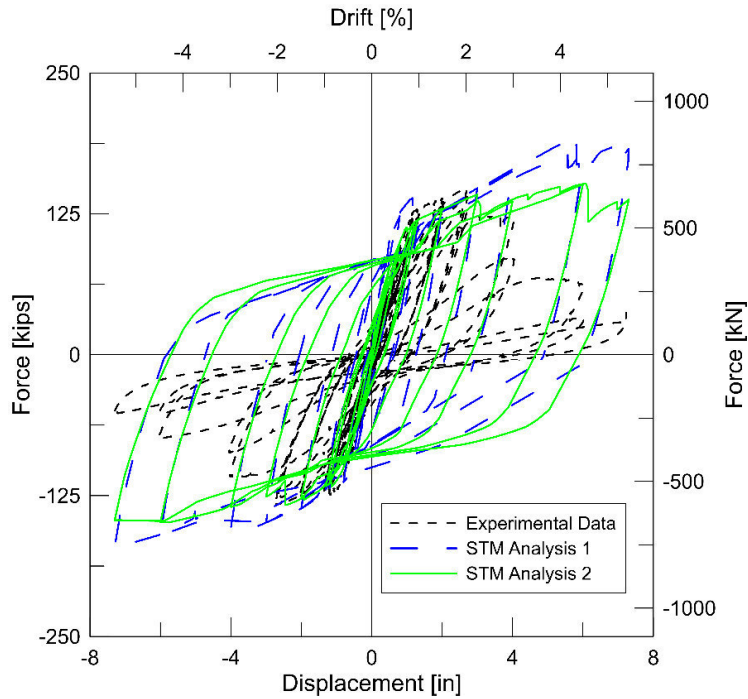


Figure 6.42: Comparison of cyclic analytical results for STM 1 & 2 of S1

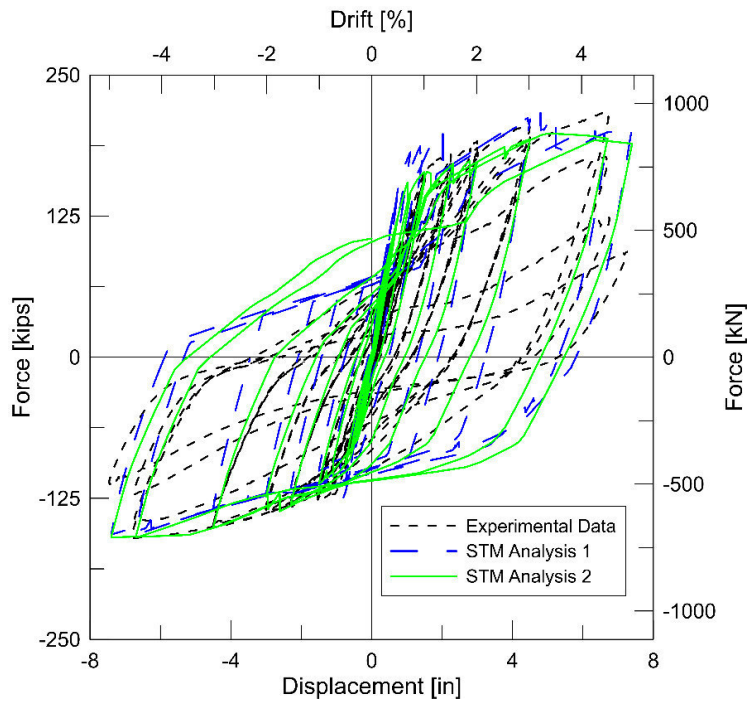


Figure 6.43: Comparison of cyclic analytical results for STM 1 & 2 of S2

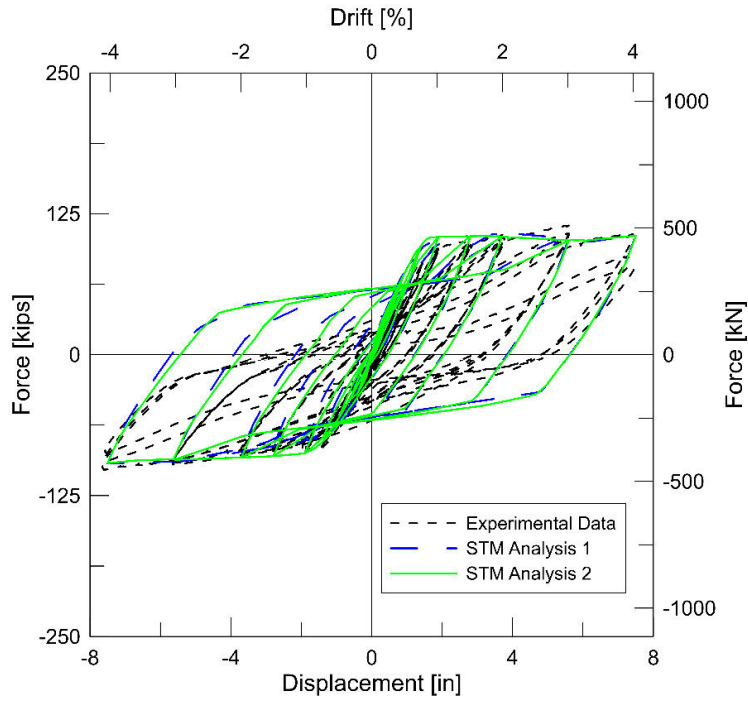


Figure 6.44: Comparison of cyclic analytical results for STM 1 & 2 of S3

6.3.3 Hysteretic Steel Material for Cyclic STM

The previous cyclic STMs were not capable of capturing the strength or cyclic degradation observed in the experimental data. To (2005) concludes that this is one of the main model deficiencies. This deficiency is due to the material models in Drain2DX which at the time were not capable of capturing strength degradation. Therefore, the next step in the analytical modeling conducted involved the implementation of a different steel model to better represent the hysteretic behavior of the experimental data. The material model chosen for the steel tie elements was the *Hysteretic* model in *OpenSees* (Figure 6.45). The *Hysteretic* material is used to model a piecewise linear constitutive relationship which incorporates strength degradation, stiffness degradation, and pinching. The inputs to the model allow up to three stress-strain data points, two pinching factors, a damage factor due to ductility, a damage factor due to energy, and factor to determine the degraded unloading stiffness based on ductility. Two stress-strain data points obtained from tensile tests of the reinforcement were used to create a bilinear curve. Additionally, factors for the ductility damage were chosen for S1, S2, and S4 such that it showed good agreement with the experimental data. The factor for the ductility damage was taken to be between 0.01-0.045 and the factor for the degraded unloading stiffness was between 0.1-0.6. Figures 6.46-6.49 below show the results of implementing the *Hysteretic* material model to STM 1. Figures 6.50-6.52 demonstrate the results of implementing the same steel material model to STM 2. Both models show satisfactory agreement with the experimental data. In particular, S1 demonstrates the strength degradation observed past peak load. The results for S2 do not show good agreement in the positive quadrant for either truss model but do demonstrate good results in the negative quadrant. For comparison, both cyclic STMS and the experimental data are plotted together in Figures 6.53-6.55.

The history of normalized cumulative hysteretic energy dissipation of the two analytical STMs was obtained to compare with experimental results. Figures 6.56-6.59 shows the results of the two STMs plotted with the experimental results presented in Chapter 5. For S1 the analytical results from both models are in good agreement up to approximately 2% drift where they begin to diverge from the data. The normalized cumulative energy at yield for STM 1 was 21.0% greater than the data whereas for STM 2 the dissipated energy at yield was 7.8% less. The normalized cumulative energy reached at peak capacity for STM 1 was 10.3% less than the experimental results and for STM 2 it was 4.9% greater.

STM 1 for S2 showed better agreement with the dissipated energy than that of STM 2, where the normalized cumulative energy at yield was 29.5% greater than the data and the predicted peak energy dissipation was 11.7% less than the data. In contrast, STM 2 overestimated the dissipated energy consistently past 1.0% drift. The predicted dissipated energy at yield for STM 2 was 63.4% greater than the results. The predicted dissipated energy at peak load was 4.3% greater than the actual dissipated energy.

The results for both analytical models of S3 show an identical trend to that of the normalized cumulative energy dissipated of the results. STM 1 begins to deviate from the data at a 1% drift and the predicted dissipated energy at yield was 61.3% greater than the actual dissipated energy. Additionally, the predicted normalized cumulative energy at peak load was 20.1% greater than the results. STM 2 predicted a normalized cumulative energy that was 17.6% greater than observed.

The predicted normalized cumulative energy at peak load was 2.3% greater than the actual dissipated energy.

The STM analysis for S4 also demonstrated good agreement with the normalized cumulative energy where the results show that the model followed closely the observed energy dissipated up to 3% drift. The normalized cumulative energy reached at yield for the STM was 31.7% greater than the normalized cumulative energy of the test data. The normalized cumulative energy dissipated at peak for the STM was 4.7% less than the normalized energy dissipated in experimental results.

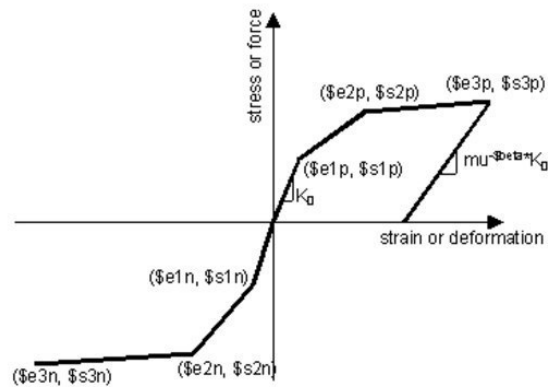


Figure 6.45: Stress-strain relationship for *Hysteretic* material in *OpenSees*

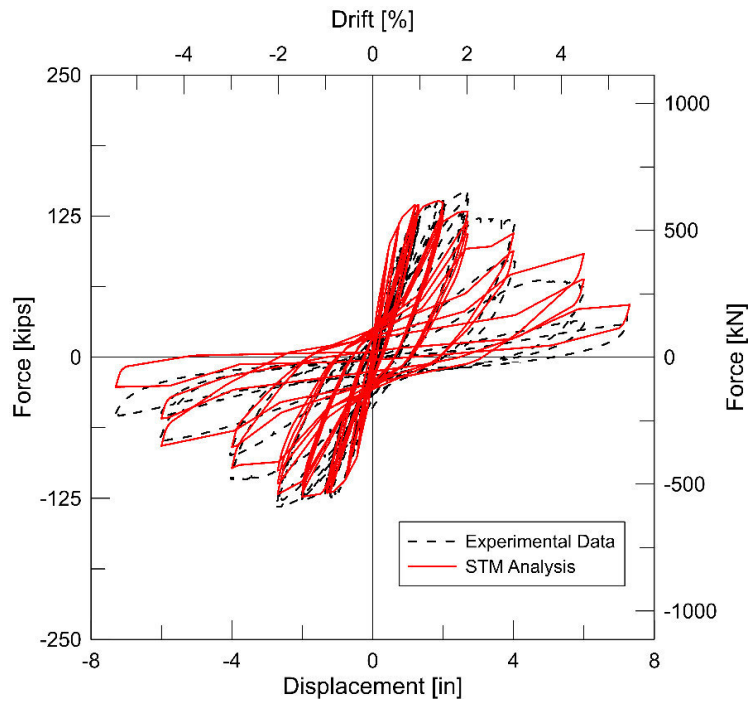


Figure 6.46: Cyclic analytical results for STM 1 of S1 with *Hysteretic* steel material model

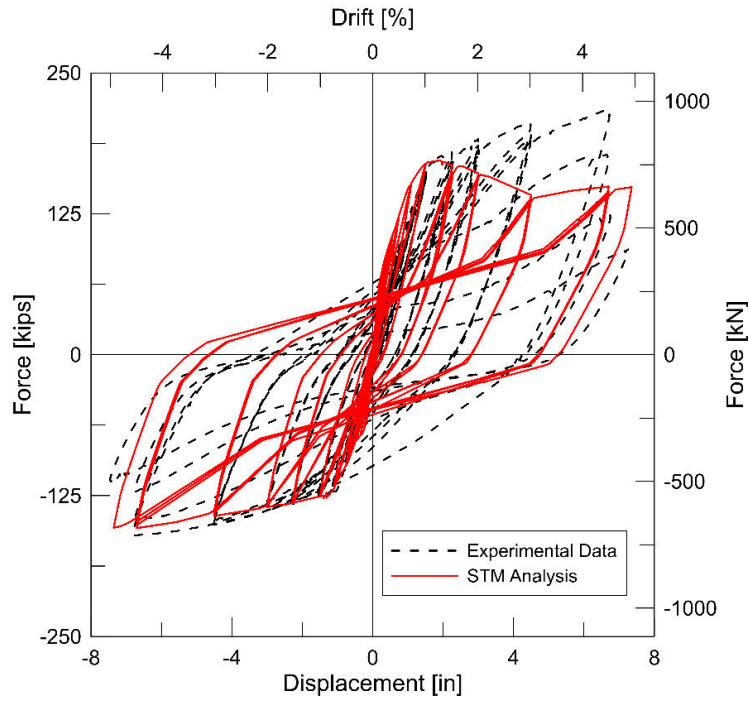


Figure 6.47: Cyclic analytical results for STM 1 of S2 with *Hysteretic* steel material model

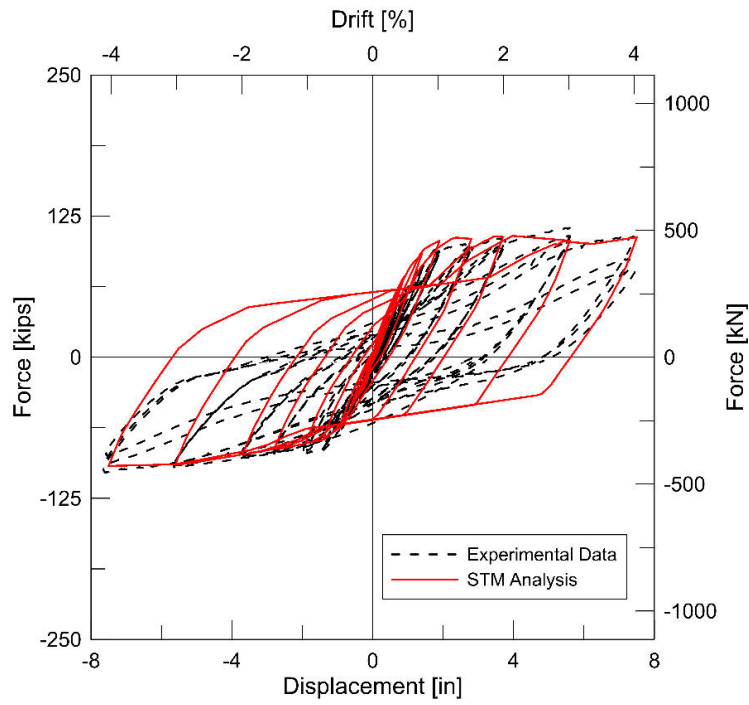


Figure 6.48: Cyclic analytical results for STM 1 of S3 with *Hysteretic* steel material model

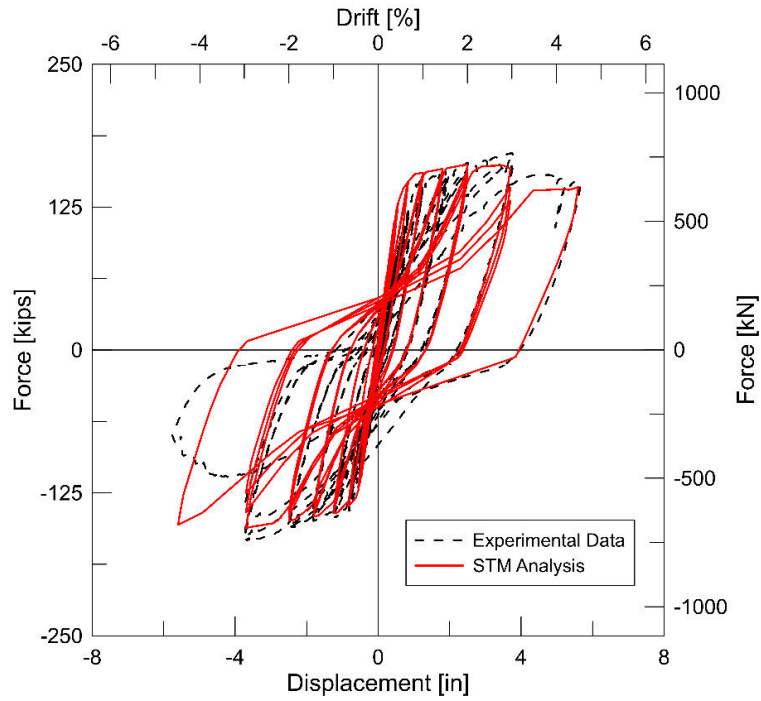


Figure 6.49: Cyclic analytical results for STM 1 of S4 with *Hysteretic* steel material model

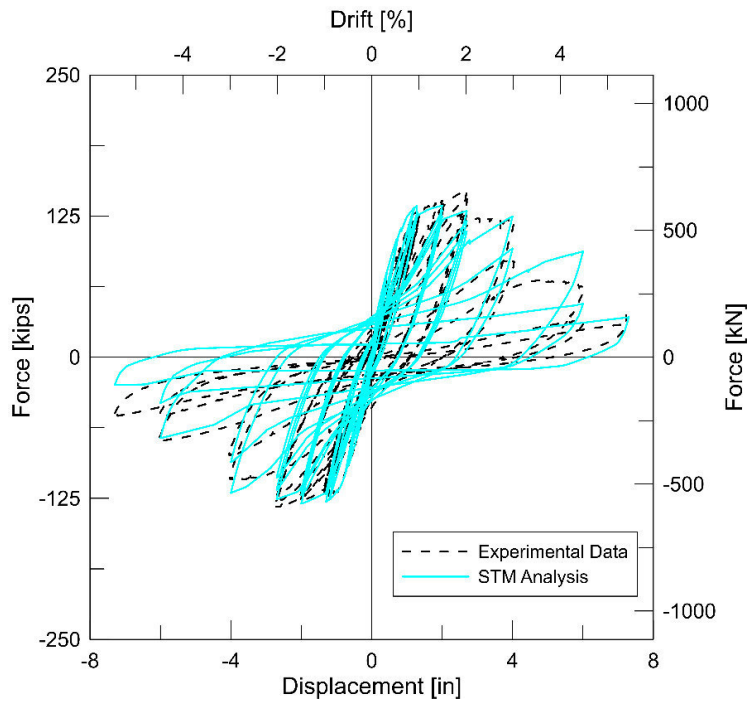


Figure 6.50: Cyclic analytical results for STM 2 of S1 with *Hysteretic* steel material model

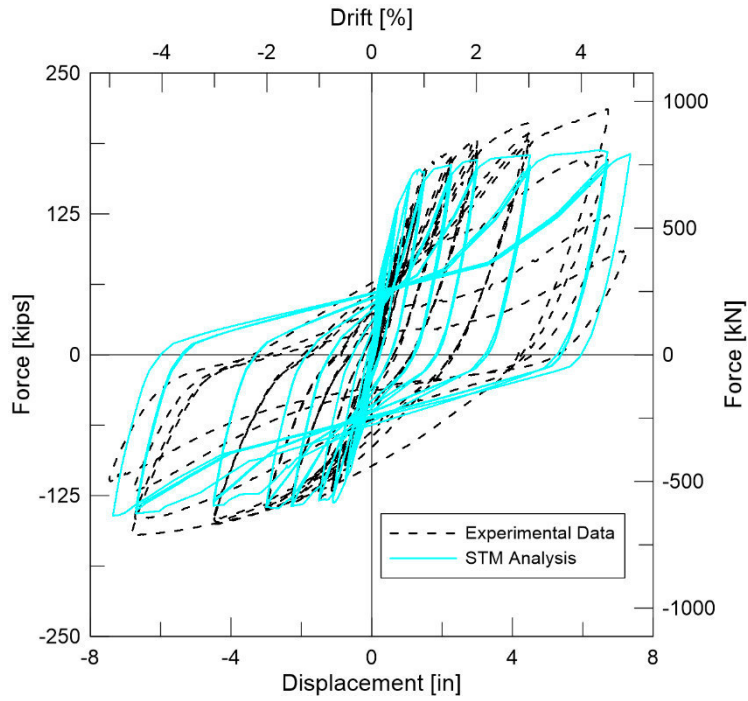


Figure 6.51: Cyclic analytical results for STM 2 of S2 with *Hysteretic* steel material model

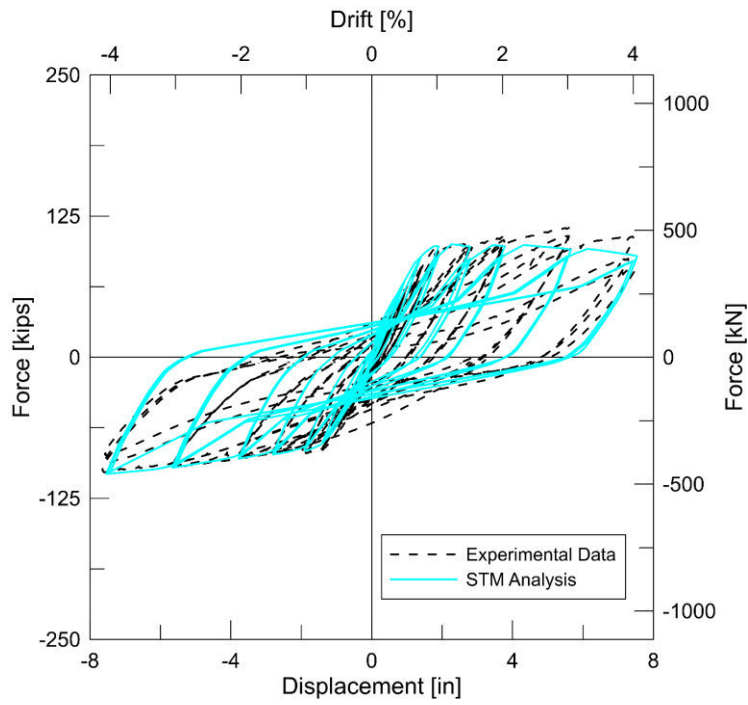


Figure 6.52: Cyclic analytical results for STM 2 of S3 with *Hysteretic* steel material model

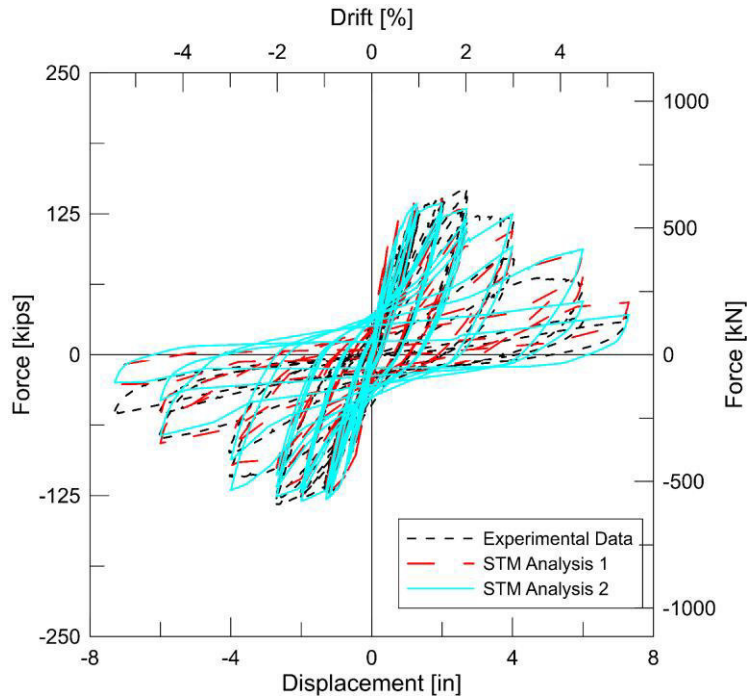


Figure 6.53: Comparison of cyclic analytical results for STMs 1 & 2 of S1 with *Hysteretic* steel material model

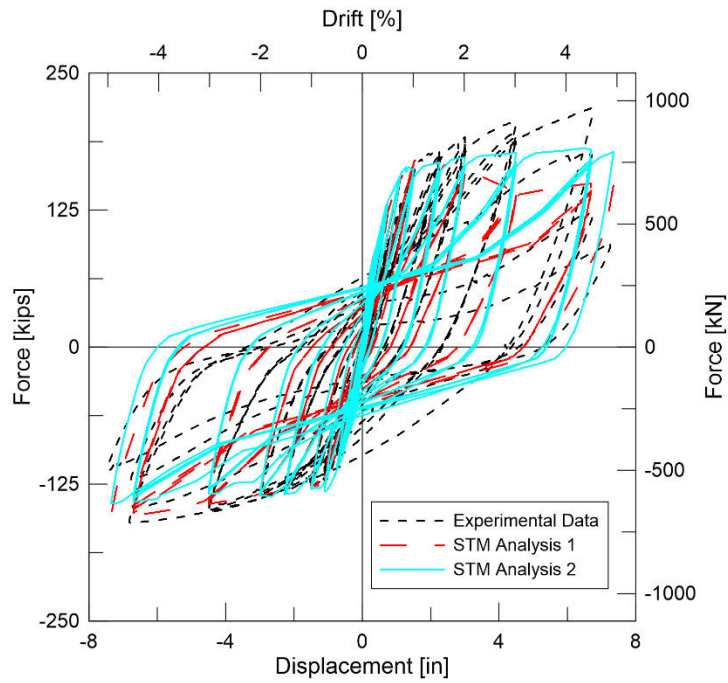


Figure 6.54: Comparison of cyclic analytical results for STMs 1 & 2 of S2 with *Hysteretic* steel material model

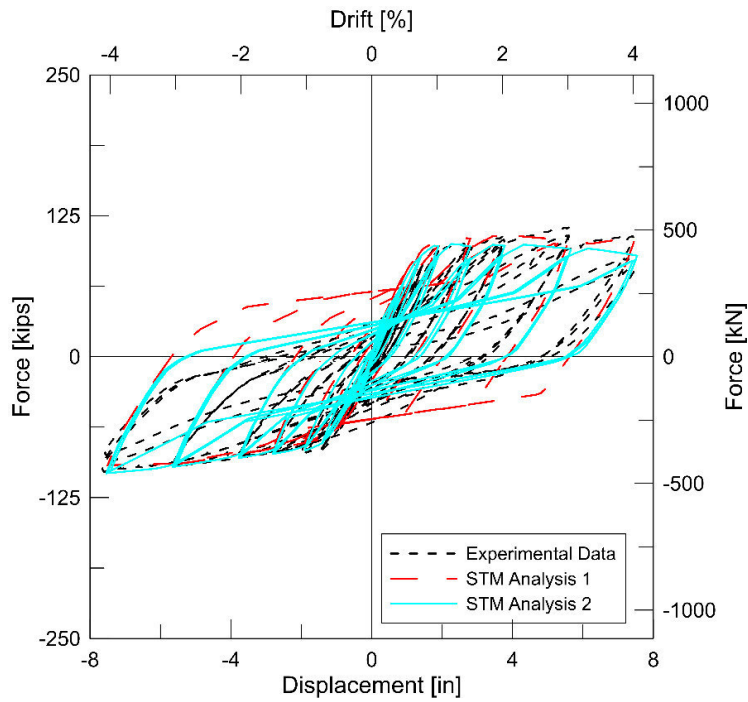


Figure 6.55: Comparison of cyclic analytical results for STMs 1 & 2 of S3 with *Hysteretic* steel material model

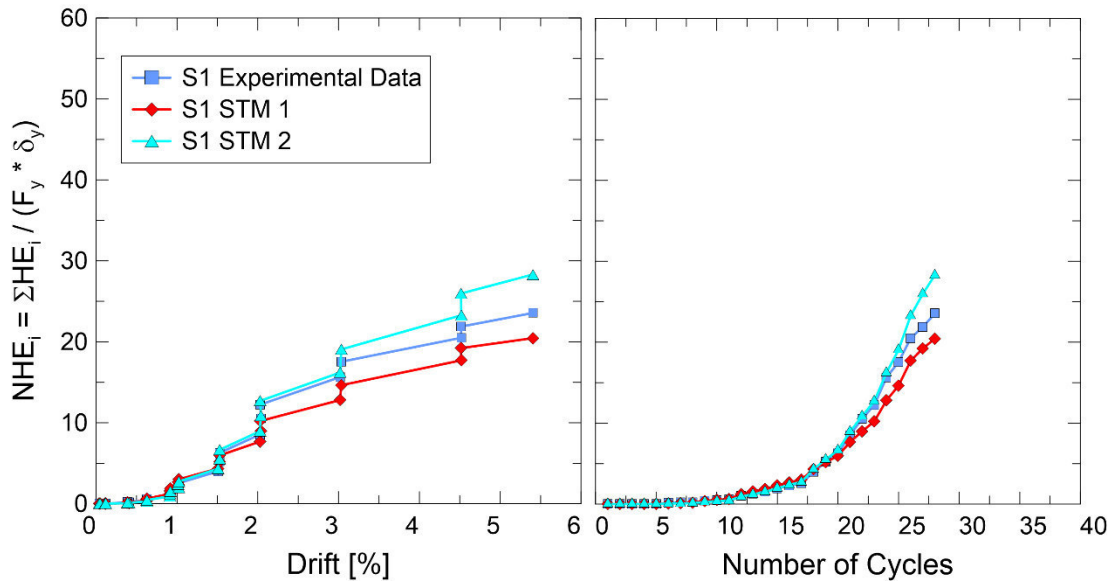


Figure 6.56: Cumulative NHE dissipation comparison between cyclic STMs and experimental results for S1

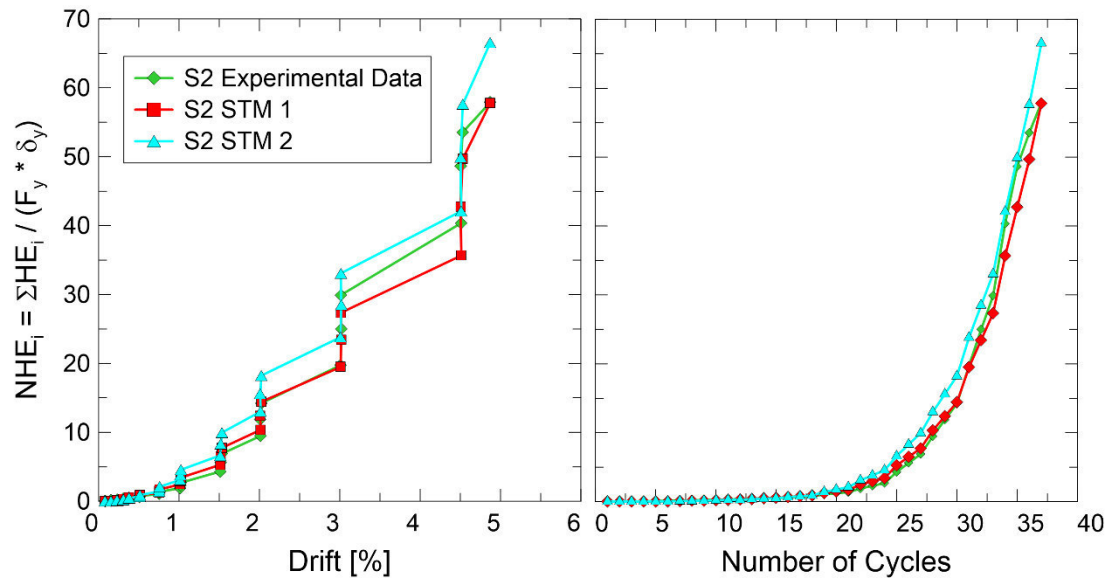


Figure 6.57: Cumulative NHE dissipation comparison between cyclic STMs and experimental results for S2

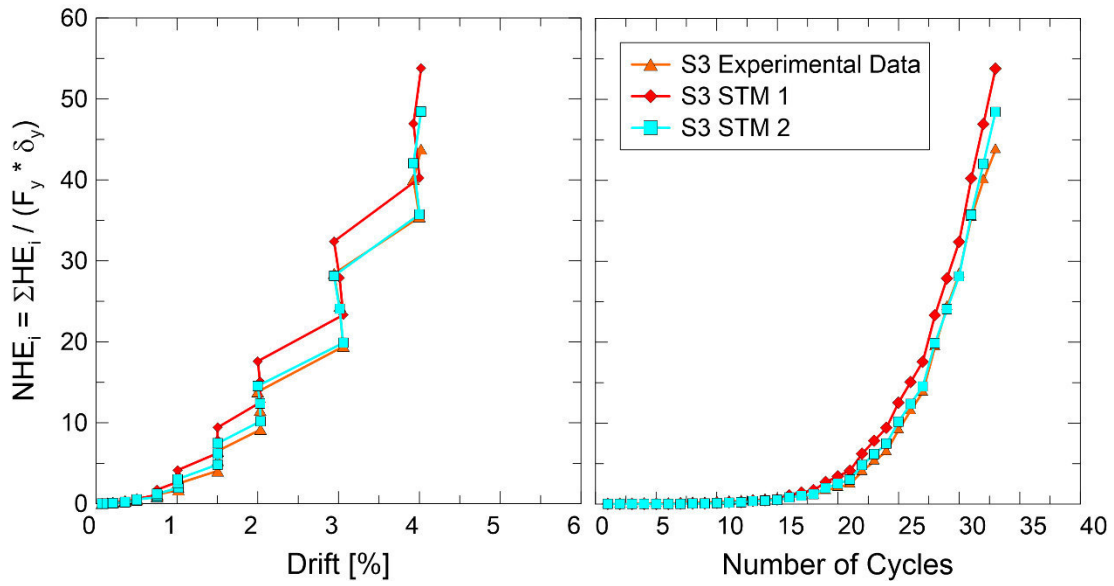


Figure 6.58: Cumulative NHE dissipation comparison between cyclic STMs and experimental results for S3

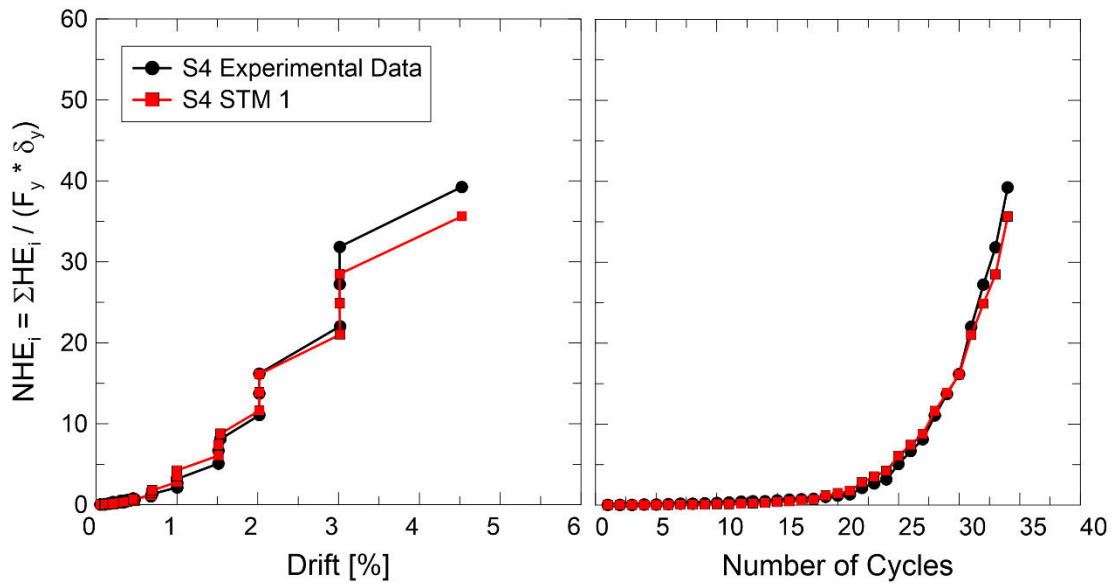


Figure 6.59: Cumulative NHE dissipation comparison between cyclic STMs and experimental results for S4

Chapter 7 Summary and Conclusions

This paper presents a unique case study of four reinforced concrete moment-frame beams located in an existing building in California. Replica specimens were constructed as half-length cantilevers scaled to 80% of the dimensions and reinforcement sizes of the existing RCMRF beams and tested to complete structural failure under quasi-static cyclic load reversals. Three replica specimens (S1- S3) were constructed with rectangular web openings and one replica specimen (S4) served as reference beam without an opening. The beam openings were not accounted for in the original building design and limited accompanying structural information is currently available. To assess the seismic capacity of the perforated members and to develop potential strengthening mechanisms, large scale testing was executed at the Structural Laboratory at the University of CA, Irvine. The effect of the beam's different reinforcement schemes and the influence of the opening were evaluated based on observed crack and damage development, hysteric response curves, strength and stiffness degradation, energy dissipation and the contribution of flexural and shear deformations to the overall beam displacement. The results of these studies can be summarized as follows:

- The additional reinforcement, provided around the web openings of specimens S1, S2 and S3, consisting of additional longitudinal bars near the top and bottom faces of the opening (jamb bars), as well as short stirrups in both chords, attenuated brittle failure at the region weakened by the opening.

- Only specimen S1 failed at the opening. Cracking patterns suggest that the top chord failed primarily in shear, while the bottom chord displayed a predominantly bond splitting failure mode. This is likely due to an inadequate reinforcement detailing around the opening consisting of an abrupt discontinuity of the longitudinal reinforcement near the opening mid-section.
- Crack propagation in all specimens originated at the beam column interface in all specimens and was dominated by alternating flexural and diagonal cracks. As plastic hinging initiated, shear was identified as an important contributor to the inelastic response.
- An analysis of shear and flexural displacement components via externally installed instrumentation revealed that the contribution of flexural deformations to the tip displacement dominates all other deformation modes. In addition, specimens S2 and S4 showed severe bottom bar buckling at the beam-column interface.
- Specimens S2 – S4 showed typical MRF type failure by developing a plastic hinge at the beam-column and specimens S2 and S3 retained full structural integrity in the opening region. Hereby strong shear reinforcement and detailing along with continuous chord reinforcement were crucial.
- A nonlinear strut and tie modeling formulation was utilized to study the monotonic response of the beam specimens. The truss model formulated consisted of a small truss around the perimeter of the opening intended to transfer the load to the support. The results

indicated good agreement with the elastic stiffness and yield strength of all beam specimens with only one exception (S2).

- Nonlinear cyclic strut and tie models were developed with two truss model arrangements and utilizing two steel material models. The *Hysteretic* material model demonstrated better agreement with the data in terms of strength and stiffness degradation past yield. Both truss model geometries developed performed similarly well when predicting the initial stiffness and yield strength. The second strut and tie model (STM 2) yielded better results in terms of initial elastic stiffness in the downward loading direction. The strut and tie models also indicate similar progression of cumulative energy dissipation with the experimental results.

The successful performance of specimens S2 & S3 demonstrates that openings in moment resisting frame beams can be introduced if careful detailing in the region of beam discontinuity can be guaranteed. Based the case study presented, an extensive numerical study including a parametric evaluation of the influence of opening geometry and location is currently underway and will be part of a future publications that focuses on providing design guidance for perforated MRF beam components.

References

1. ACI Committee, American Concrete Institute, & International Organization for Standardization. (2014). Building code requirements for structural concrete (ACI 318-14) and commentary. American Concrete Institute.
2. ACI Committee, American Concrete Institute, & International Organization for Standardization. (2008). Building code requirements for structural concrete (ACI 318-08) and commentary. American Concrete Institute.
3. ACI Committee, American Concrete Institute, & International Organization for Standardization. (2002). Building code requirements for structural concrete (ACI 318-02) and commentary. American Concrete Institute.
4. Allam, S. M. (2005). Strengthening of RC beams with large openings in the shear zone. *Alexandria Engineering Journal*, 44(1), 59-78.
5. Amiri, S., Masoudnia, R., & Pabarja, A. A. (2011). The study of the Effects of Web Openings on the Concrete Beams. *Australian Journal of Basic and Applied Sciences*, 5(7), 547-556.
6. Architectural Institute of Japan. AIJ standard for structural calculation of reinforced concrete building; 1994
7. ASCE/SEI Seismic Rehabilitation Standards Committee. (2007). Seismic rehabilitation of existing buildings (ASCE/SEI 41-06). American Society of Civil Engineers, Reston, VA.
8. ASSHTO, LRFD (1989). Bridge design specifications.
9. Blakeley, R. W. G., Megget, L. M., & Priestley, M. J. N. (1975). Seismic performance of two full size Reinforced concrete beam-column joint units. *Bulletin of the New Zealand National Society for Earthquake Engineering*, 8(1), 38-69.
10. Bracci, J. M., Keating, P. B., & Hueste, M. B. D. (2000). Cracking in RC bent caps (No. FHWA/TX-01/1851-1,).
11. Brown, M. D., Sankovich, C. L., Bayrak, O., Jirsa, J. O., Breen, J. E., & Wood, S. L. (2006). *Design for Shear in Reinforced Concrete Using Strut-and-Tie Models* (No. FHWA/TX-06/0-4371-2).
12. Brown, R. H., & Jirsa, J. O. (1971, May). Reinforced concrete beams under load reversals. In *Journal Proceedings* (Vol. 68, No. 5, pp. 380-390).
13. Campione, G., & Minafò, G. (2012). Behaviour of concrete deep beams with openings and low shear span-to-depth ratio. *Engineering Structures*, 41, 294-306.
14. CEB-FIP, M. C. (1978). *for Concrete Structures: CEB-FIP International recommendations 3rd edition*. Comité Euro-International du Béton, Paris, France..
15. Chan, H. C., Cheung, Y. K., & Huang, Y. P. (1992). Crack analysis of reinforced concrete tension members. *Journal of Structural Engineering*, 118(8), 2118-2132.
16. Cook, W. D., & Mitchell, D. (1988). Studies of disturbed regions near discontinuities in reinforced concrete members. *Structural Journal*, 85(2), 206-216.
17. El-Demerdash, W. E., El-Metwally, S. E., El-Zoughiby, M. E., & Ghaleb, A. A. (2014) Strut-and-tie model and 3-D nonlinear analysis for the prediction of the behavior of RC shallow and deep beams with openings.

18. El-Maaddawy, T., & El-Ariss, B. (2012). Behavior of concrete beams with short shear span and web opening strengthened in shear with CFRP composites. *Journal of Composites for Construction*, 16(1), 47-59.
19. Elwood, Kenneth, and Jack P. Moehle. Shake table tests and analytical studies on the gravity load collapse of reinforced concrete frames. No. 1. Pacific Earthquake Engineering Research Center, 2003.
20. Fang, I. K., Yen, S. T., Wang, C. S., & Hong, K. L. (1993). Cyclic behavior of moderately deep HSC beams. *Journal of Structural Engineering*, 119(9), 2573-2592.
21. Fenwick, R. C. (1983). Strength degradation of concrete beams under cyclic loading. *Bulletin of NZ Society for Earthquake Engineering*, 16(1), 25-38.
22. Fenwick, R. C., & Fong, A. (1979). The behaviour of reinforced concrete beams under cyclic loading. University of Auckland, Department of Civil Engineering.
23. Haque, M., Rasheeduzzafar, & Al-Tayyib, A. H. J. (1986). Stress distribution in deep beams with web openings. *Journal of Structural Engineering*, 112(5), 1147-1165.
24. Hu, Q., Ley, M. T., & Russell, B. W. (2014). Determining Efficient Strut-and-Tie Models for Simply Supported Beams Using Minimum Strain Energy. *ACI Structural Journal*, 111(5), 1015.
25. Hwang, T. H., & Scribner, C. F. (1984). R/C member cyclic response during various loadings. *Journal of Structural Engineering*, 110(3), 477-489.
26. Karthik, M. M., & Mander, J. B. (2010). Stress-block parameters for unconfined and confined concrete based on a unified stress-strain model. *Journal of Structural Engineering*, 137(2), 270-273.
27. Karthik, M. M., Mander, J. B., & Hurlebaus, S. (2016). Displacement-Based Compatibility Strut-and-Tie Method and Application to Monotonic and Cyclic Loading. *Journal of Structural Engineering*, 142(6), 04016010.
28. Kent, D. C., & Park, R. (1971). Flexural members with confined concrete. *Journal of the Structural Division*.
29. Kim, J. H., & Mander, J. B. (1999). Truss modeling of reinforced concrete shear-flexure behavior. In *Technical Report MCEER* (No. 99-0005). United States. Multidisciplinary Center for Earthquake Engineering Research (MCEER).
30. Kim, J. H., & Mander, J. B. (2000). Cyclic Mastic Strut-Tie Modeling of Shear-Critical Reinforced Concrete Members. *Special Publication*, 193, 707-728.
31. Kong, F. K., Robins, P. J., Singh, A., & Sharp, G. R. (1972). Shear analysis and design of reinforced concrete deep beams. *The Structural Engineer*, 50(10), 405-409.
32. Krawinkler, H., & Popov, E. P. (1973). Hysteretic Behavior of Reinforced Concrete Rectangular and T-Beams. In *Proc. of 5th WCEE* (pp. 249-258).
33. Kuchma, D. A., & Tjhin, T. N. (2001). CAST (Computer Aided Strut-and-Tie) Design Tool. In *Structures 2001: A Structural Engineering Odyssey* (pp. 1-7).
34. Kwak, H. G., & Noh, S. H. (2006). Determination of strut-and-tie models using evolutionary structural optimization. *Engineering Structures*, 28(10), 1440-1449.
35. Ley, M. T., Riding, K. A., Bae, S., & Breen, J. E. (2007). Experimental verification of strut-and-tie model design method. *ACI Structural Journal*, 104(6), 749.
36. Liang, Q. Q., Uy, B., & Steven, G. P. (2002). Performance-based optimization for strut-tie modeling of structural concrete. *Journal of Structural Engineering*, 128(6), 815-823.
37. Lorensten, M. (1962). Holes in reinforced concrete girders. *Byggmastaren*, 41(7), 141-152.


38. Lu, Y., & Panagiotou, M. (2013). Three-dimensional cyclic beam-truss model for nonplanar reinforced concrete walls. *Journal of Structural Engineering*, 140(3), 04013071.
39. Lu, Y., & Panagiotou, M. (2016). Three-dimensional beam-truss model for reinforced concrete walls and slabs—part 2: modeling approach and validation for slabs and coupled walls. *Earthquake Engineering & Structural Dynamics*, 45(11), 1707-1724.
40. Lu, Y., Panagiotou, M., & Koutromanos, I. (2014). Three-Dimensional Beam-Truss Model for Reinforced-Concrete Walls and Slabs Subjected to Cyclic Static or Dynamic Loading (No. PEER Report 2014/18).
41. Lu, Y., Panagiotou, M., & Koutromanos, I. (2014). Three-Dimensional Beam-Truss Model for Reinforced-Concrete Walls and Slabs Subjected to Cyclic Static or Dynamic Loading (No. PEER Report 2014/18).
42. Lu, Y., Panagiotou, M., & Koutromanos, I. (2016). Three-dimensional beam-truss model for reinforced concrete walls and slabs—part 1: modeling approach, validation, and parametric study for individual reinforced concrete walls. *Earthquake Engineering & Structural Dynamics*, 45(9), 1495-1513.
43. Ma, S. Y. M., Popov, E. P., & Bertero, V. V. (1976). Experimental and analytical studies on the hysteretic behavior of reinforced concrete rectangular and T-beams. Berkeley, CA: University of California.
44. Mander, J. B., Priestley, M. J., & Park, R. (1988). Theoretical stress-strain model for confined concrete. *Journal of structural engineering*, 114(8), 1804-1826.
45. Mansour, M., Lee, J. Y., & Hsu, T. T. (2001). Cyclic stress-strain curves of concrete and steel bars in membrane elements. *Journal of Structural Engineering*, 127(12), 1402-1411.
46. Mansur, M. A. (1998). Effect of openings on the behaviour and strength of R/C beams in shear. *Cement and concrete composites*, 20(6), 477-486.
47. Mansur, M. A. (2006, September). Design of reinforced concrete beams with web openings. In *Proceedings of the 6th Asia-Pacific Structural Engineering and Construction Conference (ASPEC 2006)* (pp. 5-6).
48. Mansur, M. A., & Alwis, W. A. M. (1984). Reinforced fibre concrete deep beams with web openings. *International Journal of Cement Composites and Lightweight Concrete*, 6(4), 263-271.
49. Mansur, M. A., & Tan, K. H. (1999). *Concrete beams with openings: Analysis and design* (Vol. 20). CRC Press.
50. Mansur, M. A., Tan, K. H., & Lee, S. L. (1984). Collapse loads of r/c beams with large openings. *Journal of Structural Engineering*, 110(11), 2602-2618.
51. Marti, P. (1985). How to treat shear in structural concrete. *Structural Journal*, 96(3), 408-414.
52. Martin, B. T., & Sanders, D. H. (2007). Verification and implementation of strut-and-tie model in LRFD bridge design specifications. *NCHRP Project*, 20-07.
53. Massone, L. M., & Wallace, J. W. (2004). Load-deformation responses of slender reinforced concrete walls. *ACI Structural Journal-American Concrete Institute*, 101(1), 103-113.
54. Massone, L. M., Orakcal, K., & Wallace, J. W. (2009). Modeling of squat structural walls controlled by shear. *ACI Structural Journal*, 106(5), 646.
55. McKenna, F., Fenves, G. L., Scott, M. H., and Jeremic, B. (2000). OpenSees Version 2.3.2 [Computer software]. Berkeley, Univ. of California.
56. Moehle, J. P., Hooper, J. D., & Lubke, C. D. (2008). Seismic Design of Reinforced Concrete Special Moment Frames. *US Department of Commerce*.

57. Mondal, S., Bandyapadhyaya, J. N., & Gautam, C. P. (2011). Strengthening and rehabilitation of reinforced concrete beams with opening. *International Journal of Civil and Structural Engineering*, 2(1), 127.
58. Mörsch, E. (1902). Der eisenbetonbau, seine anwendung und theorie. *Wayss and Freytag, AG, Im selbstverlag der Firma, Neustadt ad Haardt, May.*
59. Muttoni, A., Schwartz, J., & Thürlimann, B. (1996). Design of concrete structures with stress fields. Springer Science & Business Media.
60. Nasser, K. W., Acavalos, A., & Daniel, H. R. (1967, January). Behavior and design of large openings in reinforced concrete beams. In *Journal Proceedings* (Vol. 64, No. 1, pp. 25-33).
61. Nielsen, M. P., Braestrup, M. W., Jensen, B. C., & Bach, F. (1978). Concrete plasticity, beam shear–shear in joints–punching shear. *Special Publication*, 1-129.
62. Panagiotou, Marios, et al. "Nonlinear cyclic truss model for reinforced concrete walls." *ACI Structural Journal* 109.2 (2012): 205.
63. Park, H., & Eom, T. (2007). Truss model for nonlinear analysis of RC members subject to cyclic loading. *Journal of Structural Engineering*, 133(10), 1351-1363.
64. Perera, R., & Vique, J. (2009). Strut-and-tie modelling of reinforced concrete beams using genetic algorithms optimization. *Construction and Building Materials*, 23(8), 2914-2925.
65. Pimanmas, A. (2010). Strengthening R/C beams with opening by externally installed FRP rods: Behavior and analysis. *Composite Structures*, 92(8), 1957-1976.
66. Popov, E. P., Bertero, V. V., & Krawinkler, H. (1972). Cyclic behavior of three RC flexural members with high shear. College of Engineering, University of California.
67. Prakhya, G. K. V., & Morley, C. T. (1990). Tension-stiffening and moment-curvature relations of reinforced concrete elements. *Structural Journal*, 87(5), 597-605.
68. Ritter, W. (1899). Die Bauweise Hennebique (Hennebiques Construction Method).
69. Salam, S. A. (1977). Beams with openings under different stress conditions. In *Proceeding of 3rd conference on our world in concrete and structures. CI-Premier. Singapore* (pp. 259-67).
70. Salem, H. M., & Maekawa, K. (2006). Computer-aided analysis of reinforced concrete using a refined nonlinear strut and tie model approach. *Journal of Advanced Concrete Technology*, 4(2), 325-336.
71. Schlaich, J., Schäfer, K., & Jennewein, M. (1987). Toward a consistent design of structural concrete. *PCI journal*, 32(3), 74-150.
72. Scott, R. M., Mander, J. B., & Bracci, J. M. (2012a). Compatibility strut-and-tie modeling: Part I-Formulation. *ACI Structural Journal*, 109(5), 635.
73. Scott, R. M., Mander, J. B., & Bracci, J. M. (2012b). Compatibility Strut-and-Tie Modeling: Part II-Implementation. *ACI Structural Journal*, 109(5), 645.
74. Shanmugam, N. E., & Swaddiwudhipong, S. (1988). Strength of fibre reinforced concrete deep beams containing openings. *International Journal of Cement Composites and Lightweight Concrete*, 10(1), 53-60.
75. Somayaji, S., & Shah, S. P. (1981, May). Bond stress versus slip relationship and cracking response of tension members. In *Journal Proceedings* (Vol. 78, No. 3, pp. 217-225).
76. Somes, N. F., & Corley, W. G. (1974). Circular openings in webs of continuous beams. *Special Publication*, 42, 359-398.
77. Standard, C. S. A. (1984). A23. 3-04. *Canadian standard association*, 232.
78. Tjhin, T. N., & Kuchma, D. A. (2007). Integrated analysis and design tool for the strut-and-tie method. *Engineering Structures*, 29(11), 3042-3052.

79. Tjokrodimuljo, K. (1985). Behavior of Reinforced Concrete Columns Under Cyclic Loading. Department of Civil Engineering, University of Auckland.
80. To, N. H. T. (2005). *Nonlinear structural analysis using strut-and-tie models* (Doctoral dissertation, ResearchSpace@ Auckland).
81. To, N. H. T., Ingham, J. M., & Sritharan, S. (2002). Strut-and-tie computer modelling of reinforced concrete bridge portal frames. *Bulletin of the New Zealand Society for Earthquake Engineering*, 35(3), 165-189.
82. To, N. H. T., Ingham, J. M., Davidson, B. J., & Sritharan, S. (2003)b. Cyclic strut-and-tie modeling of reinforced concrete structures. In *Pacific Conf. on Earthquake Engineering*.
83. To, N. H., Ingham, J. M., & Sritharan, S. (2003)a. Strut-and-tie computer modelling of reinforced concrete bridge joint systems. *Journal of earthquake engineering*, 7(03), 463-493.
84. To, N. H., Sritharan, S., & Ingham, J. M. (2009). Strut-and-tie nonlinear cyclic analysis of concrete frames. *Journal of structural engineering*, 135(10), 1259-1268.
85. Tuchscherer, R. G., Birrcher, D. B., & Bayrak, O. (2012). Experimental examination of ACI 318 strut and tie modeling provisions. In *Symposium Honoring James O. Jirsa's Contributions in Structural Concrete: A Time to Reflect at the ACI Spring 2012 Convention*. American Concrete Institute.
86. Tuchscherer, R. G., Birrcher, D. B., Williams, C. S., Deschenes, D. J., & Bayrak, O. (2014). Evaluation of existing strut-and-tie methods and recommended improvements. *ACI Structural Journal*, 111(6), 1451.
87. Vecchio, F. J., & Collins, M. P. (1986). The modified compression-field theory for reinforced concrete elements subjected to shear. *ACI J.*, 83(2), 219-231.
88. Visnjic, T. (2014). Design Considerations for Earthquake-Resistant Reinforced Concrete Special Moment Frames.
89. Visnjic, T., Antonellis, G., Panagiotou, M., & Moehle, J. P. (2016). Large Reinforced Concrete Special Moment Frame Beams under Simulated Seismic Loading. *ACI Structural Journal*, 113(3), 469.
90. Wight, J.K & MacGregor, J. G. (2012). *Reinforced concrete: mechanics and design*.
91. Yang, K. H., & Ashour, A. F. (2008). Effectiveness of web reinforcement around openings in continuous concrete deep beams. *ACI Structural Journal*, 105(4), 414.
92. Yun, Y. M. (1999). Nonlinear strut-tie model approach for structural concrete. *Structural Journal*, 97(4), 581-590.
93. Yun, Y. M. (2000). Computer graphics for nonlinear strut-tie model approach. *Journal of Computing in Civil Engineering*, 14(2), 127-133.

Appendix A- Material Properties

This appendix provides concrete mix design proposal. Additionally, mill certificate from the reinforcement and the tensile test results obtained from Twining Laboratories Inc. are also provided.



18030 Mt. Washington Boulevard
Fountain Valley, California 92780

To Place an Order, Call:
(800) PRE-MIXX

CONCRETE MIX DESIGN PROPOSAL

CONTRACTOR: Hadrian Construction
Attention Anne Lemtizer

PROJECT: U.C. Irvine
Irvine, CA

MIX USE: Appendix A5

PLANT MANAGER: Don Baillie -- (714) 966-0231
BATCH PLANT: Fountain Valley ~ #45

DATE: January 15, 2013
MIX DESIGN #: 19946
MAX SIZE AGG: 3/8"
DESIGN STRENGTH: 6000 Psi @ 28 days
W/(C+P): 0.40
SLUMP: 5.0" (+/- 1.0")
PLACEMENT METHOD: Pump (3" line) / Place

MATERIAL SOURCES:
CEMENT: ASTM C-150 Type II/V
FLY ASH: ASTM C-618 Class F
COARSE AGGREGATE: Hanson, Irwindale
FINE AGGREGATE: Hanson, Irwindale
ADMIXTURES: Euclid Chemical Co.

PRIMARY AGGREGATE GRADATION
(%Passing U.S. Standard Sieve)

SIZE:	1.5"	1.0"	3/8"	WCS	COMB.
Agg%:	0%	0%	35%	65%	100%
2.0"	100	100	100	100	100
1.5"	98	100	100	100	100
1.0"	22	95	100	100	100
3/4"	8	46	100	100	100
3/8"	2	1	92	100	97
#4		1	15	99	70
#8			3	81	54
#16			2	59	39
#30			1	39	25
#50			1	19	12
#100				6	4
#200				3	2
F.M.	7.92	7.52	5.88	2.97	3.99

CONCRETE MIX DESIGN FOR 1 CUBIC YARD (SSD BASIS)

MATERIAL:	SP.GR.	ABS.VOL.	BATCH WT.	
		CU.FT.	LBS.	
Cement:	9.90	Sks. 3.15	4.02	791
Fly Ash:	15.0%	"F" 2.30	0.97	140
1.5" Agg.:	0.0%	2.65	0.00	0
1.0" Agg.:	0.0%	2.66	0.00	0
3/8" Agg.:	35.0%	2.65	5.48	906
W/C Sand:	65.0%	2.66	10.18	1689
Water:	44.5	Gal. 1.00	5.94	371
Air %	1.50%		0.41	
Totals:		27.00	3897	

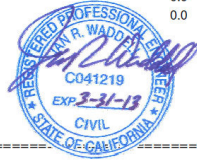
ADMIXTURE:

			Dosage Range:	
Eucon WR-75	4.0	fl.oz./100# cmt.	2-6 oz / 100wt	37.22
Admix No. 2	0.0	fl.oz./100# cmt.		0.0
Admix No. 3	0.0	fl.oz./100# cmt.		0.0

NOTES:

PERTINENT PROPERTIES:

Unit Weight, pcf:	Cementitious Factor:	W/(C+P):
Plastic: 144.3 PCF	9.90 Sk/Cu. Yd.	0.40 By Wt.
	15.0% Replacement	4.49 Gal/Sack



REMARKS: Mix design requested by Anne Lemtizer @ U.C. Irvine.

Technical Services Manager: **Robert Graine**

PREPARED BY: **Brandon Agles** **MIX DESIGN NUMBER:** 19946

Technical Services

**This mix is a recommendation only. It should perform as indicated so long as the maximum slump is not exceeded. This mix should be approved by the structural engineer or architect. The soils report was not shared or disclosed to Associated RMC. Dosage(s) of admixture(s) may be adjusted to compensate for variable jobsite conditions (per manufacturer's recommendations). Please note that aggregate weights may change slightly due to required adjustments in gradations or changes in specific gravity.

Please send test results to: (949) 580-1804 -- 25901 Towne Centre Dr. -- Foothill Ranch, California 92610; Bagles@AssocRMC.com

This mix design represents a combination of materials evaluated and established in accordance with section 19058.3.1.1 Method B of the California Building Code. This mix is to be used only as designated, with no substitutions or additions. This mix to be used only for the job address indicated or as approved. FAILURE TO ADHERE TO ASTM STANDARDS IN SAMPLING, SLUMP, MAKING AND CURING SAMPLES, TRANSPORTING SAMPLES AND TESTING WILL RESULT IN A SUBSTANTIAL REDUCTION IN COMPRESSIVE STRENGTHS LISTED ABOVE. Notes: SOUTHWEST SPECIAL TESTING HAS NOT SEEN THE SOILS REPORT FOR THE PROJECT CONTRACTOR MUST ADHERE TO THE GUIDELINES OF UBC TABLE 19.

REBAR ENGINEERING, INC.
REBAR ENGINEERING, INC.
 10706 PAINTER AVE SANTA FE SPRINGS, CA. 90670
 TEL (562) 946-2461 FAX (562) 941-7740
 LICENSE NO. 25-4219

PHYSICAL AND CHEMICAL TEST REPORT

DATE: 01/25/13

JOB NAME: UCI RESEARCH

CONTRACTOR: UCI - ATTN: ACCT DEPT

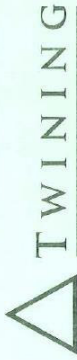
CONTRACT#: 2200 **RELEASES:** 1,1A,2,2A,3,3A,4,4A

ADDRESS:

Inch/Lb SIZE	Metric SIZE	HEAT No	WEIGHT	MILL	GRADE	YIELD POINT	TENSILE STRENGTH	ELNGTN IN 8"	BEND	C	MN	P	S	CE
3	10	1220788401		NUCOR (U)	60	70,365	110,745	13.00	O.K.	0.40	0.95	0.013	0.047	0.560
COIL 3	COIL 10	1290011595		NUCOR (AZ)	60/A706	67,785	99,447	17.00	O.K.	0.24	1.14	0.017	0.035	0.450
COIL 4	COIL 13	1290011880		NUCOR (AZ)	60/A706	67,582	99,969	17.00	O.K.	0.27	1.19	0.012	0.032	0.490
4	13	1210496501		NUCOR (U)	60	78,111	115,879	16.00	O.K.	0.41	1.14	0.014	0.022	0.630
COIL 5	COIL 16	1290011543		NUCOR (AZ)	60/A706	65,412	101,908	15.00	O.K.	0.29	1.25	0.018	0.039	0.520
7	22	1220515901		NUCOR (U)	60	64,613	106,524	15.00	O.K.	0.41	1.16	0.011	0.045	0.630
8	25	1210402801		NUCOR (U)	60	66,406	110,368	16.00	O.K.	0.44	1.17	0.018	0.039	0.670
9	29	1210752201		NUCOR (U)	60	66,959	107,120	18.00	O.K.	0.41	1.18	0.011	0.036	0.610
10	32	1210502101		NUCOR (U)	60	66,470	108,367	14.00	O.K.	0.43	1.18	0.016	0.047	0.650
10	32	4019923		CMC	60	82,100	106,300	11.00	O.K.	0.33	1.02	0.011	0.024	0.560

TOTAL WEIGHT 0
 ALL MATERIALS CONFORM TO: ASTM A615
 NEW BILLET STEEL OR ASTM A706 - 93A & 93B.

GENERATED BY: NAOMI
 WE CERTIFY THE ABOVE RESULTS TO BE CORRECT AS CONTAINED IN
 THE ORIGINAL MILL TEST REPORT IN THE RECORDS OF THE COMPANY.



Long Beach 562.426.3355 / Sacramento 916.649.9000 / San Bernardino 909.383.6660
 San Diego 858.974.3759 / Ventura 805.644.5100 / www.twininginc.com

W01-13-096604
 LAB ID STICKER

DATA SHEET FOR TENSION/BEND TESTING OF METAL SPECIMENS

CLIENT: VOI CLASS TL JOB NO: DAVIDING 1306041
 JOB NAME: _____ DSA FILE NO: _____
 ADDRESS: _____ DSA APPL /OSHPD/PERMIT NO: _____
 ARCHITECT: _____ CONTRACTOR: _____
 ENGINEER: _____ STEEL CONTRACTOR: _____
 TYPE OF MATERIAL: REBAR PRESTRESS STRAND STRUCTURAL STEEL OTHER

SPECIFICATION: _____
 REPRESENTING COMPANY: _____
 SAMPLED BY: Helmut Engineering DELIVERED BY: Client
 SAMPLED AT: Rebar Engineering HOURS/UNITS: _____
 DATE SAMPLED: 7/13 TIME: _____ RECEIVED ON: 8/30/13

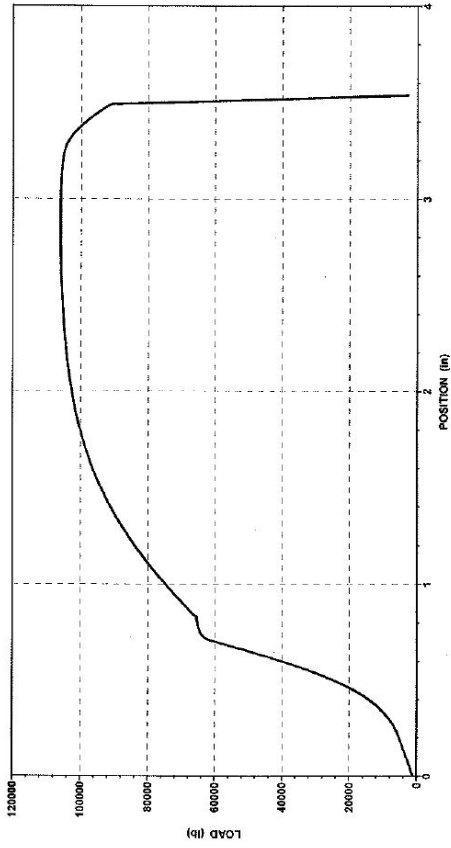
STEEL DESC. OR SIZE	ASTM SPEC.	SPEC & GRADE FROM		MACHINED DIMENSIONS, in	AREA (sq.in.)	MFR. OR MILL	HEAT NO.	PACK / COIL NO.	WEIGHT (lbs)	STRENGTH		T/Y or Y/T or Min. Req'd Stress (°)	EL. %	G.L. in.	BEND / MOE-10 ⁶
		MATL	CERT							YIELD (Y)	TENSILE (T)				
9	A615	60		1.00	1.00	N/A				64,300	105,940	16.75%			X
8				0.79						66,500	110,300	20.3%			
7				0.60						66,700	108,300	19%			

COMPLIANCE: MATERIAL COVERED BY THIS REPORT COMPLIES DOES NOT COMPLY WITH ASTM SPECIFICATION.
 TESTED BY: Sean Kelly DATE TESTED: 9-5-13 TEST METHOD: A370 EQUIPMENT NO: Satec
 (*) Check for: Tensile/Yield for ASTM A706 (1.25 minimum); Yield/Tensile for ASTM A992 (0.85 maximum); Required Stress for ASTM A1035 (60,000 psi minimum at 0.0085 in/in strain).
 REMARKS: * Needs load vs displacement graph
 TL labform TL-lab07 steel 4FEB09

TWINING, INC
3310 AIRPORT WAY, LONG BEACH, CA 90806

Specimen #: _____
OPERATOR: _____
JOB NAME: _____
Geometry: _____
Gage Length: _____
Area: _____

S. KELLEY
VCI
Area
8.0000 in
1.0000 sq in



Date: 09/05/13

Time: 10:07:01
Elapsed: 00:02:10

Peak Load
Peak Stress
Max. Elong. @ Break

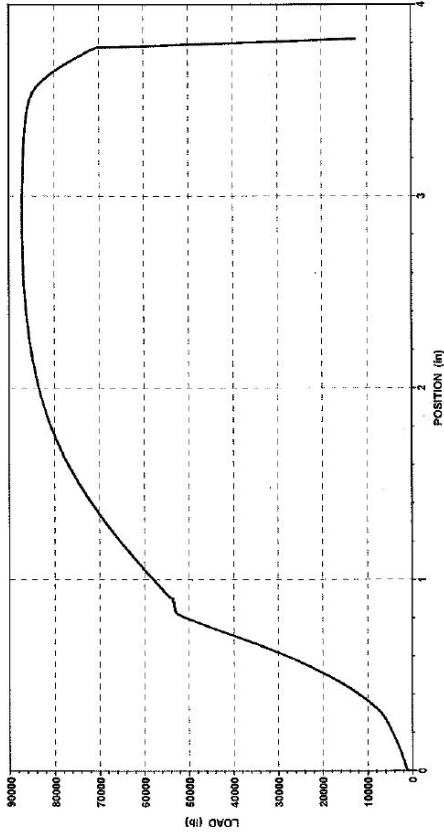
105940 lb
10995 psi
16.75 %

TWINING INC
3310 AIRPORT WAY, LONG BEACH, CA 90806

Specimen #: S.KELLEY
OPERATOR: VCI
JOB NAME: Area
Geometry: 8.0000 in
Gage Length: 0.7900 sq in
Area:

Time: 10:19:17
Elapsed: 00:01:56

Date: 09/05/13



Peak Load: 87100 lb
Peak Stress: 110235 Psi
Max. Elong.: @ Break

87100 lb
110235 Psi
@ Break

TWINING INC
3310 AIRPORT WAY, LONG BEACH, CA 90806

Specimen #:
OPERATOR:
JOB NAME:
Geometry:
Gage Length:
Area:

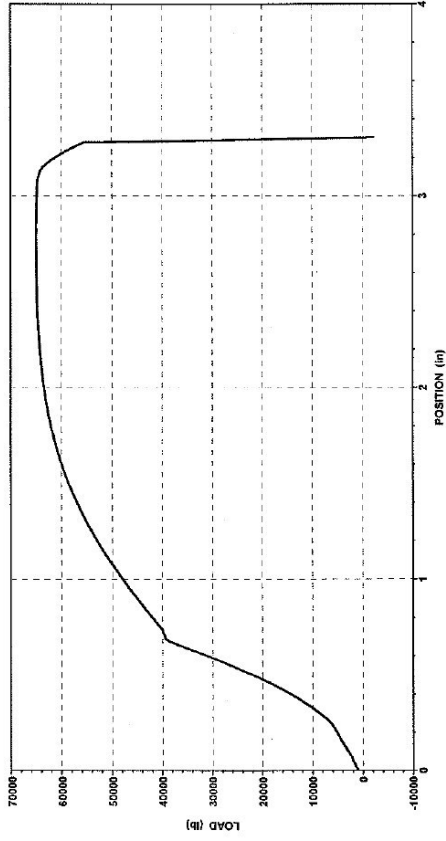
S. KELLEY
VCI
Area
8.0000 in
0.6000 sq in

Date: 09/05/13

Time: 10:23:05
Elapsed: 00:01:31

Peak Load
Peak Stress
Max. Elong. @ Break

65000 lb
108333 MPa
19.00 %



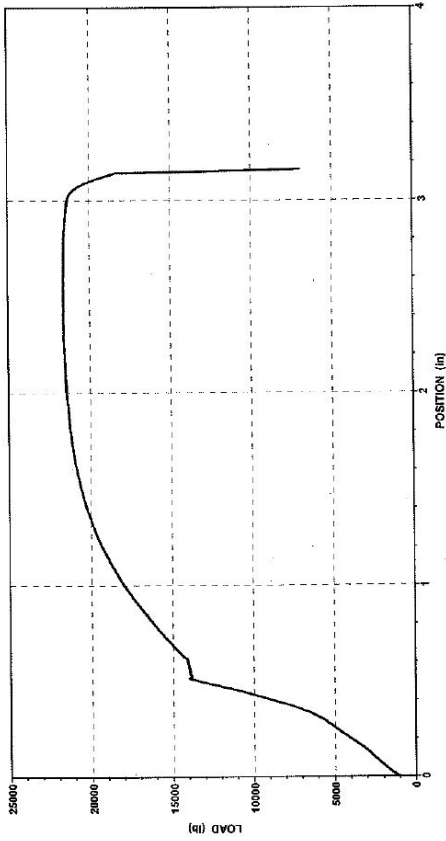
TWINING INC
3310 AIRPORT WAY, LONG BEACH, CA 90806

Specimen #:
OPERATOR:
JOB NAME:
JOB NUMBER:

Geometry:
Gage Length:
Area:

S. KELLEY
UCI

Area
8.0000 in
0.2000 sq in



Date: 09/12/13

Time: 14:05:14
Elapsed: 00:02:12

Peak Load
Peak Stress
Max. Elong. @ Break
Yield-Halt of Force

21600 lb
108000 psi
15.83 %
68630 psi